

THESE

Pour l'obtention du grade de
DOCTEUR DE L'UNIVERSITÉ DE POITIERS
UFR des sciences fondamentales et appliquées
Pôle poitevin de recherche pour l'ingénieur en mécanique, matériaux et énergétique - PPRIMME
(Diplôme National - Arrêté du 7 août 2006)

École doctorale : SIMMEA - Sciences et ingénierie en matériaux, mécanique,
énergétique et aéronautique
Secteur de recherche : Génie mécanique, productique, transports

Cotutelle : Universitatea politehnica (Bucarest)

Présentée par :
Daniela Georgeta Coblaș

Procedures for the rheological characterization of the nonlinear behaviour of complex fluids in shear and squeeze flows

Directeur(s) de Thèse :
Mohamed Hajjam, Corneliu Bălan

Soutenue le 01 novembre 2012 devant le jury

Jury :

Président	Constantin Bulac	Profesorul, Universitatea Politehnica București
Rapporteur	Benyebka Bou-Saïd	Maître de conférences, INSA de Lyon
Rapporteur	Romeo Susan-Resiga	Profesorul, Universitatea Politehnica Timișoara
Membre	Mohamed Hajjam	Professeur des Universités, Université de Poitiers
Membre	Corneliu Bălan	Profesorul, Universitatea Politehnica București
Membre	Aurelian Fatu	Maître de conférences, Université de Poitiers
Membre	Alexandru Rădulescu	Maitre de conferințe, Universitatea Politehnica București

Pour citer cette thèse :

Daniela Georgeta Coblaș. *Procedures for the rheological characterization of the nonlinear behaviour of complex fluids in shear and squeeze flows* [En ligne]. Thèse Génie mécanique, productique, transports . Poitiers : Université de Poitiers, 2012. Disponible sur Internet <<http://theses.univ-poitiers.fr>>



UNIUNEA EUROPEANĂ



GUVERNUL ROMÂNIEI
MINISTERUL MUNCII, FAMILIEI
ȘI PROTECȚIEI SOCIALE
AMPFUNDRIU



Fondul Social European
POSDRU 2007-2013



Instrumente Structurale
2007-2013



MINISTERUL
EDUCAȚIEI
CERCETĂRII
TINERETULUI
ȘI SPORTULUI



UNIVERSITATEA "POLITEHNICA"
din BUCUREȘTI

FONDUL SOCIAL EUROPEAN

Investește în oameni!

Programul Operațional Sectorial pentru Dezvoltarea Resurselor Umane 2007 – 2013

Proiect POSDRU/88/1.5/S/60203 – Dezvoltarea de cariere științifice competitive prin programe de burse doctorale (COMPETE)



UNIVERSITATEA POLITEHNICA DIN BUCUREȘTI

Facultatea Inginerie Energetică

Catedra Hidraulică, Mașini Hidraulice și Ingineria Mediului

UNIVERSITE DE POITIERS

Ecole Doctorale SI-MMEA

Institut P³ - UPR 3346



Nr. Decizie Senat _____ din _____

TEZĂ DE DOCTORAT

Procedures for the Rheological Characterization of the Nonlinear Behavior of Complex Fluids in Shear and Squeeze Flows

Proceduri pentru Caracterizarea Comportamentului Reologic Neliniar al Fluidelor Complexe în Mișcări de Forfecare și Expulzare

Autor: **Ing. DANIELA GEORGETA COBLAȘ**

COMISIA DE DOCTORAT

Președinte	Prof. dr. eng. Constantin BULAC	de la	Universitatea Politehnica București
Conducător de doctorat-1	Prof. dr. eng. Corneliu Bălan	de la	Universitatea Politehnica București
Conducător de doctorat-2	Prof.dr.eng. Mohamed Hajjam	de la	Université de Poitiers, France
Referent	Prof. dr. eng. Bou-Said Benyabka	de la	INSA-Lyon, France
Referent	Prof. dr. eng. Romeo Susan-Resiga	de la	Universitatea Politehnica Timișoara
Referent	Conf. dr. eng. Aurelian Fătu	de la	Université de Poitiers, France
Referent	Conf. dr. eng. Alexandru Rădulescu	de la	Universitatea Politehnica București

București 2012

I dedicate this thesis to my wonderful mother.

Aknowlegements

Dear reader, I am very grateful for the attention you dedicate to read these lines, because saying “*thanks!!!*” is the most important thing when people around are showing you kindness and encouragement. You have to know that when I look back at the three years dedicated to this thesis I have a smile on my face thinking at all the great people that I met during this time, at all the things I have learned and all the places I have visited. I certainly believe that this PhD is like a gift for me, for the person I am now and the one I will be later on.

During the elaboration of this thesis I have received advices and encouragements from many people to whom I express my sincere consideration and to which I will be grateful each time I will read my thesis, talk about it or remember the PhD years.

Firstly I would like to express my deep and sincere gratitude to my principal thesis advisor, *Prof. Corneliu Bălan* for his continuously support, for the encouragement I received from his part, the enthusiasm and immense knowledge that he shares with us, the students. I also want to thank him for all the priceless advices about science, about life and the philosophy necessary to understand and live with both of them.

I wish to express my warm and sincere thanks to my thesis advisor *Prof. Mohamed Hajjam* for his guidance that started long before this thesis, during the preparation of my license project. Without his inestimable guidance, without his patience, flexibility, genuine and valuable kindness I would have not stepped in the doors of “science” and “research” that brought me here today.

I owe my deepest gratitude to *Conf. Diana Broboană* for her infinite friendship, for the scientific, administrative and financial support that she offered me unconditionally during this three years. I hope that over the years to come I will still enjoy this beautiful friendship from this wonderful person.

This thesis would not have been possible without the unconditioned scientific support and friendship that I have received from *Conf. Alexandru Rădulescu*, to whom I want to express my heartfelt gratitude.

It is a pleasure to thank *Hdr. Aurelian Fătu* for all the help I received from his part, the generosity with which he helped me during my license dissertation and thesis stages in Angouleme, for his friendship, understandings and encouragements.

I am very grateful to *Dr. Tiberiu Bărbat* for his priceless and essential help in numerical simulations I conducted with Fluent software.

I warmly thank my colleagues from REOROM group, especially *Dr. eng. Cătălin Bălan*, *Dr. eng. Roland Kadar* and *Dr. eng. Cătălin Mărculescu* for their unconditioned support and for providing a stimulating and fun-filled environment without whom even the most dedicated PhD student loses motivation.

I would like to thank also to all the members of *Structures and Interfaces Team*, LMS from *Poitiers University*, to all the members of the *Hydraulic Machines and Environmental Engineering Department* from *Polytechnica University* and all the professors and colleagues who have helped me with my work and received me with open arms and beautiful smiles when I needed the most.

Last, but by no means least, I thank my family and my friends for all their understanding, their never fading support and the love that they showed me not only during the last three years.

I owe my loving thanks to my mother, to *David* and to my best friends *Mirela*, *Dana* and *Iosif* for their caring, concern, friendship and love.

Thank you!

SCIENTIFIC WORK

ISI Papers:

1. **Coblaș D.**, Broboană D., Bălan C., *Simple shear of materials characterized by steady non-monotonous flow curve*, Proceedings of the seventh International Symposium on Advanced Topics in Electrical Engineering, ISSN 2068-7966, Bucharest, 12-14, May, 2011, pp. 121-124.
2. **Coblaș D.**, Broboană D., Bălan C., *Characterization of yield state in soft matter*. Appl. Rheology, submitted paper

Published B+ and BDI articles:

1. **Coblaș D.**, Cristea A., *Theoretical analysis of film squeeze for a stepped pin immersed in a newtonian fluid*. U.P.B Scientific Bulletin, Series D - accepted for publication.
2. **Coblaș D.**, Bălan C., *Numerical and experimental analyse of viscous fluids in oscillatory squeezing flow*. Mathematical Modeling in Civil Engineering - Scientific Journal, Volume 7 - No. 1-2, March, 2011, 8 pp.
3. **Coblaș D.**, Broboană D., Bălan C., *Characterization of viscous fluids in oscillatory squeezing flows*. U.P.B Scientific Bulletin, Series D, Vol. 72, No 3, Bucharest, Romania, 2010, pp. 176-184.
4. **Coblaș D.**, Hajjam M., Rădulescu A., *Slip/no-slip influence on the behavior of a radial bearing with a static load. EHD analyzes*. Innovative Technology – Machine Building, Vol. 61/ 2-3, Bucharest, Romania, 2009, pp. 51-54.
5. **Coblaș D.**, Fătu A., Rădulescu A., *Slip/no-slip influence on the behavior of a radial bearing with a static load. HD analyzes*. Innovative Technology – Machine Building, Vol. 61/2-3, Bucharest, Romania, 2009, pp. 55-58.

Papers in international conference proceedings:

1. **Coblaș D.**, Hajjam M., Rădulescu A., Bălan C., *Experimental investigation of pure viscous fluids in constant velocity squeeze flow*, Proceedings of the International Conference BALTTTRIB'2011, Lithuania, 17-19, November, 2011, 7 pp.
2. **Coblaș D.**, Broboană D., Bălan C., *Yield-stress fluids behavior analyze in large amplitude oscillatory shear flow*. Proceedings of « Le 45-eme colloque anuel de Group Francais de Rheologie (GFR) », Lyon, France, 3-5, November, 2010, 4 pp.
3. **Coblaș D.**, Broboană D., Rădulescu A., *Oscillatory squeeze flow: experimental and numerical analyzes*. Proceedings of « Le 45-eme colloque anuel de Group Francais de Rheologie (GFR) », Lyon, France, 3-5, November, 2010, 4 pp.

Papers in national conference proceedings:

1. **Coblaș D.**, Broboană D., Bălan C., Hajjam M., *Numerical simulations of constant velocity squeeze flow*. Proceedings of the 7th Hydro-Energetic Romanian Conference, Dorin Pavel, Bucharest, Romania, 24-25, Mai, 2012, pp. 116-125.
2. **Coblaș D.**, Broboană D., Bălan C., *Rheology of yield stress fluids: experiments, constitutive relation, numerical simulations*, Proceedings of the 33rd "Caius Iacob" Conference on Fluid Mechanics and its Technical Applications, Bucharest, Romania, 29-30, September, 2011, pp. 43-49.
3. **Coblaș D.**, Broboană D., Bălan C., *Rheology of yield stress fluids: constitutive relations and experiments*. Proceedings of the 2nd Summer School of Rheology (SSR), Vol. II, Iași, Romania, 28 August – 3 September, 2011, pp. 58-67.
4. Broboană D., **Coblaș D.**, Bălan C., *Rheology of complex fluids characterized by non-monotonous flow curve*, Proceedings of the Conference: Dynamics of Complex Fluids, Iași, Romania, 5-7, May, 2011, pp. 30-40.

5. **Coblaș D.**, Broboană D., Bălan C., *Rheological analysis of lubricants in oscillatory squeeze flows*. Proceedings of the 1st Summer School of Rheology (SSR), Vol. I, Cluj-Napoca, Romania, 26-29, August, 2010, pp. 111-112.
6. **Coblaș D.**, Broboană D., Bălan C., *Rheological characterization of viscous fluids in oscillatory squeezing flows*. Proceedings of the 6th Hydro-Energetic Romanian Conference, Dorin Pavel, Bucharest, Romania, 2010, pp. 113-120.

International Congresses:

1. **Coblaș D.**, Broboană D., Bălan C., *Rheology of complex fluids with discrete viscosity function*. Proceedings of the XVIth International Congress on Rheology, Lisabon, Portugal, 5-10, August, 2012. (book of abstracts). *Oral presentation*.
2. Broboană D., **Coblaș D.**, Bălan C., *Numerical rheometry of complex fluids with yield stress*. Poster session at the XVIth International Congress on Rheology, Lisabon, Portugal, 5-10, August, 2012. (book of abstracts). *Poster session*

International Conferences:

3. **Coblaș D.**, Broboană D., *Numerical solutions of non-newtonian flows in thin films*. Minilubes Scientific Workshop, Iași, Romania, 23-23, April, 2012. *Oral presentation*.
4. **Coblaș D.**, Broboană D., Bălan C., *Viscosity function of materials with apparent yield stress*, Non-Newtonian Fluid Mechanics: Progress and Challenges, Portmeirion, U.K., 18april 2011 - 20april 2011. *Poster Session*.
5. **Coblaș D.**, Broboană D., Bălan C., *Rheological characterization of yield stress fluids using oscillatory tests*. DRG Annual Meeting, Berlin, Germany, 31 March – 01 April, 2011 (book of abstracts). *Oral presentation*.
6. **Coblaș D.**, Broboană D., Bălan C., *Transient viscosity function of biocompatible creams and pastas*. Proceedings of the 4th International Conference “Biomaterials, Tissue Engineering & Medical Devices” BiomMedD, Sinaia, Romania, 23-25, September, 2010, pp. 119. *Oral presentation*.
7. Broboană D., **Coblaș D.**, Bălan C., *Hemodynamics of coronary stented artery*. Proceedings of the 4th International Conference “Biomaterials, Tissue Engineering & Medical Devices” BiomMedD, Sinaia, Romania, 23-25, September, 2010, pp. 148. *Poster session*.

Editor:

1. Bălan C., Broboană D., **Coblaș D.**, *Proceedings of the 1st Summer School of Rheology – SSR 2010*, Vol. I. Cluj-Napoca, Romania, 26-29, August, 2010, ISSN 2066-5790. Also part of organizing comitee.
2. Bălan C., Broboană D., **Coblaș D.**, *Proccedings of the 2nd Summer School of Rheology - SRR 2011*, Vol. II. Bucarest and Iași, Romania, 28 August – 3 September, ISSN 2066-5790.
3. Bălan C., Broboană D., **Coblaș D.**, *Proceedings of CNCS-UEFISCDI Exploratory Workshop Program: “Actual research topics in fluid mechanics in relation to hystory and philosophy of science”*. Sinaia, Romania, 5-8, June, 2012, ISSN 2066-5790.

National and International funding:

The work has been funded by the Sectoral Operational Programme Human Resources Development 2007-2013 of the Romanian Ministry of Labour, Family and Social Protection through the Financial Agreement **POSDRU/88/1.5/S/60203**.

Scientific Afiliations:

Romanian Society of Rheology, SRR – since 2009

Groupe Francais de Rheologie, GFR – since 2009

TABLE OF CONTENTS

Aknowlegements	i
SCIENTIFIC WORK.....	iii
LIST OF FIGURES	4
LIST OF TABLES	13
LIST OF NOTATIONS.....	14
Chapter 1. INTRODUCTION	17
1.1. THE CONTEXT OF THIS STUDY AND ITS MOTIVATION	17
1.2. THESIS STRUCTURE.....	19
Chapter 2. RHEOLOGY AND RHEOMETRY.....	21
2.1. CAUCHY'S EQUATION OF MOTION AND THE STRESS TENSOR.....	22
2.2. RHEOLOGICAL PROPERTIES OF SIMPLE AND COMPLEX FLUIDS	24
2.3. RHEOMETRY – TESTING PROCEDURES FOR SIMPLE AND COMPLEX FLUIDS.....	29
2.3.1. Viscometric motions.....	29
2.3.2. Extensional motions	35
2.3.3. Complex motions – squeeze of fluid films.....	36
2.4. NON-LINEAR VISCOELASTICITY	40
2.4.1. Large amplitude oscillatory shear tests	44
2.5. ADHERENCE AND CAPILLARITY PHENOMENA.....	45
2.5.1. Capillarity phenomena and surface tension.....	46
2.5.2. Adherence and contact angle.....	50
Chapter 3. SQUEEZE FLOW	53
3.1. CURRENT STAGE OF RESEARCH	55
3.1.1. Squeeze flow applications.....	55
3.1.2. Rheological squeeze tests and configurations of the testing geometries	57
3.2. THEORETICAL CONSIDERATIONS.....	58
3.2.1. Analytical formulation of squeeze motion in various geometries	58
3.2.2. Influence of contact surfaces inclination.....	64
3.2.3. Influence of adherence	69
3.2.4. Presence of inertial effects	73
3.2.5. Squeeze flow for generalised Newtonian fluids and viscoelastic fluids	73
Chapter 4. NUMERICAL MODELLING OF SQUEEZING FLOW PHENOMENON	77
4.1. DESCRIBING THE NUMERICAL PROCEDURES – NUMERICAL CODE FLUENT.....	78
4.1.1. Volume of fluids method (VOF).....	79
4.1.2. End Effects. Superficial tension and contact angle in numerical simulation of real flows.....	81
4.2. GEOMETRY DEFINITION AND FLOW DOMAIN MESHING	82
4.2.1. Description of geometries used for single phase numerical simulations.....	83
4.2.2. Description of geometries used for multiphase numerical simulations.....	86
4.3. NUMERICAL STUDY OF OSCILLATORY SQUEEZE FLOW	88

Contens

4.3.1. Comparative analysis between numerical solutions and theoretical predictions for Newtonian fluids	88
4.3.2. The oscillatory squeezing flow of generalized Newtonian fluids	92
4.3.3. Nonlinear behavior of viscoelastic samples in oscillatory squeezing flow	95
4.3.4. End effects obtained numerically for oscillatory squeeze flow	98
4.3.5. Free surface evolution in oscillatory squeeze flow simulations	100
4.4. NUMERICAL MODELING OF CONSTANT VELOCITY SQUEEZE FLOW	104
4.4.1. Qualitative and quantitative analysis between transient and quasi-steady approximations.....	104
4.4.2. End effects in single phase constant velocity squeeze flow	107
4.4.3. Multiphase modeling of simple squeeze flow	108
4.5. COMPARISON BETWEEN NUMERICAL SOLUTIONS: GENERALIZED REYNOLDS EQUATION AND NAVIER-STOKES EQUATIONS FOR OSCILLATORY SQUEEZE FLOW	117
4.5.1. Results obtained for Newtonian fluids	119
4.5.2. Results obtained for Carreau-Yasuda model	120
4.6. CONCLUSIONS	122
Chapter 5. EXPERIMENTAL INVESTIGATIONS OF SQUEEZE FLOW	124
5.1. EXPERIMENTAL SETUPS AND TESTING PROCEDURES	124
5.1.1. Devices and procedures for oscillatory squeezing flow	124
5.1.2. Instrumentation and procedures for constant velocity squeezing flow	127
5.2. PURE VISCOUS FLUIDS RHEOLOGY IN OSCILLATORY SQUEEZING TESTS..	130
5.3. THE RHEOLOGY OF COMPLEX FLUIDS IN OSCILLATORY SQUEEZING FLOW.....	136
5.4. THE RHEOLOGICAL BEHAVIOR OF NEWTONIAN FLUIDS IN CONSTANT VELOCITY SQUEEZE FLOW	140
5.4.1. Establishing the reliability domain depending on the fluid film thickness	141
5.4.2. Dimensionless force formulation	142
5.4.3. Free surface influence in constant velocity squeeze flow	146
5.5. COMPLEX FLUIDS RHEOLOGY IN SIMPLE SQUEEZE FLOW	149
5.6. CONCLUSIONS	151
Chapter 6. NONLINEAR BEHAVIOR OF COMPLEX FLUIDS IN SHEAR TESTS	153
6.1. MATERIALS AND METHODS	153
6.2. NONLINEAR VISCOELATIC BEHAVIOR IN DYNAMIC SHEAR TESTS	155
6.3. NONLINEAR VISCOELASTICITY IN SIMPLE SHEAR FLOWS	162
6.4. FOURIER ANALYSIS AND INVESTIGATION OF SLIP OCCURRENCE	166
6.5. CONCLUSIONS	168
Chapter 7. THE INFLUENCE OF SURFACE MICROSTRUCTURE ON THE SQUEEZING FORCE	172
7.1. THE INFLUENCE OF SURFACE MICROSTRUCTURE ON NEWTONIAN FLUIDS ADHESION PROPERTY	172
7.1.1. The experimental setup	172
7.1.2. Contact angle between various Newtonian sample and micro-structured surfaces.....	174
7.2. CONSTANT VELOCITY SQUEEZE FLOW IN THE PRESENCE OF MICRO- STRUCTURED SURFACES.....	175

Contens

7.3. NUMERICAL SIMULATION OF CONSTANT VELOCITY SQUEEZE FLOW IN THE PRESENCE OF MICRO-STRUCTURED SURFACES	179
7.3.1. The construction and meshing of the flow domain	179
7.3.2. Simulation results for mineral oil sample.....	180
7.4. CONCLUSIONS	183
Chapter 8. FINAL CONCLUSIONS	184
8.1. GENERAL ASPECTS	184
8.2. PRACTICAL APPLICATIONS OF SQUEEZE FLOW MOTION	186
8.3. ORIGINAL CONTRIBUTIONS	186
8.4. FURTHER DEVELOPMENT OF THE STUDY	188
Bibliography	189
ANNEXES 1	
ANNEX 1. Rheological models dependency on their constitutive parameters.....	A.1
ANNEX 2. Approximation of the experimental modules of a viscoelastic fluid by a <i>Maxwell</i> model with 8 elements	A.2
ANNEX 3. Determination of radial and axial velocity formulations for the simple squeeze flow of newtonian fluids between paralel plates.	A.4
ANNEX 4. Geometries construction and meshing for single phase quasi-steady approximation of squeeze flow simulations. Influence of the free surface geometry.	A.9
ANNEX 5. Generalized Reynold Equations	A.12
ANNEX 6. The evolution of the free surface for all Newtonian samples in constant velocity squeeze flow, at all speeds.....	A.14
ANNEX 7. Cream and polysiloxane microstructure, before and after a simple shear test ...	A.25
ANNEX 8. Microstrucured surfaces details.....	A.25

LIST OF FIGURES

Fig. 1.1. Rheological characterization of fluids using experimental measurements, numerical modeling and analytical constitutive models.	188
Fig. 2.1. Variation of shear stress (a) and of viscosity function (b) depending on the rheological behavior of fluids.....	26
Fig. 2.2. Variation of viscosity function (a) and shear stress (b) for different rheological models.	27
Fig. 2.3. Maxwell (a) and Kelvin-Voigt (b) analogical models.	27
Fig. 2.4. The Maxwell model with “ <i>m</i> ” elements connected in parallel.	28
Fig. 2.5. The schematic representation of the viscometric motion of the incompressible Newtonian fluids in various geometries used in usual rheometric tests: <i>Hagen-Poiseuille</i> flow in a capillary tube (a) and the <i>Couette</i> rotation flow in a geometry with coaxial cylinders (b), a cone-plate geometry (c) and a plate-plate geometry (d).	30
Fig. 2.6. The applied shear stress (a) and the variation of the strain rate (b) for a Polysiloxane sample, results obtained following a Creep test, at $T = 20^{\circ}\text{C}$	31
Fig. 2.7. The imposed shear rate (a) and relaxation of stress (b) for a Polysiloxane sample, results obtained following a Relaxation test, at $T = 20^{\circ}\text{C}$	32
Fig. 2.8. Phase angle variation for different types of materials (a) and complex modulus definition depending on its elastic and viscous components (b).	33
Fig. 2.9. Approximation of the experimental modules G' and G'' for a viscoelastic solution with the <i>Maxwell</i> model with 8 elements, with variable relaxation time steps, at different amplitudes of the applied strain: $\gamma_0 = 0.01$ [–] (a); $\gamma_0 = 0.1$ [–] (b) and $\gamma_0 = 1$ [–] (c).....	34
Fig. 2.10. Usual geometries used in extensional tests: forming of fluid filaments on horizontal (a) and vertical directions (b, c); aspiration of fluids in tubes with small diameters (d).....	35
Fig. 2.11. Fluid squeezed between two parallel surfaces.	37
Fig. 2.12. Squeeze of a fluid between two parallel surfaces in case of a constant area squeeze flow (a) and of a constant volume of fluid (b).....	39
Fig. 2.13. Illustration of the non-linear behavior of complex fluids with yield stress σ_0 by the material flow curve (non-monotonous variation $\sigma(\gamma)$).....	41
Fig. 2.14. Deformation of stress output signal for complex in large amplitude oscillatory shear flow. The input deformation signal is a pure sinusoid with increasing strain amplitude.....	42
Fig. 2.15. Variation of complex moduli components depending on the type of rheological behavior associated to the material: strain thinning (a); strain hardening (b); weak strain overshoot (c); strong strain overshoot (d).....	43
Fig. 2.16. The Lissajous diagram for viscous and viscoelastic fluids at different values of the	44
Fig. 2.17. Action of cohesion forces over liquid molecules, inside it and at the.....	46
Fig. 2.18. Effects of capillarity and superficial stress: breaking of a jet and formation of drops (a); formation of spherical drops when breaking soap bubbles (b); water column rising in capillary tubes (c); transport and retention of fluids in plants capillaries (d); formation of foams and emulsions (e); floating small objects on the water surface (f); adhesion between the polymeric wires of a brush (g).....	47
Fig. 2.19. Deformation of any free area under the action of the superficial stress forces (a) and the raising phenomenon of a fluid in a capillary vessel of circular section.....	48
Fig. 2.20. Rising of fluid on a solid wall (a) and formation of the meniscus (hydrodynamic bridge) between two solid surfaces (b).....	49
Fig. 2.21. The contact angle in a liquid-solid-gaseous system and its variation depending on the no slip properties of the solid surface (from total adherence – left side, to perfect slip – right side).....	50
Fig. 2.22. Velocity profile on the fluid film thickness in a plane shear motion for various fluid-solid adherence conditions: no slip (a); partial slip (b); perfect slip (c).	51

List of Figures

Fig. 3.1. Axial-symmetric squeeze flow of a fluid between two solid surfaces of different sizes.	58
Fig. 3.2. Immersed plates geometries (in the volume of fluid).	58
Fig. 3.3. The squeeze flow of a viscous fluid of thickness h_0 between parallel plane discs (axial symmetric flow with $v_r \gg v_z$).	59
Fig. 3.4. Flow of a viscous fluid in the thin layer of thickness h_0 between two solid surfaces.	60
Fig. 3.5. The oscillatory squeeze flow of a viscous fluid of thickness h_0 between parallel plane discs.	62
Fig. 3.6. The squeeze flow of a viscous fluid of thickness h_0 between two parallel plates of infinite length (axially symmetric motion with $h_0 \ll B$, $h_0 \ll L$, $v_r \gg v_z$).	63
Fig. 3.7. The squeeze flow of a viscous fluid of thickness h_0 between an annular surface and a plane circular surface (axially symmetric motion with $v_r \gg v_z$).	63
Fig. 3.8. The squeeze flow of a viscous fluid of thickness h_0 between a spherical surface and a plane disc (symmetrical axial flow with $h_0 \ll R$ and $v_r \gg v_z$).	64
Fig. 3.9. The squeeze flow of a viscous fluid due to the immersion of a solid plate into a fluid tank.	65
Fig. 3.10. The squeeze flow of a viscous fluid of thickness h_0 between two discs. The upper disc is inclined with the angle α	67
Fig. 3.11. Plane squeeze flow (2D) of a viscous fluid of thickness h_0 between two discs. The lower disc is inclined with the angle α	68
Fig. 3.12. Plane squeeze flow (2D) of a viscous fluid of thickness h_0 between two discs. The lower disc is inclined with the angle α	68
Fig. 3.13. Form of fluid blocks in the squeeze flow for visco-plastic materials: in the presence of a sheared fluid layer in the vicinity of walls (a) and in its absence (b).	74
Fig. 4.1. Quasi-steady approximation sketch of the unsteady constant velocity squeeze flow.	79
Fig. 4.2. The computation of cell volume fraction α_A and the interpolation of two fluid phases interface.	80
Fig. 4.3. The S1 geometry used for the numerical simulation of the oscillatory squeezing flow, boundary conditions definition and the meshed flow area.	84
Fig. 4.4. S2 and S3 geometries used for the unsteady constant velocity squeeze flow, boundary conditions definition and the meshed flow area.	84
Fig. 4.5. CS1 geometry used for the quasi-steady approximation of constant velocity squeeze flow: boundary conditions definition and the meshed flow area (a); variation of geometry dimensions depending on the initial film thickness (b).	85
Fig. 4.6. VOF1 geometry used for two phase simulation of oscillatory squeezing flow: construction and meshing of the flow area (a); defining the fluid phases (b).	86
Fig. 4.7. VOF2 geometry used for two phase simulation of constant velocity squeezing flow: construction and meshing of the flow area (a); setting the boundary conditions (b); defining the fluid phases (c).	87
Fig. 4.8. Viscosity dependence on the testing temperature for mineral oil.	89
Fig. 4.9. The maximum amplitude of the force signal obtained by numerical simulations and using the analytical expression for different values of h_0 , ω_s , and a constant input amplitude of $\varepsilon_0 = 0.75 \mu m$	89
Fig. 4.10. The maximum amplitude of the force signal obtained by numerical simulations and using the analytical expression (a) and the relative errors between them (b) for different values of h_0 , ε_0 , constant oscillatory frequency of $\omega_s = 10 Hz$ (simulation time step $Ts = 2 \cdot 10^{-4}$	90
Fig. 4.11. The maximum amplitude of the force signal obtained by numerical simulations and using the analytical expression (a) and the relative errors between them (b) for different values of ε_0 , a constant oscillatory frequency of $\omega_s = 10 Hz$ and $h_s = 150 \mu m$	91
Fig. 4.12. Computational time step influence on the relative error between numerical simulation results and analytical predictions for different values of oscillatory frequency ω_s , constant oscillatory amplitude $\varepsilon_s = 0.75 \mu m$ and two different gaps: $h_s = 300 \mu m$ (a) și $h_s = 150 \mu m$ (b).	91

List of Figures

Fig. 4.13. Computational time step influence on the relative error between numerical simulation results and analytical predictions for different values of oscillatory amplitude ε_0 , constant oscillatory frequency $\omega_s = 10 \text{ Hz}$ and $h_s = 150 \mu\text{m}$	92
Fig. 4.14. PAA rheology in shear tests: complex viscosity and shear stress variation (a); storage and loss modulus variation (b).....	92
Fig. 4.15. Experimental force and displacement signals for mineral oil sample (a) and PAA sample (b) in oscillatory squeezing flow motion at $h_s = 300 \mu\text{m}$, $\varepsilon_0 = 0.30 \mu\text{m}$, $\omega_s = 10 \text{ Hz}$	93
Fig. 4.17. Radial velocity vectors distribution trough the gap and along plate radius for the Newtonian mineral oil sample (a) and a polymer sample described by Carreau-Yasuda model (b).....	94
Fig. 4.16. Force and displacement signals obtained trough numerical simulation of the oscillatory squeezing flow for a polymer sample described by the Carreau-Yasuda model at $h_0 = 300 \mu\text{m}$, $\varepsilon_0 = 0.30 \mu\text{m}$ and $\omega_s = 10 \text{ Hz}$	95
Fig. 4.18. Viscosity dependence on shear rate (a) and the flow curve, usual curve for positive flow index and with the occurrence of a plateau for negative flow index (b) for different parameters of the rheological Carreau-Yasuda model which can approximate the behavior of polymer solutions.....	95
Fig. 4.19. Quasi-steady linear $n > 0$ (a1,b1,c1) and nonlinear $n < 0$ (a2,b2,c2) behavior of a polymer solution described by the generalized Newtonian Carreau-Yasuda model (PAA1, PAA2, see Table 4.2). The results are obtained from numerical simulations of oscillatory squeezing flow characterized by $h_0 = 150 \mu\text{m}$, $\omega_s = 10 \text{ Hz}$ și $\varepsilon_0 = 0.30 \mu\text{m}$ (a), $\varepsilon_0 = 0.60 \mu\text{m}$ (b), $\varepsilon_0 = 0.90 \mu\text{m}$ (c).....	97
Fig. 4.20. Quasi-steady linear $n > 0$ (a1,b1) and nonlinear $n < 0$ (a2,b2) behavior of an emulsion described trough generalized Newtonian Carreau-Yasuda model (Cream1, Cream2, see Table 4.2). The results are obtained from numerical simulations of oscillatory squeezing flow characterized by $h_0 = 150 \mu\text{m}$, $\omega_s = 10 \text{ Hz}$ and $\varepsilon_0 = 0.60 \mu\text{m}$ (a) respectively $\varepsilon_0 = 0.90 \mu\text{m}$ (b).....	98
Fig. 4.21. Pressure distribution on upper and lower walls obtained numerically, in comparison with the analytical formulation at: $h_0 = 300 \mu\text{m}$ (a), $h_0 = 150 \mu\text{m}$ (b), $h_0 = 50 \mu\text{m}$ (c). Results for oscillatory squeezing flow of mineral oil at $\omega_s = 10 \text{ Hz}$ and $\varepsilon_0 = 0.75 \mu\text{m}$	99
Fig. 4.22. Iso-pressure lines in the gap (in the vicinity of the outlet zone) obtained trough the numerical simulation of the oscillatory squeezing flow of mineral oil at $\omega_s = 10 \text{ Hz}$, $\varepsilon_0 = 0.75 \mu\text{m}$, and different initial film thickness: $h_0 = 50 \mu\text{m}$ (a), $h_0 = 150 \mu\text{m}$ (b), $h_0 = 300 \mu\text{m}$ (c).....	99
Fig. 4.23. Oil-air interface evolution (for a complete oscillation) obtained for the numerical simulation of oscillatory squeezing flow ($h_0 = 150 \mu\text{m}$, $\omega_s = 10 \text{ Hz}$, $\varepsilon_0 = 0.90 \mu\text{m}$,) in the absence of gravity by using GR scheme (a) and in the presence of gravitational effects by using CICSAM scheme (b).....	101
Fig. 4.24. Force signal obtained trough numerical simulations of single and multiphase squeeze flow. Numerical results are compared with the analytical predictions and the experimental measurements for the following conditions: $h_0 = 150 \mu\text{m}$, $\omega_s = 10 \text{ Hz}$, $\varepsilon_0 = 0.90 \mu\text{m}$	102
Fig. 4.25. Oil-air interface and velocity vector distributions obtained for oscillatory squeezing flow in the presence of surface tension and liquid-solid contact angle ($h_0 = 150 \mu\text{m}$, $\omega_s = 10 \text{ Hz}$, $\varepsilon_0 = 0.90 \mu\text{m}$). Case F1: Solver GGCB, GR scheme for interface tracking; Cae F2: Solver GGNB, GR scheme for interface tracking; Case F3: Solver GGNB, CICSAM scheme for interface tracking.....	103
Fig. 4.26. Normal force dependence on film thickness and squeeze velocity obtained numerically using transient and quasi-steady approximations of the constant velocity squeeze motion of mineral oil.....	104
Fig. 4.27. Radial velocity distribution in the gap, for the mineral oil sample, at a constant squeezing velocity of $\dot{h} = 0.01 \text{ mm/s}$ and $h = 0.1 \text{ mm}$. Comparison between analytical solution and the numerical simulations using a quasi-steady approximation (case a) and.....	105

List of Figures

Fig. 4.28. Axial velocity distribution in the gap, for the mineral oil sample, at a constant squeezing velocity of $\dot{h} = 0.01 \text{ mm/s}$ and $h = 0.1 \text{ mm}$. Comparison between analytical solution and the numerical simulations using a quasi-steady approximation (case a) and.....	105
Fig. 4.29. Pressure distribution on the upper wall for the mineral oil sample at a constant squeezing velocity of $\dot{h} = 0.01 \text{ mm/s}$ and $h = 0.1 \text{ mm}$. Comparison between analytical solution and the numerical simulations using a quasi-steady approximation (case a) and.....	106
Fig. 4.30. Different shapes of the free surface in squeeze motion, observed experimentally (red curve) and as considered by most of the numerical solutions and analytical model.....	107
Fig. 4.31. Pressure distribution on upper and lower walls (a) and pressure isolines in the gap (b) for the transient numerical solution of constant velocity squeeze flow, mineral oil sample	107
Fig. 4.32. Pressure distribution on upper and lower walls (a) and pressure isolines in the gap (b) for the transient numerical solution of constant velocity squeeze flow, mineral oil sample	108
Fig. 4.33. Pressure distribution on upper and lower walls (a) and pressure isolines in the gap (b) for the transient numerical solution of constant velocity squeeze flow, mineral oil sample	108
Fig. 4.34. Oil-air interface and velocity vectors obtained numerically for the constant velocity squeeze flow using VOF2 geometry with different boundary conditions: two pressure outlet zones - red line (a) and a single outlet zone (b, c). The simulation settings imply the use of Pressure-Based solver with GGNC model and GR (a, b) and CICSAM (c) interface tracking methods. The simulation is performed without taking into account gravity, surface tension or contact angle.....	109
Fig. 4.35. The development of oil-air interface obtained trough numerical simulation of constant velocity squeeze flow ($\dot{h} = 1 \text{ mm/s}$) without.....	111
Fig. 4.36. Development of oil-air interface obtained trough numerical simulation of constant velocity squeeze flow ($\dot{h} = 1 \text{ mm/s}$) for different wetting conditions imposed on the lower walls, (corresponding to case D1, D2 and D3 – see Figure 4.37-4.38).....	112
Fig. 4.37. The development of oil-air interface obtained trough numerical simulation of constant velocity squeeze flow ($\dot{h} = 1 \text{ mm/s}$), in the presence of gravity and surface tension, using different slip conditions: no slip condition on all walls (case D1); partial slip, only on the external lower wall (case D2); almost perfect slip on the entire lower surface (case D3). Comparison with the experimental visualizations for $h \in 0.892 \div 0.306 \text{ mm}$	113
Fig. 4.38. The development of oil-air interface obtained trough numerical simulation of constant velocity squeeze flow ($\dot{h} = 1 \text{ mm/s}$), in the presence of gravity and surface tension, using different slip conditions: no slip condition on all walls (case D1); partial slip, only on the external lower wall (case D2); almost perfect slip on the entire lower surface (case D3). Comparison with the experimental visualizations for $h \in 0.210 \div 0.01 \text{ mm}$	114
Fig. 4.39. The variation of the upper plate displacement Δh_{wall} and the advance of the fluid column on the margin Δh_{fluid} with fluid film thickness. Comparison between experimental measurements and numerical simulation results for the constant velocity squeeze flow ($\dot{h} = 1 \text{ mm/s}$), using different wetting conditions (see case D1, D2 and D3).....	115
Fig. 4.40. The development of oil-air interface obtained trough numerical simulation of constant velocity squeeze flow ($\dot{h} = 1 \text{ mm/s}$) in comparison with the analytical predictions. Results are obtained in the presence of gravity and surface tension, using different adherence conditions: perfect adherence (a); almost no adherence (b).	115
Fig. 4.41. Radial velocity distribution in the gap, for the mineral oil sample, at a constant squeezing velocity of $\dot{h} = 0.01 \text{ mm/s}$ and $h = 0.1 \text{ mm}$. Comparison between numerical simulations: single phase quasi-steady approximation (case a);	

List of Figures

	transient multiphase approximation with no slip condition (case b), transient multiphase approximation with perfect slip condition (case c).....	116
Fig. 4.42.	Axial velocity distribution in the gap, for the mineral oil sample, at a constant squeezing velocity of $\dot{h} = 0.01 \text{ mm/s}$ and $h = 0.1 \text{ mm}$. Comparison between numerical simulations: single phase quasi-steady approximation (case a); transient multiphase approximation with no slip condition (case b), transient multiphase approximation with perfect slip condition (case c).....	116
Fig. 4.43.	Normal force distribution for constant velocity squeeze flow ($\dot{h} = 1 \text{ mm/s}$) of mineral oil sample. Comparison between numerical simulations results in both single and multi phase modes and the experimental measurements performed at different testing temperatures.....	117
Fig. 4.44.	Winteracter console and the affichage of input data for numerical simulations with the personalized code created in Fortran.....	118
Fig. 4.45.	Comparison between numerical simulations results obtained with FORTRAN code and analytical predictions. Oscillatory squeeze flow of mineral oil sample, $h_0 = 300 \text{ }\mu\text{m}$, $\omega_s = 10 \text{ Hz}$ and:.....	119
Fig. 4.46.	Comparison between numerical simulations results obtained with FORTRAN code (red dots), analytical predictions (black line) and numerical simulations obtained with FLUENT code for a larger (green dots) and a smaller time step (blue dots). Oscillatory squeeze flow of mineral oil sample, $h_0 = 300 \text{ }\mu\text{m}$, $\varepsilon_0 = 0.75 \text{ }\mu\text{m}$, and $\omega_s = 20 \text{ Hz}$ (a); $\omega_s = 30 \text{ Hz}$ (b).	120
Fig. 4.47.	Comparison between numerical simulations results obtained with FORTRAN code (red dots), analytical predictions (black line) and numerical simulations obtained with FLUENT code for a larger (green dots) and a smaller time step (blue dots). Oscillatory squeeze flow of mineral oil sample, $h_0 = 150 \text{ }\mu\text{m}$, $\omega_s = 10 \text{ Hz}$ and: $\varepsilon_0 = 1 \text{ }\mu\text{m}$ (a); $\varepsilon_0 = 10 \text{ }\mu\text{m}$ (b).....	120
Fig. 4.48.	Results obtained with Fortran Code, for a Carreau-Yasuda fluid in oscillatory squeezing flow ($h_0 = 150 \text{ }\mu\text{m}$, $\omega_s = 10 \text{ Hz}$ and different ε_0). The parameters (PAA3) are indicated in Table 4.2.....	121
Fig. 4.49.	Results obtained with Fortran Code, for a Carreau-Yasuda fluid in oscillatory squeezing flow ($h_0 = 150 \text{ }\mu\text{m}$, $\omega_s = 10 \text{ Hz}$). The parameters (PAA3 and PAA 4) are indicated in Table 4.2. Comparison between a positive and negative flow index of the constitutive model, at $\varepsilon_0 = 0.90 \text{ }\mu\text{m}$ (a) and force signals obtained for a negative flow index and different oscillatory amplitudes.....	121
Fig. 5.1.	Micro Fourier Rheometer- MFR 2100 (a) and the parallel plate.....	124
Fig. 5.2.	Outline drawing of MFR 2100 rheometer.	125
Fig. 5.3.	Experimental scheme of the setup used for oscillatory squeezing flow.	127
Fig. 5.4.	Physica MCR 301Rheometer: experimental setup (a) and the parallel plate.....	128
Fig. 5.5.	Schematic representation of the Peltier system used temperature control.	129
Fig. 5.6.	Experimental force and displacement signals obtained in oscillatory squeezing flow of mineral oil sample at $\varepsilon_0 = 0.30 \text{ }\mu\text{m}$, $\omega_s = 10 \text{ Hz}$, $h_0 = 300 \text{ }\mu\text{m}$	130
Fig. 5.7.	Filtered force signal obtained in oscillatory squeezing flow of mineral oil sample	131
Fig. 5.8.	Comparison between experimental and theoretical force (a) and displacement (b) signals obtained in oscillatory squeezing flow of mineral oil sample.....	131
Fig. 5.9.	Displacement signal fitting (a), by using 5000 (b) or 10.000 points (b) for the interpolation. The results correspond to an oscillatory squeezing test of mineral oil sample at $\varepsilon_0 = 0.75 \text{ }\mu\text{m}$, $\omega_s = 10 \text{ Hz}$ and $h_0 = 300 \text{ }\mu\text{m}$	132
Fig. 5.10.	Comparison between theoretical and experimental force signals for mineral oil sample in oscillatory squeezing flow: different initial film thickness, $h_0 = 150 \text{ }\mu\text{m}$ (a, b, c) and $h_0 = 300 \text{ }\mu\text{m}$ (d, e, f); different values of oscillatory displacement amplitude, $\varepsilon_0 = 0.30 \text{ }\mu\text{m}$ (a, d), $\varepsilon_0 = 0.60 \text{ }\mu\text{m}$ (b, e), $\varepsilon_0 = 0.90 \text{ }\mu\text{m}$ (c, f) and $\omega_s = 10 \text{ Hz}$	133
Fig. 5.11.	Experimental and corresponding theoretical force magnitude (a) and force amplitude difference (b), as function of ω_s and ε_0 at $h_0 = 300 \text{ }\mu\text{m}$. Values extracted from the signals for mineral oil sample investigations in oscillatory squeezing flow tests.....	134

List of Figures

Fig. 5.12. Comparison between theoretical and experimental force signals (measured and corrected) for glycerin sample in oscillatory squeezing flow at $h_0 = 300 \mu m$; $\omega_s = 10 \text{ Hz}$, and different values of oscillatory displacement amplitude: $\varepsilon_0 = 0.30 \mu m$ (a), $\varepsilon_0 = 0.45 \mu m$ (b), $\varepsilon_0 = 0.60 \mu m$ (c), $\varepsilon_0 = 0.75 \mu m$ (d), $\varepsilon_0 = 0.90 \mu m$ (e), $\varepsilon_0 = 1 \mu m$ (f).	135
Fig. 5.13. Chemical structure of polysiloxane (PDMS).	136
Fig. 5.14. Time dependent displacement and force signals obtained in oscillatory squeezing flow of PAA sample at $h_0 = 300 \mu m$, $\omega_0 = 10 \text{ Hz}$ and different oscillatory amplitudes: $\varepsilon_0 = 0.30 \mu m$ (a).	137
Fig. 5.15. Time dependent displacement and force signals obtained in oscillatory squeezing flow of PS sample at $h_0 = 300 \mu m$, $\varepsilon_0 = 1 \mu m$ and different oscillatory frequencies: $\omega_s = 1 \text{ Hz}$ (a), $\omega_s = 5 \text{ Hz}$ (b) and $\omega_s = 10 \text{ Hz}$ (c).	138
Fig. 5.16. Lissajous figures obtained in oscillatory squeezing flow for the mineral oil (a) and	138
Fig. 5.17. Lissajous figures obtained in oscillatory squeezing flow for the PS sample. The curves correspond to $h_0 = 300 \mu m$, $\varepsilon_0 \in 0.75 \div 1 \mu m$ and different oscillatory frequencies, $\omega_s = 1 \text{ Hz}$ (a), $\omega_s = 3 \text{ Hz}$ (b), $\omega_s = 5 \text{ Hz}$ (c), $\omega_s = 7 \text{ Hz}$ (d), $\omega_s = 10 \text{ Hz}$ (e) and to $h_0 = 300 \mu m$, $\varepsilon_0 = 1 \mu m$	139
Fig. 5.17. Lissajous figures obtained in oscillatory squeezing flow for the PAA sample	140
Fig. 5.19. Comparison between experimental measurements and theoretical predictions for mineral oil sample in constant velocity squeeze flow ($\dot{h} = 0.01 \text{ mm/s}$) at different temperature values. Establishing the reliability domain depending on the fluid film thickness.	141
Fig. 5.20. Comparison between experimental measurements and theoretical predictions for mineral oil sample in constant velocity squeeze flow ($\dot{h} = 0.01 \text{ mm/s}$) and $T = 10 \div 20^\circ\text{C}$.	141
Fig. 5.21. Comparison between experimental measurements and theoretical predictions for mineral oil sample in constant velocity squeeze flow at different temperature values and $\dot{h} = 0.1 \text{ mm/s}$ (a); $\dot{h} = 1 \text{ mm/s}$. (b)	142
Fig. 5.22. Dimensionless experimental values (using different viscosity coefficients) and theoretical predictions for mineral oil sample in constant velocity squeeze flow at $\dot{h} = 0.01 \text{ mm/s}$ and $T = 20^\circ\text{C}$.	143
Fig. 5.23. Dimensionless experimental values and theoretical predictions for mineral oil sample in constant velocity squeeze flow at $\dot{h} = 0.01 \text{ mm/s}$ and different temperatures.	143
Fig. 5.24. Dimensionless experimental values and theoretical predictions for mineral oil sample in constant velocity squeeze flow at different temperatures and: $\dot{h} = 0.1 \text{ mm/s}$ (a), $\dot{h} = 1 \text{ mm/s}$ (b).	144
Fig. 5.25. Dimensionless experimental values and theoretical predictions for glycerin sample in constant velocity squeeze flow at different temperatures and: $\dot{h} = 0.01 \text{ mm/s}$ (a),	144
Fig. 5.26. Dimensionless experimental values and theoretical predictions for honey in constant velocity squeeze flow at different temperatures and: $\dot{h} = 0.001 \text{ mm/s}$ (a),	145
Fig. 5.27. Master curve representing the dimensionless experimental and theoretical force distribution for all investigated Newtonian samples in constant velocity squeeze flow at different temperatures:	146
Fig. 5.28. Free surface development depending on film thickness (h) for the glycerin solution in constant velocity squeeze flow, $\dot{h} = 1 \text{ mm/s}$.	147
Fig. 5.29. Free surface evolution during constant velocity squeeze flow ($\dot{h} = 0.1 \text{ mm/s}$) for mineral oil (a), glycerin (b) and honey (c). The captured images correspond to the beginning of the test (a1, b1, c1); an intermediate observational time (a2, b2, c2) and the end of the test (a3, b3, c3).	148
Fig. 5.30. Comparison between experimental measurements and analytical predictions (Power-Law model) of squeezing force for the analyzed samples (IK, PS, CR and GEL) at different squeezing velocities $\dot{h} = 0.01 \text{ mm/s}$ (a), $\dot{h} = 1 \text{ mm/s}$ (b).	149

List of Figures

Fig. 5.31. Comparison between experimental measurements and analytical predictions (Power-Law model) of squeezing force for the CR (a) and PS (b) samples at different squeezing velocities.....	150
Fig. 5.32. Squeeze viscosity for: Newtonian fluids (honey - MI, glycerin - GL, oil - IK),(a); PS sample (b); cosmetic cream sample CR (c) and gel sample (d).....	152
Fig. 6.1. Dynamic strain sweeps at constant angular frequency, $\omega = 1 \text{ rad/s}$ (a) and $\omega = 10 \text{ rad/s}$ (b): cosmetic cream (CR), polysiloxane (PS), lanolin (LN) and glycerin (GL). Hollow marks indicate the points where the Lissajous figures were extracted.	155
Fig. 6.2. Oscillatory shear stress output for CR sample as function of the strain amplitude input $\omega = 1 \text{ rad/s}$, corresponding to the points selected in Figure 6.1.	156
Fig. 6.3. Dynamic strain sweeps at various angular frequency values for CR (a) and PS (b) sample. The delimitation of the flow regimes as function of the input strain amplitude and shear stress variation.....	157
Fig. 6.4. Dynamic strain sweeps at various angular frequency values for CR (a,b) and PS (c,d) sample. The delimitation of the flow regimes as function of the input strain amplitude: storage modulus (a,c)	158
Fig. 6.5. Lissajous figures, oscillatory stress vs. oscillatory strain, for CR sample corresponding to the points indicated in Figure 6.1, $\omega = 1 \text{ rad/s}$. (a); the detail P3 point marks the onset of non-linearity (b).....	159
Fig. 6.6. Lissajous figures, oscillatory stress vs. oscillatory strain, for PS sample corresponding to the points indicated in Figure 6.1, $\omega = 1 \text{ rad/s}$. (a). And a detail on P4 and P5 points (b).	159
Fig. 6.7. Normalized Lissajous figures corresponding to the maximum of G'' for CR and PS samples at $\omega = 1 \text{ rad/s}$ (see Figure 6.1).	160
Fig. 6.8. Dynamics moduli vs. angular frequency in SAOS regime for CR and PS samples: gel structure for CR, respectively transition region for PS.	161
Fig. 6.9. Area of Lissajous figures vs. strain amplitude for the tested sample, oscillatory stress vs. oscillatory strain (a) and oscillatory stress vs. oscillatory shear rate (b) at $\omega = 1 \text{ rad/s}$	161
Fig. 6.10. Transient up (filled points) and down (hollow points) flow curves (shear stress vs. shear rate) for CR sample (stress controlled experiments at $\sigma \in 1 \div 400 \text{ Pa}$).	162
Fig. 6.11. Critical strain value emphasized for CR sample in shear experiments (see Figure 6.10): applied shear stress vs. strain (a) and strain vs. time (b).....	163
Fig. 6.12. Time dependent viscosity curves obtained through multiple Creep tests for PS sample.....	164
Fig. 6.13. Viscosity dependence on shear rate for PS sample and the interpolation of the measured values using Carreau-Yasuda model: comparison between dynamic shear tests (strain controlled) and simple shear tests (stress controlled), (a); construction of a transient flow curve from multiple	164
Fig. 6.14. Quasi-steady flow curve for PS sample (multiple stress and strain controlled shear tests).	165
Fig. 6.15. Creep curves performed for the PS sample: a) constant shear stress, see Fig. 7; b) shear stress sweep. In both experiments is emphasized the same value of critical strain, i.e. $\gamma_{cr} \cong 3$ [-].....	165
Fig. 6.16. Answers of CR sample in oscillatory tests under different experimental conditions (strain/stress amplitude sweep $\omega = 1 \text{ rad/s}$), see also Figure 6.1.	166
Fig. 6.17. Frequency sweep (controlled strain and controlled stress experiments) for CR sample. The corresponding values of loss tangent are: $\tan\delta = 2.6$ (point A – controlled strain), respectively $\tan\delta = 0.52$ (point B – controlled stress), see Figure 6.16.	167
Fig. 6.18. Shear stress amplitude and loss tangent in frequency sweep test at different input strain amplitudes (CR sample). It is important to remark that rheological characteristics recorded in the stress controlled experiment from Figure 6.17 are also found in the strain controlled test, see location of point B in the two graphs.	167

List of Figures

Fig. 6.19. The normalized Fourier harmonics extracted from stress input (a) and strain input (b) tests at $\omega = 1 \text{ rad/s}$. The results mark the same interval for critical values of strain, respectively stress, amplitudes from which the materials start to flow.	168
Fig. 6.20. The evidence of plateau behavior in the topology of Lissajous figures shear stress vs. shear rate for CR sample: a) well defined flow behavior at $\sigma_0 > 120 \text{ Pa}$, b) detail with the transition/plateau domain (input stress amplitude tests at $\omega = 1 \text{ rad/s}$).	169
Fig. 6.21. Doubled Lissajous figures for different imposed stress magnitude. In the flow domain the difference between two consecutive tests is sharp increasing, see Figure 22, which suggest.....	170
Fig. 6.22. The difference in maximum rate magnitude between two consecutive cycles of oscillatory tests performed at imposed stress amplitude. In detail is shown the variation of maximum rate amplitude with the shear stress. The region were possible slip can be observed follows the instability domain, which is associated with the plateau.	171
Fig. 7.1. Video acquisition system used to determine the influence of surface microstructure on Newtonian fluids contact angle: experimental assembly (a) silicon surface micro textured (b) and micro-spiral (c).	173
Fig. 7.2. Contact angle determination by measurements of the droplet height and the radius of circle segment corresponding fluid-solid contact, performed using <i>Image-Pro</i> software.	173
Fig. 7.3. Influence of surface microstructure on Newtonian fluids contact angles: water (a1, a2, a3), glycerin (b1, b2, b3), honey (c1, c2, c3), mineral oil (d1, d2, d3). The contact surfaces have different micro architectures: plane surface (a1, b1, c1, d1); micro-textured surface (a2, b2, c2, d2); micro-spiral surface (a3, b3, c3, d3). All images correspond to an observational time of 80 s at which the drop is considered to have reached steady state value.	174
Fig. 7.4. <i>Re</i> number variation in constant velocity squeeze flow of mineral oil (a) and honey (b) at $\dot{h} \in 0.001 \div 2 \text{ mm/s}$	176
Fig. 7.5. Normal force dependency on film thickness for a mineral oil sample during simple squeeze tests at $\dot{h} \in 0.005 \div 1 \text{ mm/s}$, $T = 20^\circ\text{C}$ and $h_0 = 1 \text{ mm}$. Surface microstructure influence on the normal force: plane plate (P_{SI}), micro-textured plate (P_{TXT}), micro-spiral plate (P_{SP})	177
Fig. 7.6. Normal force dependency on film thickness for a honey during simple squeeze tests at $\dot{h} \in 0.01 \div 0.1 \text{ mm/s}$, $T = 20^\circ\text{C}$ and $h_0 = 2 \text{ mm}$. Surface microstructure influence on the normal force: plane plate (P_{SI}), micro-textured plate (P_{TXT}), micro-spiral plate (P_{SP})	178
Fig. 7.7. Influence of patterned surfaces on shear viscosity of pure viscous, mineral oil sample (a) and viscoelastic, PAA solution (b) in simple and oscillatory shear tests	179
Fig. 7.7. Construction of geometries and meshing of floe area for the micro-spiral geometry: top view of the lower plate (a); 3D arbitrary view of the geometry (b); transversal section of the mesh at $z=0$ with detail on the outlet zone (c)	180
Fig. 7.8. Transversal iso-surface construction (at $z = 0$) for numerical results representation of the simple squeeze flow of mineral oil (a), pressure distribution in the gap for a squeezing velocity of $\dot{h} = 1 \text{ mm/s}$	181
Fig. 7.9. Wall shear stress distribution in the gap obtained from the numerical simulation of constant velocity squeeze flow ($\dot{h} = 1 \text{ mm/s}$) of mineral oil sample for: micro-spiral geometry (a) with detain on the last two microchannels near the outlet area (b) and the parallel plane plate geometry (c).	181
Fig. 7.10. Velocity distribution in the gap obtained from the numerical simulation of constant velocity squeeze flow ($\dot{h} = 1 \text{ mm/s}$) of mineral oil sample for: micro-spiral geometry (a) with detain on the last two microchannels near the outlet area (b) and the parallel plane plate geometry (c).	181

List of Figures

Fig. 7.11. Velocity vectors in the gap obtained from the numerical simulation of constant velocity squeeze flow ($\dot{h} = 1 \text{ mm/s}$) of mineral oil sample for the micro-spiral geometry. Fluid recirculation in the microchannel.....	182
Fig. 7.12. Cells Re number distribution in the gap obtained from the numerical simulation of constant velocity squeeze flow ($\dot{h} = 1 \text{ mm/s}$) of mineral oil sample for: micro-spiral geometry (a) with detain on the last two microchannels near the outlet area (b) and the parallel plane plate geometry (c).....	182
Fig. A. 1. Viscosity curve variation for Carreau-Yasuda model, depending on constitutive parameters.....	A.1
Fig. A. 2. Viscosity curve variation for Bingham model, depending on constitutive parameters:.....	A.2
Fig. A. 3. Analysis module of <i>Origin 8.0</i> software used for the aproximation of the experimental measurements.....	A.3
Fig. A. 4. Squeeze flow of Newtonian incompressible fluid between paralell plates	A.4
Fig. A. 5. Boundary conditions imposed for both simple and oscillatory squeeze flow, in the case of transient dynamic mesh approximation.	A.10
Fig. A. 6. Boundary conditions imposed for both simple squeeze flow, in the case of quasis-teady aproximation.	A.10
Fig. A. 7. Boundary conditions imposed for multiphase (VOF) simulations of squeezing flow.	11
Fig. A. 8. Geometries construction and meshing for single phase quasi-steady approximation of squeezing flow. Investigation of end effects by using different shapes of the outlet area.....	A.12
Fig. A. 9. Free surface evolution depending on film thickness (h) for the mineral oil sample in constant velocity squeeze flow, $h = 0.01 \text{ mm/s}$	A.16
Fig. A. 10. Free surface evolution depending on film thickness (h) for the mineral oil sample in constant velocity squeeze flow, $h = 0.1 \text{ mm/s}$	A.17
Fig. A. 11. Free surface evolution depending on film thickness (h) for the mineral oil sample in constant velocity squeeze flow, $h = 1 \text{ mm/s}$	A.18
Fig. A. 12. Free surface evolution depending on film thickness (h) for glycerin sample in constant velocity squeeze flow, $h = 0.01 \text{ mm/s}$	A.19
Fig. A. 13. Free surface evolution depending on film thickness (h) for glycerin sample in constant velocity squeeze flow, $h = 0.1 \text{ mm/s}$	A.20
Fig. A. 14. Free surface evolution depending on film thickness (h) for glycerin sample in constant velocity squeeze flow, $h = 1 \text{ mm/s}$	A.21
Fig. A. 15. Free surface evolution depending on film thickness (h) for honey sample in constant velocity squeeze flow, $h = 0.01 \text{ mm/s}$	A.22
Fig. A. 16. Free surface evolution depending on film thickness (h) for honey sample in constant velocity squeeze flow, $h = 0.1 \text{ mm/s}$	A.23
Fig. A. 17. Free surface evolution depending on film thickness (h) for honey sample in constant velocity squeeze flow, $h = 1 \text{ mm/s}$	A.24
Fig. A. 18. Samples microstructure: cream before (a1) and after (a2) shear test; polysiloxane before (b1) and after (b2) shear test.....	A.25
Fig. A. 19. Micro textured surface details.....	A.26
Fig. A. 20. Micro-spirals plate details.....	A.26

LIST OF TABLES

Table 2.1. Definition of material functions depending on the type of viscometric motion and on the flow domain geometry.	31
Table 4.1. Carreau-Yasuda parameters used to approximate	93
Table 4.2. Carreau-Yasuda parameters used to approximate the linear and nonlinear rheological behavior of emulsions and polymer solutions in shear flow.....	96
Table 4.3. Imposed values for the dynamic contact angle at solid-fluid interface (θ), used for the multiphase numerical simulation of constant velocity squeeze flow.....	110
Table 5.1. Technical specifications of Physica MCR 301 Rheometer [(Anton-Paar)].....	128
Table 5.2. Corrected force amplitude, apparent viscosity and relative error of measured viscosity (in comparison with shear viscosity) for the glycerin sample in oscillatory squeezing flow.	134
Table 5.3. Testing parameters for different Newtonian samples in constant velocity squeeze flow.	140
Table 5.4. Parameters used for the approximation of experimental force distribution of analyzed samples in constant velocity squeeze flow, by using Power-Law force expression.	150
Table 5.5. Parameters used for the approximation of experimental force distribution for CR and GEL samples in constant velocity squeeze flow by using Power-Law force expression.	151
Table 7.1. Measured contact angles for all tested samples in contact with different silica micro structured surfaces: plane surface, micro textured surface, micro—spiral surface.....	175
Table 7.2. Normal force values obtained through the numerical simulations of constant velocity squeeze flow of mineral oil sample, using the quasi-steady approximation of the flow. Surface microstructure influence on force values. Comparison with the theoretical prediction for parallel plate geometries.....	182
 Table. A. 1. Parameters used for the representation of Careau-Yasuda model dependency	A.1
Table. A. 2. Parameters used for the representation of Bingham model dependency	A.2
Table. A. 4. The relaxation times and corresponding viscosities values for the aproximation of fluid viscoelastic behavior with a Maxwell model (8 elements) for a initial applied deformation of.....	A.3
Table. A. 5. The relaxation times and corresponding viscosities values for the aproximation of fluid viscoelastic behavior with a Maxwell model (8 elements) for a initial applied deformation of.....	A.3
Table. A. 6. The relaxation times and corresponding viscosities values for the aproximation of fluid viscoelastic behavior with a Maxwell model (8 elements) for a initial applied deformation of $\gamma_0 = 1$ [—].	A.3

List of Notations

LIST OF NOTATIONS

Symbol	Description	Unit of measurements
a	Carreau-Yasuda exponent	$[-]$
\mathbf{a}	acceleration vector	$[m/s^2]$
A	area	$[m^2]$
\mathbf{b}	specific mass vector	$[m/s^2]$
b_x, b_y, b_z	specific mass vector components	$[m/s^2]$
B	plate width	$[m]$
Bn	Bingham number	$[-]$
Ca	Capillary number	$[-]$
C_g	geometric constant	$[-]$
CN	Courant number	$[-]$
C_f	correction factor for experimental oscillatory squeeze flow	$[%]$
d_e	distance from the initial position of the pressure distribution	$[m]$
\mathbf{D}	symmetric rate tensor	$[-]$
D_e	outer diameter of the ring	$[m]$
D_i	inner diameter of the ring	$[m]$
De	Deborah number	$[-]$
e	the center of pressure distribution	$[-]$
f_{num}	numerical force amplitude	$[N]$
f_{th}	analytical force amplitude	$[N]$
F	time dependent squeeze velocity	$[N]$
F_0	constant squeeze velocity	$[N]$
F_t	total force acting on a Wilhelmy plate	$[N]$
F_G	gravity force	$[N]$
F_A	archimedic force	$[N]$
\bar{F}	dimensionless squeeze force	$[-]$
G	elastic modulus	$[Pa]$
G^*	complex modulus	$[Pa]$
G'	storage modulus (elastic component)	$[Pa]$
G''	loss modulus (viscous component)	$[Pa]$
h	time dependent film thickness, testing gap	$[m]$
\bar{h}	dimensionless film thickness	$[-]$
h_L	maximum height of a liquid column lifting in a capillary tube	$[m]$
h_{min}	minimum film thickness in a inclined plate geometry	$[m]$
h_0	initial film thickness, initial gap	$[m]$
\dot{h}	squeeze velocity	$[m/s]$
\mathbf{i}	momentum vector	$[kg \cdot m/s]$
\mathbf{I}	unit tensor	$[-]$
I_2	second invariant of deformation tensor	$[s^{-2}]$
k	consistency index	$[Pa \cdot s^n]$
K	geometric constant	$[-]$
l_c	capillary length	$[m]$
l_s	slip length	$[m]$
L	plate length	$[m]$
\mathbf{L}	velocity gradient	$[s^{-1}]$
m	number of elements of Maxwell model	$[-]$
m_s	slip coefficient, friction coefficient	$[-]$
M	momentum	$[Nm]$

List of Notations

n	flow behavior index	$[-]$
\mathbf{n}	normal vector (or normal)	$[-]$
N_1	first normal stress difference	$[Pa]$
N_2	second normal stress difference	$[Pa]$
p	pressure	$[Pa]$
Δp	pressure difference	$[Pa]$
p_{sup}	free surface pressure	$[Pa]$
Δp_{sup}	pressure difference along the interface	$[Pa]$
Q	flow rate	$[m^3/s]$
r_c	capillary radius	$[m]$
R	plate radius, cylinder radius for Couette geometry	$[m]$
R_s	sphere radius	$[m]$
R_2, R_1	radii of curvature in each of the axes that are parallel to the	$[m]$
S	plasticity number	$[-]$
t	time	$[s]$
\bar{t}	dimensionless time	$[-]$
t_0	observation time	$[s]$
t_∞	necessary time to achieve plates contact	$[s]$
T	temperature	$[^\circ C]$
\mathbf{T}	Cauchy stress tensor	$[Pa]$
$\dot{\mathbf{T}}$	objective derivative introducing the nonlinearity	$[Pa \cdot s^{-1}]$
\mathbf{T}_E	extra stress tensor	$[Pa]$
Tr	dimensionless Trouton number	$[-]$
T_s	computational time step	$[s]$
\mathbf{v}	velocity vector	$[m/s]$
v_x, v_y, v_z	velocity vector components in a Cartesian coordinate system	$[m/s]$
v_r, v_θ, v_z	velocity vector components in a Cylindrical coordinate system	$[m/s]$
V_{pi}	lower plate velocity in shear motion	$[m/s]$
V_{ps}	upper plate velocity in shear motion	$[m/s]$
V_f	fluid bulk velocity	$[m/s]$
V_f^*	fluid velocity at the wall	$[m/s]$
V_0	constant squeeze velocity	$[m/s]$
Wi	dimensionless Weissenberg number	$[-]$
α	inclination angle of a solid surface	$[^\circ]$
β^*	slip parameter	$[-]$
β	cone inclination angle (cone-plate geometry)	$[^\circ]$
δ	phase angle	$[^\circ]$
δ_c	correction value of phase lag	$[-]$
ε	hencky strain	$[-]$
ε_0	oscillatory strain amplitude, oscillatory squeeze amplitude	$[m]$
ω	angular frequency	$[rad/s]$
ω_s	frequency (squeeze flow)	$[Hz]$
$\dot{\varepsilon}$	specific deformation rate (extensional flow)	$[s^{-1}]$
$\Delta \varepsilon$	relative error	$[\%]$
γ	strain (angular deformation in shear motion)	$[-]$
$\dot{\gamma}$	shear rate	$[1/s]$
γ_0	strain amplitude	$[-]$
γ_1, γ_2	corresponding strain of viscoelastic mechanical models	$[-]$
η	shear viscosity	$[Pa \cdot s]$

List of Notations

η^*	complex viscosity	[Pa.s]
η'	elastic component of complex viscosity	[Pa.s]
η''	viscous component of complex viscosity	[Pa.s]
η_B	Bingham viscosity	[Pa.s]
η_e	extensional viscosity	[Pa.s]
η_0	zero shear viscosity	[Pa.s]
η_∞	infinite shear viscosity	[Pa.s]
λ	relaxation time	[s]
θ	contact angle	[°]
Π	wetted perimeter	[m]
ρ	density	[kg/m ³]
σ	shear stress	[Pa]
σ_0	critical Yield value, yield point	[Pa]
σ_1, σ_2	corresponding shear stress of viscoelastic mechanical models	[Pa]
$\sigma_{rr}, \sigma_{\theta\theta}, \sigma_{zz}$	normal components of stress tensor \mathbf{T} in a Cylindrical coordinate system	[Pa]
σ_w	wall shear stress	[Pa]
σ_c	critical wall shear stress	[Pa]
σ_{SG}	solid-gas interfacial energy	[N/m]
σ_{SL}	solid-liquid interfacial energy	[N/m]
σ_{LG}	liquid-gas interfacial energy or surface tension	[N/m]
$\sigma_{11}, \sigma_{22}, \sigma_{33}$	normal component of stress tensor \mathbf{T} in a Cartesian coordinate system	[Pa]
\mathcal{V}	volume	[m ³]
κ	mean curvature (of a free surface)	[1/m]
*	arbitrary function	[*]
∇	nabla operator	[1/m]

Chapter 1. INTRODUCTION

1.1. THE CONTEXT OF THIS STUDY AND ITS MOTIVATION

The technological advance has encouraged, during the last decade, the manufacturing and use of new materials, with complex micro-structures and innovating properties. Their existence has been and still is conditioned by the need to enhance the efficiency of certain technological processes, of the advance in important fields such as medicine, manufacturing of medicines and of cosmetics, the food and cosmetic industries, the production of energy, recycling of resources, industry of transports, of car manufacturing, etc.

Within the thesis framework, we may assert that, as regards complex fluids, the three mandatoy stages– development, production and use – are conditioned by the possibility to understand and model fluid rheological behavior, both at macroscopic level, and at the micro or nanoscale levels. Fluid reology is implicitly determined by its properties of viscosity, elasticity and plasticity. A high interest has always been shown to the viscoelastic behavior of materials, viscoelasticity being the property of a material to manifest simultaneously a rheological behavior that is both viscous, and elastic, when it is subject to a deformation, due to the application of stress.

Fluids rheological characterisation supposes the determination of the extra stress tensor, present in the equations of motion, starting from rheological measurements. Extra stress tensor expression depends on deformation (applied strain) and on the deformation rate, is called a constitutive relation. The rheological characterization, respectivley material functions modelling, is made by submitting the samples (fluids) to various mechanical tests that implicate shear motions, extension motions or squeeze flow.

In the last years, the analysis of the materials with nonlinear viscoelastic behavior has become one of the main problems in the field of rheology. The understanding, use and correction of testing procedures; the correlation between the macroscopic response of fluids obtained following the applied deformations (viscosity curves, flow curves, components of the complex module) with the changes occurred in the microstructure of materials (chemical reactions, particles dynamics); classification of materials depending on the nonlinear viscoelastic response; all these aspects represent important steps which form the basis of nonlinear viscoelasticity theory. Covering all these steps is imperative for science and

research advance, for the human society needs to manufacture new complex materials with specific properties, to process and use them.

The present thesis „*Procedures for the Rheological Characterization of the Nonlinear Behavior of Complex Fluids in Shear and Squeeze Flows*”, represents an analysis of rheological testing procedures for simple and complex fluids in both linear and nonlinear viscoelasticity domains. The study has been achieved following the agreement of joint supervision between the *Polytechnic University of Bucharest* and the *Poitiers University of France*. Therefore, the entire activity has been financed out of the *European Social Fund through the Operational Sectorial Programme of Development of Human Resources - POSDRU 2007-2013*. The research activity has been carried out within the *REOROM Laboratory, Interaction Field-Substance (BIOINGTEH Platform)*, the *Department of Hydraulics and of Hydraulic Machines, the Faculty of Energetics of the Polytechnic University of Bucharest*, and within the *Structure and Interference Laboratory of Axa TriboLub of the Mechanic Engineering Department and Complex Systems, the Poitiers University of France*.

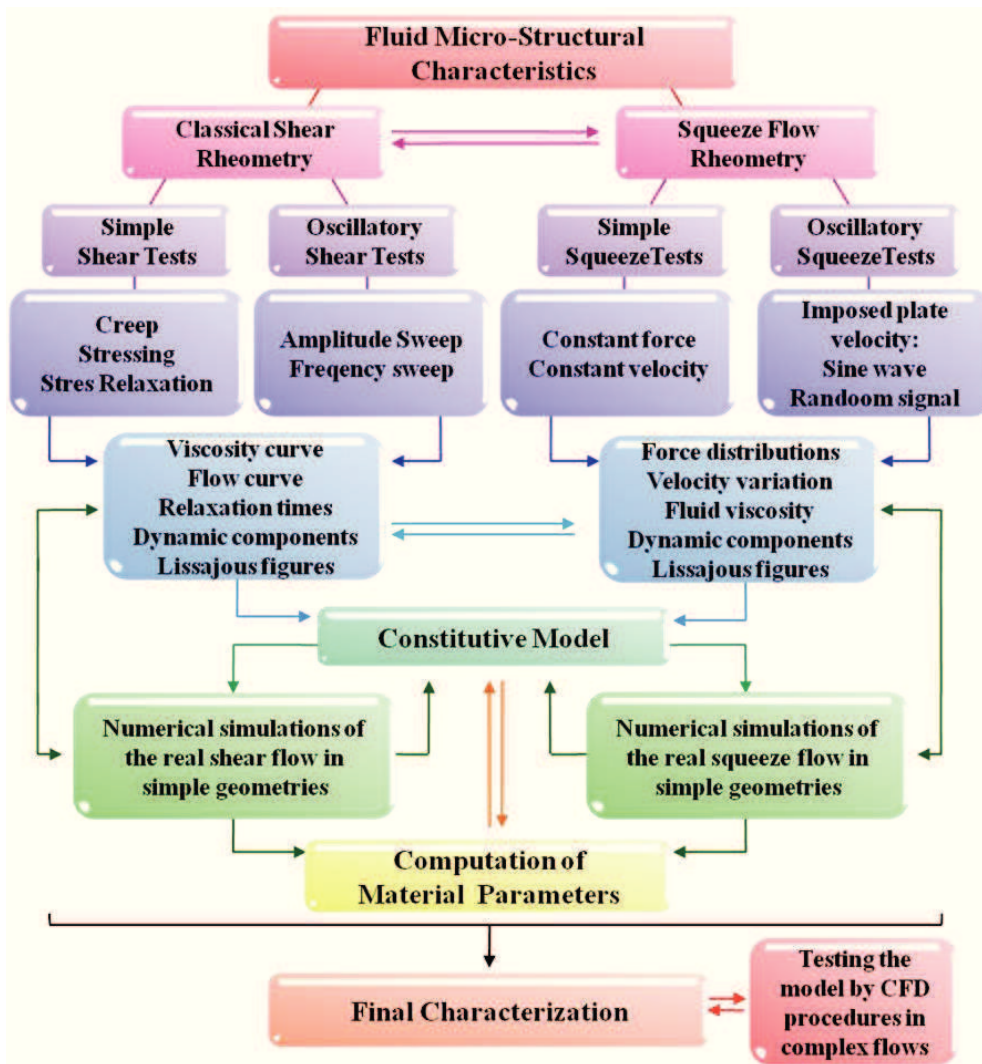


Fig. 1.1. Rheological characterization of fluids using experimental measurements, numerical modeling and analytical constitutive models.

The importance and innovative character of this work is justified by the correlation of the experimental testing procedures with the numerical modelling of the flow processes, technically supporting a new concept in the field of rheology, namely the **Computational Rheometry** (see [Figure 1.1](#)).

The limitations of experimental instrumentation for rheometric measurements available nowadays (fulfillment of “no slip” or adherence condition during tests, visualisation of flow dynamics within the testing gap) encourages the findings of new investigations solutions, the understanding of dynamics and kinematics of flow motions used in rheometric tests.

Thus, in this work, rheometrical experimental procedures are correlated with numerical simulations of the real flows, allowing the analysis of velocity fields and fluid kinematics in the testing gaps, adherence condition influence on flow kinematics and implicitly over the rheological properties measured during the experimental investigations.

Equally, the complexity of the study is justified by the correlation of the simple shear tests with the complex squeeze motion, both in simple or dynamic controll of the applied deformation.

1.2. THESIS STRUCTURE

The approach of an extended range of rheological testing procedures, and a variety of fluids behaviors, requires the presentation of theoretical continuum mechanics, rheology and rheometry, presentend in **Chapter 2** and **Chapter 3**.

Thus **Chapter 2. Rheology and Rheometry** presents some fundamental notions of *Fluid Mechanics* and *Rheology*, concepts regarding rheological properties of simple and complex materials (viscosity, elasticity, surface tension, adherence), the linear and non-linear viscoelastic behavior and, not least, the shear, extension and squeeze motions commonly used in rheometric tests.

Since a large part of the thesis is dedicated to the complex motion of fluid squeeze, **Chapter 3. The Squeeze Flow** represents a wide study on current stage of research concerning squeeze flow and the theoretical expressions of the flow in various geometries, tests, with or without the influence of no slip, inertia or thermal conditions. Also in [Paragraph 3.2.5](#) are presented several analytical solutions used for the squeeze flow of generalised Newtonian fluids, and the studies achieved so far for viscoelastic fluids in squeeze flow.

Chapter 4. Numerical Investigations of the Squeeze Phenomenon represents a broad study of the squeeze phenomenon by using numerical simulations, for both constant velocity and oscillatory motions. In this chapter are presented simulations of the real yield both in the

Chapter 1. Introduction

presence of the fluid-solid-air interface, and in its absence. In **Chapter 5. Experimental Investigations of the Squeeze Flow** are presented the results obtained following the experimental investigations of simple and complex fluids, both in the constant velocity squeeze flow, and in the oscillatory squeeze flow.

Chapter 6. Non-linear Behavior of Complex Fluids in Shear Motions includes a wide study of complex fluids in the field of non-linear viscoelasticity, making the correlation between the testing procedures that use simple shear motions and dynamic shear tests, associating the viscoelastic non-linear behavior with the yield stress of complex fluids included in the category of soft solids.

In Chapter 7. Influence of the Microstructure of Contact Surfaces over the Squeeze Force is studied the influence of the microstructure of contact plates over the adherence/slip properties of Newtonian fluids and implicitly on the rheological measurements performed in the presence of patterned surfaces.

Chapter 8. Final Conclusions ends this paper by summarising the most important conclusions, quantifying the original contributions of the entire PhD thesis and evidencing the further directions of study.

\

Chapter 2. RHEOLOGY AND RHEOMETRY

The objective of this chapter is to review the fundamental notions in the field of rheology, the rheological properties of simple and complex fluids, the classification of fluids depending on the rheological behavior, as well as the main methods to determine material functions.

The term „*Rheology*” appeared for the first time in 1929, being proposed by *Eugene Cook Bingham*, professor and manager of the Chemistry Department of the *Lafayette College* of Pensnsylvania USA. Inspired by the motto of the renowned *Heraclitus*, „*Panta rhei*”, translated as „*everything flows*”, the term was officially recognized together with the incorporation of the first Society of Rheology, in December 1929. When defining rheology as an independent field of study, we must also specify the contribution of *Markus Reiner*, who introduced Deborah’s number, $De = \lambda/t_0$, as the main parameter of characterization of the rheological behavior, where λ is the relaxation time step of the material (an elastic feature) and t_0 is the flow observation time step. A purely viscous fluid is characterized by $De \rightarrow 0$, while a purely elastic material is defined by $De \rightarrow \infty$. In the field $\in (0, \infty)$, materials have a viscoelastic behavior, whose study defines the purpose of rheology.

Rheology studies the flow of the matter, mainly focusing on the analysis of fluids, without however excluding the “soft” solid materials which, during certain exterior stresses, show flows instead of elastic deformities. In this context, *Flow* is defined as the deformation whose value increases permanently under the actions of efforts (stresses), is not fully recovered after removing the exterior stress. The main objective of rheology science is to define mathematical models (called constitutive relations) capable of representing the answer of materials to mechanical stresses. Rheological characterization and material properties (quantitative and qualitative relations between deformation and stress), is performed using experimental testing procedures, studied and improved within „*Rheometry*” domain. Rheology determines fluids behavior depending on the ratio between applied stesses and changes that occur within materials internal structure, these aspects are not described by classical methods in fluids mechanics or elasticity. Beginning with the XVII century, studies regarding the representation of the ideal elastic solid have appeared, being materialized in representative works like those of *Boyle* (1660), *Hook* (1678) and later *Young* (1807) and

Cauchy (1827). In the same period were published the first representative works, analyzing ideal fluids, without viscosity, belonging to *Pascal* (1663), *Bernoulli* (1738), *Euler* (1755). Departing from the definition of the fluid viscosity concept by *Isaac Newton* (1687), based on the principles pronounced by him, the evolution of the research leading to the definition of the fundamental equation of flow of linear viscous fluids (Newtonian) by *Navier* (1823) and *Stokes* (1845).

The first model of viscoelastic fluid belongs to *Maxwell* (1867), being described by a first order differential equation which expresses the dependence on the deformation shear stress (by viscosity), in the presence of the material stress relaxation, due to elasticity. In 1878, *Boltzmann* proposes the principle of superposition by which it is deemed that the value of a function characteristic to a system (for instance stress) is given by the sum of the history of said process (in this case, of deformations). The *Maxwell* model is extended in 1888 by *Thomson (Lord Kelvin)* by a new concept of the distribution of relaxation time steps of the material, and in 1902 he introduces, together with *Poynting*, the well-known mechanic model, formed of an elastic element (spring) and a viscous element (buffer). Later, the bases of the theory of generalised Newtonian fluids have been set, in remarkable works such as those published by *Bingham* (1922), *Ostwald* (1925), *Herchel & Bulkley* (1926), continuing with studies about the visco-elastic behavior of certain complex fluids, suspensions (*Einstein, Jefferys*), polymers (*Sconbein, Baekeland, Carothers*), and introducing the concept of extensional viscosity (*Barus, Trouton, Tamman & Jenkel*).

Further on, basic mathematical models in rheology were developed by *Oldroyd* (1950) – the model of continuous media, *Lodge* (1956) – the theory of microscopic networks for viscoelastic materials belonging to him, and the *Doi-Edward* model (1978), explaining the networks and formations appeared in the structure of polymers. For a more detailed description of the evolution of theoretical models and of experimental results in the field of rheology, the following works are recommended [26], [70], [141], [166], [217].

2.1. CAUCHY'S EQUATION OF MOTION AND THE STRESS TENSOR

As part of the mechanic of continuous media, the mechanic of fluids is based on four principles of preservation, incorporating the fundamental physical parameters defining a dynamic process: mass of bodies, impulse, energy and entropy. The application of these principles and the solution of the corresponding balance equations allows the description of continuous media flow kinematics, depending on material's constitutive relation.

Mass conservation principle

The mass of any fluid body with the density ρ that occupies a spatial field $D(t)$ is constant in time during the execution of the motion, the local form of this principle being given by the relation [60], [119]:

$$\frac{d\rho}{dt} + \rho \nabla \mathbf{v} = 0 \quad (2.1)$$

where

$$\frac{d*}{dt} = \frac{\partial *}{\partial t} + (\mathbf{v} \cdot \nabla) * \quad (2.2)$$

defines the material derivative.

Equation of motion (impulse conservation)

The sum of the mass and surface forces acting over the body is equal to the variation in time of the impulse defined by the relation:

$$\mathbf{i} = \int_{D(t)} \rho \cdot \mathbf{v} \cdot d\mathcal{V} \quad (2.3)$$

$$\frac{d\mathbf{i}}{dt} = \int_{D(t)} \rho \cdot \mathbf{b} d\mathcal{V} + \int_{\partial D(t)} \mathbf{T} \cdot \mathbf{n} dA \quad (2.4)$$

The local form of the relation (2.4) is:

$$\rho \cdot (\mathbf{a} - \mathbf{b}) = -\nabla p + \nabla \mathbf{T}_E \quad (2.5)$$

where \mathbf{a} is the acceleration, \mathbf{b} the mass force, and \mathbf{T} is the *Cauchy* symmetrical stress tensor,

$$\mathbf{T} = -p\mathbf{I} + \mathbf{T}_E \quad (2.6)$$

where \mathbf{T}_E is the extra-stress tensor defining the contribution of the body deformation to the state of stress, and p is the pressure (spherical compression stress) [60], [119], [155]. The correlation between the extra-stress tensor and the body deformation is achieved by an equation called constitutive relation (or material equation). For a Cartesian coordinates system, *Cauchy's* equations of motion have extended form:

$$\begin{cases} \rho \left(\frac{\partial v_x}{\partial t} + v_x \frac{\partial v_x}{\partial x} + v_y \frac{\partial v_x}{\partial y} + v_z \frac{\partial v_x}{\partial z} \right) = -\frac{\partial p}{\partial x} + \left(\frac{\partial \sigma_{xx}}{\partial x} + \frac{\partial \sigma_{yx}}{\partial y} + \frac{\partial \sigma_{zx}}{\partial z} \right) + \rho b_x \\ \rho \left(\frac{\partial v_y}{\partial t} + v_x \frac{\partial v_y}{\partial x} + v_y \frac{\partial v_y}{\partial y} + v_z \frac{\partial v_y}{\partial z} \right) = -\frac{\partial p}{\partial y} + \left(\frac{\partial \sigma_{xy}}{\partial x} + \frac{\partial \sigma_{yy}}{\partial y} + \frac{\partial \sigma_{zy}}{\partial z} \right) + \rho b_y \\ \rho \left(\frac{\partial v_z}{\partial t} + v_x \frac{\partial v_z}{\partial x} + v_y \frac{\partial v_z}{\partial y} + v_z \frac{\partial v_z}{\partial z} \right) = -\frac{\partial p}{\partial z} + \left(\frac{\partial \sigma_{xz}}{\partial x} + \frac{\partial \sigma_{yz}}{\partial y} + \frac{\partial \sigma_{zz}}{\partial z} \right) + \rho b_z \end{cases} \quad (2.7)$$

The *Navier-Stokes* equation represents a particular form of the impulse preservation principle, in the hypothesis that the analyzed fluid is a purely viscous fluid in laminar motion. In the equation of motion,

$$\rho \cdot \left(\overbrace{\frac{\partial \mathbf{v}}{\partial t} + (\mathbf{v} \cdot \nabla) \mathbf{v}}^{\text{Inertia}} \right) = \overbrace{-\nabla p + \nabla \mathbf{T}_E}^{\text{stress divergence}} + \rho \mathbf{b}$$

$\underbrace{\frac{\partial \mathbf{v}}{\partial t}}_{\text{unsteady acceleration}} \quad \underbrace{(\mathbf{v} \cdot \nabla) \mathbf{v}}_{\text{convective acceleration}} \quad \underbrace{-\nabla p}_{\text{pressure gradient}} \quad \underbrace{\nabla \mathbf{T}_E}_{\text{extra-stress}}$

(2.8)

for an incompressible Newtonian fluid, the following constitutive relation is used:

$$\mathbf{T}_E = 2\eta_0 \mathbf{D}$$
(2.9)

where \mathbf{D} is the symmetrical tensor of the specific deformation rate, and η_0 is the viscosity, exclusively dependent on temperature and pressure, for a purely viscous fluid,

$$\eta_0 = \eta_0(T, p).$$
(2.10)

In this paper, unless additional specifications are made, motions are considered isothermal and isochoric, therefore $\eta_0 = \eta = ct$. The *Navier-Stokes* equation becomes in this case:

$$\rho \left(\frac{\partial \mathbf{v}}{\partial t} + (\mathbf{v} \cdot \nabla) \mathbf{v} \right) = -\nabla p + \eta_0 \Delta \mathbf{v} + \rho \mathbf{b}.$$
(2.11)

As regards the incompressible generalised Newtonian fluids, the extra-stress tensor has the form:

$$\mathbf{T}_E = 2\eta(\dot{\gamma}) \mathbf{D},$$
(2.12)

with $\text{tr } \mathbf{D} = 0$ (isochoric motion condition).

Viscosity is, in this case, a function which depends on the second invariant of the deformation tensor, $\dot{\gamma} = 2\sqrt{|I_2|}$,

$$I_2 = -\frac{1}{2} \text{tr } \mathbf{D}^2.$$
(2.13)

For details regarding this paragraph, the following works are recommended [12], [59], [60], [119], [155].

2.2. RHEOLOGICAL PROPERTIES OF SIMPLE AND COMPLEX FLUIDS

The rheology of a fluid is implicitly determined by its properties of viscosity and elasticity. Viscoelasticity is a material the property manifest simultaneously a rheological behavior, both viscous and elastic, when subject to a deformation (due to an applied stress).

The rheological characterisation of a fluid supposes the determination of the extra stress tensor, present in the equations of motion, starting from rheological measurements. The expression of the extra stress tensor, which depends on strain and strain rate, is called a constitutive relation. In the case of a Newtonian fluid, the dependence between stress and deformation rate is a linear one, and the viscosity coefficient has a constant value. In a simple motion, the incompressible Newtonian fluid (2.9) is defined by the relation:

$$\sigma = \eta_0 \cdot \dot{\gamma} \quad (2.14)$$

where η_0 is the dynamic viscosity of the fluid, σ is the shear stress and $\dot{\gamma}$ is the shear rate. This category of fluids includes water, mineral oils, car lubricants, glycerine, honey etc.

In the case of the incompressible generalized Newtonian fluids (2.12), this dependence no longer has a linear character, viscosity being a function which depends on the specific deformation rate, $\eta = \eta(\dot{\gamma})$, but which is independent of time (therefore it does not have the elasticity property).

The generalized Newtonian fluids are divided into two categories: pseudoplastic fluids (*shear thinning*), for which the viscosity coefficient decreases with the shear rate ($\eta_0 > \eta_\infty$), and dilatant fluids (*shear thickening*), where the viscosity increases with the shear rate, ($\eta_0 < \eta_\infty$), where $\eta_0 = \lim_{\dot{\gamma} \rightarrow 0} \eta(\dot{\gamma})$ and $\eta_\infty = \lim_{\dot{\gamma} \rightarrow \infty} \eta(\dot{\gamma})$ represent „zero” viscosity, namely „infinite” viscosity (constant values). The rheological behavior of these materials is described by the flow curve $\tau(\dot{\gamma})$ and the variation of viscosity depending on the shear rate $\eta = \eta(\dot{\gamma})$, (see Figure 2.1).

The most common „classic” models used to describe viscosity functions for generalized Newtonian fluids are:

a. The Power Model - Power Law, is the simplest model, proposed by *Ostwald –de Wale*:

$$\eta = k \cdot \dot{\gamma}^{n-1} \quad (2.15)$$

b. The Carreau Yassuda Model

$$\eta = \eta_\infty + (\eta_0 - \eta_\infty) \cdot [1 + (\lambda \dot{\gamma})^a]^{\frac{n-1}{a}} \quad (2.16)$$

c. The Cross Model, similar to Carreau-Yasuda model, describing a pseudoplastic fluid:

$$\eta = \eta_\infty + (\eta_0 - \eta_\infty) \frac{1}{1 + (\lambda \dot{\gamma})^n} \quad (2.17)$$

d. The Bingham model, where the critical yield stress appears:

$$\eta = \eta_B + \frac{\sigma_0}{\dot{\gamma}} \quad (2.18)$$

for $\sigma = \eta \dot{\gamma} > \sigma_0$.

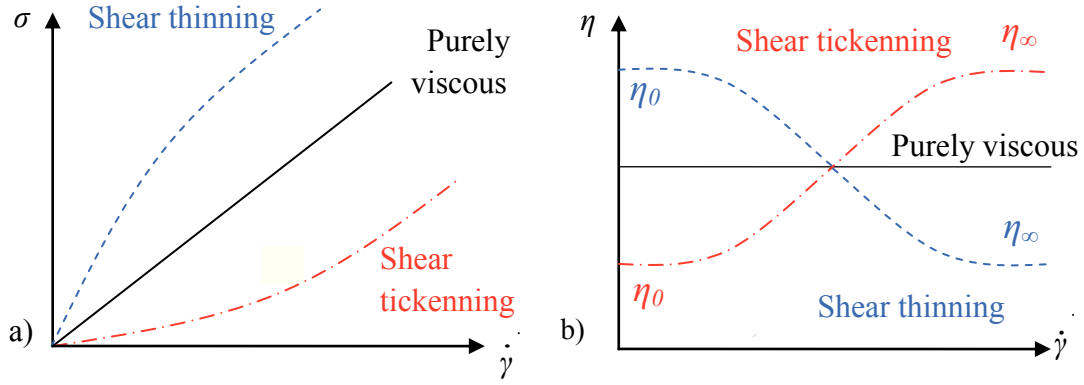


Fig. 2.1. Variation of shear stress (a) and of viscosity function (b) depending on the rheological behavior of fluids.

In (2.15 - 2.18), the material constants are: k – consistency index, n – flow index, λ – characteristic time step, a – Yassuda exponent ($a = 2$ in the Carreau model), σ_0 represents the Bingham tangential stress, or the yield point, η_B is the Bingham viscosity.

e. The Herschel-Bulkley Model (which generalizes the Bingham Model),

$$\mathbf{T}_E = 2 \left(\frac{\sigma_0}{\dot{\gamma}} + m(\dot{\gamma})^{\frac{n-1}{2}} \right) \mathbf{D} \quad (2.19)$$

where $m(\dot{\gamma})$ is a material function (for a null value of the deformation tensor, the model describes a solid behavior).

f. The Papanastasiou Model eliminates the discontinuity present in the Herchel-Bulkley model at the critical value of the stress point:

$$\mathbf{T}_E = 2 \left(\frac{\sigma_0(1 - e^{-a\dot{\gamma}})}{\dot{\gamma}} + m(\dot{\gamma})^{\frac{n-1}{2}} \right) \mathbf{D} \quad (2.20)$$

g. The Oldroyd Model

$$\sigma = \frac{1 + k_i \cdot (1 - a^2)(\lambda_i \dot{\gamma})^2}{1 + (1 - a^2)(\lambda_i \dot{\gamma})^2} \cdot \eta_o \cdot \dot{\gamma} \quad (2.21)$$

where $|a| \leq 1$, where k_i are constitutive constants and λ_i is the relaxation time.

A representation of these models both for the viscosity function, and for the variation of the shear stress depending on the deformation rate is described in Figure 2.2. Each of these model parameters influences the variation of the flow curve and viscosity distribution.

Thus, these models can be adapted to the various rheological behaviors of generalized Newtonian incompressible fluids. Model's dependency on their constitutive parameters is shown in Annex 1. In order to describe the behavior of the viscoelastic fluids, mechanical analogical models are used. These models are formed of elastic elements (elastic springs) and

viscous elements (viscous dashpots), connected in series or in parallel, each model summing up at least one viscous and one elastic element.

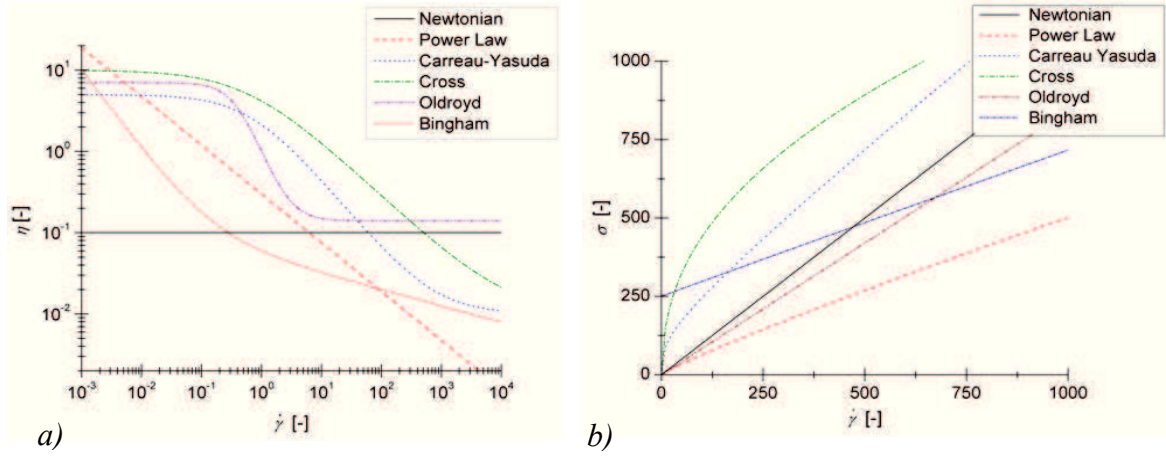


Fig. 2.2. Variation of viscosity function (a) and shear stress (b) for different rheological models.

The simplest analogical models are the *Maxwell* model (an elastic and a viscous element connected in series) and the *Kelvin-Voigt* model (an elastic and a viscous element connected in parallel) shown in Figure 2.3. The *Maxwell* Model is used to describe the behavior of viscoelastic fluids and the relaxation phenomena, and the *Kelvin-Voigt* model describes the behavior of the solid-viscoelastic materials [59], [89], [94], [140], [141], [142], [222]. For the *Maxwell* model, the tangential efforts are equal, and the deformation sums up the elastic and viscous components, as follows:

$$\begin{cases} \gamma = \gamma_1 + \gamma_2 \\ \sigma = \sigma_1 = \sigma_2 \end{cases} \quad (2.22)$$

with $\sigma_1 = G\gamma$ (the Hooke solid), G being the elastic shear module and $\sigma_2 = \eta\dot{\gamma}$ (the Newtonian fluid). In this case, the *Maxwell* model is defined as follows:

$$\lambda\dot{\sigma} + \sigma = \eta\dot{\gamma} \quad (2.23)$$

where $\lambda = \eta/G$ is the characteristic relaxation time of the fluid.

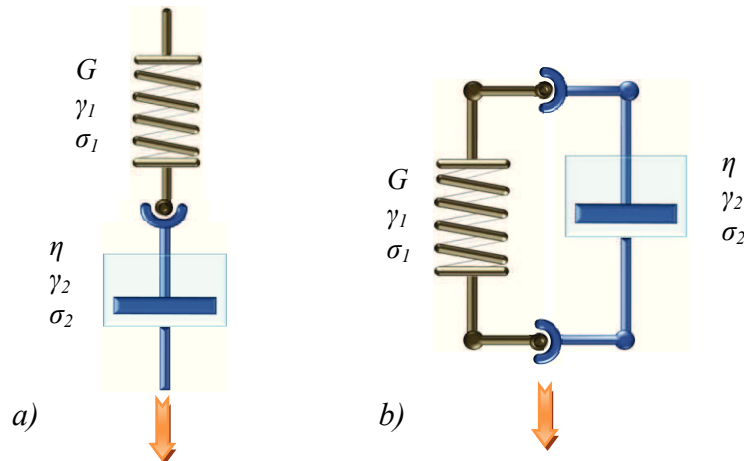


Fig. 2.3. Maxwell (a) and Kelvin-Voigt (b) analogical models.

If the elastic element becomes rigid, a purely viscous behavior of the fluid will be obtained. In the case of the *Kelvin–Voigt* model, the corresponding deformations are equal, and the characteristic tangential stress is obtained by summing up the stresses of the components,

$$\begin{cases} \gamma = \gamma_1 = \gamma_2 \\ \sigma = \sigma_1 + \sigma_2 \end{cases} \quad (2.24)$$

the constitutive relation of the model being:

$$\sigma = G\gamma + \eta\dot{\gamma} \quad (2.25)$$

By connecting these analogical models in parallel or in series, one can determine complex models as: *Burger* model, obtained by the serial connection of a *Maxwell* model with a *Kelvin–Voigt* model, the *Maxwell* model connected to a viscous element describes the *Jefferys* fluid, the *Letherich* model, the *Zener* model, etc. Any other mechanic model is a combination of *Maxwell* and *Kelvin–Voigt* models [26], [69], [89], [141], [142], [155], [222]. In the linear viscoelasticity domain, real fluids characterization is made by connecting in parallel „*m*” *Maxwell* elements (see Figure 2.4), thus determining for each element a certain relaxation time step and a corresponding viscosity value.

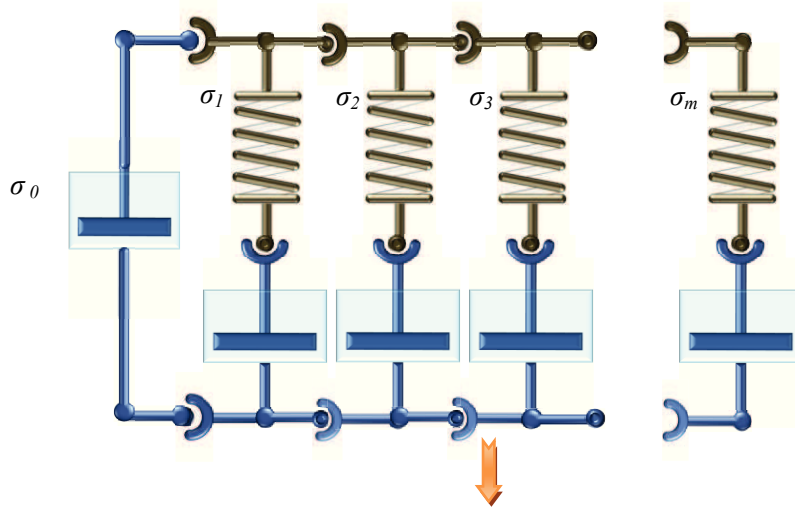


Fig. 2.4. The Maxwell model with “*m*” elements conected in parallel.

Understanding the viscoelastic rheological behavior and the relaxation/recovery phenomena, is essential for a proper characterization of the materials. The analogical models presended above may describe corectley the viscoelasticity mechanism only in the linear viscoelatic domain. However, viscoelastic fluids behavior is not always linear, cause the present state of stress depends on deformation history by differential equations or non-linear integrals. For instance, in the tri-dimensional representation, the Maxwell fluid (eq. 2.23) has the form

$$\lambda \tilde{T} + T = 2\eta_0 D \quad (2.26)$$

where \tilde{T} is the objective derivative that introduces non-linearity. The non-linear relations (in this case, the Oldroyd model with two material constants, λ and η_0) have the capacity to model not only the relaxation phenomenon, but also the effects of the normal stresses (exclusively due to the presence of elasticity), [38], [141], [149], [155]. Some of these characteristic effects exclusive to the viscoelastic fluids are the Weissenberg effect (the lifting on a rod of the viscoelastic liquids, the purely viscous liquids forming a funnel along the rod), the swelling of the jet when coming out into the atmosphere from a tube (the Barus effect), the unstable flow of polymer meltings through the capillaries or outlets of various configurations (fractures, elastic turbulences and distortions when the shear stress increases), [149], [155], [199].

2.3. RHEOMETRY – TESTING PROCEDURES FOR SIMPLE AND COMPLEX FLUIDS

The determination of the rheological behavior of fluids, respectively of the material functions and constants, is made by submitting them to various mechanic tests that implicate shear, extension or squeeze flows. In this chapter different flow types used in rheometric tests are presented: (i) simple viscometric and extensional motions; (ii) complex squeeze flow, the latter being detailed in the following chapter. Fluids rheological characterization (regardless the testing procedure motion – shear, extension, squeeze) is conditioned by the determination (measurement) of the stresses (that act on the volume elements in motion), deformations and the characteristic velocity distributions.

2.3.1. Viscometric motions

The shear tests (also called viscometric) suppose only one flow direction, the velocity varying only on the normal direction. Due to the simple kinematics, the viscometric motions are commonly used for fluids rheological characterization.

Depending on the type of motion, they may be simple shear tests or oscillatory tests, the expressions of the material functions being defined accordingly. Depending on the construction of the experimental devices, namely of the rotational or capillary rheometers, the rheometric tests are classified in tests with the control of the shear stress (*stress control*) and tests with imposed strain (*strain control*).

2.3.1.1. Simple shear tests

In the case of the simple shear motion, there is only one tangential shear stress $\sigma_{xy} = \sigma_{yx} = \sigma$, the extra stress tensor having the following form:

$$\mathbf{T}_E = \begin{bmatrix} \sigma_{11} & \sigma & 0 \\ \sigma & \sigma_{22} & 0 \\ 0 & 0 & \sigma_{33} \end{bmatrix} \quad (2.27)$$

the rate of deformation tensor being defined by:

$$\mathbf{D} = \frac{1}{2} \begin{bmatrix} 0 & \dot{\gamma} & 0 \\ \dot{\gamma} & 0 & 0 \\ 0 & 0 & 0 \end{bmatrix} \quad (2.28)$$

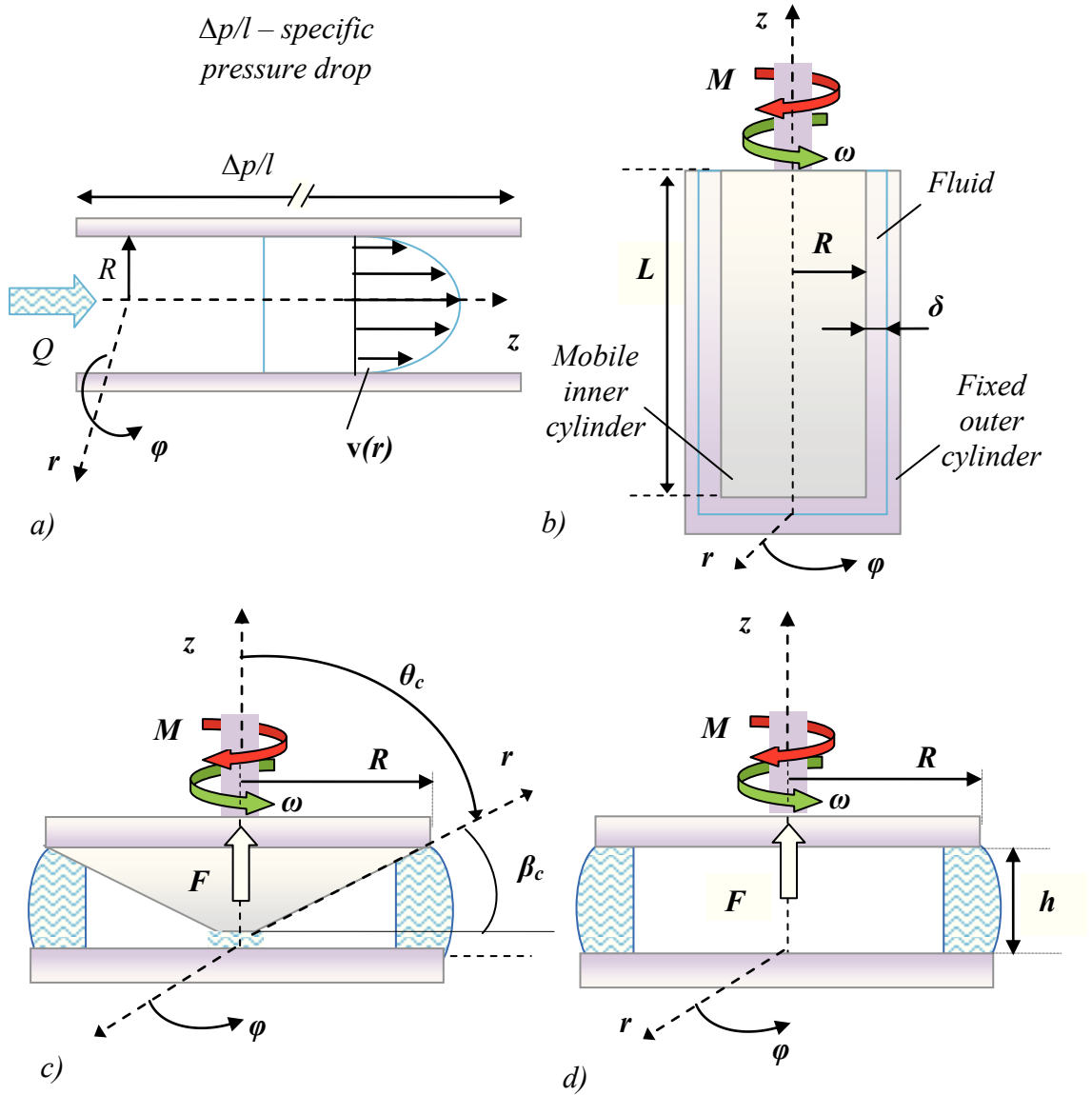


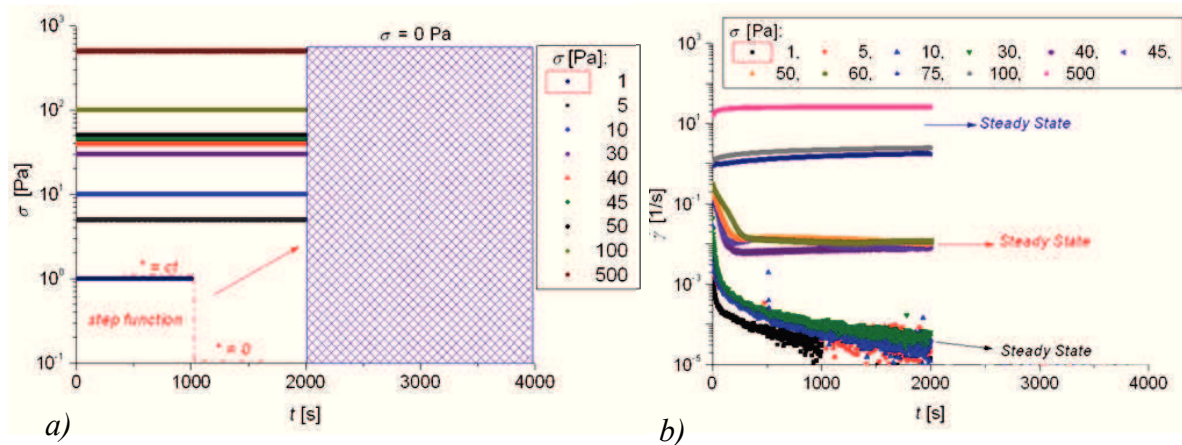
Fig. 2.5. The schematic representation of the viscometric motion of the incompressible Newtonian fluids in various geometries used in usual rheometric tests: *Hagen-Poiseuille* flow in a capillary tube *a*) and the *Couette* rotation flow in a geometry with coaxial cylinders *b*), a cone-plate geometry *c*) and a plate-plate geometry *d*).

Table 2.1. Definition of material functions depending on the type of viscometric motion and on the flow domain geometry [12].

Type of flow	Geometry	Geometrical parameters	Measurable quantities	σ [Pa]	$\dot{\gamma}$ [s^{-1}]	N_1 [Pa]
<i>Couette</i>	Coaxial cylinders	R, l, δ $\delta \ll R; R \ll L$	M, ω	$\frac{M}{2\pi R^2 L}$	$\frac{\omega R}{\delta}$	-
<i>Couette</i>	Plate-plate	R, h $h \ll R$	M, ω	$\frac{3M}{2\pi R^3}$	$\frac{\omega R}{h}$	-
<i>Couette</i>	Cone-Plate	R, β_c $\beta \leq 4^\circ$	M, ω, F	$\frac{3M}{2\pi R^3}$	$\frac{\omega}{\beta_c}$	$\frac{2F}{\pi R^2}$
<i>Poiseuille</i>	Capillary tube	R, l_c $R \ll l_c$	$\Delta p, Q$	$\frac{\Delta p R}{2l_c}$	$\frac{4Q}{\pi R^3}$	-

During a viscometric motion, the fluid is characterized by three material functions: (i) the viscosity function $\eta = \sigma / \dot{\gamma}$; (ii) the first difference of the normal stresses $N_1 = \sigma_{11} - \sigma_{22}$; (iii) the second difference of the normal stresses $N_2 = \sigma_{22} - \sigma_{33}$; all these functions being exclusively dependent on $\dot{\gamma}$.

The gaps used in the *Couette* geometries are small ($< 1 \text{ mm}$), thus providing almost constant values of the shear stress and of the strain velocity specific in the used volume. The testing procedure supposes that the constant rotation velocity $\dot{\gamma} \sim \omega$ (*strain controlled*), or of a constant shear stress $\sigma \sim M$ (*stress controlled*) are imposed, measuring the torque of shearing, respectively the rotation velocity ω . The measurable specific quantities and the expressions corresponding to the type of viscometric motion and of the used geometry are shown in Table 2.1.


Fig. 2.6. The applied shear stress (a) and the variation of the strain rate (b) for a Polysiloxane sample, results obtained following a Creep test, at. $T = 20^\circ \text{C}$.

The main rheometric tests performed with the presented geometries are the *Creep tests* and the *Relaxation test*. In the case of a *Creep test*, the flow is controlled by imposing a

constant shear stress (Figure 2.6.a), watching the evolution of the shear rate, respectively of the specific angular strain γ in time (Figure 2.6.b). Following such a test, one may determine the characteristic time step necessary for each fluid to reach the steady state in order to determine the material functions. Materials relaxation time steps depend on their own structure, properties and the intensity of the applied deformation.

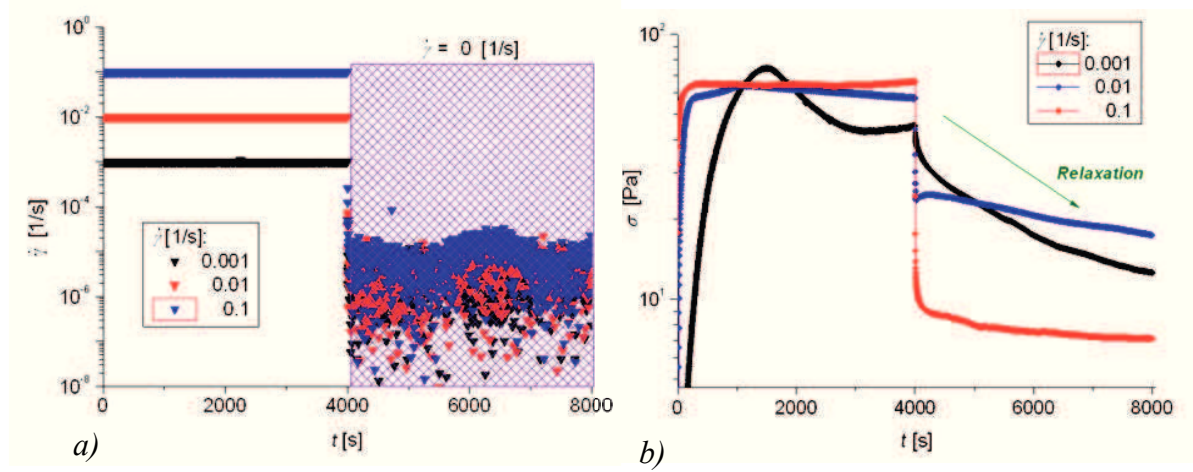


Fig. 2.7. The imposed shear rate (a) and relaxation of stress (b) for a Polysiloxane sample, results obtained following a Relaxation test, at $T = 20^{\circ}\text{C}$.

For a *Relaxation test*, a constant shear rate is imposed for one of the surfaces defining the gap (see Figure 2.7.a), following the relaxation of the shear stress in time (see Figure 2.7.b). During the deformation caused by the rotation of the plate, the material stores stress tension in its internal structure, which is dissipated once the rotation is stopped. Measuring the evolution of shear stresses after plate rotation is stopped, one may notice material's relaxation, this type of test being an indicator for elasticity presence: (i) for purely viscous fluids, once plate stops rotating, the shear stress drops abruptly towards zero; (ii) for viscoelastic fluids, the stress is decreasing gradually, as recorded for the material presented in Figure 2.7.b.

2.3.1.2. Oscillatory shear tests

Two main procedures are available for the determination of fluid viscoelastic properties using shear motion: (i) analysis of the material response by simple shear tests (previously presented); (ii) dynamic mechanical measurements. For dynamic tests, a time-dependent input is considered (periodic motion), generally with sinusoidal shape. The input signal is characterized by an oscillatory angular frequency ω and oscillatory amplitude (γ_0 for the *strain controlled* test). Thus, the variation of the strain in time may be expressed by the formula:

$$\gamma(t) = \gamma_0 \sin \omega t \quad (2.29)$$

For viscoelastic materials with linear behavior, the response to such a stress (shear stress, $\sigma = \sigma_0 \cdot \sin(\omega t + \delta)$), will have a sinusoidal distribution (at equilibrium), dephased compared to the entry signal with the angle δ . Phase angle (difference between stress and strain) contains information on rheological characteristics of fluids (see Figure 2.8).

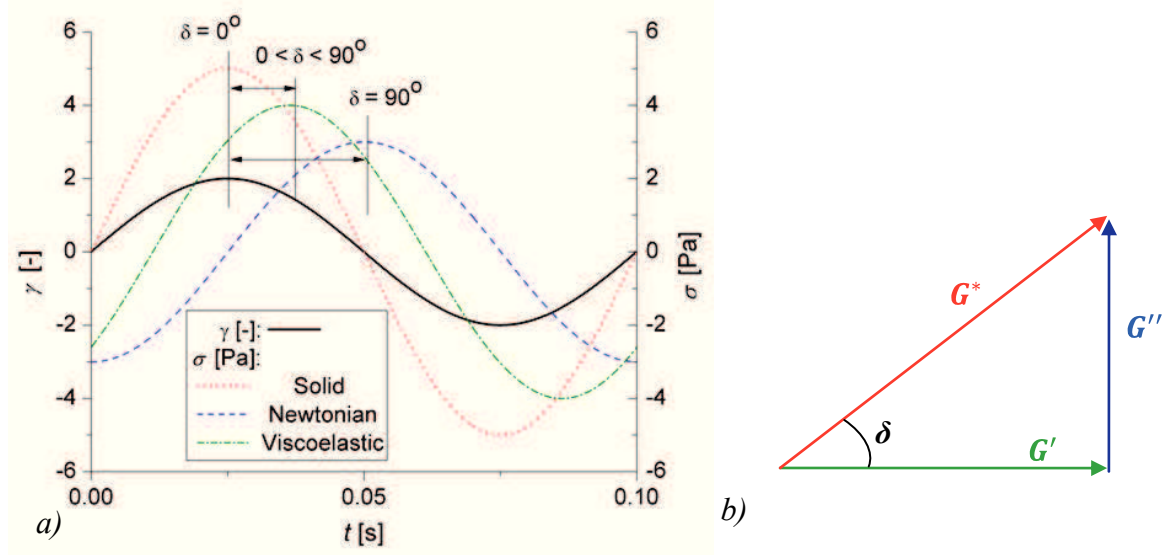


Fig. 2.8. Phase angle variation for different types of materials (a) and complex modulus definition depending on its elastic and viscous components (b).

The shear stress may be expressed depending on the elastic module G' and on the viscous module G''

$$\sigma(t, \omega) = \gamma_0 \cdot [G' \sin(\omega t) + G'' \cos(\omega t)] \quad (2.30)$$

or

$$\sigma = G' \gamma + \frac{G''}{\omega} \dot{\gamma} \quad (2.31)$$

where the components have the expressions:

$$\begin{cases} G' = \frac{\sigma_0}{\gamma_0} \cdot \cos \delta \\ G'' = \frac{\sigma_0}{\gamma_0} \cdot \sin \delta \end{cases} \quad (2.32)$$

Elastic modulus defines the energy stored in material's structure and the viscous modulus expresses the energy dissipated during the flow, both being determined as function of tangential stress component and the applied deformation see Figure 2.8. The complex modulus is a sum of elastic and viscous components, having the following form:

$$G^* = G' + iG'' \quad (2.33)$$

The complex viscosity of the fluid may be decomposed the same as the complex modulus in the dynamic viscosity ($\eta' = G''/\omega$) and the dynamic rigidity ($\eta'' = G'/\omega$).

$$\eta^* = \eta' + i\eta'' \quad (2.34)$$

In the integral form, the complex module is the following:

$$G^* = i\omega \int_0^\infty G(s)e^{-i\omega s} ds \quad (2.35)$$

For viscoelastic analogical models (previously presented), the complex modulus, respectively its components, take particular forms. For instance, in the case of the *Maxwell* model, the viscous and the elastic moduli have the following expressions:

$$\begin{cases} G' = \frac{\eta\lambda\omega^2}{1 + \lambda^2\omega^2} \\ G'' = \frac{\eta\omega}{1 + \lambda^2\omega^2} \end{cases} \quad (2.36)$$

where the term $(\eta_s\omega)$ expresses the purely viscous component of the material.

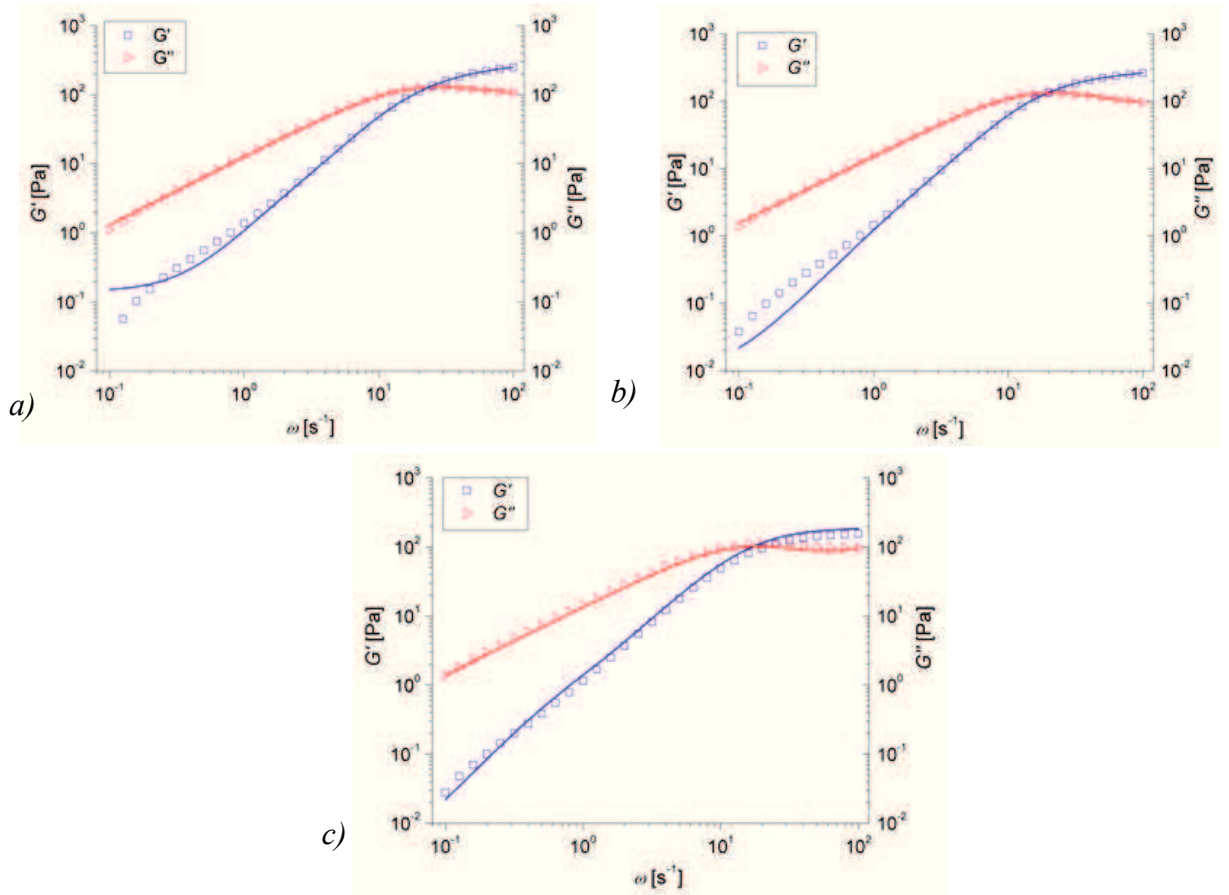


Fig. 2.9. Approximation of the experimental modules G' and G'' for a viscoelastic solution with the *Maxwell* model with 8 elements, with variable relaxation time steps, at different amplitudes of the applied strain: $\gamma_0 = 0.01$ [–] (a); $\gamma_0 = 0.1$ [–] (b) și $\gamma_0 = 1$ [–] (c).

The representation of viscoelastic fluid rheological behavior, a Maxwell model with „ m ” elements connected in parallel is used, as shown in Figure 2.3. Complex moduli

expressions are obtained, in this case, by summing the relations (2.36), for details see [89], [141], [142], [155], [222]:

$$\begin{cases} G' = \sum_{i=1}^m \frac{\eta_i \lambda_i \omega^2}{1 + \lambda_i^2 \omega^2} \\ G'' = \eta_s \omega + \sum_{i=1}^m \frac{\eta_i \omega}{1 + \lambda_i^2 \omega^2} \end{cases} \quad (2.37)$$

The relaxation spectrum is one of the most important characteristics of linear viscoelastic fluids, and it may be determined using relations (2.36 - 2.37). Figure 2.8 presents the approximation of the experimental moduli of a viscoelastic fluid (shampoo) by a *Maxwell* model with 8 elements connected in parallel. The relaxation times vary depending on the intensity of the applied strain, respectively of the stresses stored in fluid internal structure during the flow, the values obtained for relaxation times and corresponding viscosity coefficienta are indicated in Annex 2.

Rheological characterization of low viscous fluids using conventional rotational rheometers is very difficult due to the influence of measuring systems inertia and moment transducers limitations. Hence, for low viscous fluids, the use of capillary rheometers (mainly used for high shear rates flows) is recommended [38], [222].

2.3.2. Extensional motions

Extensional motions find their applicability in many important industrial processes: manufacturing process of optical fibers, fluids flow through porous layers, grooves and slits (divergent and convergent flows), moulding plastic materials in complex forms. The main types of extensional motions are uniaxial, biaxial and plane.

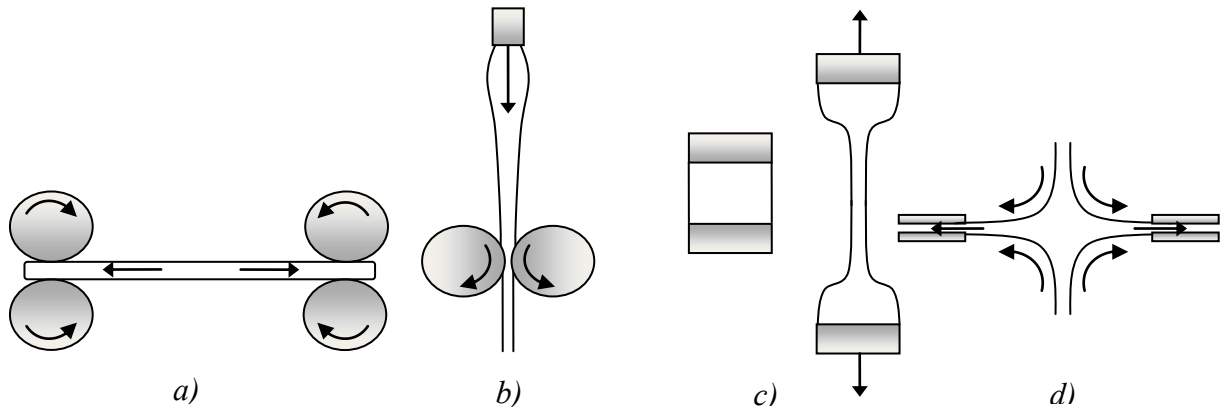


Fig. 2.10. Usual geometries used in extensional tests: forming of fluid filaments on horizontal (a) and vertical directions (b, c); aspiration of fluids in tubes with small diameters (d).

As regards pure uniaxial motions, both extra stress tensor (relation 2.38) and strain rate tensor (relation 2.39) depend on the strain rate $\dot{\varepsilon}(t)$, where ε is the specific extensional strain (*Hencky strain*), [69], [89], [141], [142], [155]:

$$\mathbf{T} = \begin{bmatrix} \sigma_{11} & 0 & 0 \\ 0 & \sigma_{22} & 0 \\ 0 & 0 & \sigma_{33} \end{bmatrix}, \quad (2.38)$$

$$\mathbf{D} = \frac{1}{2} \begin{bmatrix} 2\dot{\varepsilon} & 0 & 0 \\ 0 & -\dot{\varepsilon} & 0 \\ 0 & 0 & -\dot{\varepsilon} \end{bmatrix}. \quad (2.39)$$

The velocity vector, in a Cartesian coordinates system, has the form:

$$\mathbf{v} = \frac{1}{2} \begin{bmatrix} 2\dot{\varepsilon} x \\ -\dot{\varepsilon} y \\ -\dot{\varepsilon} z \end{bmatrix}. \quad (2.40)$$

A fluid in uniaxial elongational flow is characterized by the extensional viscosity $\eta_e(\dot{\varepsilon}) = (\sigma_{11} - \sigma_{22})/\dot{\varepsilon}$, proportional with the dynamic viscosity, $\eta_e = Tr \cdot \eta$, where $Tr(\dot{\varepsilon})$ is the dimensionless *Trouton* number dependent on the material ($Tr = 3$, for a purely viscous fluid) in a simple extension [89].

The main uniaxial extensional tests are based on the forming of fluid filaments on horizontal (Figure 2.10.a) or vertical (Figure 2.10.b and c) directions, flows by convergent geometries or with diameter leaps or fluid aspiration in tubes with small diameters (Figure 2.10.d), aiming at measuring the diameter of the fluid filament, of the flow rate, of the extensional stresses and in the end the calculation of elongational (extensional) viscosity. We must specify that the non-monotonous dependence of the $Tr(\dot{\varepsilon})$ number is a manifestation exclusively of the fluid elasticity.

In numerous cases (polymers), the Tr number may reach very high values ($Tr \gg 3$), which indicates fluids capacity to support very high extensional stresses compared to the Newtonian fluids of the same viscosity.

2.3.3. Complex motions – squeeze of fluid films

The *squeezing flow* (*squeeze flow*, *compression flow*) may be defined as being the “complex flow in which a fluid is compressed and deformed between two solid surfaces that approach one to each other, determining the expulsion of the fluid outside the gap” (see Figure 2.11).

The term of “complex motion” defines a very important feature of the phenomenon: unlike the previously described simple motions (shear or extensional motions), in the axial

symmetric squeeze flow two flow directions appear - on radial and axial directions- the strain rate tensor having one component. Commonly, squeeze flow is associated to the term of *thin films*, due to the very small spaces between the surfaces in relative motion.

Practical applications of the motion are met in various fields as: engineering (lubrication, thin films and fluid dampers, metal or plastic processing), [145], [207], [208], bioengineering (dynamics of biofluids), rheology (characterization of simple and complex fluids), food and cosmetic industries (manufacturing processes), etc. Squeeze flow is used to determine rheological properties for a varied range of fluids: purely viscous, visco-elastic [183], [184], [185], [186], [187], visco-plastic fluids (with yield point or “*yield stress fluids*”) [206], [207], [208], [209], simple fluids and complex fluids [78], [112], [165], [207], [239], more details being provided in Chapter 3.

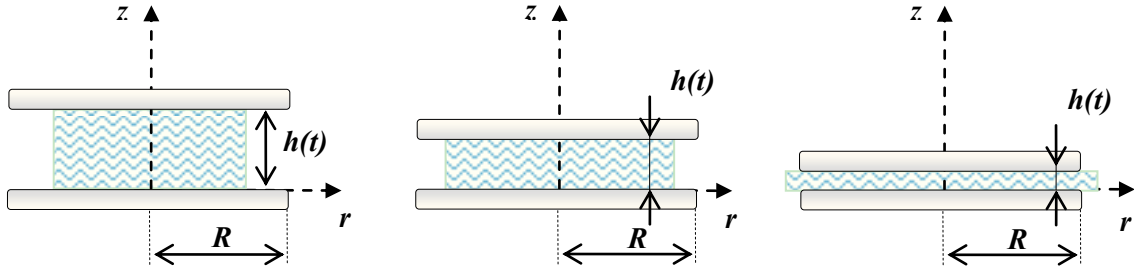


Fig. 2.11. Fluid squeezed between two parallel surfaces.

Commonly, the testing procedure implicates a fixed lower surface and a displacement of upper wall (plate), followed by the deformation and squeezing of the film from the gap. In most cases, the two surfaces are circular, the induced motion being axial-symmetrical.

Depending on the testing procedure used, the rheometric squeeze tests are divided into two categories: (i) squeeze tests in which the plate motion follows a monotonous profile $h(t)$ in time (achieved by imposing a constant plate rate or by applying a constant load in time); (ii) oscillatory squeeze tests, in which the motion is periodical, in most cases a sinusoidal displacement profile being imposed. In the general case, the continuity equation and the *Cauchy* motion equations for the axially symmetric squeeze flow of incompressible fluids between solid surfaces (in the absence of mass and inertia forces) have the expressions:

$$\left\{ \begin{array}{l} \frac{1}{r} \frac{\partial r v_r}{\partial r} + \frac{\partial v_z}{\partial z} = 0 \\ -\frac{\partial p}{\partial r} = \frac{1}{r} \frac{\partial r \sigma_{rr}}{\partial r} + \frac{\partial \sigma_{rz}}{\partial z} - \frac{\sigma_{\theta\theta}}{r} \\ -\frac{\partial p}{\partial z} = \frac{1}{r} \frac{\partial r \sigma_{rz}}{\partial r} + \frac{\partial \sigma_{zz}}{\partial z} \end{array} \right. \quad (2.41)$$

The extra stress tensor has the following form:

$$\mathbf{T}_E = \begin{bmatrix} \sigma_{rr} & 0 & \sigma_{rz} \\ 0 & \sigma_{\theta\theta} & 0 \\ \sigma_{zr} & 0 & \sigma_{zz} \end{bmatrix} \quad (2.42)$$

The cinematic of motion is characterized by the rate gradient:

$$\mathbf{L} = \begin{bmatrix} \frac{\partial v_r}{\partial r} & 0 & \frac{\partial v_r}{\partial z} \\ 0 & \frac{v_r}{r} & 0 \\ \frac{\partial v_z}{\partial r} & 0 & \frac{\partial v_z}{\partial z} \end{bmatrix}, \quad (2.43)$$

the rate of deformation tensor being:

$$\mathbf{D} = \frac{1}{2}(\mathbf{L} + \mathbf{L}^T) = \begin{bmatrix} \frac{\partial v_r}{\partial r} & 0 & \frac{1}{2}\left(\frac{\partial v_r}{\partial z} + \frac{\partial v_z}{\partial r}\right) \\ 0 & \frac{v_r}{r} & 0 \\ \frac{1}{2}\left(\frac{\partial v_z}{\partial r} + \frac{\partial v_r}{\partial z}\right) & 0 & \frac{\partial v_z}{\partial z} \end{bmatrix} \quad (2.44)$$

In 2.41 - 2.44, v_r and v_z represent velocity components on radial, respectively axial directions for squeeze motion (see Figure 2.11). In the case of the symmetrical axial squeeze flow with constant rate, the solution of the relation 2.41 (respectively the solution of the equation *Navier-Stokes*) for the two velocity components is (see Annex 3):

$$v_r(r, z) = 3 \frac{\dot{h}}{h^3} r(z^2 - hz), \quad (2.45)$$

$$v_z(r, z) = -\frac{\dot{h}}{h^3} (2z^3 - 3hz^2). \quad (2.46)$$

For a constant velocity squeeze test $\dot{h} = \text{const.}$ (velocity is imposed for the upper plate), normal force expression takes two distinct forms, depending on the actual contact surface between the fluid and solid surfaces: (i) constant contact area, defined by the geometrical dimensions of the test surfaces (eq. 2.47); (ii) constant fluid volume (eq. 2.48), the area of the actual contact surface being variable in this case (see Figure 2.12).

For a constant area squeeze flow, the normal force takes the form,

$$F(t) = -\frac{3\pi\eta_0 R^4}{2h^3} \dot{h} \quad (2.47)$$

and in the case of a constant volume (\mathcal{V}) of fluid, the force expression becomes:

$$F(t) = -\frac{3\eta_0 \mathcal{V}^2}{2\pi h^5} \dot{h} \quad (2.48)$$

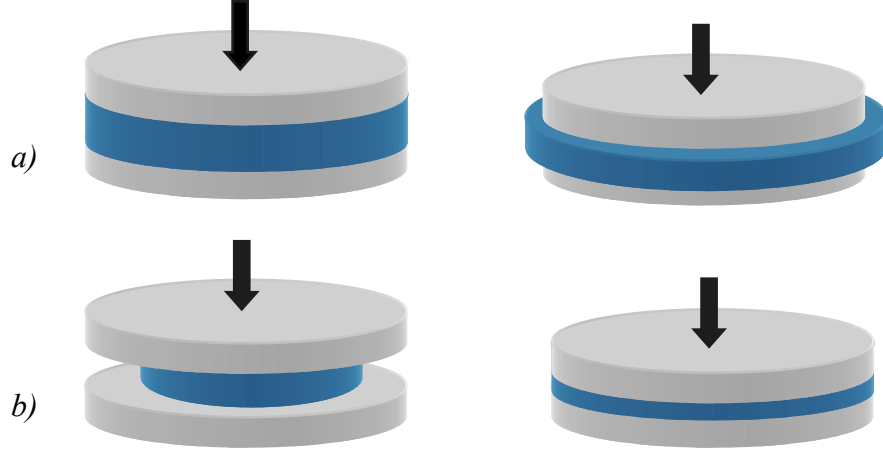


Fig. 2.12. Squeeze of a fluid between two parallel surfaces in case of a constant area squeeze flow (a) and of a constant volume of fluid (b).

In the case of a constant velocity squeezing test, with known plate velocity ($\dot{h} = \partial h / \partial t$) and geometrical quantities ($h(t)$, R respectively \mathcal{V}), the normal force $F(t)$ measured during test allows the use of the previously presented expressions to determine the dynamic viscosity η_0 of the incompressible Newtonian fluids. For an imposed constant squeeze force F_0 , fluid film thickness variation in time is given by [12]:

$$h(t) = - \frac{h_0}{\sqrt{1 + \frac{4F_0 h_0^2}{3\pi\eta_0 R^4} t}}, \quad (2.49)$$

expression used also to determine Newtonian viscosity, where h_0 is the initial thickness (see Figure 2.12.a).

In the case of oscillatory squeezing flow, a time-depenent (periodical) displacement profile is considered for the upper plate (commonly with sinusoidal shape), $\varepsilon = \varepsilon_0 \cdot \sin(\omega t)$, with $\varepsilon_0 \ll h_0$. Thus, film thickness variation in time is described by:

$$h(t) = h_0 + \varepsilon_0 \cdot \sin(\omega t). \quad (2.50)$$

In this case, upper plate velocity is:

$$\dot{h} = \varepsilon_0 \cdot \omega \cdot \cos(\omega t), \quad (2.51)$$

where ω is the imposed oscillatory frequency. For the mentioned hypothesis, the squeeze force becomes:

$$F(t) = - \frac{3\pi\eta_0 R^4}{2h^3} \cdot \varepsilon_0 \cdot \omega \cdot \cos(\omega t). \quad (2.52)$$

For a given geometry (R , h_0), the relation (2.52) may be used to determine the Newtonian viscosity η_0 , by measuring the force $F(t)$. Squeezing tests are also used to

determine characterize Newtonian generalised and viscoelastic fluids, the force expression changes depending on the viscosity function associated to each type of rheological behavior. All these aspects will be presented in detail in [Chapter 3](#).

2.4. NON-LINEAR VISCOELASTICITY

In the previous chapters were introduced the rheometric techniques used to determine the rheological properties of viscoelastic fluids in linear regime, characterized by a proportional variation of the material response with the applied strain amplitude or shear rate. Nevertheless, for almost all complex materials (for instance: polymers [64], [88], [111], [115], emulsions [29], concentrated suspensions of solid, soft or glass particles [31], [44], [135], [128], [204], [231], greases [14], [17], [125], [126], metastable colloidal systems – gels, entangled materials, wormlike micellar solutions, branched or unbranched polymers – *soft entangled materials* [107], [196], [250], biomaterials [81], [82], [83], [146], soft solids, etc.), the complexity of the inner structure leads to structural changes at the microscopic level under external loads which induce a non-linear rheological behavior.

This behavior is noticed at the macroscopic level during the application of high deformations through: (i) occurrence of a plateau of the flow curve in simple shear flows; (ii) preferential directions of the flow, non-homogeneity of viscosity function; (iii) nonlinear dependence of material functions on the applied stress; (iv) unusual “peaks” in the distributions of the components of the complex module in dynamic tests). The non-linear character depends on time, on the size of the input signal, and it leads to loss of proportionality between input and output quantities [149], [158].

This behavior is encountered in viscoelastic materials with yield stress, being highlighted especially for the phase transition zone, from one state of the material to another (solid-liquid, respectively liquid-solid), reached in the vicinity of the yield shear stress σ_0 [14], [20], [114], [250]. This category of viscoelastic fluids will be particularly studied in this paper. The scientific literature provides multiple definitions of the yield stress, all of them being associated to the time scales related to the dynamic process: the relaxation times of the material, the experimental (testing) time, the chemical reaction times in which the components of the material react, the characteristic time in the sol-gel transition [236], [242].

The transition from one rheological regime to another is performed in a domain where the instability of the material is obvious. According to literature, the change of the rheological behavior may be due to different factors, however depending on the material internal structure: as regards polymers, this may be due to the destruction of the internal network

(elastic) structure of the material or to the creation of new chemical bonds (the phenomena of *reptation*, *branching*, *cross-linking*) [107], [116], [115], [114], [196], [146]; as regards the suspensions of soft or solid particles and the emulsions, this may be due to the formation of particle agglomerations (clusters) or liquid bubbles. Sometimes, the instability of the material is associated, at the macroscopic level, with phenomena such as wall slipping, depletion [44], [115], [114], [126], [196], [231], or with the forming of bands in the material (shear banding phenomenon) [57], [84], [85], [92], [111].

For yield stress fluids, the evolution of the yield curve and of the components of the complex moduli depending on the strain rate, respectively on the value of the strain amplitude, allows the characterization of the rheological regimes as follows: the linear regime at small amplitudes and reduced shear rates, where the regime generally corresponds to the solid-elastic state or viscoelastic behavior with pronounced elasticity, field generically called SAOS (*Small Amplitude Oscillatory Shear*) [31], [52], [196]; the transitory regime at medium amplitudes, MAOS (*Medium Amplitude Oscillatory Shear*) and medium strain rates where the two rheological states, solid-liquid, coexist [115], [116]; the third domain corresponds to the large strain amplitude area LAOS (*Large Amplitude Oscillatory Shear*) or to the high strain rates where the material behavior is preponderantly viscous [14], [31], [52], [81], [83], [233].

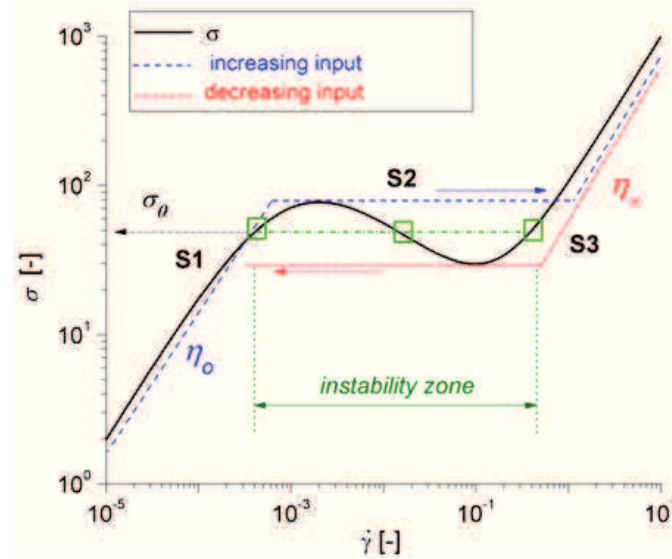


Fig. 2.13. Illustration of the non-linear behavior of complex fluids with yield stress σ_0 by the material flow curve (non-monotonous variation $\sigma(\dot{\gamma})$).

At present, there are multiple techniques for rheological characterization, the most common being the oscillatory tests with large amplitudes, the analysis of non-linear response is made by various methods: *Fourier* analysis [10], [31], [44], [129], [175] *Cebishev* polynomials [196], [197], *Lissajous* and *Pipkin* diagrams [83], [143], analysis of complex module evolution [44], [114]. At the macroscopic level, the non-monotonic behavior is

recorded also during simple shear tests by a “jump” (plateau) in flow curve distribution (see Figure 2.13) for which, at the same value of the critical shear stress, three values of the shear rate correspond [14], [243]. The “jump” occurs for a certain domain of the applied stress, being solely dependent on the deformation history (the time in which the material reaches the yield point). Therefore the jump depends on the initial testing conditions (initial state of stress within the material) and it takes place when reaching σ_0 , which defines the yield stress [11], [13], [16], [17], [45], [189], [243].

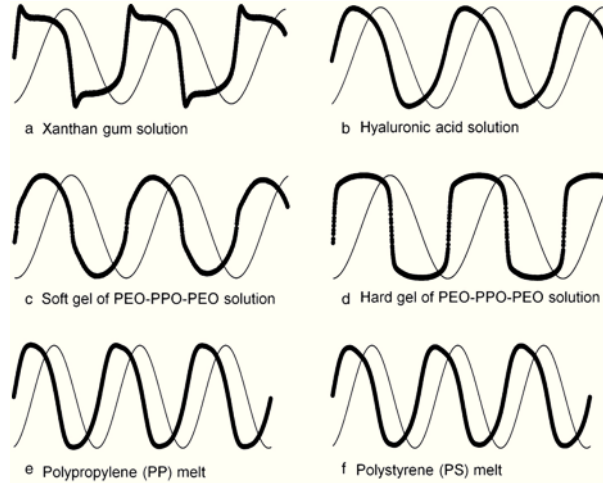


Fig. 2.14. Deformation of stress output signal for complex in large amplitude oscillatory shear flow [114]. The input deformation signal is a pure sinusoid with increasing strain amplitude.

It must be specified that the *S1* and *S3* solutions may be experimentally obtained during the simple shear tests, but the *S2* solution cannot be obtained experimentally, as it has a purely theoretical character (and it is unstable). At high shear rates, beyond the yield stress, the behavior of the fluid shows a dependence $\sigma(\dot{\gamma})$ of the power-law type, with a small flow index ($n < 1$), below the yield stress the viscosity being almost constant [20], [114], [192], [158], [250]. Another indicator of non-linear regime is the deformation of output stress signal [114], [117], [126], [143], [146], (see Figure 2.14) and the strain amplitude dependence of dynamic moduli in oscillatory tests [29], [114], [128], (see Figure 2.15).

Depending on the evolution of the elastic and viscous components, we may determine the non-linear rheological character specific to the analysed fluid, being set, so far, four large categories of specific behavior: (1) pseudo-plastic, depending on the strain amplitude (*strain thinning*), (Figure 2.15.a); (2) dilatant, depending on the strain amplitude (*strain hardening*), (Figure 2.15.b); (3) with a small jump in the stress distribution (*weak strain overshoot*), (Figure 2.15.c); (4) with significant jump in the stress distribution (*strong strain overshoot*), (Figure 2.15.d), [114], [128], [169]. Of interest for this study are the categories 3 and 4, in which the occurrence of the non-linear viscoelasticity is emphasized. The third category of

materials (Figure 2.15.c) is characterized by a maximum occurred in the distribution of the viscous model, in the MAOS field, this behavior being associated to the suspensions, pastes, concentrated emulsions, polymer solutions and soft glassy materials [29], [114], [128], [117].

The *strong strain overshoot* behavior (the fourth category) is characterized by an almost equal contribution of the dynamic modules in the area of small amplitudes (SAOS) and by the presence of maximum points in the distribution of both components (in the MAOS field), as seen in Figure 2.15.d. It was noticed that the maximum points occur in the vicinity of the crossing point between the two components. This behavior has been noticed so far in the solutions of associative polymers [117], [116], [114], [128]. Some times, the distribution of the viscous model presents two maximum points, regardless of the parameter that it depends on - $G''(\gamma)$ [52], [169], $G''(\omega)$ [107], $G''(\sigma)$ - this behavior being recorded for various materials: homopolymer smelting - polystyrene, solutions of lecithin and urea, solutions of biopolymers, suspensions of anisotropic particles, suspensions with solid particles, peanut butter.

The output signal deformed shape (Figure 2.14) and the evolution of the *Lissajous* diagrams (Figure 2.16) may also be related to the materials structure [31], [81]. Moreover, the area of the *Lissajous* figure may be an indicator for the energy accumulated in the inner network of the material and its viscous dissipation, strictly connected to the relaxation of stresses within the material [114], [143].

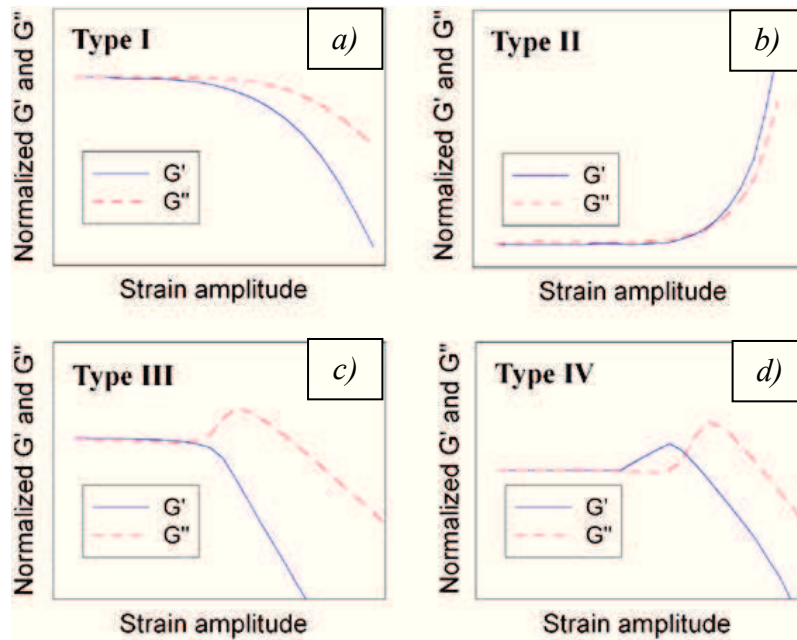


Fig. 2.15. Variation of complex moduli components depending on the type of rheological behavior associated to the material: *strain thinning* (a); *strain hardening* (b); *weak strain over shoot* (c); *strong strain overshoot* (d) [114], [128].

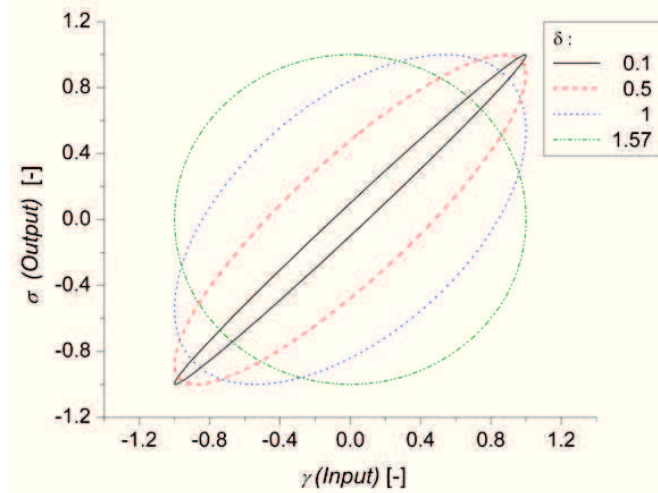


Fig. 2.16. The Lissajous diagram for viscous and viscoelastic fluids at different values of the phase difference angle δ .

The analysis of complex moduli, deformations of stress signals and evolution of *Lissajous* curves shape provides mainly a qualitative characterization of the non-linearity phenomenon and consequently a method for materials classification by associating their response with a certain type of rheological behavior [81], [82], [83], [114], [146]. In particular, in order to quantify their non-linearity, it is necessary to accurately establish a critical yield point (in simple shear tests), a critical specific strain (in dynamic tests) and an analysis of the harmonic components of the material response signal following a *Fourier* analysis [31], [44], [129], [130], [196], [233]. Some of the samples investigated in this thesis belong to the category of yield stress materials (see. Chapters 5 and 6).

2.4.1. Large amplitude oscillatory shear tests

In the case of a dynamic oscillation test with strain amplitudes $\gamma = \gamma_0 \cdot \sin(\omega t)$ the response of the material (under stress) will have the form:

$$\sigma = \sigma_0 \cdot \sin(\omega t + \delta) \quad (2.53)$$

where $\delta = \delta(\omega)$ corresponds to a linear yield regime and $\delta = \delta(\omega, \gamma_0)$ corresponds to the non-linear regime. The application of the *Fourier* transform supposes the decomposition of the response function (shear stress) into a sum of odd harmonic contributions (the viscosity function being an even function by definition):

$$\sigma \sim a_1 \cos \omega t + a_2 \cos 3\omega t + a_3 \cos 5\omega t + \dots \quad (2.54)$$

where the superior harmonics indicate the dependence of the viscosity η_0 on the strain rate, $\dot{\gamma} = \omega \gamma_0 \cdot \cos(\omega t)$, which may be written under the form:

$$|\dot{\gamma}| = \omega \gamma_0 \cdot \left(\frac{2}{\pi} + \frac{4}{\pi} \left(\frac{\cos 2\omega t}{1 \cdot 3} + \frac{\cos 4\omega t}{3 \cdot 5} + \frac{\cos 6\omega t}{5 \cdot 7} - \dots \right) \right) \quad (2.55)$$

$$|\dot{\gamma}| \sim a + b \cos 2\omega t + c \cos 4\omega t + \dots \quad (2.56)$$

The presence of the even components of the frequency spectrum (eq. 2.54) is generally associated to phenomena which are not directly dependent on material functions, but particularly they may be due to the lack of the material adherence to the solid surface. Data acquisition procedure for a suitable *Fourier* analysis supposes an initial determination of various parameters as: data acquisition time step (to record the discrete signal); maximum harmonic contribution that can be recorded; the optimum signal-noise ratio for the case of oversampling. More details regarding this procedure can be found in the following papers [38], [71], [108], [212], [233], [246].

As it will be demonstrated throughout this work, the presence of the critical yield point associated to the non-linear behavior of complex fluids may also be emphasized by building a transitory flow curve based on several creep tests at various constant shear stress values [54]. In this work, the non-linear character of the materials has been analysed by correlating the simple shear tests with the high amplitude oscillatory tests, setting a procedure to determine the type of material and the rheological behavior by qualitative analysis (*Lissajous* curves, form of the output deformed signal, range of linearity and non-linearity) and by quantitative analysis of the flow curves (determination of the critical values of the yield point, i.e. the values of yield stress and yield strain). The analysis and correct understanding of the non-linearity mechanisms is necessary for an optimum design of manufacturing and processing of these complex materials. The correlation of the various testing procedures (viscometric simple shear, and dynamic tests) is important to correctly establish the rheological properties of the fluids and their non-linear range [54], [114], [196].

2.5. ADHERENCE AND CAPILLARITY PHENOMENA

The squeeze flow is associated with the theory of thin films due to the narrow testing gaps in which the process takes place (ex. plane case, parallel discs $R \gg h_0$ and $h \ll 1 \text{ mm}$). Thus, for small squeezing velocities (small Re numbers), adhesion forces and superficial tension have a significant influence on fluid film kinematics and evolution of the free surface formed at the edge of the gap (fluid-gas interface). End effects analysis in squeeze flow is necessary to quantify their influence on pressure distributions within the gap, respectively over normal force variation. It is well known that, in the squeeze flow, at the outlet area (edge

of the gap) a decrease of pressure in the fluid film is sometimes recorded (and it may significantly influence the resulting force). Equally, the accumulation of the fluid at the edge of the gap may create an additional force. Fluid motion both in the gap, and outside it, is directly influenced by adherence/slip conditions and surface tension influence. This paragraph is dedicated to the theoretical aspects of the *capillarity surface tension phenomena*.

2.5.1. Capillarity phenomena and surface tension

The lack of adherence and the presence of end effects (where capillarity plays an important part) influences directly squeezing flow, respectively the pressure distribution in the gap. Capillarity is the property of a fluid to flow through narrow gaps without the influence of exterior forces.

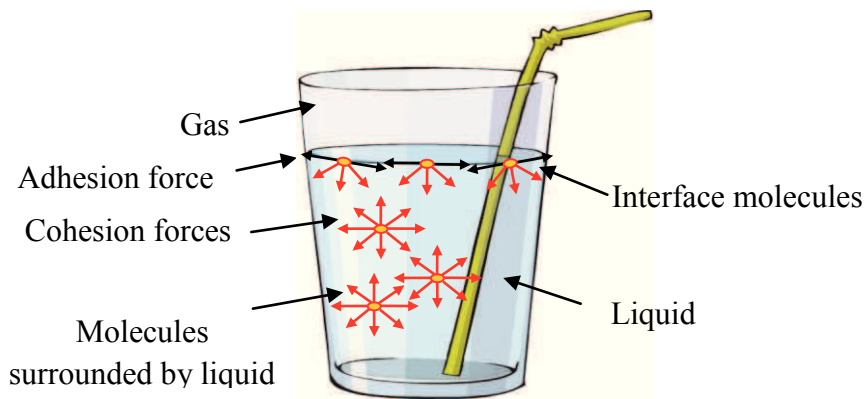


Fig. 2.17. Action of cohesion forces over liquid molecules, inside it and at the liquid-gas interface.

The capillarity phenomenon is determined by the dominating presence of the intermolecular adhesion forces between liquid and solid (solid-liquid interfacial stress σ_{SL}) compared to that of intermolecular cohesion forces inside the liquid and of the solid-gas interfacial stress σ_{SG} (Figure 2.17), and it may induce an ascending flow of water in a capillary tube (Figure 2.18.d and 2.19), opposed to the descending flow induced by gravity.

Determined by the surface tension σ_s (the specific linear stress manifested at the liquid-gas interface) and the fluid-solid adherence (liquid-solid adhesion forces), the capillarity phenomena have numerous applications encountered in the natural environment and not only: breaking of the fluid jet and formation of drops (Figure 2.18. a); formation of spherical drops when breaking soap bubbles due to the tendency to minimize the area, respectively the number of molecules on the interface (Figure 2.18. b); a liquid columns rising in capillary tubes (Figure 2.18. c); transport and retention of fluids in plants capillaries (Figure 2.18. d); formation of foams and emulsions (Figure 2.18. e); floating small objects on the water surface

due to the balance between gravitational and surface tension forces (Figure 2.18. f); adhesion between the polymeric wires of a brush (Figure. 2.18. g).

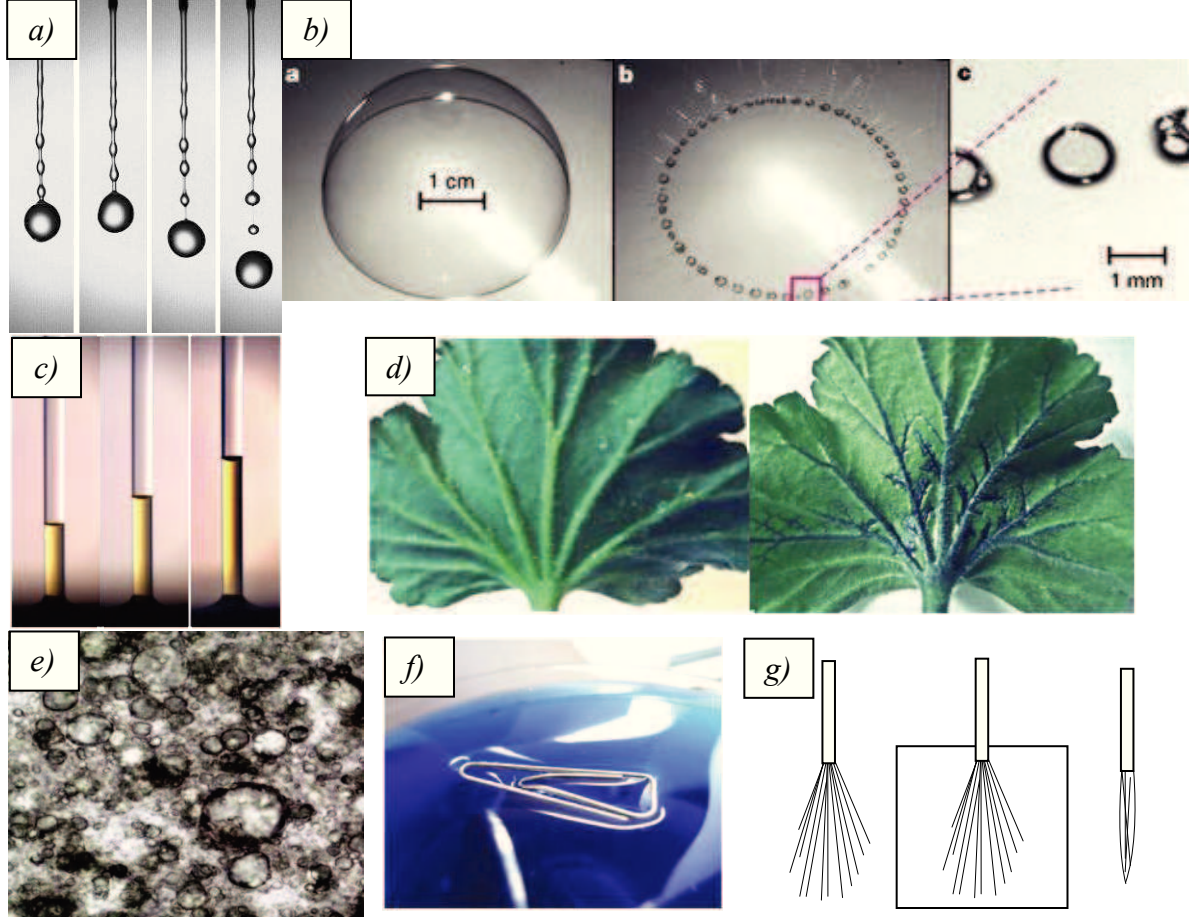


Fig. 2.18. Effects of capillarity and superficial stress: breaking of a jet and formation of drops (a); formation of spherical drops when breaking soap bubbles (b) [24]; water column rising in capillary tubes (c); transport and retention of fluids in plants capillaries (d); formation of foams and emulsions (e); floating small objects on the water surface (f); adhesion between the polymeric wires of a brush (g) [19].

The influence of the capillarity phenomena in narrow gaps flows may be estimated by a dimensionless parameter called *Capillarity Number*, defined by the ratio between viscous and surface tension [19], [25], [65], [162], [168]:

$$Ca = \eta \dot{h} / \sigma_s \quad (2.57)$$

Surface tension forces are manifested on the contact surface between a fluid and a gas (free surface) or on the interface between two immiscible fluids, in this case being called interface stress forces (interfacial). In the case of an interface (liquid membranes) at rest, the state of balance is given by the offset of the normal force at the surface with the surface tension that act tangentially on the interface edge (Figure 2.19.a). The presence of the surface tension σ_s creates a pressure difference Δp on the curvature of the area, expressed by the *Young-Laplace* relation depending on the area curvature [19], [73], [222]:

$$\Delta p = \sigma_s \left(\frac{1}{R_1} + \frac{1}{R_2} \right) = 2\kappa\sigma_s \quad (2.58)$$

where R_1 and R_2 are the radiuses of curvature after every axis parallel to the surface, and κ is the medium curvature of the surface.

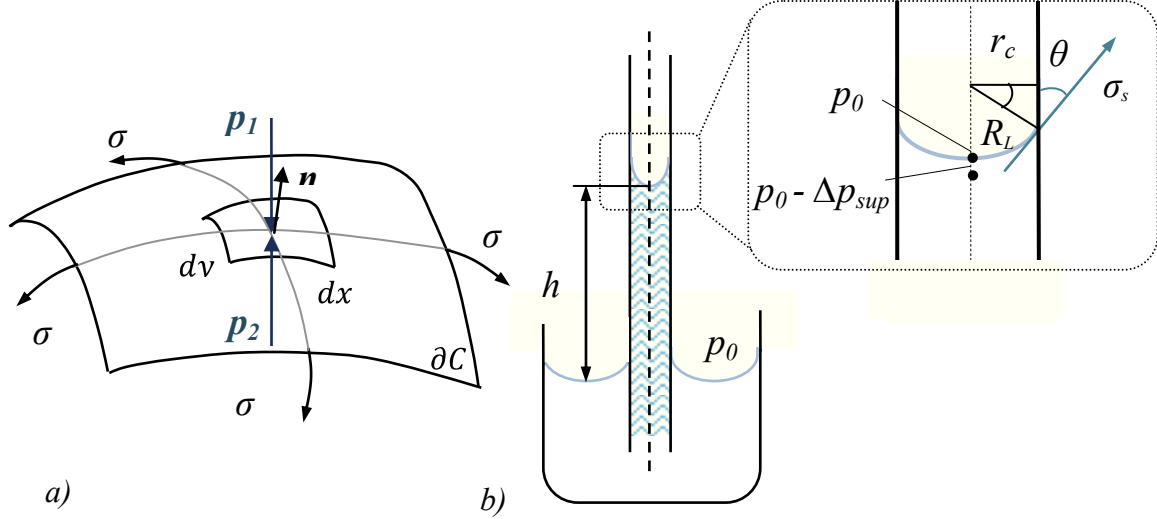


Fig. 2.19. Deformation of any free area under the action of the superficial stress forces (a) and the raising phenomenon of a fluid in a capillary vessel of circular section (forming of meniscus at the free surface in detail) (b).

In the case of rising of a liquid column in a capillary tube with circular section, the liquid-air surface inside the tube will be considered to have a spherical shape. The radiuses of curvature are identical, determining the curvature of the meniscus from the equation (2.58):

$$R_1 = R_2 = R_L \cong \frac{r_c}{\cos \theta} \quad (2.59)$$

where θ is the contact angle of the capillary wall-liquid-air system, and r_c is the radius of the capillary tube. The hydrostatic balance relation supposes that the pressure at the level of the free surface should be equal to the pressure of the free surface in the capillary tube (with the approximation $\kappa \sim 1/R_L$):

$$\Delta p_{sup} = \rho g h_L \quad (2.60)$$

where $\Delta p_{sup} = 2\sigma_s/R_L$ expresses the difference of pressure along the interface, the maximum height of the liquid may increase in the capillary tube h_L being reached in the state of balance. The approximate time step to raise the fluid column in a capillary tube is determined considering the flow as a quasi-static *Hagen-Poiseuille* flow in a tube with circular section [18], [136]:

$$t = \frac{8\eta}{\rho g r_L^2} \left(\frac{2\sigma_s \cos \theta}{r_c} + \rho g h_L \cos \theta \right) \quad (2.61)$$

One of the common methods to determine the superficial stress of a fluid, called the *Wilhelmy* plate method, supposes the partial immersion of a metallic plate in a volume of fluid and the determination of the superficial stress from the balance relation of the forces acting over the plate (gravity force, superficial stress forces and Archimedic force) [73], [222]:

$$\sigma_s = \frac{F_t}{2\Pi} \quad (2.62)$$

where $F_t = F_G - F_A$ and Π represent the wetted perimeter of the plate. Generalising this case, the same phenomenon happens when bringing in contact a solid disc of a given thickness and a volume of fluid (Figure 2.20. a).

Under the action of capillarity forces, the fluid wets the edge of the disc, raising at the height h_L . Out of the interface balance relation neighbouring the wall, considering a very small variation of the column height compared to Ox , we may determine its maximum value:

$$h_L(x) = l_c \operatorname{ctg} \theta e^{-\frac{x-R}{l_c}} \quad (2.63)$$

with $x \gg R$; where $l_c = \sqrt{\sigma_s / \rho \cdot g}$ is a material constant, called capillary length and R_d is the radius of the disc. Figure 2.20.b describes the case of a fluid volume \mathcal{V} existing in the gap formed by two solid discs of infinite radius ($R \gg h$).

In order to reach the state of balance and to form a stable interface, a force F is applied over the upper plate. In this case, the capillary pressure may be determined in the fluid volume by approximating the form of the drop with a toroidal surface, respectively:

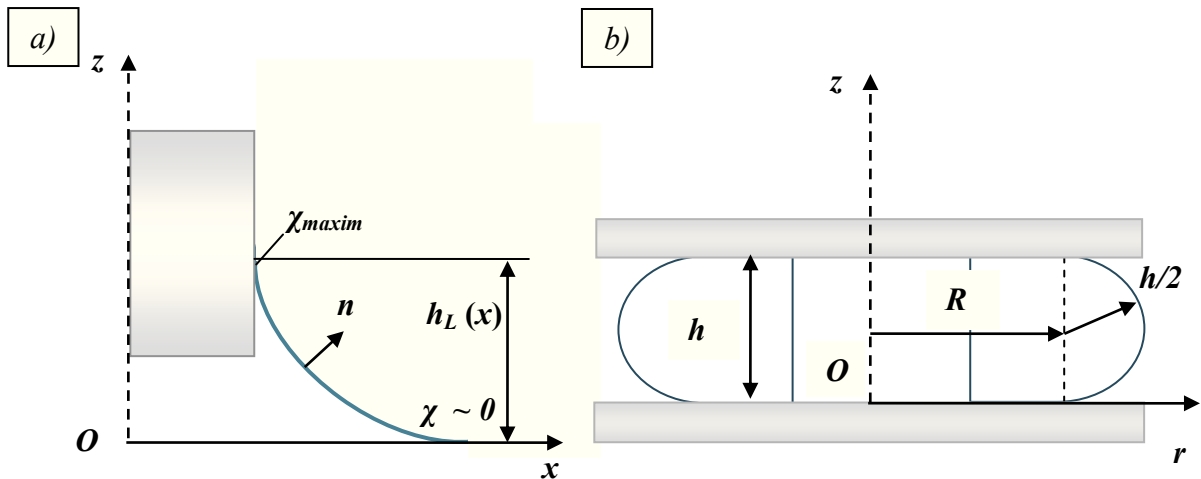


Fig. 2.20. Rising of fluid on a solid wall (a) and formation of the meniscus (hydrodynamic bridge) between two solid surfaces (b).

$$F = \frac{\pi R^2 2\sigma_s}{h} = \frac{2\sigma\mathcal{V}}{h^2} \quad (2.64)$$

The hydrostatic balance relation $2\pi rQ + 2\pi r\dot{h} = 0$ (where $\dot{h} = \partial h / \partial t$ and Q is the volumic flow per unit le length of the drop perimeter) gives the expression of pressure in the volume of fluid:

$$p(r) = \frac{2\sigma_s}{h} - \frac{3\eta\dot{h}(R^2 - r^2)}{h^3}, \quad (2.65)$$

the expression of the surface tension being [136]:

$$\sigma_s = \frac{3\eta\dot{h}R^2}{4h^2}. \quad (2.66)$$

Eliminating \dot{h} from the expressions, the result is a pressure distribution independent on the viscosity of the fluid or of the time scale [136]:

$$p(r) = \frac{4\sigma_s}{h} \left(\frac{r}{R} \right)^2 - \frac{2\sigma_s}{h} \quad (2.67)$$

2.5.2. Adherence and contact angle

The adherence of fluids to solid surfaces has a significant influence over their hydrodynamics and in the investigated dynamic process.

Determined by fluid-solid adhesion forces, the property of adherence may be quantified by measuring the contact angle that fluid forms with a solid surface. In the case of the solid (S) - liquid (L) – gas (G) contact, apart from the superficial stress ($\sigma_s = \sigma_{LG}$), the adherence stresses of the two fluids at the solid surface also intervene: σ_{SG} and σ_{SL} (Figure 2.21).

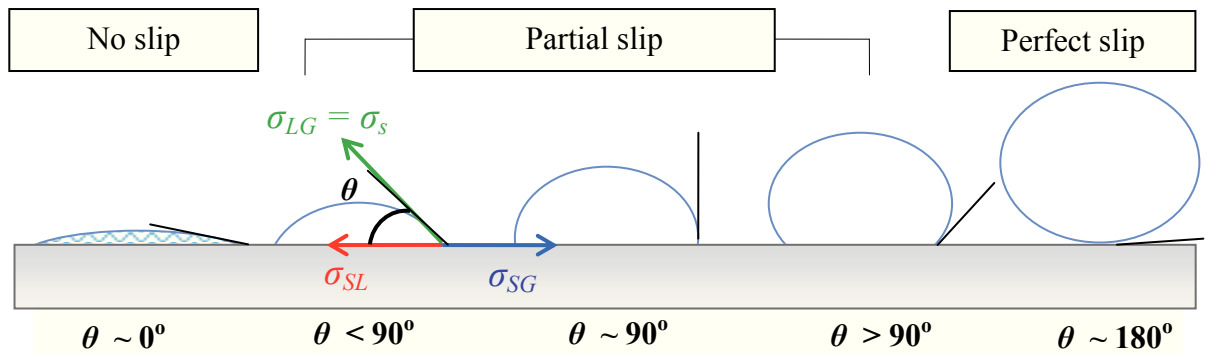


Fig. 2.21. The contact angle in a liquid-solid-gaseous system and its variation depending on the no slip properties of the solid surface (from total adherence – left side, to perfect slip – right side).

The contact angle plays, in this case, the part of the boundary condition existing at the interface between fluid and solid, being determined by *Young's* relation [65], [222]:

$$\sigma_{SG} = \sigma_{SL} + \sigma_{LG} \cos \theta \quad (2.68)$$

where σ_{SG} represents the solid-gas interfacial energy, σ_{SL} represents the solid-liquid interfacial energy, and σ_{LG} is the liquid-gas interfacial energy or the superficial stress – surface tension.

The no slip property is directly influenced by the superficial stress of the fluid and by the nature of the solid surface with which it enters in contact, the fluid dynamic control being achieved by modifying the adhesion forces (solid-liquid intermolecular forces). The specialized literature provides a multitude of methods to control the yielding dynamics in narrow gaps, used more often in the field of microfluidics, observing the conveyance of fluids in micro-channels: hydrophilic and hydrophobic areas; solid areas with specific no slip gradients; application of thermal gradients; modification of interface stress by application of an electrical field; use of reactive fluids (containing surfactants) that modify stresses at the solid-liquid interface; opto-adherence, etc. [18].

In this paper, the importance adhesion phenomenon control is motivated by the influence of this property on the performed rheological tests and to determine the properties of material. The theoretical models used to determine the rheological properties of the fluids are obtained in the hypothesis that the fluid adheres perfectly to the solid surfaces that define the flow domain. Thus, in a simple shear motion between two plates (the stationary lower plate with $V_s = 0$ and the upper plate moves on the Ox direction with the rate $V_{ps} > 0$), for perfect adherence, the fluid velocity at the wall V_f^* must be equal to the velocity of the walls. If the no slip condition is fulfilled, the velocity profile in the gap is modified (see Figure 2.22); fluid velocity that is in contact with the stationary wall is no longer zero in case of slip (total or partial), which determines the slip length $l_s > 0$.

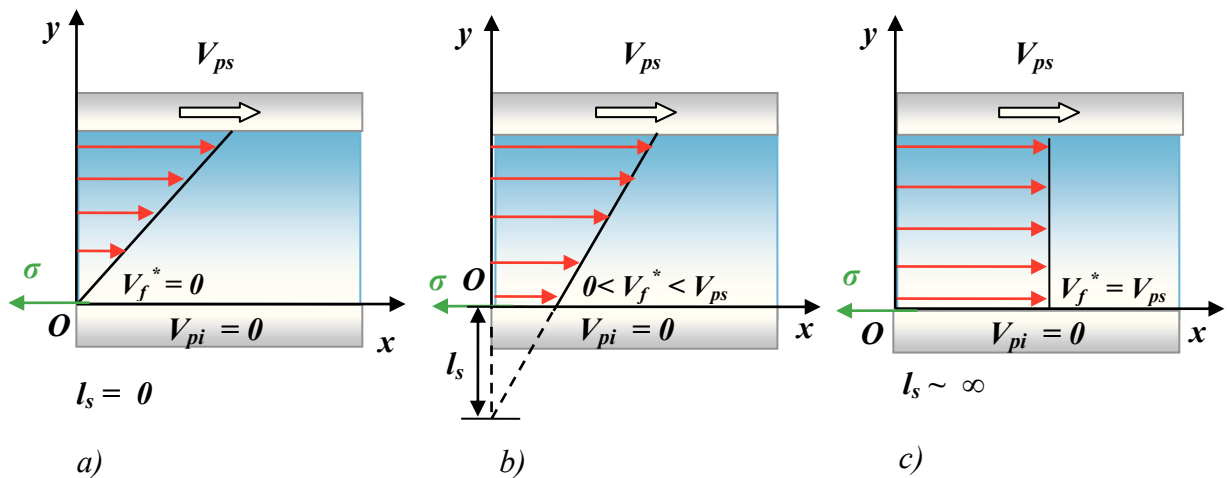


Fig. 2.22. Velocity profile on the fluid film thickness in a plane shear motion for various fluid-solid adherence conditions: no slip (a); partial slip (b); perfect slip (c).

The lack of adherence modifies fluid's velocity profile, therefore: unrealistic predictions of the rheological properties may be obtained in rotational rheometers; slip phenomenon equally influences pressure distributions in squeeze flows and finally the measured thrust. The slip phenomenon may be theoretically quantified by determining the slip length l_s , concept introduced by *Navier* in case of slip with $0 < V_f^* < V_{ps}$. The tangential friction stress σ^* in the vicinity of the wall may have equivalent formulas:

$$\sigma^* = k_f V_f^* \quad (2.69)$$

$$\sigma^* = \eta \left. \frac{\partial V_f}{\partial y} \right|_{y=0} \quad (2.70)$$

Fluid velocity at the wall being:

$$V_f^* = \frac{\eta}{k_f} \left. \frac{\partial V_f}{\partial y} \right|_{y=0} \quad (2.71)$$

where $l_s = \frac{\eta}{k_f}$ is the slip length, and k_f represents the wall friction coefficient (*Coulomb friction coefficient*) dependent on the material and the quality of the solid surface [72], [182].

Chapter 3. SQUEEZE FLOW

The purpose of this chapter is to present analytical models and formulas used to represent the squeeze flow of a fluid between two parallel surfaces. The main scientific works published will be reviewed, mainly referring to the effects that determine deviations from the classical Newtonian theoretical solutions, respectively to the influence of geometry, adherence, inertia and fluid structure.

The first investigation of the squeeze phenomenon dates from **1874**, when professor *Josepf Stephan* drafts an analytical solution to the normal force necessary to distance two immersed plates, between which a fluid film is placed. This formula (eq. 2.45), was obtained in the hypothesis of a constant contact surface between fluid and plates (see Figure 2.12.a) for a purely viscous incompressible fluid. After a short while (**1886**), *O. Reynolds* deduces the “*Reynolds* approximation for lubrication” from the *Navier-Stokes* system and confirms *Stephan’s* theory [172]. *J.R. Scott* makes the transition from purely viscous fluids to fluids with a generalized Newtonian behavior in **1931**, investigating the squeeze phenomenon of polymeric materials (resins) by means of an innovative experimental device called “parallel plate platometer”. He formulated the expression of the squeeze force for a generalized Newtonian fluid using the power-law model, a model used to confirm the experimental data in several studies of that time (*Peek*, **1932**). The first dynamic squeeze test was performed in **1933**, by *Eisenschitz and Philippoff* for polymers and polymer solutions, using, for comparison, *Scott’s* analytical solution.

The analytical solution for a constant fluid volume (eq. 2.46) appears later, in **1946**, thanks to professors *Diennes and Kelmm* (see Figure 2.12.b). In **1964**, *D.F. Moore* introduces another manner to investigate the fluid squeeze phenomenon, by immersing a rigid element (a solid plate) in a fluid bath and determining the pressure distribution that acts over it. This type of experiment is resumed later (**1976**) by *D. Whicker and M. Rohde*. They use a composite plate with an elastic layer following a practical industrial application: the contact between a tyre and the wet asphalt.

The first study of the non-Newtonian viscoelastic fluids in squeeze flow is published by *Tanner* in **1965**, and does not include inertial effects. They are considered later, in **1967**, by *D.C. Kuzma*, in a study performed on purely viscous fluids, in **1976** by *R.J. Grimm*, and in **1979** by *Phan-Thien*, who formulates a general solution of velocity and pressure distributions

for the oscillatory squeeze flow, including the inertial effects. In **1987**, this issue is resumed by *Bird*, who writes an analytical formulation of squeezing force, derived from Stephan's equation, formulation that emphasizes properly inertial contributions for Newtonian fluids. In **1981**, *Chartei*, *Macosco* and *Winter* make the first squeeze test in perfect slip conditions, using plates initially lubricated for the study of polymers in biaxial extension. Thermal effects are taken into consideration in a study performed by *J.S. See* and *A.B. Metzner* in **1982**, by imposing a viscosity gradient on the thickness of the fluid film. In the same year, *Phan-Thien* and *R.I. Tanner* make a numeric study for visco-elastic fluids using the *Maxwell* model and neglecting the mass forces and the boundary effects. A similar study is published in **1984** by *Lee*, *Den*, *Metzner*. In this study, the constant velocity squeeze flow modeled numerically, for a *Maxwell* model, determining the evolution of the fluid film thickness in time, obtaining oscillations in the distribution of the film thickness both experimentally, and numerically. They specify that an analytical solution cannot be found for this model, but they analytically formulate the same flow (2D plane and axisymmetric) for a *Jeffreys* model (*Oldroyd B*) using rate fields for Newtonian fluids, ignoring the retardation time and the non-linear inertial terms. In **1985** *Phan-Thien* makes a numeric study about viscoelastic materials.

Partial fluid adherence phenomenon (known also as partial slip) is considered for the first time in the squeeze flow in the same year by *Bagley* and *Christianson*. In **1999**, *H. Martin*, *Laun* and *Hassager* solve the squeeze flow study with “partial no slip conditions”, this time, by using the *Power-Law* model. In **1992**, a first publication on the squeeze flow of electrorheological (ER) fluids appears, belonging to *Stanway* and *Sproston*. One year later, *Sproston* and *Williams* write an analytical model for the oscillatory squeeze flow of ER fluids, imposing a critical yield point by approximating ER fluids behavior with the Bingham and bi-viscous models. The targeted industrial applications were the fluid dampers and the electrical engines. An important work about viscoelastic fluids modelling in squeezing flow is published in **1996** by *J.S. Field*, *M.W. Swain* and *Phan-Thien*. They formulate a transfer function between the power spectrum and the oscillatory squeeze velocity, for experimental investigations performed on a prototype rheometer (*Micro-Furier/MFR 2100*). They also determine the complex modulus for various viscoelastic solutions (hialuronic acid, sinovial fluids, *Boger* fluids). In **1998**, *F. Yang* performs a numeric study about visco-plastic fluids in squeeze flow, modeling the rheological behavior using the Herschel Bulkley and the bi-viscous models also used by *Adams* in **1994** but considering the perfect slip (no adherence) condition for fluid-solid contact.

A first analysis of complex fluids non-linear behavior in the squeeze flow is published in **2000** by *N. Phan-Thien*, *S. Nasser* and *L.E. Bilston*. The study includes experimental

investigations on biological complex materials (pig kidneys) in oscillatory squeeze flow on the *MFR 2100* rheometer. They determine an analytical expression of the squeeze force for a bi-viscous fluid and for the *Maxwell* model, however ignoring the components of the normal stress normally present in the equations of motion.

In **2002**, Jiang, H. See, Swain and Phan-Thien make a similar analysis for a composite material (impression material). They impose an arbitrary displacement profile in an oscillatory squeeze flow using the same *Micro-Fourier* prototype rheometer, determining the rheological behavior of the material during the curing process. In the last years, the tendency to miniaturize technological devices and to develop new materials that must be tested using very small samples (several micro-litres) has led to the diminishing of the spatial scale from the macro level to the micro or nano levels, even for the study of the squeezing flow. Thus, micro devices have been developed for the study of the squeeze flow, and micro rheometers for the analysis of the rheological behavior of fluids during squeeze flow.

This chapter, presents several domains of applicability, the common geometries used in squeeze flow tests, the procedures used for the rheological analysis of fluids during squeeze flows, and some of the existing analytical models. Several analytical solutions of squeeze flow and the influencing factors over the main parameters deduced following the squeezing tests are presented throughout [Paragraph 3.2](#).

3.1. CURRENT STAGE OF RESEARCH

3.1.1. Squeeze flow applications

Squeeze phenomenon of a material (fluid or soft solid) is generated by the compression and deformation of the material between two solid surfaces (so called extensional biaxial motion). Generally, the gap between the plates is considered very small in comparison with the plates sizes, the flow is considered to take place in the *thinn film approximation*. The interest shown to this complex flow is due to various applications: the presence of this motion in various domains (mechanical engineering and tribology [[152](#)], rheology [[72](#)], biology, geology, constructions [[221](#)]); industrial processes of production or processing (hot stamping [[249](#)], gluing with adhesives, lithography by nano-printing [[121](#)]); compression of construction materials [[208](#)], food industry [[79](#)], [[112](#)]; natural and biologic processes (mastication, joints, valves, biofluids, earth settling), [[216](#)].

As specified in [Paragraph 2.3.3](#), squeeze flow between two plates is a motion generated by the application of a force over one or both surfaces or by applying an axial velocity on one

of the solid surfaces. The parameters that characterize the entire process are: film thickness, necessary squeeze force, squeeze velocity and pressure distribution in the gap.

Applications in engineering

At the macroscopic level, the squeeze flow has as main application the phenomenon of fluid lubrication in bearings, gear couplings, machines, car engines, naval engines, the fluid film preventing the solid-solid contact and the surface deterioration. Another important application is found in the fluid damping mechanism often encountered in the car building industry. The elasto-hydrodynamic contact of car tyres with the wet asphalt supposes the squeezing of the fluid among the skid-proof grooves of the tyre. At the microscopic scale, the applications are found in the so-called *Micro-Electro-Mechanical Systems - MEMS*: fluid micro-buffers, sensors, actuators [48], [50], [51], [62], [74], [176], [201], [226], [240] the manufacturing process of lithography by nano-printing of micro and nano-devices [37].

Applications in biology and medicine

The most obvious application is encountered in human articulations. The sinovial fluid is squeezed and sheared between the articular cartilages. The squeeze motion between porous layers has been studied intensely in relation to the biomedical applications. Apparently, the squeeze flow is also present in the blood micro-circulation. The contraction and relaxation of muscles triggers a squeeze flow of blood in veins and creates the necessary pressure to open and close valves. The squeeze phenomenon is also present during the closing of human cardiac valves and mechanical cardiac valves, used as prostheses in case of occurrence of certain cardio-vascular diseases. When the valve is closed, the blood is sheared and squeezed, forming the so-called squeeze jet which causes turbulence, cavitation and which deteriorates the artificial valves.

Squeeze flow in Rheometry and rheology

The squeeze process is a complex motion which includes both shear components (in the vicinity of solid walls defining the squeeze process) and elxtension components (in the middle of the gap). Due to these kinematic features, the squeeze flow has been intensely used along the years to determine the rheological properties of simple and complex fluids. In the specialized literature, there are numerous studies where the rheology of the various classes of materials is studied based on squeeze flows:

- (i) The rheology of food products includes studies concerning chewing gum, mayonnaise [61], [112], mustard [251], peanut butter [42], [52], corn dough [179], honey, chocolate [52], syrup, milk scum, vegetal oils, etc.
- (ii) Polymeric materials: studies on polyacrylamide, PEG, PIB, Boger fluids;

- (iii) Rheology of cosmetic and pharmaceutical products: toothpaste, gels, lotions, emulsions [6], [160], [191];
- (iv) Rheology of suspensions [1], [23], [67], [77], [198], [123], foams [207], pastes [2], [120], [131], [206] and composites [203] in squeeze flows;
- (v) Electrorheological and magneto-rheological materials in view of obtaining a larger yield point, as direct application for fluid dampers [86], [106], [138], [218].

Squeeze flow in Constructions and Geology

The ground settling and the pressing of building materials is the most obvious application. Several types of materials have been studied in squeeze flow: granular, sand, concrete, mud, and other building materials [79], [208].

3.1.2. Rheological squeeze tests and configurations of the testing geometries

In the previous chapter, two configurations used in the squeeze flow have been specified: (i) constant contact surface or (ii) constant fluid volume. A third geometry supposes the penetration of the upper disc in a fluid volume situated on the lower surface. In this case, the surfaces do not have the same sizes (see Figure 3.1), the upper disc generally having a smaller radius than the lower one, and the form of the free surface is not known [72], [109], [214]. When using constant area geometry the fluid is pushed out from the gap, the main advantage being the fluid-solid contact surface that is considered “known” and “unchanged” during the test. Some experimental issues in this case are: (i) the accumulation of material at the edge of the gap, which creates additional pressure in the fluid; (ii) free surface evolution that may lead to significant end effects, introducing errors in the measurements. End effects influence is significant especially for small squeezing velocities, of high viscosity materials or in the case of high temperature gradients [155]. Generally, analytical formulations and numerical simulations of squeeze flow assume that free surface has always a cylindrical shape, although, experimentally it may be easily observed that the free surface varies according to the fluid properties (surface tension, contact angle, viscosity, elasticity).

Another geometry is composed of two immersed plates (see Figure 3.2), geometry encountered in the case of fluid dampers and lubrication mechanisms (in this case the squeezing flow being considered imperfect), [109], [214]. Regardless the testing geometry, squeeze flow characteristic parameters remain the same: film thickness, squeeze force, pressure and velocity distributions. The control and measurement of these characteristic parameters is performed specialized pressure, force and displacement sensors, or by using

visualisation methods. The simplest testing procedure using squeeze motion supposes a constant descent velocity imposed for the upper plate, while the lower plate is kept at rest.

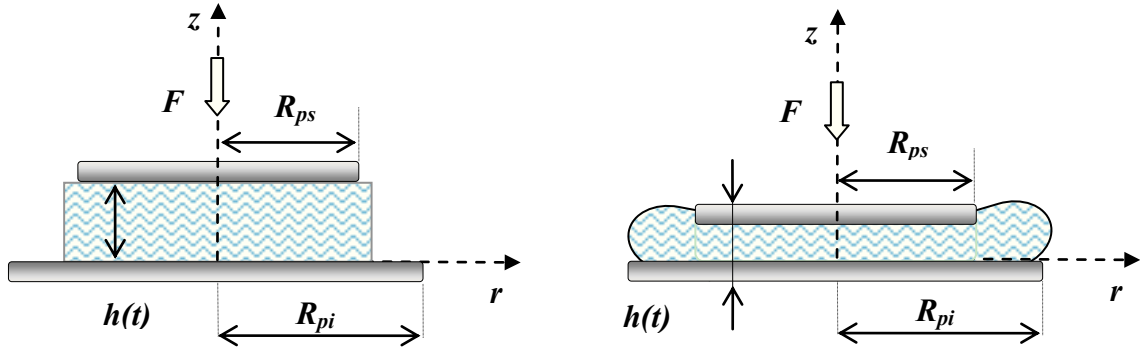


Fig. 3.1. Axial-symmetric squeeze flow of a fluid between two solid surfaces of different sizes.

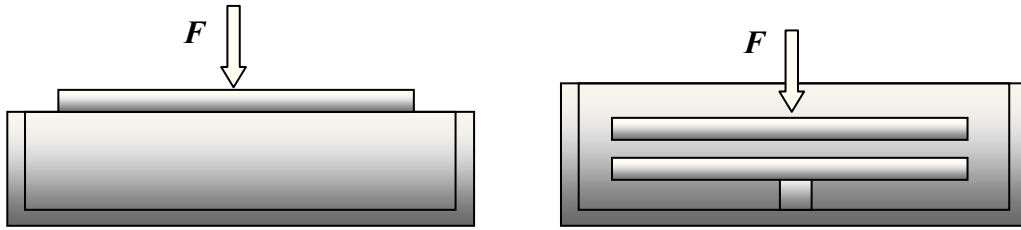


Fig. 3.2. Immersed plates geometries (in the volume of fluid).

The result of this test is an increase of the normal force (necessary to squeeze the fluid) once the upper plate moves towards the fixed plate and the gap diminishes. Based on such an experiment, several tests may be performed: (i) relaxing stresses within the material (ii) determination of the yield point or (iii) measuring the properties of viscosity or elasticity for a varied range of fluids. Another experiment implies the motion of the upper disc with a variable velocity in time, the motion having an imposed profile periodical in time (sinusoidal/random). Both types of tests are analysed in the following chapters of the thesis.

3.2. THEORETICAL CONSIDERATIONS

3.2.1. Analytical formulation of squeeze motion in various geometries

3.2.1.1. Squeeze flow between two parallel discs

As mentioned in the previous chapters, in a squeeze flow, a volume of fluid is deformed between two solid surfaces that get closer to one another, forcing the fluid out of the gap formed between them. Figure 3.3 illustrates a geometry that is often encountered in the case of the analysed phenomenon: the fluid is between two parallel plane surfaces of circular section, the lower surface is fixed, and the upper surface has a constant descent velocity.

The characteristic dimensions of the gap formed by the two surfaces are the height $h(t)$ and the radii of the lower and upper surfaces, R , being equal in this case. In general, the height $h(t)$ is significantly smaller than the dimension of the surfaces that delimit the gap, the squeeze phenomenon being in many cases associated to the hydrodynamic motion of thin fluid films with applicability preponderantly in lubrication and rheology.

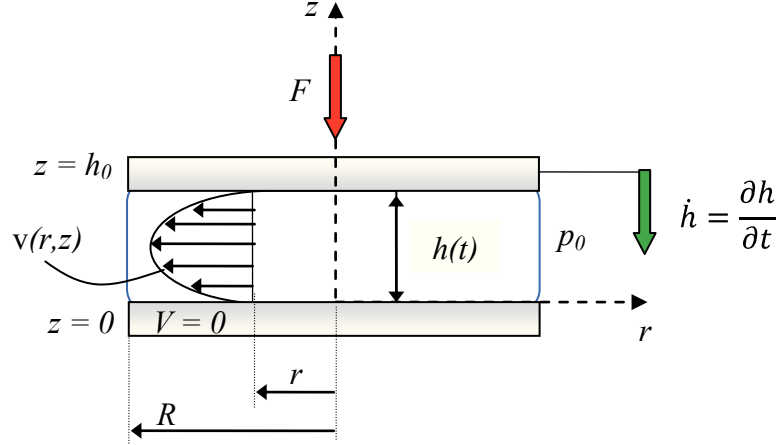


Fig. 3.3. The squeeze flow of a viscous fluid of thickness h_0 between parallel plane discs (axial symmetric flow with $h_0 \ll R$, $v_r \ll v_z$).

Thus, the squeeze flow is described analytically by *Reynolds Equation for Lubrication*, derived from the *Navier-Stokes System of Equations*. The general hypotheses of hydrodynamic lubrication theory assume the validity of analytical formulations only for: (i) purely viscous incompressible fluids in laminar flow, hence, in *Stokes Approximation*; (ii) a geometry defined by solid and impermeable surfaces to which the fluid adheres. In this case, the characteristic *Reynolds* number is sufficiently small to neglect the influence of inertial forces:

$$Re = h \frac{\dot{h} \rho}{\eta_0} \quad (3.1)$$

where $\dot{h} = V$ is the plate velocity (thus, the fluid velocity). Consequently, inertia and gravitational forces are neglectable in comparison with pressure forces and to those due to viscous friction. No other exterior mass force is considered to be an influencing factor on squeeze flow.

The motion of a fluid film with $h \ll B$, $h \ll L$ between two solid surfaces (see [Figure 3.4](#)) is characterized by the velocity components v_x and v_y , the component v_z being neglectable. Moreover, the rate gradients on the directions Ox and Oy are neglectable compared to the rate gradient on the normal direction [12], [60], [182].

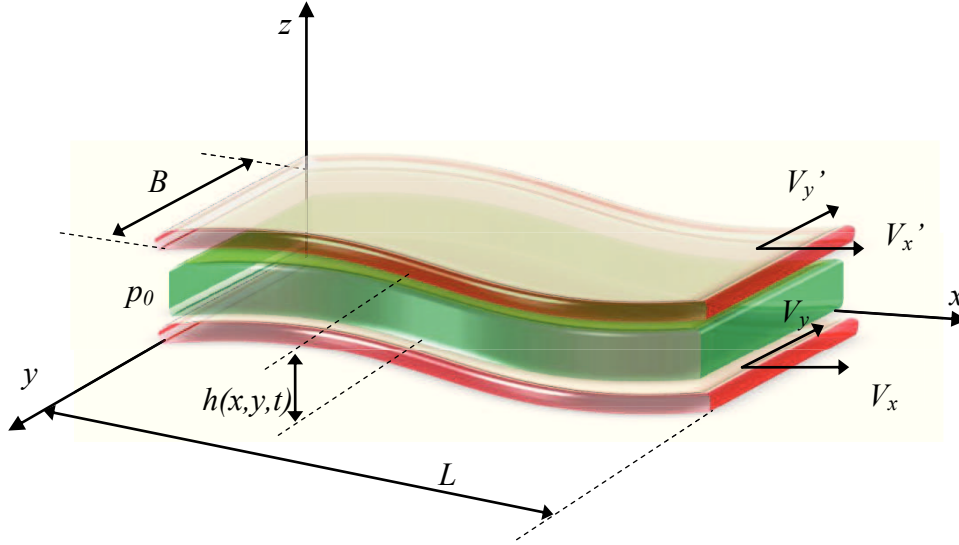


Fig. 3.4. Flow of a viscous fluid in the thin layer of thickness h between two solid surfaces.

Considering the previously mentioned hypotheses, the system of equations (Navier-Stokes) has the simplified form (particular case of *Stokes Approximation*, completed by the *Continuity Equation* (see Chapter 2, eq. 2.5):

$$\begin{cases} -\frac{\partial p}{\partial x} + \eta_o \frac{\partial^2 v_x}{\partial z^2} = 0 \\ -\frac{\partial p}{\partial y} + \eta_o \frac{\partial^2 v_y}{\partial z^2} = 0 \\ -\frac{\partial p}{\partial z} = 0 \\ \frac{\partial v_x}{\partial x} + \frac{\partial v_y}{\partial y} + \frac{\partial v_z}{\partial z} = 0 \end{cases} \quad (3.2)$$

The *Reynolds* equation for lubrication derives from 3.2 (plane case):

$$\frac{\partial}{\partial x} \left[h^3 \frac{\partial p}{\partial x} \right] + \frac{\partial}{\partial y} \left[h^3 \frac{\partial p}{\partial y} \right] = 12\eta_o \frac{\partial h}{\partial t} + 6\eta_o \left[\frac{\partial h}{\partial x} (V_x + V'_x) + \frac{\partial h}{\partial y} (V_y + V'_y) \right], \quad (3.3)$$

where $p = p(x, y)$ is pressure distribution in the thin layer of viscous fluid. The boundary conditions are imposed by the surfaces velocities (V_x, V_y respectively V'_x, V'_y), the pressure outside the field being p_0 [60], [140], [220]. In the case of a thin film squeezed between two parallel discs (see Figure 3.3), the radial velocity of the fluid is considered much larger than the descending velocity of the upper disc ($v_r \gg \dot{h}$), hence, the radial flow direction characterizes the motion. Since the solid surfaces move only in Oz direction and $h = h(t)$, relation (3.3) becomes (with $\dot{h} = \partial h / \partial t$, $V_x = V'_x = V_y = V'_y = 0$):

$$\frac{\partial}{\partial x} \left[\frac{\partial p}{\partial x} \right] + \frac{\partial}{\partial y} \left[\frac{\partial p}{\partial y} \right] = 12\eta_o \frac{1}{h^3} \dot{h}. \quad (3.4)$$

Chapter 3. Squeeze Flow

Using the cylindrical coordinate system, with $r = \sqrt{x^2 + y^2}$, one obtains:

$$r \frac{d}{dr} \left(\frac{1}{r} \frac{\partial p}{\partial r} \right) + 2 \frac{1}{r} \frac{\partial p}{\partial r} = 12\eta_0 \frac{1}{h^3} \dot{h}, \quad (3.5)$$

a successive integration, leads to:

$$\frac{d}{dr} \left(\frac{1}{r} \frac{\partial p}{\partial r} \right) = 12\eta_0 \frac{1}{h^3} \dot{h}r, \quad (3.6)$$

$$\frac{\partial p}{\partial r} = 12\eta_0 \frac{\dot{h}}{h^3} \frac{r}{2} + \frac{C_1}{r}. \quad (3.7)$$

The integration constant C_1 is nought cause the pressure must be finite in the axis (at $r = 0$), therefore:

$$p(r, t) = p_0 + \frac{3\eta_0}{h^3} \dot{h}(r^2 - R^2) \quad (3.8)$$

where $p = p_0$ at $r = R$. By integrating the pressure distribution, we obtain the necessary force to squeeze the fluid film

$$F = \int_0^R \frac{3\eta_0}{h^3} \dot{h}(r^2 - R^2) 2\pi r dr, \quad (3.9)$$

respectively the expression (2.47)

$$F(t) = -\frac{3\pi\eta_0 R^4}{2h^3} \dot{h}. \quad (3.10)$$

This formula has been published in the specialized literature ever since 1874, in a classical paper pertaining to *Joseph Stefan*, dedicated to the analysis of the squeezing of fluid films in dampers, for which the plate velocity is negative for the fluid compression ($\dot{h} < 0$) and positive ($\dot{h} > 0$) for the extensional motion [214]. For a constant imposed force $F = F_0$ is obtained by integrating the variation of the film thickness in time (see 2.49); in a dimensionless form, the following expression is obtained:

$$\bar{h}(\bar{t}) = \frac{1}{\sqrt{1 + \frac{4h_0^2}{3R^2} \bar{t}}}, \quad (3.11)$$

where h_0 is the initial height of the upper mobile disc against the lower fixed plate, $\bar{h} = h/h_0$ and $\bar{t} = p_0 t / \eta_0$, with $p_0 = F_0 / \pi R^2$. For a constant descending velocity of the upper disc, the variation of the dimensionless force in time is given by the expression:

$$\bar{F}(\bar{t}^*) = \frac{3}{2} \frac{R^2/h_0^2}{(1 - \bar{t}^*)^3}, \quad (3.12)$$

where $\bar{t}^* = V_0 t / h_0$ and

$$\bar{F} = \frac{F}{\eta_0 \cdot (V_0/h_0) \cdot \pi R^2}, \quad (3.13)$$

with $V_0 \equiv \dot{h}$.

For an imposed sinusoidal displacement profile of the upper disc $\varepsilon = \varepsilon_0 \cdot \sin(\omega t)$, where the amplitude ε_0 is much smaller than the nominal gap h_0 ($\varepsilon_0 \ll h_0$), the expression (3.10) approximates correspondingly the force $F(t)$ between the plates (see Figure 3.5). Upper plate velocity and normal force variation in time are in these conditions expressed by the relations (2.51), respectively (2.52), previously described (see Paragraph 2.3.3). Considering that upper plate displacement is of the order of microns or smaller, in a quasi-static approximation of the phenomenon, the fluid viscosity will have the expression:

$$\eta_0 = C_g \frac{F_0}{\varepsilon_0 \omega} \quad (3.14)$$

where $F_0 = |F(t)|$ is the force amplitude, and $C_g = 2h_0^3/3\pi R^4$ is a geometric constant.

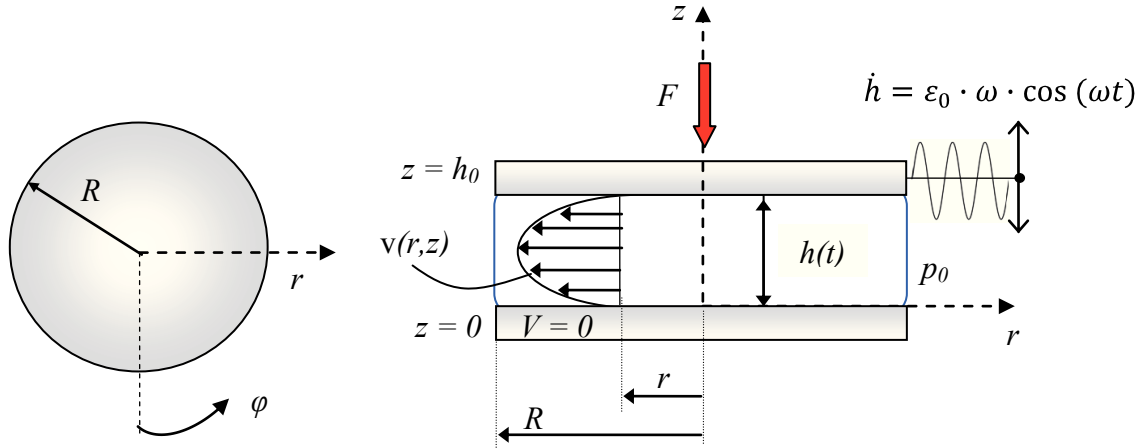


Fig. 3.5. The oscillatory squeeze flow of a viscous fluid of thickness h_0 between parallel plane discs (axially symmetric motion, $h_0 \ll R$, $v_r \ll v_z$).

We are specifying that the formula (3.14) is valid for $\varepsilon_0 \ll h_0$, $h_0 \ll R$ și $\omega < \omega_{max}$; in the practical cases $h_0 \in (0.2 \div 1) \text{ mm}$, $R \geq 10 \text{ mm}$, $\varepsilon_0 \leq 2 \mu\text{m}$ și $\omega_{max} = 50 \text{ Hz}$.

The real squeeze phenomenon is a complex flow, and the external and internal factors that may manifest their influence are numerous. From among them, the conditions of fluid-solid contact, particularly the wall slip, play a major role over the local dynamics (see Paragraph 3.3.3).

However, the influence of the end effects must not be neglected (considering the material properties: superficial tension, contact angle), nor the system inertia and the variation of viscosity for the generalised Newtonian fluids; note that the presented relations do not take these effects into account.

3.2.1.2. Squeeze flow between two parallel plates [182]

Similarly, we may obtain the characteristic parameters of the squeeze flow between two parallel plates (see Figure 3.6), with the geometric dimensions L (length) and B (width). The pressure distribution for $B \ll L$ is approximated in this case by the relation:

$$p = \frac{6\eta_0 \dot{h}}{2h^3} \left(\frac{B^2}{4} - z^2 \right) \quad (3.15)$$

By integrating the pressure distribution on the surface of contact, we obtain the expression of the squeeze force:

$$F(t) = -\frac{\eta_0 L B^3}{2} \dot{h} \quad (3.16)$$

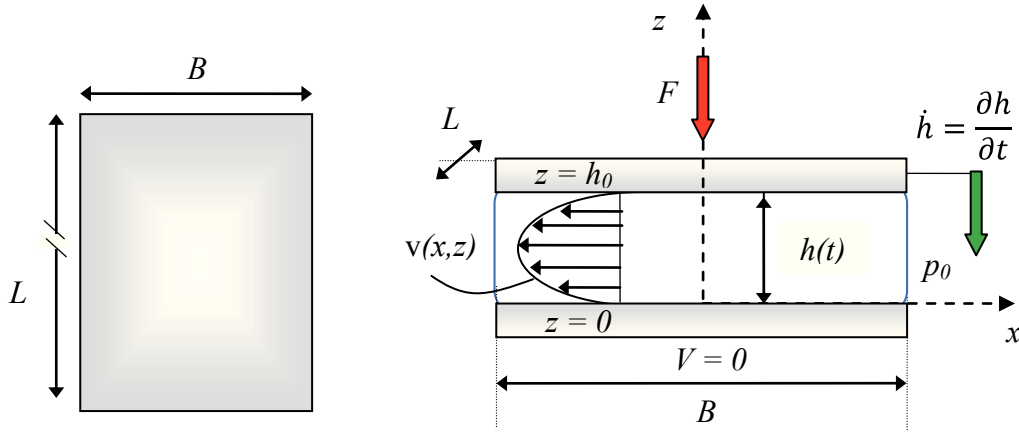


Fig. 3.6. The squeeze flow of a viscous fluid of thickness h_0 between two parallel plates of infinite length (axially symmetric motion, $h_0 \ll B$, $h_0 \ll L$, $v_r \ll v_z$).

3.2.1.3. The squeeze flow between annular surfaces

In the case of an annular contact surface, the fluid-solid contact area is defined by the exterior diameter D_e and the interior diameter D_i of the ring.

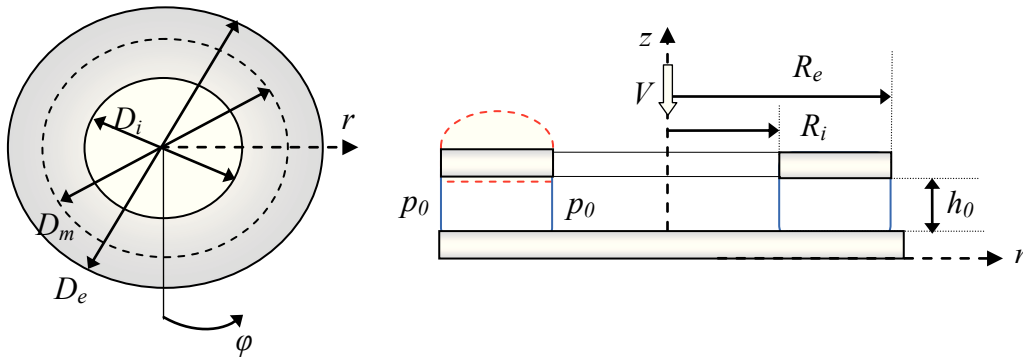


Fig. 3.7. The squeeze flow of a viscous fluid of thickness h_0 between an annular surface and a plane circular surface (axially symmetric motion, $v_r \ll v_z$).

The pressure field is given by the relation:

$$p = \frac{6\eta_0 \dot{h}}{2h^3} \left(\frac{(D_e - D_i)^2}{16} - z^2 \right) \quad (3.17)$$

By successive integration, we obtain the expression of the squeeze force:

$$F(t) = -\frac{\pi\eta_0 \dot{h}}{16h^3} (D_e - D_i)^3 (D_e - D_i) \quad (3.18)$$

3.2.1.4. The squeeze flow between a spherical surface and a plane surface [77]

The thickness of the fluid film in the squeeze flow presented in Figure 3.8 (between a spherical surface and a plane one) may be expressed by the relation:

$$h(t) = h_0 + R_s - \sqrt{(R_s^2 - r^2)} \quad (3.19)$$

The pressure gradient has the following form:

$$\frac{\partial p}{\partial r} = \frac{6\eta r \dot{h}}{(h_0 + R_s - \sqrt{(R_s^2 - r^2)})^2} \quad (3.20)$$

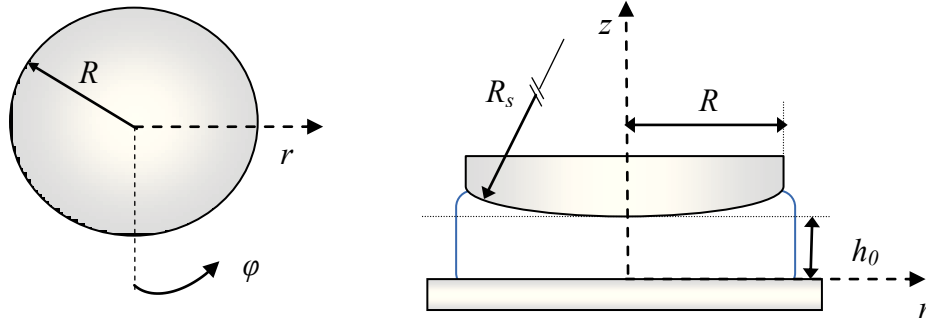


Fig. 3.8. The squeeze flow of a viscous fluid of thickness h_0 between a spherical surface and a plane disc, $h_0 \ll R$.

For this geometry, the squeeze force takes the expression:

$$F = 6\pi\eta\dot{h}(h_0 + R_s) \left(\frac{R^2}{2(6\eta\dot{h} - \sqrt{R_s^2 - R^2})} + \frac{6\eta\dot{h}}{6\eta\dot{h} - \sqrt{R_s^2 - R^2}} - \frac{6\eta\dot{h}}{6\eta\dot{h} - \sqrt{R_s^2}} \right) \dots$$

$$\dots + 6\pi\eta\dot{h} \left(\frac{18\eta\dot{h} \ln(6\eta\dot{h} - \sqrt{R_s^2 - R^2})}{6\eta\dot{h} - \sqrt{R_s^2}} + \sqrt{R_s^2 - R^2} - \sqrt{R_s^2} \right) - \frac{6\pi\eta\dot{h}R^2}{6\eta\dot{h} - \sqrt{R_s^2 - R^2}} \quad (3.21)$$

3.2.2. Influence of contact surfaces inclination

The squeeze flow is generally modelled using the previously presented formulas, considering that the contact surfaces are parallel. Nevertheless, in the real setup there is not

always achieved a perfect parallelism between the contact surfaces, the influence of their inclination being one of the most important aspects discussed in the analysis of experimental results for squeeze flow. Moreover, the plate parallelism ensures the condition of symmetry used to deduce functional parameters in the squeeze flow for most geometries used in rheometric tests: disc-disc, plate-plate, sphere-plate (see Paragraph 3.3.1).

In general, experimental devices allow the adjustment of parallelism by various methods: positioning of the lower plate on a screw- ball, U-joint [75], [78], [90] lower plate incorporated in the housing of the device [118], [253], [254], use of a compound flexture system [53]. The parallelism between the plates may be checked by using gauge blocks, ruby spheres, force cells, [75] - [78] optical measurement techniques by white light interferometry [53] or visually, observing the spreading of the fluid between the plates, in this case being necessary to use transparent plates [72].

The influence of the parallelism of the surfaces has been studied since 1965 [172], the squeeze flow being associated to the immersion of a square plate in a volume of liquid (see Figure 3.9). It was noticed that the plate inclination angle decreases from the initial value α_i to a much smaller value α_n , corresponding to the position when the plate reaches the bottom of the tank.

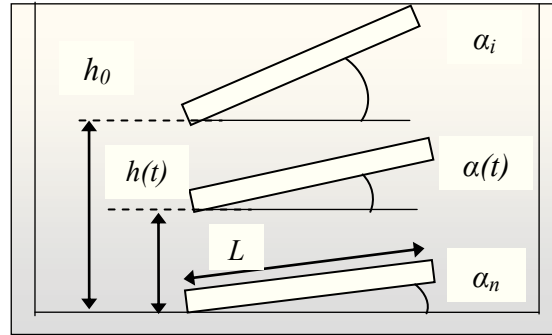


Fig. 3.9. The squeeze flow of a viscous fluid due to the immersion of an inclined solid plate into a fluid tank.

Depending on the inclination angle, we may define the plate immersion velocity and the thickness of the fluid film present between the plate and the tank bottom. Following the study, it was decided that, together with the immersion of the plate, the plate velocity increases, and for very small values $\alpha(t)$ the influence of the inclination over the pressure distribution may be neglected. Later it has been demonstrated that the inclination angle significantly influences the pressure distribution, shifting the pressure centre towards the inclined corner by up to 15% of the plate length, even for smaller values of $\alpha(t)$ [232]. It has been confirmed that, for a rigid element, the immersion velocity increases at small values of the inclination angle.

As regards the rheological measurements by the oscillatory squeeze flow using the usual geometry disc-disc, the plates lack of parallelism leads to the decrease of the normal force values, therefore to the sub-estimation of material viscosity, especially at small film thicknesses ($h_0 \in [30 \div 400] \mu m$). For the same material, in the same testing conditions, the use of geometries with upper spherical surface and a lower inclined plane (see [Figure 3.12](#)), leads to a significant improvement of the experimental results, fact which is experimentally and numerically demonstrated by [\[77\]](#).

Also, the 2D analytical solution of the squeeze flow shows that the inclination of the contact surfaces leads to the loss of the condition of axisymmetry, the pressure distribution centre (e) being at the distance d_e from the initial position (the initial position corresponds to the symmetry axis), a distance which varies according to the inclination angle (see [Figures 3.11-3.12](#)).

The pressure distribution is dominant in the area with small film thicknesses, in the case of inclined plates, leading to an excessive increase of the normal force in this area. Considering that the pressure depends on the azimuthal coordinate [\[195\]](#), we may estimate that the force developed in the area with small film thicknesses exceeds the necessary value to compensate for the decrease of pressure in the area with large film thicknesses. As regards the spherical surface, the distribution of the pressure field and the squeeze flow are concentrated in the middle of the geometry, because the film thickness h_0 at the centre of geometry is much less influenced by the plate inclination, compared to the disc-disc geometry. This has also been demonstrated for an inclined cone-plate geometry [\[76\]](#).

In conclusion, the use of a spherical upper surface or of an inclined cone-plate geometry is recommended when the parallelism of the contact surfaces cannot be ensured. The analytical solutions for an inclined disc-plate geometry, inclined plate-plate and inclined sphere-plate, are presented in [Paragraphs 3.3.2.1 - 3.3.2.2](#).

3.2.2.1. The squeeze flow between an inclined disc and a circular plane surface [\[77\]](#)

For an inclined disc-plate geometry ([Figure 3.10](#)), the initial thickness of the fluid film is expressed by the relation:

$$h_0 = h_{min} + \tan \alpha (R - r \sin \theta) \quad (3.22)$$

In this case, the pressure distribution becomes:

$$\frac{\partial p}{\partial r} = \frac{12\eta r \dot{h}}{(h_{min} + R \tan \alpha)[2(h_{min} + R \tan \alpha)^2 + 3(r \tan \alpha)^2]} \quad (3.23)$$

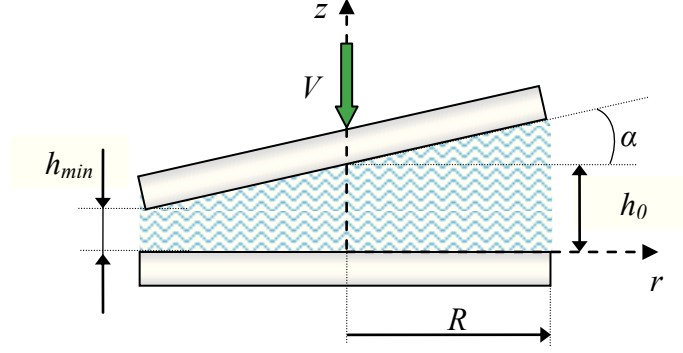


Fig. 3.10. The squeeze flow of a viscous fluid of thickness h_0 between two discs. The upper disc is inclined with the angle α .

By successive integration, the following normal force expression is obtained [77]:

$$F = \frac{4\eta r \dot{h}}{6 \tan^4 \alpha (h_{min} + R \tan \alpha)} \times \dots$$

$$\dots \times \left(2(h_{min} + R \tan \alpha)^2 \ln \left(\frac{2(h_0 + R \tan \alpha)^2}{2(h_{min} + R \tan \alpha)^2 + 3(R \tan \alpha)^2} \right) + 3R^2 \tan^2 \alpha \right) \quad (3.24)$$

Adopting the notations

$$\begin{cases} \tan \alpha = \varphi h_{min} / 2R \\ A_1 = \frac{4\eta r \dot{h}}{\tan^2 \alpha (h_{min} + R \tan \alpha)} \\ a_1 = 2(h_{min} + R \tan \alpha)^2 \\ b_1 = 3 \tan^2 \alpha \\ c_1 = 2(h_{min} + R \tan \alpha)^2 3(R \tan \alpha)^2 \end{cases} \quad (3.25)$$

the expression of the force may be written in a simplified form:

$$F = \frac{A_1}{2b_1} \left(a \ln \left(\frac{a_1}{c_1} \right) + b_1 R^2 \right) \quad (3.26)$$

Another approximation is the 2D solution where the lower plate is inclined. This approximation has as practical application the oscillatory squeeze flow performed experimentally on a system which allows the adjustment of the parallelism by inclining the lower plate, similar to the rheometer *MFR 2100* used in this study.

Due to the plate inclination angle α , a new system of coordinates is adopted, with the origin in the pressure distribution centre e , at the distance d_e from the initial position (see Figure 3.10) corresponding to the symmetry axis. Thus, the initial thickness of the fluid film has the form (Figure 3.11):

$$h(x) = h_0 - (x + d_e) \tan \alpha \quad (3.27)$$

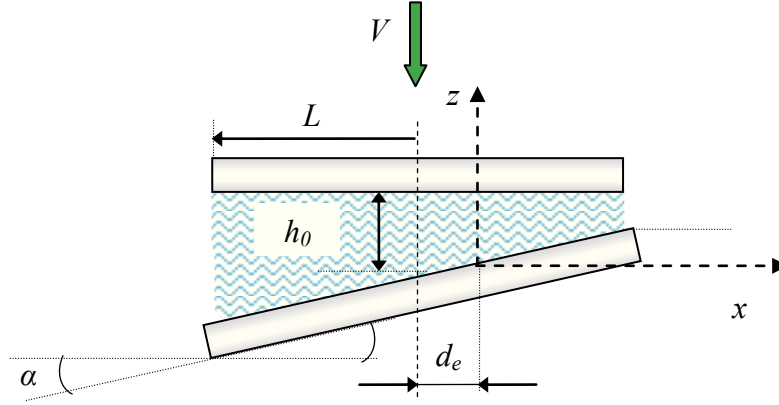


Fig. 3.11. Plane squeeze flow (2D) of a viscous fluid of thickness h_0 between two discs. The lower disc is inclined with the angle α .

The analytical expression of the normal force is obtained by the double integration of the pressure distribution [76]:

$$F = \left(\frac{h_0 - d_e \tan \alpha}{2 \tan^3 \alpha} \right) \cdot \left(\frac{1}{h_0 - L \tan \alpha} - \frac{1}{h_0 + L \tan \alpha} \right) + \dots$$

$$\dots + \frac{1}{\tan^3 \alpha} \ln \left(\frac{h_0 - L \tan \alpha}{h_0 + L \tan \alpha} \right) + 2A_1 L \quad (3.28)$$

where the position of the pressure distribution centre is obtained for the imposed boundary conditions at the geometry boundaries $x = (L - d_e)$, respectively $(-L - d_e)$:

$$d_e = \frac{(h_0 + 2L \tan \alpha)(h_0 - 2L \tan \alpha)^2 - (h_0 - 2L \tan \alpha)(h_0 + 2L \tan \alpha)^2}{\tan \alpha [(h_0 + 2L \tan \alpha)^2 - (h_0 - 2L \tan \alpha)^2]} \quad (3.29)$$

and A_1 is an integration constant:

$$A_1 = \frac{h_0 + d_e \tan \alpha - 2L \tan \alpha}{2 \tan^2 \alpha (h_0 - 2L \tan \alpha)^2} \quad (3.30)$$

3.2.2.2. Upper spherical surface [76]

In the case of a plane geometry formed of a spherical surface and of an inclined rectangular surface (Figure 3.12), the thickness of the fluid film is defined as:

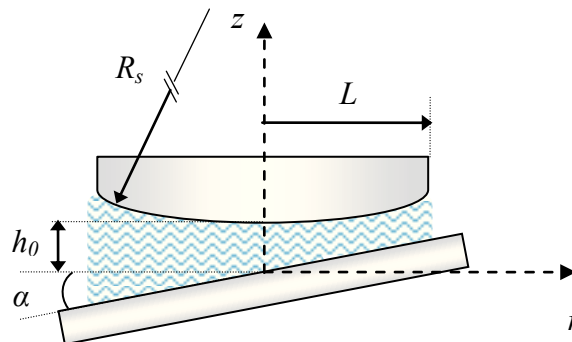


Fig. 3.12. Plane squeeze flow (2D) of a viscous fluid of thickness h_0 between a spherical surface and an inclined lower disc.

$$h(x) = h_0 + \frac{(x + d_e)^2}{2R_s} - (x + d_e) \tan \alpha \quad (3.31)$$

The distribution of pressures and the expression of the normal force are deduced in the same way as in the previous case, but the position of the pressure distribution centre obtained for the imposed boundary conditions $x = (L - d_e)$, respectively $(-L - d_e)$, is different [76]:

$$d_e = \frac{\frac{t_3}{\delta_r^2} - \frac{t_4}{\delta_l^2} - \frac{3 \tan \alpha}{k_1} \left(\frac{t_1}{\delta_r} - \frac{t_2}{\delta_l} \right) - 6 \left(\arctan \left(\frac{t_1}{k_1^{0.5}} \right) - \arctan \left(\frac{t_2}{k_1^{0.5}} \right) \right)}{\frac{t_1}{\delta_r^2} - \frac{t_2}{\delta_l^2} - \frac{3R}{k_1} \left(\frac{t_1}{\delta_r} - \frac{t_2}{\delta_l} \right) - \frac{6}{R^2 k_1^{1.5}} \left(\arctan \left(\frac{t_1}{k_1^{0.5}} \right) - \arctan \left(\frac{t_2}{k_1^{0.5}} \right) \right)} \quad (3.32)$$

where the following notations are used: $t_1 = \frac{L}{R} - \tan \alpha$, $t_2 = -\frac{L}{R} - \tan \alpha$, $t_3 = 2h_0 - L \tan \alpha$, $t_4 = 2h_0 + L \tan \alpha$, $\delta_r = 2h_0 + L^2/R - L \tan \alpha$, $\delta_l = h_0 + L^2/2R + L \tan \alpha$, $k_1 = 2h_0/R + \tan^2 \alpha$.

Based on these solutions, the correction coefficients may be calculated for the devices used in experiments, where the surface parallelism and symmetry is assumed in advance.

3.2.3. Influence of adherence

The boundary conditions at fluid-solid contact allow the formulation flow motions in three main regimes: perfect adherence (no slip condition), no adherence (perfect slip) and partial slip/adherence condition (see Paragraph 2.5.2). The analytical formulations for the squeeze flows (see Paragraph 2.3.3, 3.3.1) assume the condition of perfect adherence on the contact surfaces. In general, the no slip condition is satisfied experimentally by using surfaces with sufficiently large rugosities ($> 6 \text{ nm}$) [102] or sandpaper [4], [177], [190] being checked, in general, by performing viscometric rheological tests at various thicknesses of the fluid film [102]. In the case of the total slip condition (known in literature as *perfect slip*), the strains and stresses are considered to be uniformly spread in the material, and the expression of the squeeze force for incompressible Newtonian fluids becomes [161], [194]:

$$F = \frac{3\pi\eta_0 R^2 \dot{h}}{h_0} \quad (3.33)$$

for a constant contact surface and

$$F = \frac{3\pi\eta_0 \mathcal{V} \dot{h}}{h_0^2} \quad (3.34)$$

for a constant volume of fluid [40], [161]. The perfect slip condition has been used for the study of the squeeze flow of visco-plastic [124], [239] and viscoelastic materials.

This condition has been used mostly in the so-called squeeze tests in previously lubricated geometries (*lubricated squeezing flow*), where, between the tested material and the solid plate, a Newtonian lubricant layer is previously inserted [35], [39], [46], [105], [133], [134], [165], [213], [225]. In this case, the lubricant must be an ideal fluid (without friction) and it must remain in the gap throughout the test.

These conditions are not very easy to achieve experimentally, their violation triggering the change of the perfect slip regime into partial slip [225]. The lubricant layer may be created by using materials exuding part of their composition [42], [52], [104].

The perfect slip condition may be imposed experimentally also by using smooth plates with very small rugosities and small friction coefficients (tephlon plates [41], [43], [61], [109], plastic, mica [102], brass [177], all these aspects being also connected to the properties of the fluids wished to be tested using these surfaces [102], [165], [177].

Among the methods to obtain a surface with perfect slip properties are also found: chemical treatment of surfaces with tensioactive agents –surfactants [102]; covering of surfaces with molecule chains – polymers, proteins, sugars [102]; use of surfaces with different micro-topographies (the building of a micro-geometry on smooth surfaces) [21], [102], [238]; use of fluids with different concentration gradients on the film thickness; (also see Paragraph 2.5.2).

In reality, the experimental tests cannot clearly demonstrate the validity of one of the two previously presented conditions – perfect adherence or perfect slip, generally meeting the partial slip condition (partial no slip).

The theoretical formulation of the partial slip phenomenon may be made using two models: the model of the slip length or the model of limitation of the shear stress at the wall. The model of the slip length supposes that the slip velocity of the fluid at the wall V_f^* is proportional with the local shear rate neighbouring the wall (see Figure 2.2.1), [72], [144], [173], [214]:

$$V_f^* = \beta^* \dot{\gamma} \quad (3.35)$$

In the squeeze flow, this condition is introduced for the radial speed of the fluid v_r , which in conditions of no slip, must be null at the wall. For a disc-disc geometry, if $v_r = \dot{h}r/2h$, the fluid slips at the surface, and if $v_r = V_f^*(r/R)$, the fluid partially adheres to the surface (where V_f^* may have the maximum value of $\dot{h}R/2h$).

The expression of the squeeze force in the presence of the partial no slip condition is:

$$F = -\frac{3\pi\eta_0 R^4 \dot{h}}{8h^3} \left((1 - 2\delta^*) + \frac{4h^2}{R^2} (1 + 2\delta^*) \right) \quad (3.36)$$

where $\delta^* = -h V_f^*/R\dot{h}$ is a dimensionless parameter making the connection between the slip rate and the squeeze rate. For $\delta^* = 0$ the fluid adheres perfectly to the surface, for $\delta^* = 0.5$ it does not adhere to the surface, and for $\delta^* \in (0, 0.5)$, the condition of partial adherence is fulfilled [144].

A similar expression of the squeeze force is:

$$F = \frac{3\pi\eta_0 R^4 \dot{h}}{2h^3} \left(\frac{1}{1 + 6(\beta^*\eta_0/h)} + 2 \left(\frac{h}{R} \right)^2 \right) \quad (3.37)$$

where β^* represents the slip coefficient: for $\beta^* \sim 0$ the fluid adheres perfectly to the surface, for $\beta^* \sim \infty$ the fluid does not adhere to the surface, and for $\beta^* \in (0, \infty)$, the condition of partial no slip is met. The expressions (3.33 - 3.37) have been used in the squeeze flow to determine the influence of the perfect slip over the characteristic parameters of the squeeze flow. Another approach has been proposed by *Kaylon and Tang* in 2007 [127]:

$$F = \frac{3\pi\eta_0 R^4 \dot{h}}{2h^3} m - \frac{9\pi R^4 \dot{h}}{h^4} m^2 \beta^*. \quad (3.38)$$

They used the method of the smallest squares in the numeric simulation with finite elements of the squeeze flow to determine the parameter that defines the perfect slip condition (β^*) and the viscosity of fluids (Newtonian and generalised Newtonian – the *Power-law* model and the *Herschel-Bulkley* model), initially departing from the expression (3.38) and formulating an objective function dependent on the initial values of the squeeze force. The model of limitation of the shear stress to the wall σ^* , assumes the existence of a critical value σ_c , over which the no slip condition is no longer valid. The shear stress at the wall (σ^*) may be expressed depending on the yield point σ_0 :

$$\sigma^* = k_f \sigma_0 \quad (3.39)$$

where m is the friction coefficient. For $k_f = 0$ the fluid does not adhere to the surface and for $k_f \in (0, 1)$ the partial slip condition is met. The slip model for plastic materials supposes $\sigma^* = k_f \sigma_{zz}$, [3], [72] and for a *Bingham* fluid $\sigma^* = \sigma_0 + k_f \dot{\gamma}^n$, [5], [72], [127], [209].

The perfect slip issue has been intensely studied in the field of tribology, having as direct application the hydrodynamics of fluid films in bearings [55], [56], [153], [154], [188], [234], [244], [245]. Various theoretical and experimental studies demonstrated that the use of certain slip surfaces may increase load capacity in bearings (fluid film thickness and of pressure in the contact area), [55], [56], [87], [153], [154], [188], [244], [245].

For instance, in a shaft-bearing geometry (radial bearings), by optimizing the form and the dimensions of the surface with perfect slip properties, its positioning on the fixed surface and the correct choice of lubricants, an increase of the buoyant force will be obtained, as well as a uniform distribution of the pressure on the bearing surface and the increase of the fluids film thickness [55], [56], [87], [153], [154]. However, if the slip occurs on the mobile surface, pressure cannot be generated in the fluid film, so the bearing cannot be loaded. Also, a slip surface with too large dimensions compared to the geometry or to the presence of the perfect slip condition in areas with very small film thicknesses may lead to the decrease of the bearing performances [55], [56], [87], [153], [154], [188], [244], [245].

If the slip phenomenon takes place in the same conditions on both contact surfaces (spindle and bearing), then the loading capacity exists, but it disappears when the operation velocity exceeds a certain value [234].

An initial limitation of the shear stress is asserted to always lead to the reduction of frictions during operation. The alternance of slip-non slip surfaces, in parallel on the fixed contact surface, together with a reduced eccentricity between the shafts, increase the load capacity (buoyant force) [154].

The influence of the type of lubricant and of its properties (viscosity, properties of adhesion to the surface) is also important. In general, lubricants with reduced viscosity are used, to reduce the friction phenomenon at the contact with the contact surfaces. The influence of the slip phenomenon over the prediction of the rheological behavior in the squeeze flow may become significant especially as regards complex fluids such as greases and pastes.

The force measured in the squeeze flow is thus influenced by the presence of perfect slip areas. This phenomenon will also be noticed in the measurements presented in this paper. As previously mentioned the presence of surface roughness influences the local dynamics of the flow. The influence of the roughness has also been studied in the case of the squeeze flow [34], [110], [137], [165], [174], [210], [224].

The use of rough surfaces has been proven to lead to the satisfaction of the no slip condition, to the increase of the force and to the squeeze time step compared to the case when the surfaces are finished and have a small friction coefficient [165], [174]. Also, in this paper, I will demonstrate the influence of the microstructures of the solid surfaces over the squeeze force, experimentally measured in the constant velocity squeeze flow (see Chapter 7).

3.2.4. Presence of inertial effects

The inertial effects are another source of errors in the interpretation of the data obtained experimentally in the squeeze flow and therefore in the correct prediction of the rheological behavior of fluids. In squeeze flow, thin flow approximation (Reynolds equation for lubrication), the inertial effects are generally considered very small, neglectable in comparison with viscous forces and therefore excluded from most analytical formulations. Nevertheless, the specialized literature provides several theoretical formulations where the inertial effects are included [25], [103], [139], [219], [230].

Although analytical expressions of the normal force in the presence of the inertial effects have been published since 1968 [139], the most well known formulation belongs to Bird [25], [161]:

$$F = \frac{3\pi R^4 \eta_0 \dot{h}}{2h^3} \left[1 + \frac{5\rho h \dot{h}}{28\eta_0} + \frac{\rho h^2 \ddot{h}}{10\eta_0 \dot{h}} \right] \quad (3.40)$$

As one may expect, the inertia of the material has a significant influence over the results, especially for fluids with small viscosity and increased density, for squeeze flows at high velocity in the case of viscoelastic fluids [148].

As regards the visco-plastic fluids, the presence of the inertial effects leads to the increase of the pressure values in the film and of the squeeze force [230]. Also in the case of viscoelastic fluids, the inclusion of the inertia in the theoretical formulation of the squeeze flow shows its significant increase even for small R_e numbers ($R_e < 10$), [219].

The inertial effects have also been studied in the case of an air „film” in squeeze flow, in an air buffer, but in this case there was no significant influence noticed over the pressure, flow or force distribution [215].

3.2.5. Squeeze flow for generalised Newtonian fluids and viscoelastic fluids

3.2.5.1. Visco-plastic fluids in the squeeze flow

There are numerous rheological models used to analyse fluids with visco-plastic or viscoelastic behavior in the squeeze flow. In general, visco-plastic fluids are considered to be yield stress fluids [124]. The perfect plastic materials deform only if the strain tensor meets the „yielding criterion”, the best known yielding criterion being the *Von Misses* criterion.

When the no slip condition is considered, the squeezed material flows in blocks (with plug velocity) under various forms (see Figure 3.13).

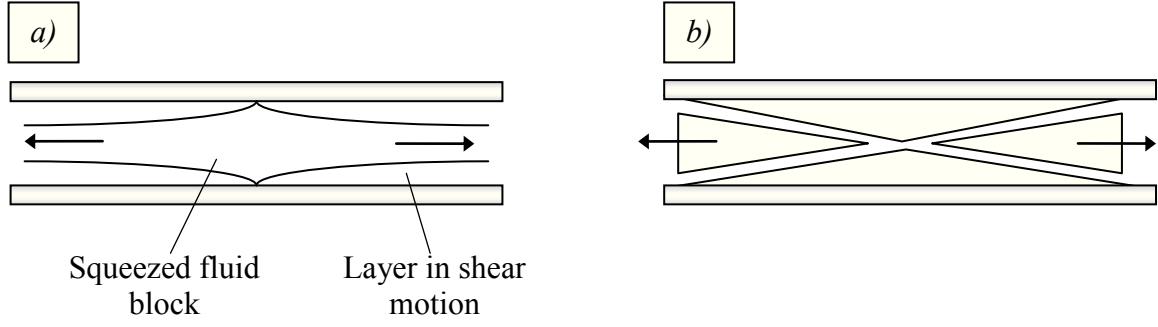


Fig. 3.13. Form of fluid blocks in the squeeze flow for visco-plastic materials: in the presence of a sheared fluid layer in the vicinity of walls (a) and in its absence (b) [72], [208].

The yielding is modelled using force expressions corresponding to the *Power-law* constitutive relation [109], [163], *Bingham* model [99], [167], [209], [207], [211], *Herschel-Bulkley* model [164], [165], [193], [205], [239]. The most used rheological model is the *Power-law* ($\sigma = k\dot{\gamma}^n$), the squeeze force having the expression [72], [127], [202]:

$$F = \left(\frac{2n+1}{n}\right)^n \left(\frac{2\pi kR}{n+3}\right) \left(\frac{\dot{h}^n}{h^{2n+1}}\right) \quad (3.41)$$

In the case of a *Bingham* fluid (eq. 2.18) the squeeze force has the following expression

$$F = \frac{\pi\sigma_0 R^3}{3h} + \frac{\pi R^3}{7h^2} |4\sigma_0 k \dot{h} R|^{1/2} \quad (3.42)$$

for $S < 0.05$ (the material behaves like a plastic solid), where $S = |k\dot{h}R/2\sigma_0 h^2|$ is the number of plasticity. For $S > 10$ (the material behaves like a liquid), the expression of force becomes [72], [208]:

$$F = \frac{\pi\sigma_0 R^3}{2h} + \frac{3\pi R^4 k}{8h^3} \quad (3.43)$$

The most important phenomenon analysed in the squeeze flow of visco-plastic fluids is the transition regime, aiming at determining the values of the critical yielding stress and of the fluid blocks with visco-plastic behavior [99]. Apparently, the yield is initially localized in the stagnation points of the yield neighbouring the solid surfaces [72], [167], [208].

The loading of visco-plastic fluid films (force necessary to onset the squeezing) increases as function of yielding stress value [99]. Also, the squeeze force grows at high *Bingham* numbers both in the disc-disc geometry, and in the plate-plate geometry, where $Bn = \sigma_0 h / \eta_0 \dot{h}$ is defined – the dimensionless *Bingham* number – in a axially symmetric squeeze geometry [124], [167]. Numerical studies performed using the *Bingham* model, showed that the transition from the solid-visco-plastic regime to the liquid one introduces discontinuities in the constitutive formulation, respectively diverges the numeric computation.

Therefore, two constitutive models are proposed to solve this discontinuity: the *Papanastasiou* constitutive model, used for the numeric solution of the squeeze flow, and the investigation of the evolution of the fluid-gas interface [124]; the model of the bi-viscous fluid which apparently behaves as a *Bingham* fluid [124], [239]. Several publications have proven that concentrated suspensions of solid spheres sometimes have in the squeeze flow a visco-plastic behavior, the experimental results of the normal force variation being approximated by the *Power-law* model, respectively the equation (3.41), [58], [67].

Also, the squeeze phenomenon of a fluid between two spheres in relative motion of proximity has been theoretically studied using the *Power-law* visco-plastic model taking into account an extended field of applicability: thin films lubrication between spherical geometries, micro-rheology of suspensions, phenomenon of settling and filtering, determination of the complex dynamics of particle cohesion phenomena, formation of clusters (particle agglomerations) or alignment of yielding solid particles [113], [237].

3.2.5.2. Viscoelastic fluids in squeeze flow

There are numerous attempts to model the viscoelastic behavior in the squeeze flow, but a clear and precise method is not yet available. The lack of analytical solutions and the complexity of numerical simulations have to be considered when the experimental results are analyzed. The first method of analyses is considering that Newtonian velocity distribution is not influenced by the fluid elasticity. The viscoelastic stresses are calculated from the integral constitutive model describing the fluid kinematics of viscous flows between the parallel planes [72], [247].

A second method assumes a material formed of multiple planes (fluid layers) initially parallel with the contact surfaces, planes which remain parallel during the squeeze (barelign). Thus, the velocity distributions may be derived from the continuity equation for a *Newtonian* fluid or of the *Power-law* type (considering geometry symmetry) provided that the axial velocity v_z should be independent of r . Nevertheless, the fluid “layers” deform during the flow, as suggested by [32]. Regardless whether the *Reynolds* approximation for lubrication is used or not, a complex system of differential equations with partial derivatives will be determined. The viscoelastic rheological behavior described by the *upper-convected Maxwell relation*, can be analyzed in squeezing only by numerical solutions [148], [186]. The behavior of a viscoelastic fluid may be also associated with the *Jeffreys* or *Olroyd-B* model, considering the velocity distribution of a purely viscous fluid and very small values of the squeezing velocity [148]. Another model used is the *Lodge* model for soft materials such as

rubber (*Lodge rubberlike liquid*). In the case of the *Maxwell* model, a set of non-linear equations is obtained, with partial differences that may be solved by the *perturbation solution* [148] or numerically by finite elements [66], [148] or finite differences [72], [186], [184], [185], [183]. When single-integral viscoelastic models are used, by imposing the perfect slip condition at the fluid-solid interface, the equations of motion and the boundary conditions are associated to the bidirectional elongation motion (valid for small Re numbers), the normal component of the stress in the fluid $\sigma_{zz}(t)$, being considered dependent on the deformation gradient and on the *Finger Tensor*. For a detailed study of this method, the paper [72] is recommended.

Elasticity influence on normal force values is conditioned by the manner chosen to impose the squeeze motion: (i) imposing a constant squeezing force (so that the motion is characterized by the dimensionless parameter *Wiesenberg*, $Wi = \dot{\epsilon}\lambda$); (ii) imposing a constant squeeze velocity (so that the flow is characterized by the dimensionless *Deborah Number*, $De = \lambda/t_\infty$). In the first situation, for very small strain rates (high observation time steps), the squeeze force increases compared to the solution for purely viscous fluids ($\lambda = 0$), [72], [148]. Also, velocity distributions are influenced by the presence of elasticity, the velocity distribution on radial direction being flattened and deformed together with the increase of the Wi values, at constant Re [186]. In the second case, the force necessary to squeeze the material is reduced compared to the case of purely viscous fluids, regardless of the value of the squeeze velocity (initially considered). This conclusion is supported by several studies, both experimentally [148] and numerically; regardless of the manner in which the theoretical analysis has been performed – the results being obtained either by the perturbation method [32], or iteratively by numeric calculation, with or without including the inertia, gravity or boundary effects [32], [148], [184], [185], [186]. Comparing the *Maxwell* fluid model with the *Oldroyd-B* fluid model, it was demonstrated that the force necessary for the squeezing is larger than for the *Oldroyd-B* fluid [184]. For a imposed constant velocity, no oscillation is noticed in the distribution of force (or of the film thickness) for *Oldroyd-B* fluids, but a propagation of the oscillations in the response of force or film thickness in time is prescribed for the *Maxwell* model (generated both by the inertia and material elasticity), [184], [148].

Boger fluids (with constant viscosity and elasticity) are modelled by *Oldroyd-B* relation. In this case, the presence of elasticity triggers the decrease of the squeeze flow compared to the Newtonian fluids (with the same viscosity) [184], [185]. Also, the viscoelastic behavior of soft solids has been analysed in the squeeze flow by [122], [183].

Chapter 4. NUMERICAL MODELLING OF SQUEEZING FLOW PHENOMENON

The numerical simulation of squeezing flow has been performed by two ways: (i) modeling the flow with a commercial CFD (*Computational Fluid Dynamics*) code, **Fluent v. 6.3** where the flow is characterized by the *Navier-Stokes Equations*; (ii) modeling the newtonian and shear-thinning rheological behavior of fluids in oscillatory squeeze flow with a special code created with **Fortran 95 v. 5.7** who's using a *Generalized Reynolds Equation* to approximate the motion.

From all available commercial products, *Ansys Fluent* is the most performant in solving the motion of real fluids in different flows, being used in both academics and industrial areas. Fluent software allows its users to study different cases like: a dynamic and moving mesh, turbulence study, acoustics, reacting flows, heat transfer, phase change, and radiation, multiphase flow and data post-processing.

Being based on applying and using the *Finite Volume Method* the use of *Fluent* implies the presence of a meshed flow domain and solving locally the equations that describe the flow, principally the *Continuity Equation*, the *Navier-Stokes System of Equations* and the *Energy Equation* [33], [93].

The second numerical code is a finite element code created in **Fortran 95**, and used with dedicated console software, **Winteracter 7.10**. The simulations were performed for Newtonian and generalized-Newtonian fluids, respectively the *Careau-Yasuda* model.

The numerical simulation of squeezing flow motion follows two imperative stages required generally for any performed numerical simulation of a flow: (i) the validation of the numerical solution within a simple flow geometry (2D, axial-symmetric in this case) for both simple and oscillatory squeezing flow by using boundary condition for whom an analytical solution is available; (ii) validation of the numerical solution for special boundary conditions (slip at the boundary, different values of the fluid-solid contact angle, the use of two fluid phases and the investigation of interface evolution in different conditions) by comparison with experimental investigations and real-time visualizations of the squeeze flow motion during performed experiments.

4.1. DESCRIBING THE NUMERICAL PROCEDURES – NUMERICAL CODE FLUENT

The numerical simulation of the squeeze flow involves an initial process of domain construction and meshing. *The Finite Volume Method* (FVM) implemented in Fluent code considers the flow domain divided into a finite number of control volumes, each volume being associated to a single node of the geometry mesh [227]. The simulation of the flow is performed by solving locally the equation of motion (2.4) where the extra-stress tensor is expressed by a generalized Newtonian model (2.12).

For a pure viscous incompressible fluid the code solves the Navier-Stokes equations (as a particular form of the equation of motion) in parallel with the mass conservation equation for incompressible fluids (2.1) for the whole flow domain and in each node of the mesh. In order to solve the partial derivative equations, FLUENT uses two types of numerical models *Density Based Model* and *Pressure Based Model*, which use the same FVM but a different methodology for linearise and solve the equations.

The *Density Based Solver* couples the continuity, momentum and (if needed) energy and transport equations, solving them simultaneously as a set or a vector of equations, using either a implicit or explicit method to couple the equations. The *Pressure Based Solver*, used for the present study, uses a special algorithm (belonging to projection method) which implies an iterative computation process of the nonlinear set of equations, computing separately the velocity and pressure gradients [49]. Practically the computed field is corrected through the pressure terms of the continuity equations and momentum conservation until the convergence criterion for the continuity equation is obtained [93].

The numerical code disposes of three computation models used for the determination of a scalar parameter gradient $\nabla\varphi$ (where φ may be the pressure, velocity components, temperature) for one of the mesh elements El : (i) *Green-Gauss Cell Based Model* - GGCB; (ii) *Green-Gauss Node Based Model* GGNB; (i) *Least Square Model* – LS. The choice of the right computation model for the analyzed flow motion leads to more precise results and reduced simulation time. In the case of *Green-Gauss Theorem* based models, the gradient in current element El is determined as the arithmetic average of the values computed in the neighboring cell centers (φ_i):

$$(\nabla\varphi)_{El} = \frac{1}{v} \sum_i \varphi_i A_i \quad (4.1)$$

For the GGCB scheme the values are computed for the neighboring cells (elements) unlike the GGNB scheme for which the values are computed for the neighboring nodes of the element's neighboring cells. The node-based averaging scheme is believed to be more accurate than the cell-based scheme, being recommended for unstructured meshes (triangular and tetrahedral meshes) [93].

The numerical simulations performed for the squeezing motion are divided in two principal categories: (i) numerical investigations in which a single phase of fluids fills the domain; (ii) the numerical modeling of the free surface found at the end of the gap by using two fluid phases to fill the flow domain, within *Volume of Fluid Model*. Both methods are applied for flow computation in case of constant velocity (simple) and oscillatory squeeze flow (OSF) motions. Velocity and pressure distributions (thus the normal force) are exclusively dependent on the vertical motion of the solid boundaries (see. Figure 2.11 - 2.12). The vertical displacement of the upper wall may be modeled by imposing a time-dependent profile for both analyzed motions (constant velocity or oscillatory squeezing), implying the use of a dynamic deformable mesh for the geometry. Likewise, for the constant velocity squeeze flow the motion can be described by a quasi-steady approximation of the unsteady flow, in which, for different values of the fluid film thickness, the displacement of the upper wall is associated with a vertical flow of the fluid by imposing as boundary condition a constant entrance velocity of the fluid on the whole upper wall (Figure 4.1). In this case the computations are performed with a fixed mesh.

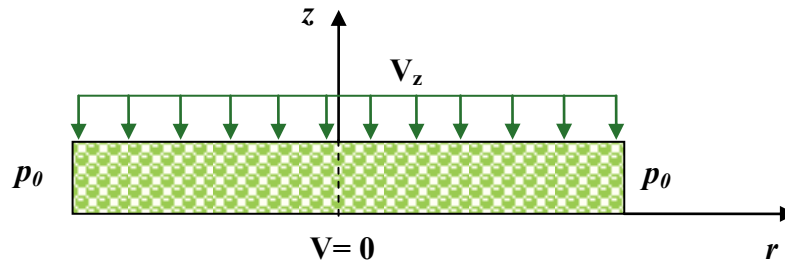


Fig. 4.1. Quasi-steady approximation sketch of the unsteady constant velocity squeeze flow.

All numerical simulations are performed using same hardware resources, two servers with eight processors running in parallel during the computations.

4.1.1. Volume of fluids method (VOF)

Free surface evolution and the influence of the end effects on the computed parameters is performed using the *Multiphase Module* available in the numerical code, which allows the analysis of steady and time dependent flow regimes in the presence of multiple fluids [93],

[100], [223]. VOF is generally used to compute time-dependent flows of two or multiple immiscible fluids, solving a single set of equations of motion for all the fluid phases' occupying the analyzed domain, tracking the volume fraction of each of the fluids throughout the domain, in order to compute the interface between them [93].

Tracking interface evolution in time is made through the solution of the continuity equation for the volume fraction α_i of one (or more) of the phases. The volume fraction equation may be solved either through implicit or explicit time discretization [93]. Face fluxes interpolation can be performed using either an interface reconstruction scheme (*Geo-Reconstruct - GR, Donor-Acceptor, DA*) either a finite volume discretisation scheme (*First Order Upwind, Second Order Upwind, CICSAM, Modified HRIC, and QUICK*).

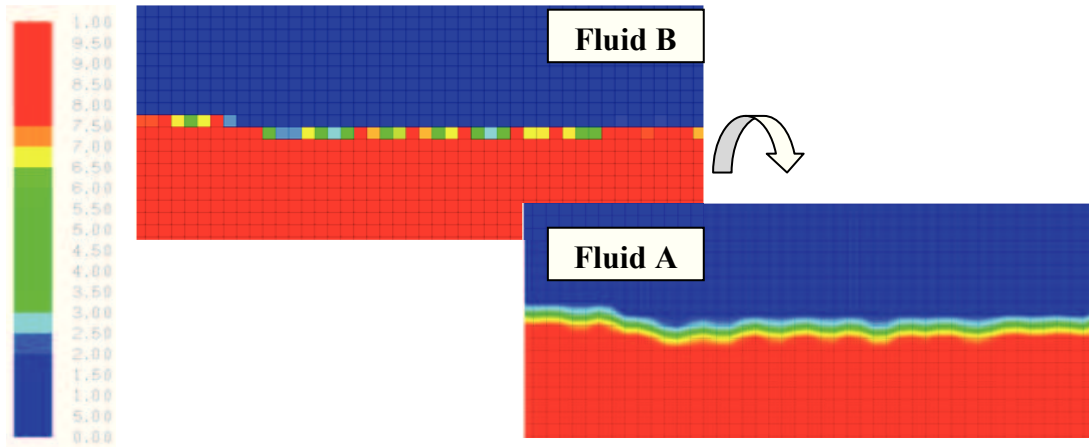


Fig. 4.2. The computation of cell volume fraction α_A and the interpolation of two fluid phases interface.

As mentioned before, the interpolation of the interface between two phases (A, B) requires firstly the computation of the volume fraction of the principal phase A (α_A) in each element, establishing if the phase occupies or not the investigated cell (volume element):

$$\begin{cases} \alpha_A = 0 \rightarrow \text{cell is empty of phase A} \\ \alpha_A = 1 \rightarrow \text{cell is filled by phase A} \\ 0 < \alpha_A < 1 \rightarrow \text{cell contains the interface between phase A and B} \end{cases} \quad (4.2)$$

To determine the shape of the interface the code solves a particular solution of the continuity equation in order to determine the volume fraction, including the mass transfer between the two phases (\dot{m}_{AB} , \dot{m}_{BA}):

$$\frac{1}{\rho_A} \left[\frac{\partial}{\partial t} (\alpha_A \rho_A) + \nabla \cdot (\alpha_A \rho_A \mathbf{v}_A) \right] = S_{\alpha_A} + \sum_{p=1}^n (\dot{m}_{AB} - \dot{m}_{BA}) \quad (4.3)$$

The volume fraction equation may be solved as mentioned through an implicit or explicit time scheme depending on the procedure used for interface approximation [93], [33],

[159]. From all numerical interface capturing schemes the most performant are GR and CICSAM (*Compressive Interface Capturing Scheme for Arbitrary Meshes*). GR scheme uses a linear interpolation on small sectors for the reconstruction, the interface having a linear slope in each cell [93]. CICSAM is a high resolution scheme [180], [181], [229] based on the *Convection Boundedness Criteria* [63], [223], [227] and two differentiation methods *Ultimate Quickest* and *Hyper-C*. The method introduces a weighting factor which takes into account the slope of the interface (relative to the main flow direction) and switches from forward differentiation to backward differentiation methods if the minimal angle between the slope of the interface and the principal flow direction is bigger than 45° [180], [181], [223], [229].

Besides, in the presence of two main flow directions (like for squeezing flows) the volume fraction is computed successively for each of them. CICSAM method allows a better control of the interface but sometimes produces a lag in pressure distribution [181], [229] or the lost of interface curvature when the flow directions are not aligned with the mesh [63]. When using an explicit method, for any unsteady computation, the VOF model uses an internal time step (different from the one indicated by the user, which is being used for the computation of transport equations) for the interpolation of the interface. The internal time step is adjusted and refined automatically by the numerical code depending on the maximum value imposed for the *Courant Number* – CN (CN is computed for each element that contains the interface and their neighbors). The *Courant Number* is a dimensionless parameter which compares the time step indicated by the user (T_s) to the characteristic time of transit, of a fluid element across a control volume:

$$CN = \frac{\Delta t}{\Delta x_{element} / \Delta v_{fluid}} \quad (4.4)$$

where Δt is the time step of simulation, $\Delta x_{element}$ represents the grid dimension and Δv_{fluid} is the velocity in which a control volume crosses through the grid element.

4.1.2. End Effects. Superficial tension and contact angle in numerical simulation of real flows.

Fluid surface tension is taken into account by adding a source term to the momentum equation, which describes the equilibrium between the forces which are present on the interface, using the continuous surface force model – CSF. The presence of surface tension creates a pressure difference on surface curvature, expressed by *Laplace & Young Equation* [93], [222]:

$$\Delta p = p_B - p_A = \sigma_s \left(\frac{1}{R_1} + \frac{1}{R_2} \right) = 2\sigma_s \kappa \quad (4.5)$$

where R_1 and R_2 are the curvature radius of the surface and κ is the mean curvature (see. Paragraph 2.5). For a two phase system the specific force volume depends on the parameters which define the interface:

$$F_{vol} = 2\sigma_s \left(\frac{\rho_m \kappa \nabla \alpha_A}{\frac{1}{2}(\rho_A + \rho_B)} \right) \quad (4.6)$$

where ρ_m is the mean density, $\nabla \alpha_A$ is the volume fraction gradient for the principal fluid phase and ρ_A, ρ_B are the densities of the two phases. The presence of an imposed value for the contact angle implies curvature adjustment near the fluid-solid contact area through a dynamic boundary condition (by modifying the normal at the surface into the cells located near the walls depending on the imposed contact angle), [30].

Surface tension and contact angle influences can be estimated as function of some dimensionless parameters: (i) at low Re numbers ($Re \ll 1$), when there is no main flow direction, the influence of surface tension can be neglected for very large values of Ca ($Ca \gg 1$); (ii) for $Re \gg 1$ the influence of surface tension can be neglected for $We \gg 1$ [12], [124]. For both constant velocity and oscillatory squeezing the motions analysed in the present paper are characterized by very low Re , therefore surface tension influence may be quantified by Ca values [93].

In the case of the oscillatory squeeze flow Ca values are very small, as example for a displacement signal characterized by $\omega_s = 50 \text{ Hz}$ and $\varepsilon_0 = 10 \mu\text{m}$, $Ca \sim 8.6 \cdot 10^{-3}$ for fluid viscosity $\eta = 0.11 \text{ Pa.s}$, (mineral oil). For the performed experiments and numerical simulations the Ca values are much smaller since the maximum oscillation amplitude is $\varepsilon_0 = 1 \mu\text{m}$, all the other fluids tested are more viscous. Re number is also small for the constant velocity squeeze flow, and the small values of Ca number highlight a significant influence of surface tension on the computed parameters.

4.2. GEOMETRY DEFINITION AND FLOW DOMAIN MESHING

For the present study, the construction of all geometries and their meshing has been made using preprocessor **Gambit 2.3.16**. The unsteady motion has been simulated using multiple geometries adapted for both dynamic (unsteady, deformable mesh) and quasi-steady (undeformed mesh) approximations of the squeezing phenomenon.

The flow area includes two fluid phases when investigating the influence of end effects and interface evolution in time for the dynamic approximation, the geometry being adapted to different shapes of the free surface, when using a quasi-steady approximation to investigate the end effects. All geometries used for the simulations have a 2D axial-symmetric construction, the symmetry axis corresponds to the Ox coordinate (which defines the vertical displacement of the upper wall). The mesh is using quadrilateral elements for all geometries, the exception being made for the quasi-steady approximation of the free surface influence where the shape of the geometry requires the use of triangular elements (see [Annex 5](#)).

4.2.1. Description of geometries used for single phase numerical simulations

The unsteady simulation of the squeezing motion uses the dynamic deformable mesh, the upper plate motion being modeled through an imposed displacement profile. For one phase simulation the geometries are S1, S2 and S3 (see [Figure 4.3](#) and [Figure 4.4](#)), using the same boundary conditions for both constant velocity and oscillatory squeeze flow. The small amplitudes of the sine displacement profile (correlated with the experimental investigations) require a refined mesh near the upper wall, in order to keep the computational time step at a reasonable level. The force is computed at the lower wall (correlated with experimental investigations), hence the refined mesh is also needed in this area. The use of very small cell dimension on Ox direction implies the use of small dimensions of the cells also for the Oy direction in order to maintain a small mesh aspect ratio and thus reduce the residuals during computation. For the same purpose, the radius of the virtual geometry was reduced from its original size (experimental parallel plate geometry): $R_{real} = 12.5 \text{ mm}$, $R_{simulation} = 5 \text{ mm}$.

Thus, the squeezing force computed on the lower wall has been corrected automatically by the numerical code with a amplification factor K , by imposing specific density, velocity and area values in the available *Reference Values Menu*:

$$F_{correctat} = K * |F| \quad (4.7)$$

According to (4.8) K is the ratio between the real geometry radius and the virtual geometry radius to the 4th power:

$$K = \left(\frac{R_{Real}}{R_{Simulare}} \right)^4 = 39.0625 \quad (4.8)$$

S1 geometry has been rebuild in the same conditions for each of the fluid film thickness analyzed, $h_0 \in \{50, 100, 150, 200, 250, 300 \text{ } \mu\text{m}\}$. Same procedure was applied for the transient (dynamic) modeling of the constant velocity squeeze motion ([Figure 4.4](#)).

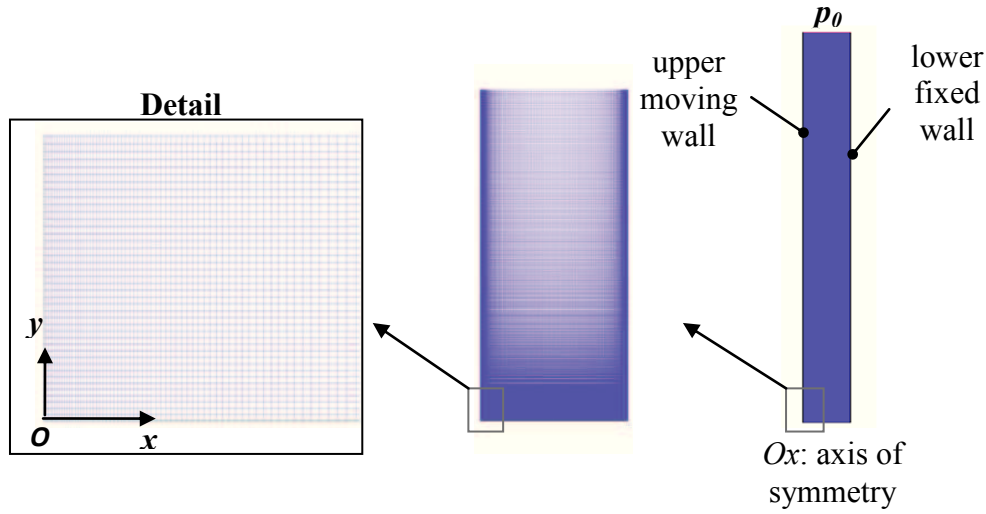


Fig. 4.3. The S1 geometry used for the numerical simulation of the oscillatory squeezing flow, boundary conditions definition and the meshed flow area (see also [Annex 4](#)).

At small squeezing velocities ($\dot{h} = 0.01 \text{ mm/s}$) a reduction of the initial film thickness has found to be necessary to reduce computational time, thus for $\dot{h} \geq 0.1 \text{ mm/s}$ S2 geometry has been used and for $\dot{h} = 0.01 \text{ mm/s}$ the S3 geometry has been used (where S2 corresponds to $h_0 = 1 \text{ mm}$ and S3 corresponds to $h_0 = 0.5 \text{ mm}$).

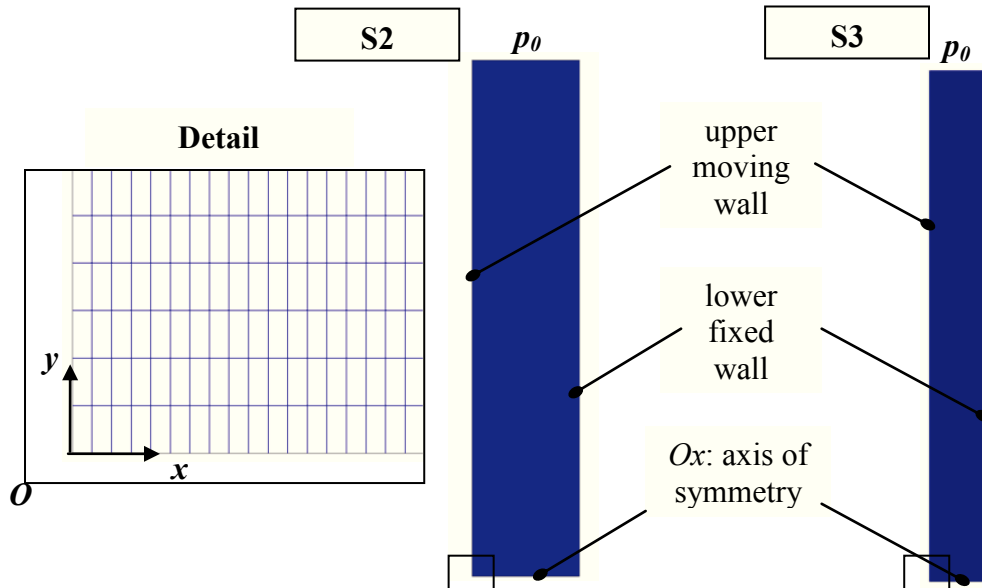


Fig. 4.4. S2 and S3 geometries used for the unsteady constant velocity squeeze flow, boundary conditions definition and the meshed flow area.

Since during a simulation the upper wall displacement covers almost the whole film thickness (from 1 mm to 0.01 mm , respectively from 0.5 mm to 0.01 mm) mesh refinement near the walls is no longer necessary to achieve proper results. However to assure the

precision of the computations and the quality of the mesh the aspect ratio is kept sufficiently small.

As mentioned before, the numerical simulation of the constant velocity squeeze flow has been made also by using a quasi-steady approximation (with undeformed mesh). For this study a number of fourteen geometries have been used, geometries with similar construction as the ones presented in [Figure 4.4](#).

The geometries have a plane 2D axial-symmetric construction, each of them corresponding to a certain film thickness $h_0 \in [0.01 \div 1] \text{ mm}$. From each simulation a single force value has been computed, depending on the imposed squeezing velocity ($\dot{h} \div \{1; 0.1; 0.01\} \text{ mm/s}$) and film thickness h_0 . [Figure 4.5](#) describes the geometry CS1 corresponding to a film thickness of $h_0 = 1 \text{ mm}$. For the geometries corresponding to $h_0 \in \{1 \div 0.1\} \text{ mm}$ the number of elements on Ox direction is 100 and the number of elements on Oy direction is 2150; for $h_0 \in \{0.05, 0.03\} \text{ mm}$ the number of elements on Ox direction is 10 and the number of elements on Oy direction is 2150; for $h_0 = 0.01 \text{ mm}$ the number of elements on Ox direction is 10 and the number of elements on Oy direction is 21500. Boundary conditions are described in [Annex 4](#).

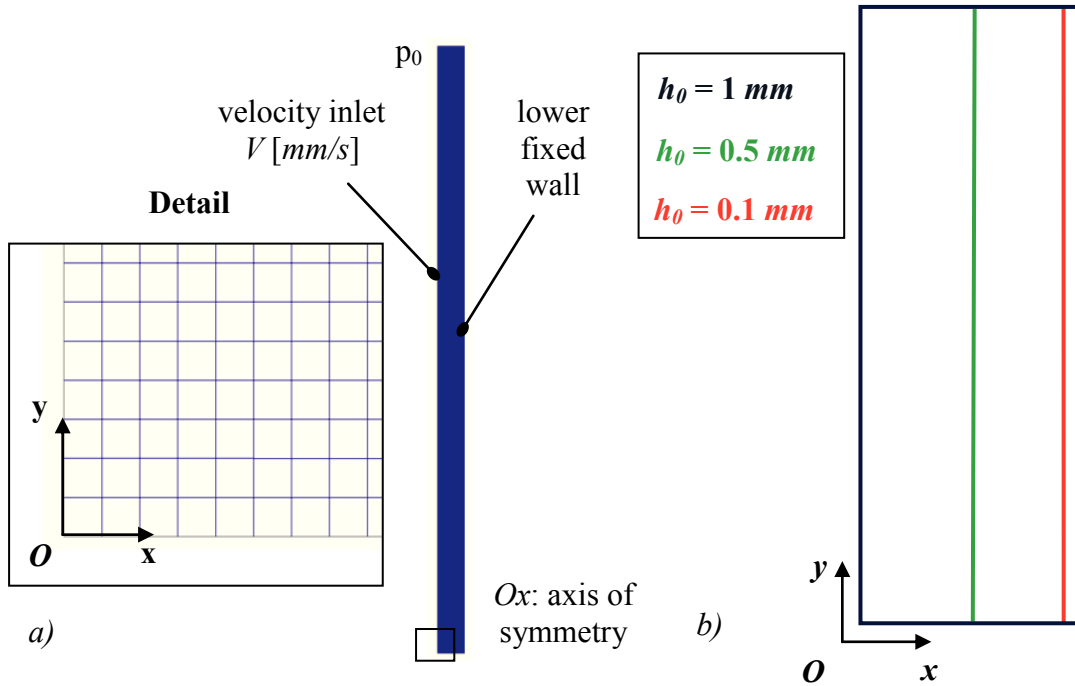


Fig. 4.5. CS1 geometry used for the quasi-steady approximation of constant velocity squeeze flow: boundary conditions definition and the meshed flow area (a); variation of geometry dimensions depending on the initial film thickness (b).

The constant velocity squeeze flow, been investigated by using a quasi-steady approximation and different geometries for whom the outlet pressure zone (the exit of the

gap) has been modeled in multiple ways in order to describe different free surface shapes observed during the experiments (see [Annex 5](#)).

4.2.2. Description of geometries used for multiphase numerical simulations

Squeeze flow modeling in the presence of two fluid phases implies the enlargement of the flow domain by adding a supplementary area at the end of the geometry (fluid outlet zone). Therefore the oscillatory squeeze flow in the presence of two phases has been modeled using VOF1 geometry (see [Figure 4.6](#)) for an initial film thickness of $h_0 = 150 \mu\text{m}$. Geometry dimensions have been reduced in comparison to the real experimental model (similar to previous simulations presented) the force signal being corrected through the *Reference Values Menu* of the numerical code.

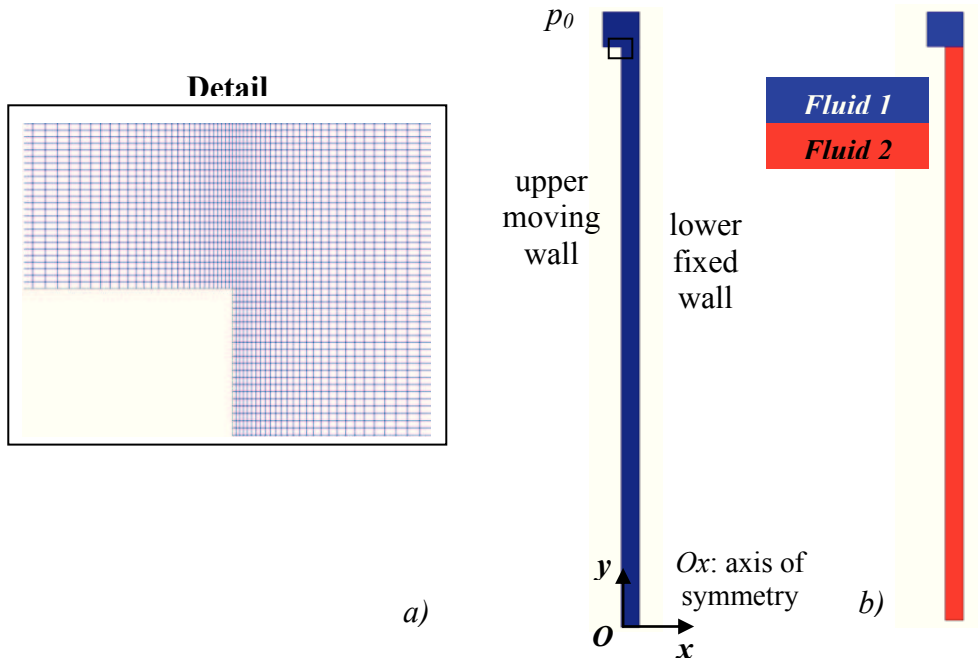


Fig. 4.6. VOF1 geometry used for two phase simulation of oscillatory squeezing flow: construction and meshing of the flow area (a); defining the fluid phases (b).

For the constant squeeze velocity squeeze flow the multiphase simulation has been realized using VOF2 geometry presented in [Figure 4.7](#). The aspect ratio of the mesh is equal to unit for the whole flow domain in order to assure mesh quality and precise results. Geometry dimensions describe closely the real model except the outer (air filled) area which is smaller than the real one ($L_{real} = 7.25 \text{ mm}$, $L_{simulation} = 5 \text{ mm}$) in order to reduce the total number of cells and thus the simulation time.

The boundary conditions were modified in order to obtain accurate results which can describe the real flow, investigating the influence of slip condition by imposing a small value of the wall shear stress either for the outer lower wall either for the whole lower surface (lower wall and external lower wall). Also, the external wall and the margin have been defined using different boundary conditions.

The whole process of construction and meshing of the flow areas presented followed the reduction of geometries dimensions, thus the reduction of the total number of elements, for each geometry. The effective computational time needed for a simulation of the oscillatory squeezing flow depends on the number of iterations that the code does for each time step (being between 20 and 100 in the case of performed analyse) and the magnitude of the time steps imposed by the user for the computation. The mono phasic simulations were performed by using a time step of $Ts = [2 \cdot 10^{-4} \div 2 \cdot 10^{-5}] s$ for the oscillatory motion and $Ts = 1 \cdot 10^{-3}$ for the constant velocity squeeze flow. Boundary conditions are described in [Annex 4](#).

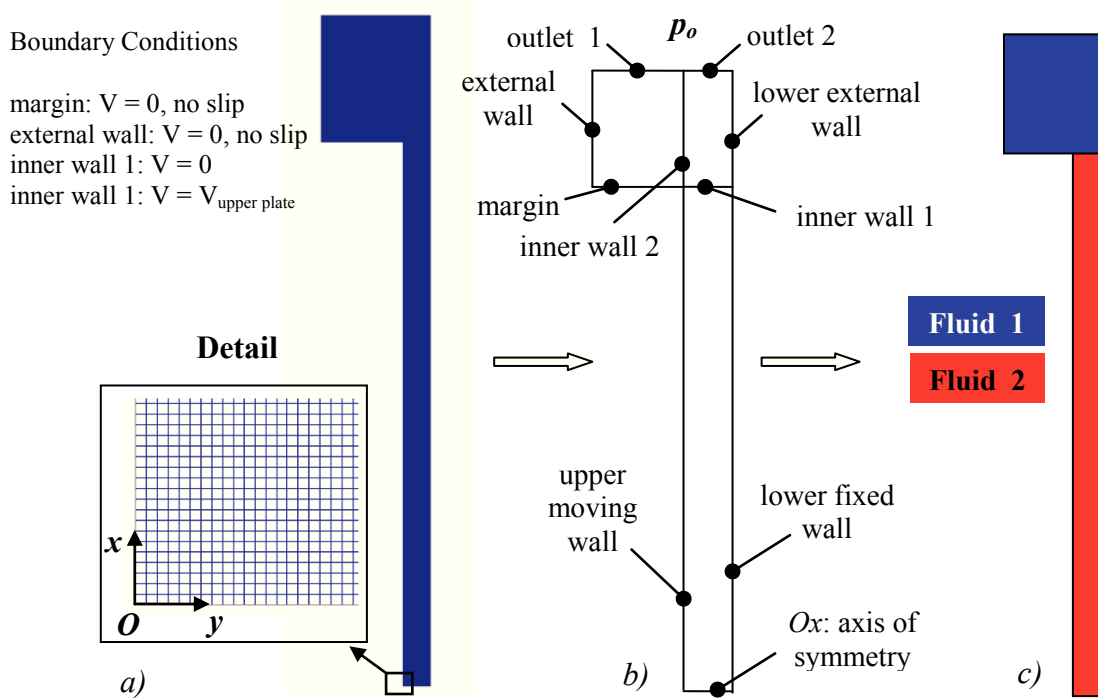


Fig. 4.7. VOF2 geometry used for two phase simulation of constant velocity squeezing flow: construction and meshing of the flow area (a); setting the boundary conditions (b); defining the fluid phases (c).

The size of a time period for the oscillatory squeeze depends exclusively on the oscillating frequency, varying between $0.033 s$ (at $\omega_s = 30 Hz$) and $0.2 s$ (at $\omega_s = 5 Hz$). To achieve a flow stability (the reduction of residual errors and thus, the convergence) one needs to perform at least two time periods, therefore it is necessary to perform between 200 and 1000 time steps.

For the constant velocity squeeze motion in order to cover the whole displacement profile there are necessary between 1000 ($\dot{h} = 1 \text{ mm/s}$) and 100.000 ($\dot{h} = 0.01 \text{ mm/s}$) time steps. In the case of multiphase simulations the time step was reduced, due to truncation errors appeared during the simulations, achieving very small values $T_s \in \{10^{-6} \div 2 \cdot 10^{-5} \text{ s}\}$. Such a numerical simulation can take around 48 h for the mono phase flows and as far as a week for multiphase simulations, depending on the available hardware resources.

The reduction of geometries dimensions by preserving a sufficiently number of elements and nodes of the flow area (maintaining the mesh quality) leads to a significant reduction of the computational time and at the efficiency of the investigation process of such flows.

4.3. NUMERICAL STUDY OF OSCILLATORY SQUEEZE FLOW

The oscillatory squeeze flow has been investigated numerically for Newtonian and generalized Newtonian fluids. The solutions obtained from mono phasic simulations of Newtonian fluids were compared to the analytical predictions, to establish a validity domain for the analytical expression of the thrust (eq. 2.52) by quantifying the differences obtained between the two theoretical approaches and also the experimental measurements. In the case of generalized Newtonian fluids the influence of shear-thinning rheological behavior on the squeezing force and velocities distributions in the gap has been investigated.

4.3.1. Comparative analysis between numerical solutions and theoretical predictions for Newtonian fluids

The simulation was performed using the rheological parameters of a pure viscous mineral oil with a shear viscosity of $\eta_0 = 0.11 \text{ Pa.s}$. The rheological characterization of the fluid was performed within simple and dynamic shear tests using *Physica MCR 301* rheometer with different testing geometries.

Considering that the samples are pure viscous the analyze followed the temperature dependence of the viscosity coefficient (Figure 4.8). It has been noticed that depending on the temperature variation the viscosity at a constant value of $T = 20^\circ$ exhibits a variation within the domain $\eta_0 \in [0.09 \div 0.15] \text{ Pa.s}$, probably due to the fact that temperature control is realized only for the lower plate of the testing geometry (see. Paragraph 5.2.1.2).

Even though the testing gap used for the determination of the sample's shear viscosity is small ($h_0 \sim 300 \mu m$), we must consider the existence of a small temperature gradient on in the gap, which may influence the viscosity measurements.

For the performed numerical simulations the viscosity coefficient of the mineral sample has been chosen to have a constant value of $\eta_0 = 0.11 Pa.s$.

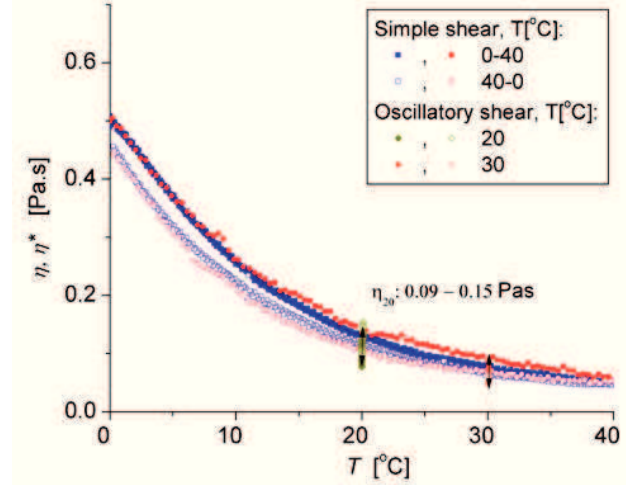


Fig. 4.8. Viscosity dependence on the testing temperature for mineral oil.

To establish a validity domain of the analytical model the investigations performed followed the determination of the relative error between the numerical results and the analytical predictions. Therefore the maximum amplitude of the force signal obtained numerically was compared with the maximum amplitude of the force signal predicted by the theoretical formulation.

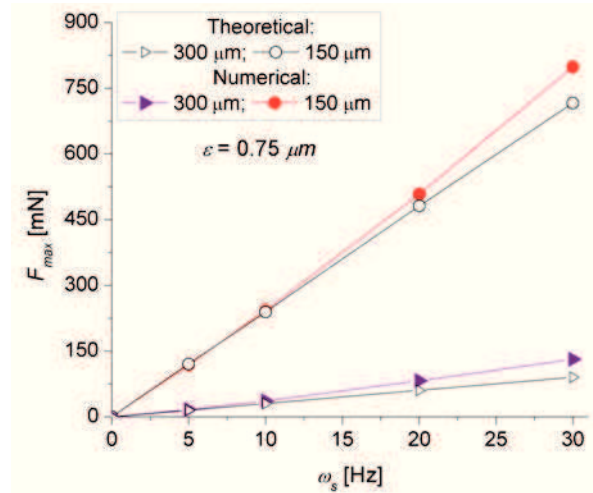


Fig. 4.9. The maximum amplitude of the force signal obtained by numerical simulations and using the analytical expression for different values of h_0 , ω_s , and a constant input amplitude of $\varepsilon_0 = 0.75 \mu m$.

The relative error furnishes a quantitative analyze of the squeezing motion, being calculated as follows:

$$\Delta\varepsilon = \frac{f_{num} - f_{th}}{f_{th}} \times 100 [\%] \quad (4.9)$$

where f_{num} and f_{th} represents the maximum force amplitude obtained numerically and analytically.

It can be noticed (Figure 4.9 - Figure 4.11) that the limitation of the analytical expression of the normal force is dependent on the three principals parameters describing the motion: the initial film thickness h_0 , oscillation frequency ω_s and oscillation amplitude ε_0 . Film thickness has a significant influence on the force variation (Figure 4.10), the relative error increasing with increasing the film thickness. Moreover all the results obtained trough numerical simulations are superior to the ones predicted by the analytical model. For $h_0 > 150 \mu m$ the relative error increases as somehow expected since the analytical formulation derives from Reynolds Lubrication Approximation for thin films. Likewise, it can be observed that $\Delta\varepsilon [\%]$ is acceptable only for small oscillation frequencies $\omega_s \leq 10 \text{ Hz}$ and small oscillatory amplitudes. Actually in order to keep $\Delta\varepsilon < 1.5 \%$ (Figure 4.11) and thus maintain a good correlation between the results the oscillation amplitude has to be $\varepsilon_0 \leq 1 \mu m$.

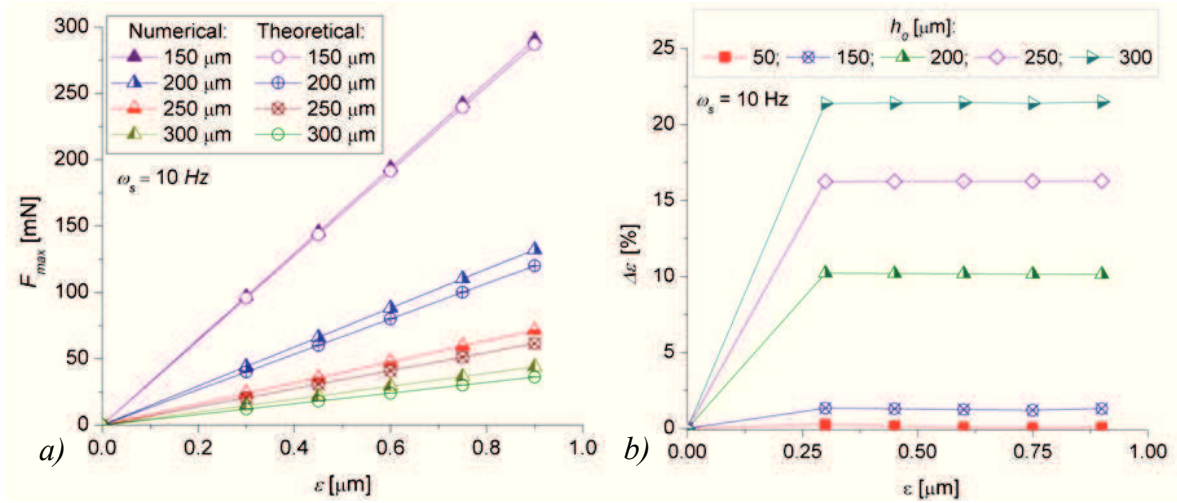


Fig. 4.10. The maximum amplitude of the force signal obtained by numerical simulations and using the analytical expression (a) and the relative errors between them (b) for different values of h_0 , ε_0 , constant oscillatory frequency of $\omega_s = 10 \text{ Hz}$ (simulation time step $T_s = 2 \cdot 10^{-4}$).

The influence of simulation time step has also been investigated, the results being presented in Figure 4.12 and Figure 4.13. The reduction of the time step with an order of magnitude brings a noticeable reduction of the relative error, enlarging the validity domain of the theoretical formulation: $\Delta\varepsilon < 10 \%$ for $\omega_s \leq 30 \text{ Hz}$, $\varepsilon_0 \leq 10 \mu m$.

Even though there is still a difference between the results, numerical values being for all performed simulations superior to the analytical predictions, this difference may be due to the inertia influence.

The analytical expression excludes inertial contributions being derived from *Reynolds Approximation*, whereas the numerical code solves the *Navier-Stokes Equations* which includes the inertial influence. The computational time step has a noticeable influence on the results proving the need of a wise choose of the simulation settings when performing numerical simulations of real flows, especially if the modeled motions are complex flows, like in this case.

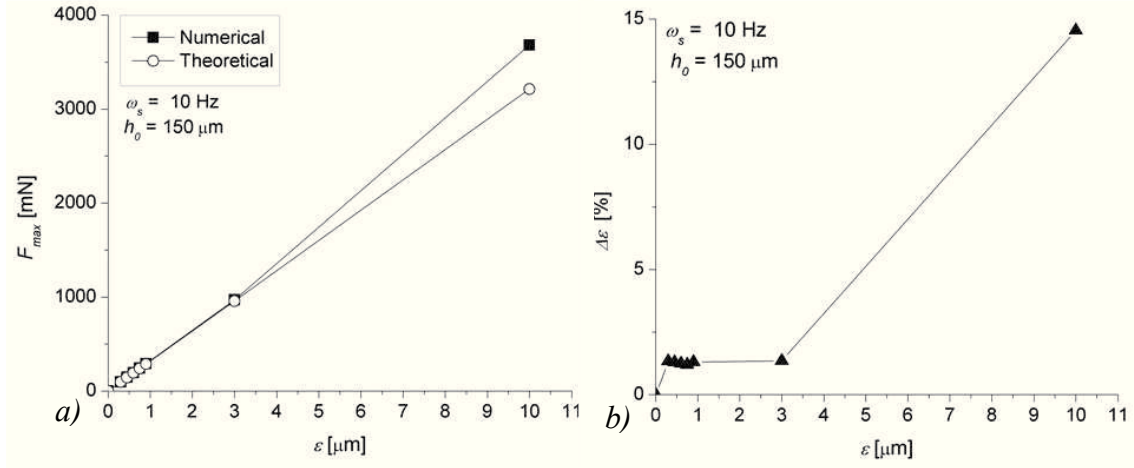


Fig. 4.11. The maximum amplitude of the force signal obtained by numerical simulations and using the analytical expression (a) and the relative errors between them (b) for different values of ε_0 , a constant oscillatory frequency of $\omega_s = 10$ Hz and $h_0 = 150$ μm.

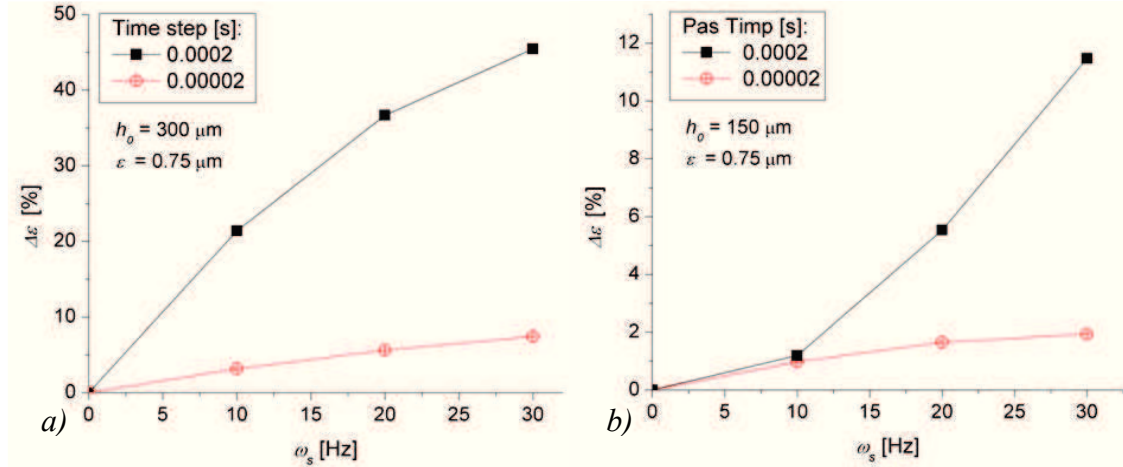


Fig. 4.12. Computational time step influence on the relative error between numerical simulation results and analytical predictions for different values of oscillatory frequency ω_s , constant oscillatory amplitude $\varepsilon_0 = 0.75$ μm and two different gaps: $h_0 = 300$ μm (a) și $h_0 = 150$ μm (b).

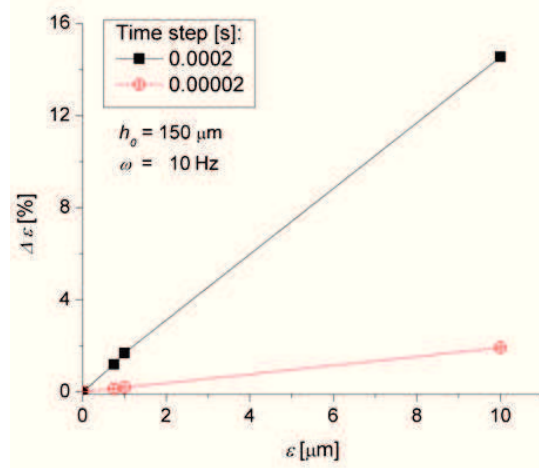


Fig. 4.13. Computational time step influence on the relative error between numerical simulation results and analytical predictions for different values of oscillatory amplitude ε_0 , constant oscillatory frequency $\omega = 10 \text{ Hz}$ and $h_0 = 150 \mu\text{m}$.

The difference between numerical and analytical results may be due to the inertial contribution, this aspect being discussed in Paragraph 4.3.4 where a comparison with experimental results is performed. We conclude that, for low viscous Newtonian liquids, the analytical expression for the squeezing force gives errors less than 2%, for $\omega_s \leq 30 \text{ Hz}$ and amplitudes $\varepsilon_0 \leq 5 \mu\text{m}$ if the normal gap is limited at $h_0 = 150 \mu\text{m}$.

4.3.2. The oscillatory squeezing flow of generalized Newtonian fluids

For the generalized Newtonian fluid, the reference sample is a polymer solution (PAA) (polyacrylamide solution with water). Its rheology was tested in dynamic shear (*Physica MCR 301 rheometer*, the cone-plate geometry, 50 mm diameter), the results being presented in Figure 4.14.

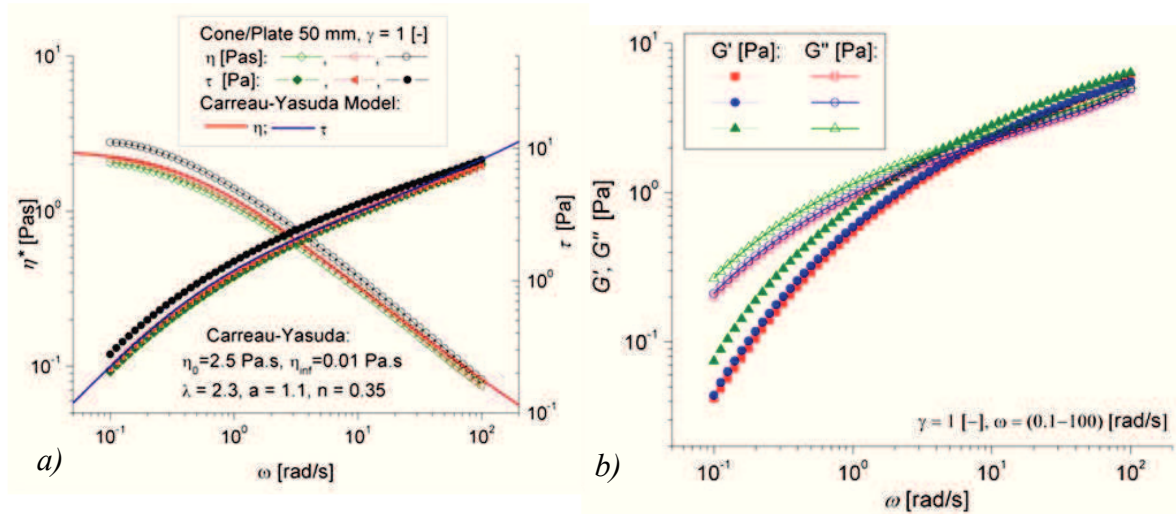


Fig. 4.14. PAA rheology in shear tests: complex viscosity and shear stress variation (a); storage and loss modulus variation (b).

The results disclose a shear-thinning viscoelastic behavior; sample's viscosity function being well approximated by the *Carreau-Yasuda* model (ec. 2.16), see Table 4.1. The sample has also been tested experimentally in oscillatory squeezing flow (for further details see Paragraph 5.3).

Table 4.1. Carreau-Yasuda parameters used to approximate the rheological behavior of the PAA sample.

η_∞ [Pa.s]	η_0 [Pa.s]	λ [s]	a [-]	n [-]
0.01	2.5	2.3	1.1	0.35

For the PAA solution it has been obtained a phase angle between the input signal (displacement, $D = \varepsilon(t)$) and the output signal (force) which is characteristic to a viscoelastic fluid response ($0^\circ < \delta < 90^\circ$), as showed in Figure 4.15.b, unlike for the Newtonian fluid (the mineral oil, $\eta_0 = 0.11$ Pa.s) for whom the phase angle is 90° (see. Figure 4.15.a).

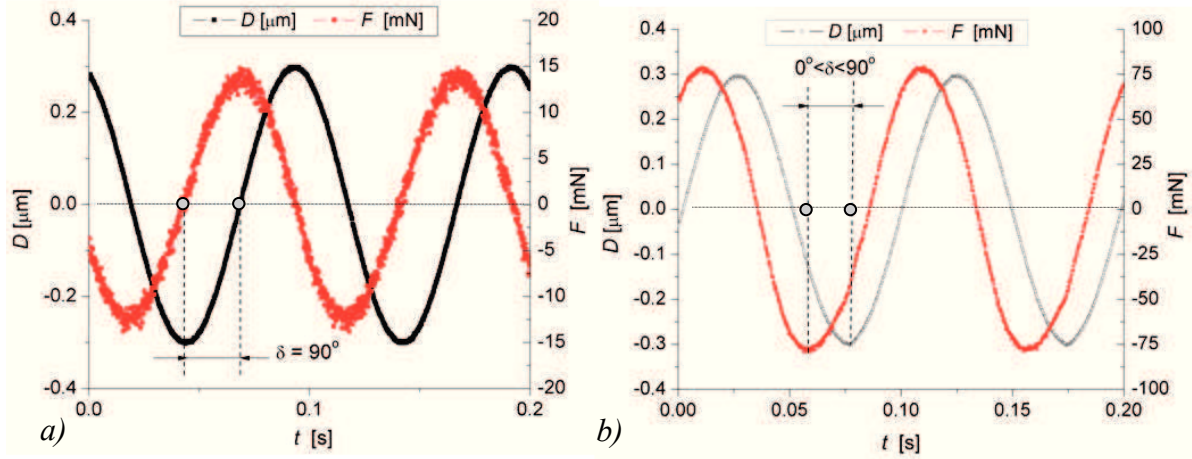


Fig. 4.15. Experimental force and displacement signals for mineral oil sample (a) and PAA sample (b) in oscillatory squeezing flow motion at $h_0 = 300 \mu\text{m}$, $\varepsilon_0 = 0.30 \mu\text{m}$, $\omega_s = 10$ Hz.

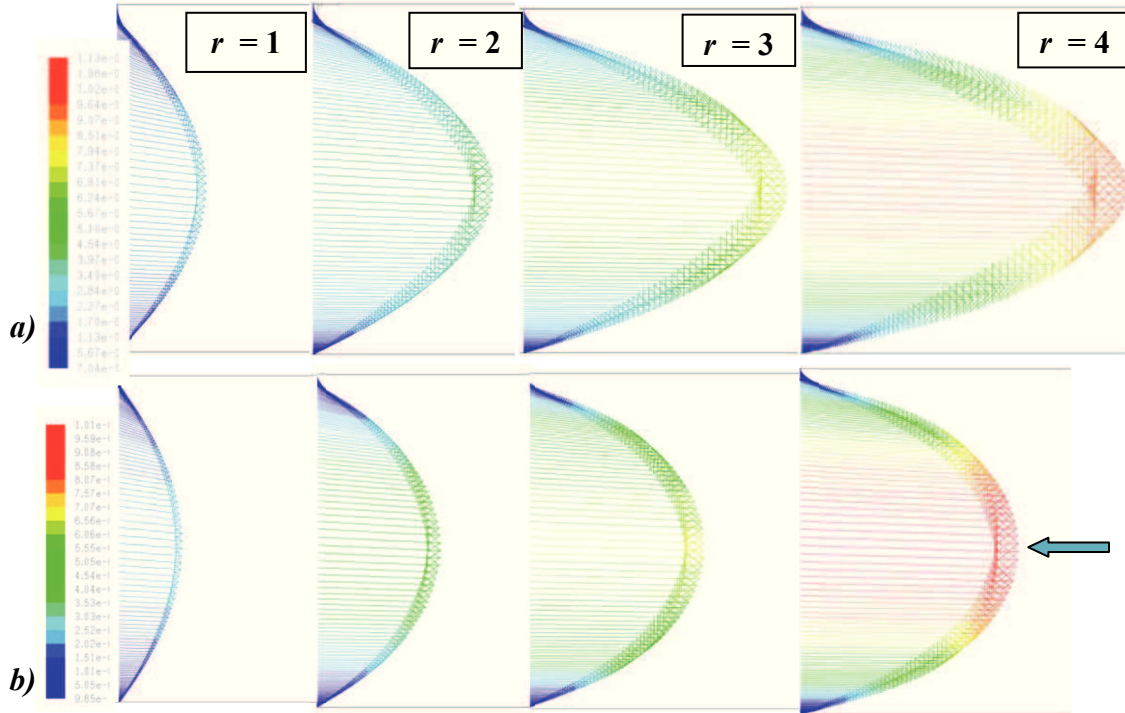


Fig. 4.16. Radial velocity vectors distribution trough the gap and along plate radius for the Newtonian mineral oil sample (a) and a polymer sample described by Carreau-Yasuda model (b).

The numerical simulation of the oscillatory squeeze flow of the PAA sample discloses a deformation of the output signal (force signal) according to the shear-thinning behavior of the sample, but the phase angle obtained from numerical simulations is $\delta = 90^\circ$ indicating the absence of the elastic component.

Actually both numerical code and approximation model cannot disclose the viscoelastic behavior, for its investigation being needed the use of a mechanical model of viscoelastic behavior such as *Maxwell* or *Kelvin-Voigt* models (see [Paragraph 2.2](#)).

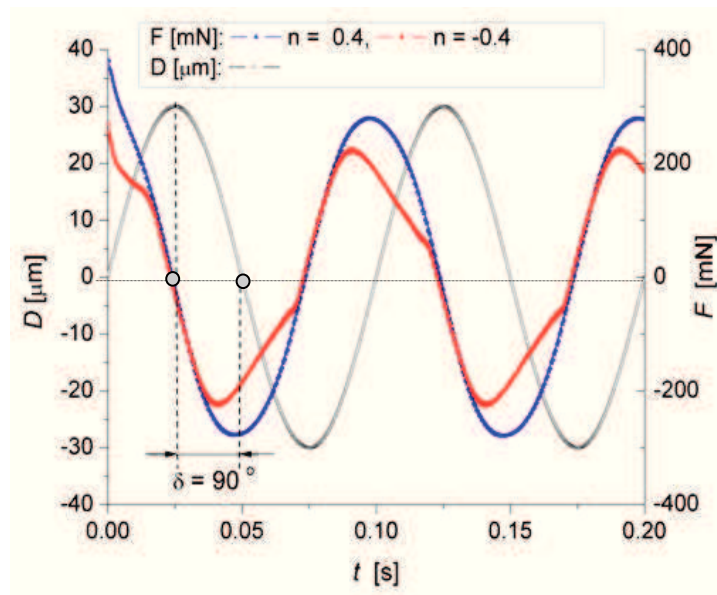


Fig. 4.17. Force and displacement signals obtained trough numerical simulation of the oscillatory squeezing flow for a polymer sample described by the Carreau-Yasuda model at $h_0 = 300 \mu m$, $\varepsilon_0 = 0.30 \mu m$ and $\omega_s = 10 \text{ Hz}$.

The investigations of viscoelastic rheological behavior trough squeezing motion is one of the most delicate problems when considering squeezing flow, a commercial numerical code which includes viscoelasticity that can solve squeezing motions being unavailable at the present time (for details see [Paragraph 3.2.5.2](#)).

However the pseudoplastic behavior of the sample is emphasized during numerical simulations by the fluid flattened radial velocity distribution in the gap (see [Figure 4.17](#)).

4.3.3. Nonlinear behavior of viscoelastic samples in oscillatory squeezing flow

The nonlinear rheological behavior of complex fluids (in particular *Yield Stress fluids*) is emphasized at medium and large amplitude oscillatory shear flows in the so called LAOS procedure (see [Paragraph 2.4](#)).

A correlation of various testing procedures, simple shear or extensional flow and complex squeeze motions, is imperative for a proper rheological characterization of complex fluids (since their processing and use implies complex flows in complex geometries) [54], [114], [196].

In shear, yield stress fluids behavior is modeled analytically with different constitutive equations [38], [141], [142], [155]. The viscosity and flow curve being well approximated by the *Carreau-Yasuda* model if the flow index has a negative value ([Figure 4.18](#)).

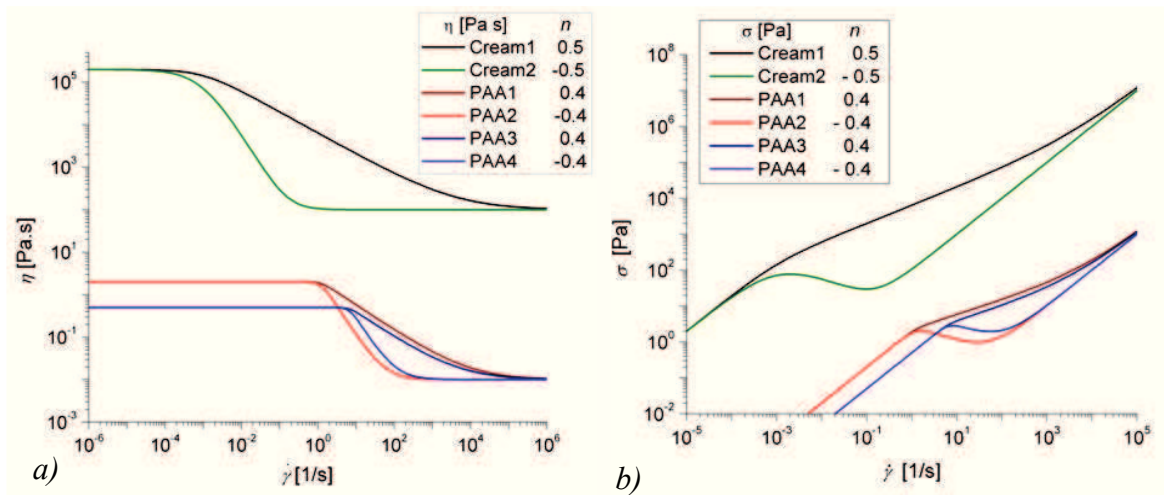


Fig. 4.18. Viscosity dependence on shear rate (a) and the flow curve, usual curve for positive flow index and with the occurrence of a plateau for negative flow index (b) for different parameters of the rheological Carreau-Yasuda model which can approximate the behavior of polymer solutions and emulsions (see [Table 4.2](#))

The non-linearity is remarkable for $n < 1$, but only the negative values generates flow curve non-monotonic character (Figure 4.18), which can model yields stress fluids. Therefore, using different parameters for the Carreau-Yasuda model with both positive ($n > 0$) and negative ($n < 0$) flow indexes the nonlinear behavior can be simulated numerically .

Figure 4.18 presents the viscosity dependence on shear rate (shear-thinning behavior) and the flow curve (usual curve for positive flow index and with the occurrence of a plateau for negative flow index) for different parameters of the rheological model, which normally can approximate the behavior of polymer solutions or emulsions, such as a cosmetic cream (see also Table 4.2). Since the numerical code *Fluent* does not include the Carreau-Yasuda model as a viscosity function in its library, the model was written into a text file and imported as a User Define Function UDF.

Table 4.2. Carreau-Yasuda parameters used to approximate the linear and nonlinear rheological behavior of emulsions and polymer solutions in shear flow.

Fluid type	Notation	$n [-]$	$\eta_0 [Pa.s]$	$\eta_\infty [Pa.s]$	$\lambda [s]$	$a [-]$
Emulsion	Cream1	0.5	$2e^6$	$1e^2$	$1e^3$	1
Emulsion	Cream2	-0.5	$2e^6$	$1e^2$	$1e^3$	1
Polymer solution	PAA1	0.4	2	0.01	0.8	4
Polymer solution	PAA2	-0.4	2	0.01	0.8	4
Polymer solution	PAA3	0.4	0.5	0.01	0.15	5
Polymer solution	PAA4	-0.4	0.5	0.01	0.15	5

Simulation results are presented in Figure 4.19 for PAA1 and PAA2 parameters and in Figure 4.20 for the emulsion parameters Cream1, Cream2). The output force signal deforms from a sine shape with increasing oscillatory amplitude even for the linear behavior of the polymer. For a nonlinear behavior the force signal deformation is significant, tending to a square-like shape at large ε_0 . For both linear and nonlinear behavior the computed phase angle is 90° , since, as mentioned before the elastic component is being neglected, the deformation of the signal being exclusively dependent on the shear-thinning behavior of the sample and the presence of nonlinearity induced by the negative flow index.

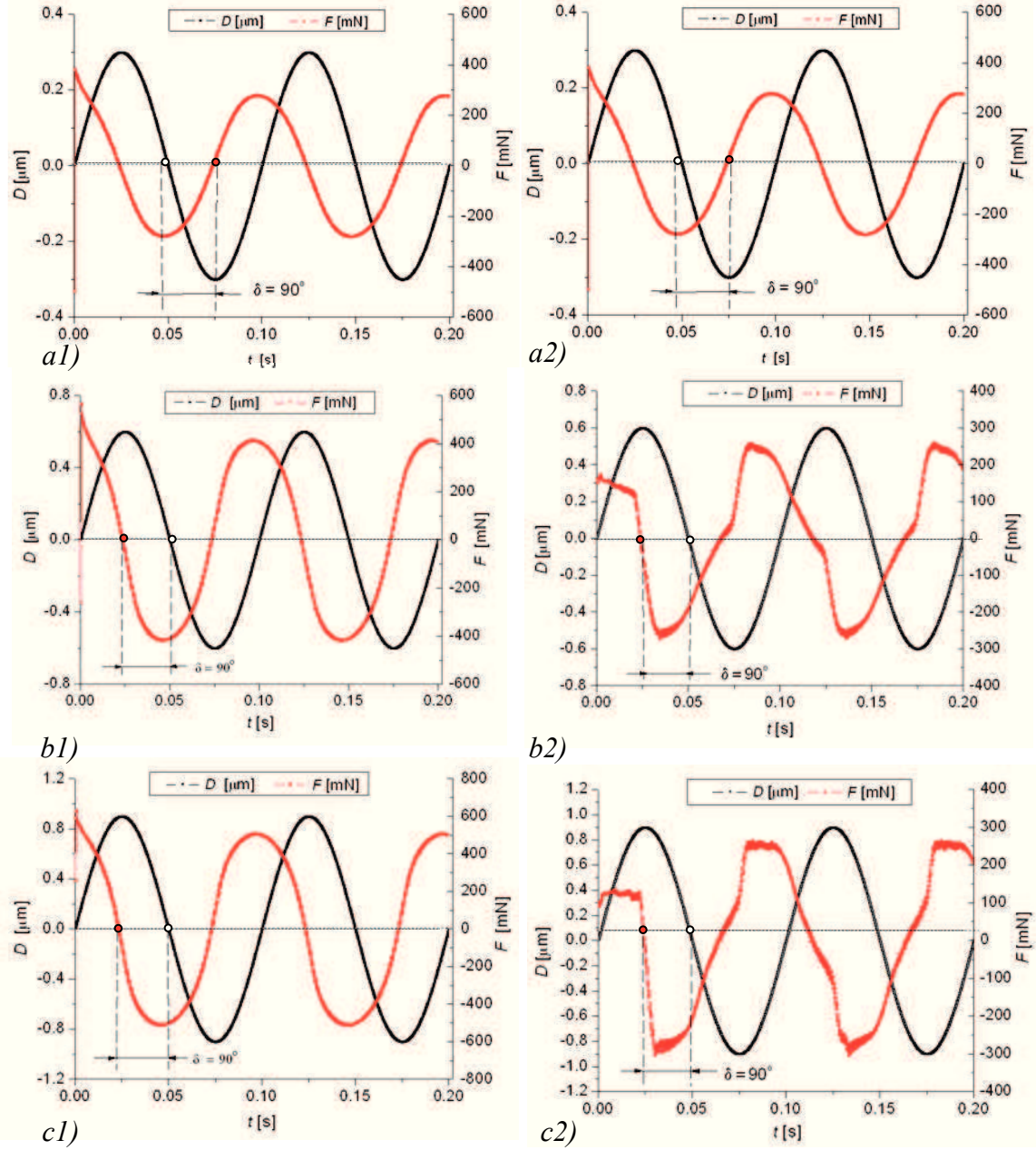


Fig. 4.19. Quasi-steady linear $n > 0$ (a1,b1,c1) and nonlinear $n < 0$ (a2,b2,c2) behavior of a polymer solution described by the generalized Newtonian Carreau-Yasuda model (PAA1, PAA2, see Table 4.2). The results are obtained from numerical simulations of oscillatory squeezing flow characterized by $h_0 = 150 \mu\text{m}$, $\omega_s = 10 \text{ Hz}$ și $\varepsilon_0 = 0.30 \mu\text{m}$ (a), $\varepsilon_0 = 0.60 \mu\text{m}$ (b), $\varepsilon_0 = 0.90 \mu\text{m}$ (c).

For both material models (which represents a polymer solution and an emulsion), the distortion of force signal is dependent on the oscillatory amplitude, as expected on the basis of shear nonlinear theory (LAOS procedures), [81], [114], [129], [233].

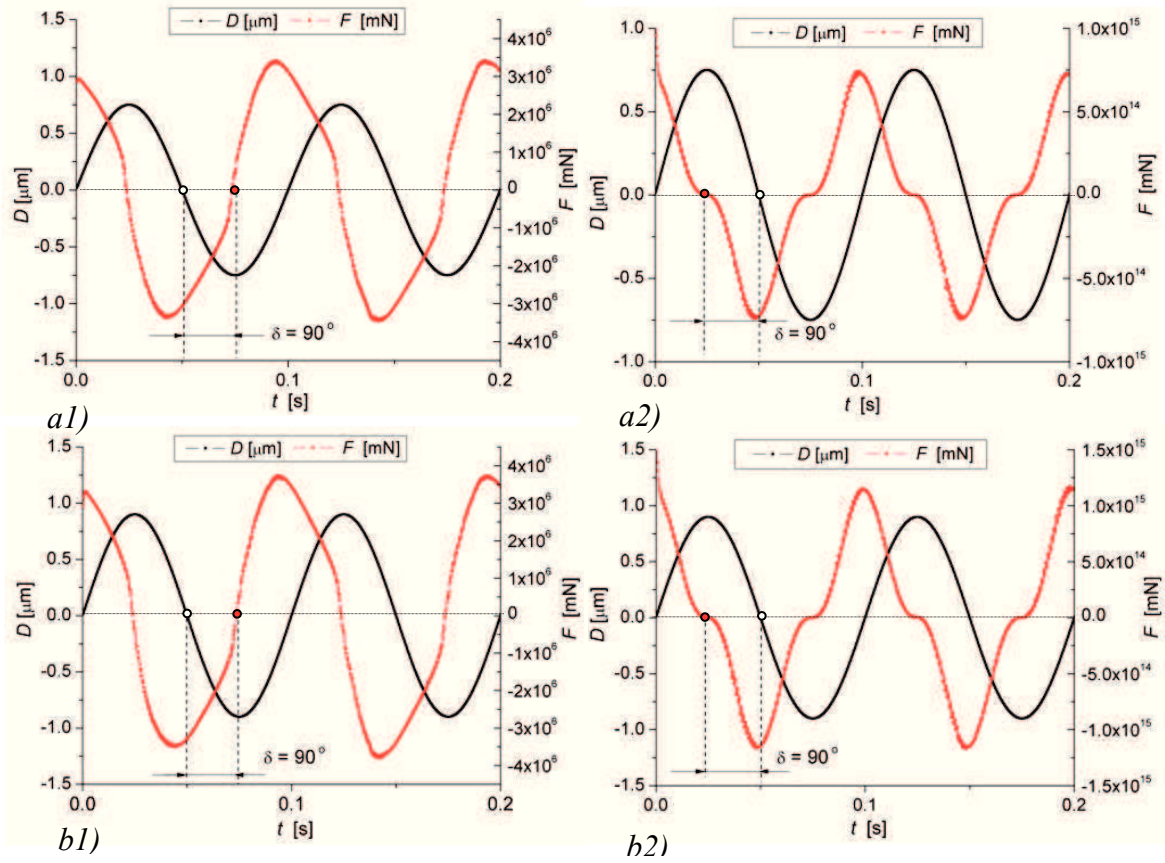


Fig. 4.20. Quasi-steady linear $n > 0$ (a1,b1) and nonlinear $n < 0$ (a2,b2) behavior of an emulsion described through generalized Newtonian Carreau-Yasuda model (Cream1, Cream2, see Table 4.2). The results are obtained from numerical simulations of oscillatory squeezing flow characterized by $h_0 = 150 \mu\text{m}$, $\omega_s = 10 \text{ Hz}$ and $\varepsilon_0 = 0.60 \mu\text{m}$ (a) respectively $\varepsilon_0 = 0.90 \mu\text{m}$ (b).

One concludes that numerical simulations of generalized Newtonian models in oscillatory squeezing gives a qualitative representation of the strain amplitude influence on the distorted output signal. The results are found to be consistent with the classical ones obtained in oscillatory shear (see also Chapter 6).

4.3.4. End effects obtained numerically for oscillatory squeeze flow

For single phase numerical simulations it has been noticed a dependency of the relative error (between numerical results and analytical predictions) on the initial film thickness (see Figure 4.10). Considering that the squeezing force is computed as a integral of the pressure field on plate radius (lower wall length), the computed pressure distribution has been analyzed in comparison with the analytical predicted pressure field. It is observed that differences between the numerical simulation and the theory are significant especially at high gaps $h_0 = 300 \mu\text{m}$ (Figure 4.21.a). This difference decreases once decreasing h_0 at $150 \mu\text{m}$

(Figure 4.21.b), and that for the smallest film thickness $h_0 = 50 \mu\text{m}$ the results are identical (Figure 4.21. c).

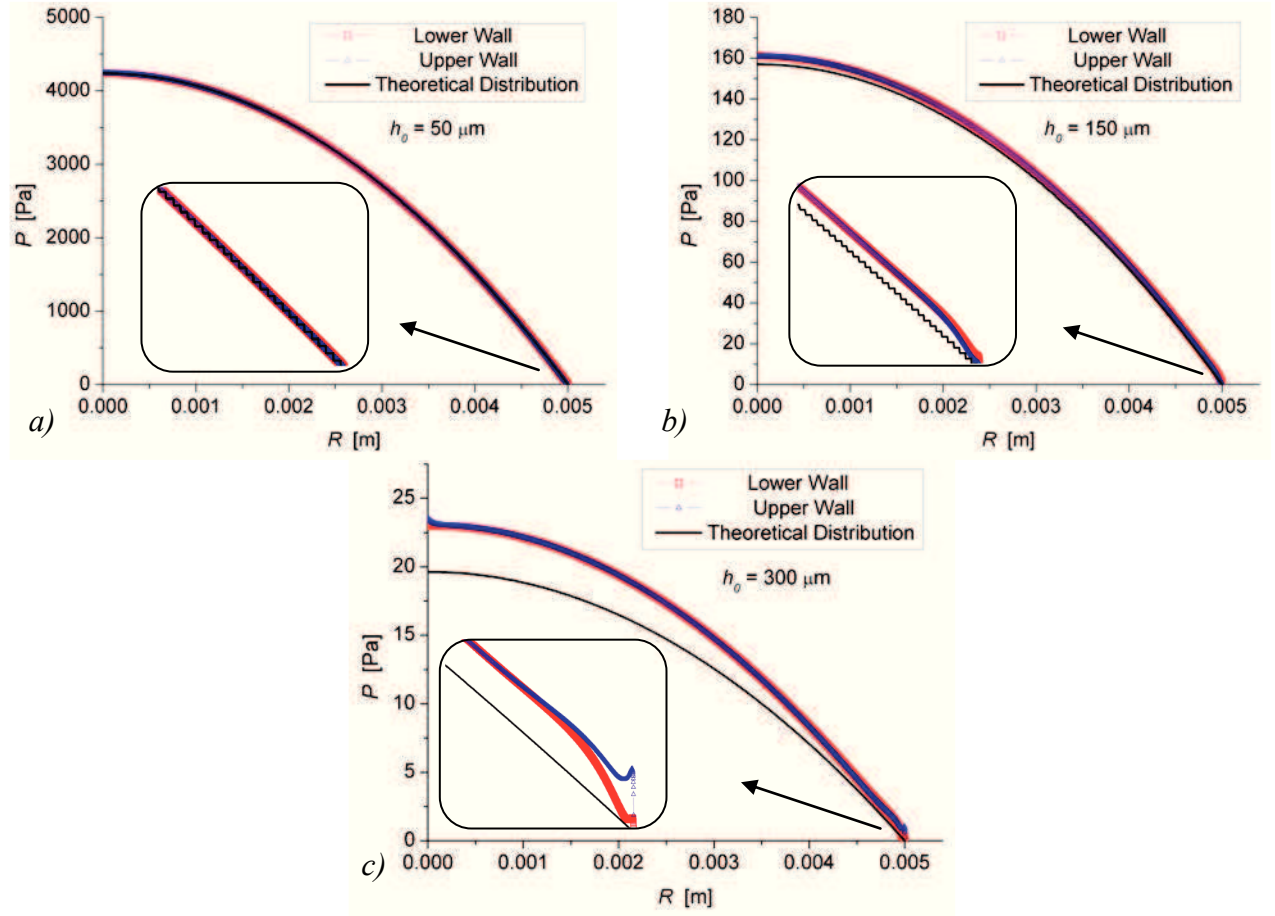


Fig. 4.21. Pressure distribution on upper and lower walls obtained numerically, in comparison with the analytical formulation at: $h_0 = 300 \mu\text{m}$ (a), $h_0 = 150 \mu\text{m}$ (b), $h_0 = 50 \mu\text{m}$ (c). Results for oscillatory squeezing flow of mineral oil at $\omega_s = 10 \text{ Hz}$ and $\varepsilon_0 = 0.75 \mu\text{m}$.

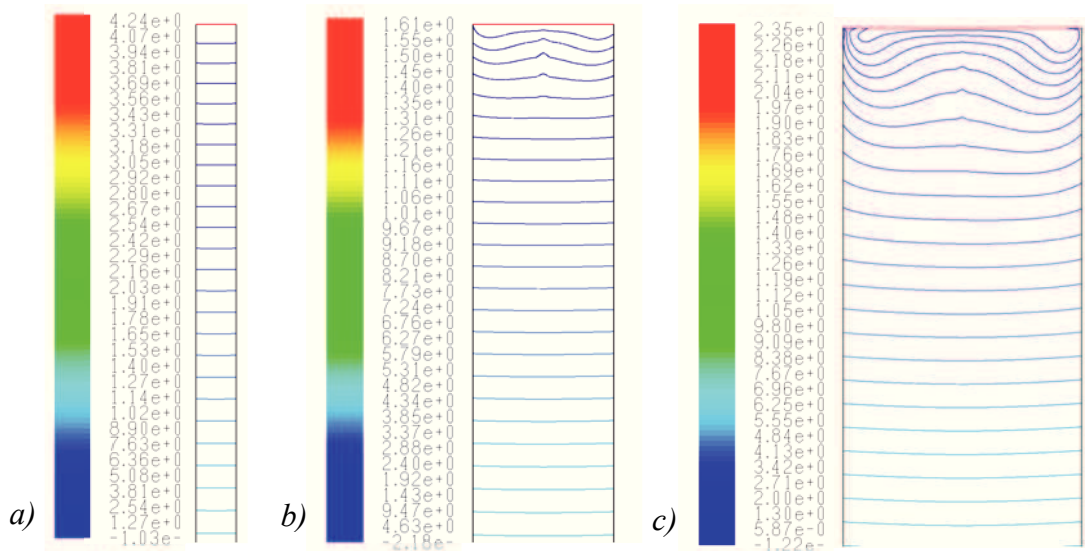


Fig. 4.22. Iso-pressure lines in the gap (in the vicinity of the outlet zone) obtained trough the numerical simulation of the oscillatory squeezing flow of mineral oil at $\omega_s = 10 \text{ Hz}$, $\varepsilon_0 = 0.75 \mu\text{m}$, and different initial film thickness: $h_0 = 50 \mu\text{m}$ (a), $h_0 = 150 \mu\text{m}$ (b), $h_0 = 300 \mu\text{m}$ (c).

The pressure spectrum in the gap discloses the deformation of the isopressure lines as increasing the initial film thickness. This gap dependent geometry may be due to some computational errors during the numerical simulation of the complex squeezing flow but equally it can be due to end effects which may appear near the exit of the flow domain.

Pressure isolines distribution (Figure 4.22) emphasize a possible influence of the end effects for gaps $h_0 > 50 \mu\text{m}$, through their deformation from a linear shape in the center of the geometry and a gradually deformed shape as approaching the outlet zone (where the boundary imposed condition is the atmospheric pressure p_0).

A more detailed analysis of the end-effects influence is presented in the following paragraphs where surface tension, contact angle and wall adhesion are taken into consideration.

4.3.5. Free surface evolution in oscillatory squeeze flow simulations

End effects influence on the normal force distribution has been performed through the tracking of free surface evolution, using the *Volume of Fluid Multiphase Model* available in the numerical code (see Paragraph 4.1 for description). From all available interface tracking techniques the GR scheme is known to be the most appropriate when the numerical simulation results must follow the real experimental shape of an interface (Paragraph 4.1). Through this method it can be successfully modeled any flow characterized by a main flow direction (flow motions like *Poiseuille* or *Couette*), obtaining through simulation an almost identical shape of the interface as the real experimental ones [18], [38], [159], [178].

In the case of oscillatory squeeze flow, the unsteady motion has been modeled numerically by using the Pressure-based solver, using two different computational models to determine local gradients (*Green-Gauss Cell Based* and *Green-Gauss Node-Based* models) shifting from one procedure to another to achieve the convergence of the numerical calculus. For *Case A* where gravity influence is not taken into account (Figure 4.23) the simulation may be performed using GR capturing scheme and the *Green-Gauss Cell Based* model to compute local gradients. When including gravitational effects in the simulation the GR scheme is not sufficient to achieve computation convergence, leading to unrealistic deformed shapes of the interface and to high values of local velocity gradients, especially in the vicinity of outlet zone (or interface). The GR scheme is limited through the CN value and the internal time steps of computation used to solve volume fraction equation. The use of CICSAM scheme and switching to *Green-Gauss Node Based* model for the computation of local gradients allows the convergence of the simulation in the presence of gravitational effects.

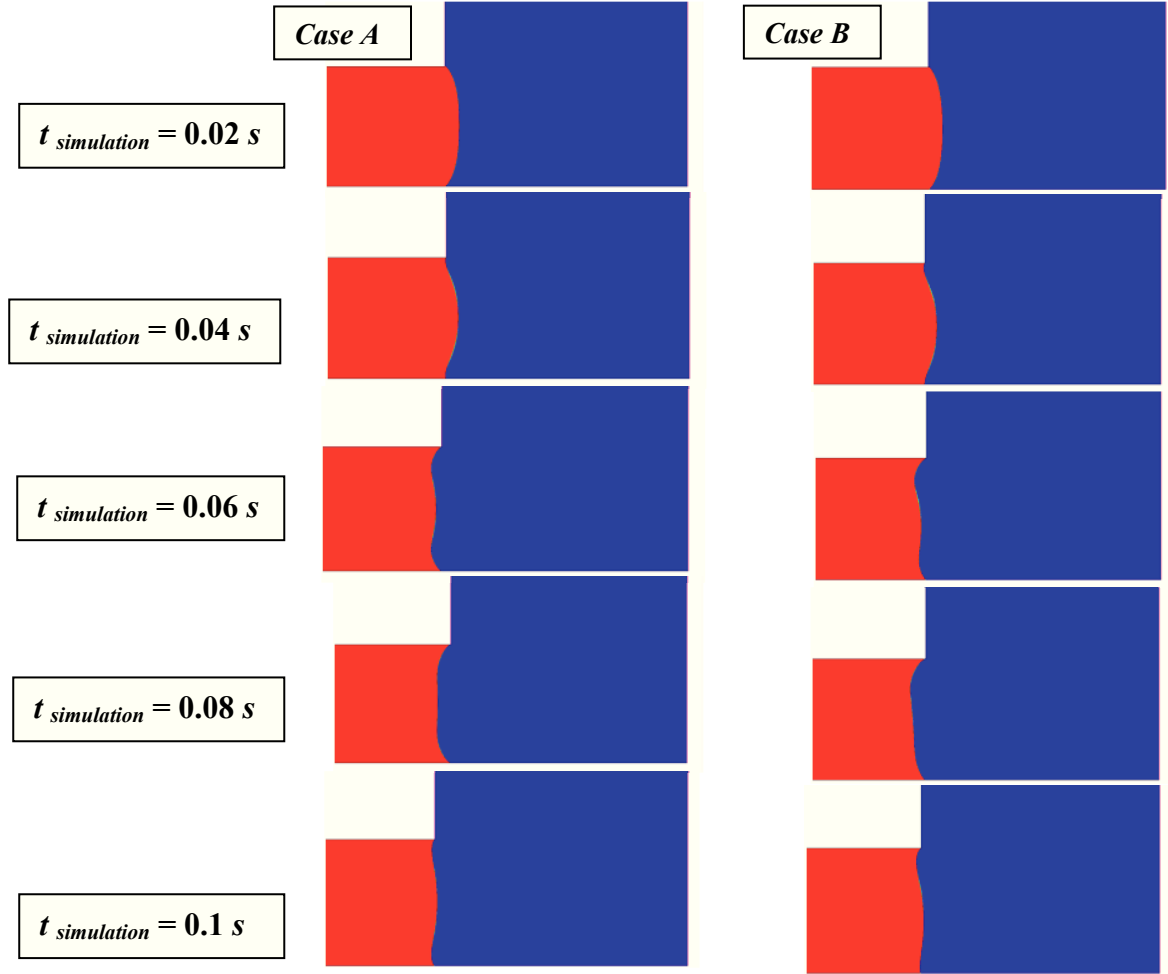


Fig. 4.23. Oil-air interface evolution (for a complete oscillation) obtained for the numerical simulation of oscillatory squeezing flow ($h_0 = 150 \mu\text{m}$, $\omega_s = 10 \text{ Hz}$, $\varepsilon_0 = 0.90 \mu\text{m}$,) in the absence of gravity by using GR scheme (a) and in the presence of gravitational effects by using CICSAM scheme (b).

Figure 4.23 presents the evolution of the free surface (fluid – gas interface) for a whole time period ($T = 0.1 \text{ s}$) obtained from the numerical simulation of the oscillatory squeezing flow of the mineral oil for a initial film thickness of $h_0 = 150 \mu\text{m}$. Gravitational effects are investigated without including contact angle or surface tension proprieties (Figure 4.23. b).

In comparison with the analytical prediction, the numerical force signal amplitude decreases when two fluid phases are involved (see Figure 4.24). Gravity seems also to reduce force amplitude, bringing it under the values obtained analytically or numerically in the absence of gravitational effects. Interface tracking is made by starting the simulation with a linear free surface (connecting the upper and lower walls, see. Figure 4.6) at the end of the gap and obtaining after one plate oscillation a deformed shape of the interface. Meniscus formation (Figure 4.23) give rise to a change between fluid phases in the vicinity of the outlet zone, a small part of the volume occupied initially by the mineral oil becomes occupied by the air surrounding the gap accordingly to the continuity equation used by the numerical code.

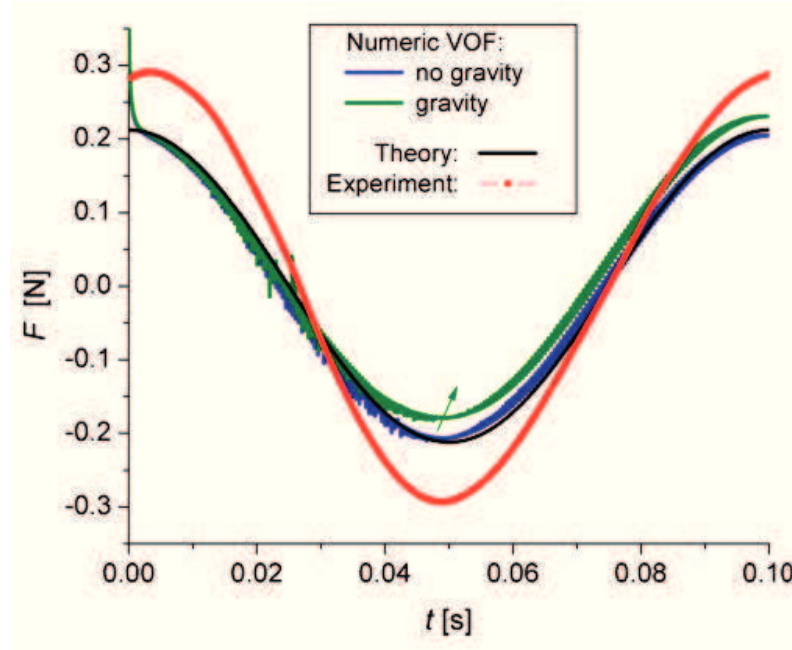


Fig. 4.24. Force signal obtained trough numerical simulations of single and multiphase squeeze flow. Numerical results are compared with the analytical predictions and the experimental measurements for the following conditions: $h_0 = 150 \mu m$, $\omega_s = 10 \text{ Hz}$, $\varepsilon_0 = 0.90 \mu m$.

This may lead to a decrease of the force signal amplitude since the air surrounding the gap (see Paragraph 4.2.2) has a much smaller viscosity than the investigated fluid, thus less thrust. In order to perform a relevant comparison between the numerical results and experimental measurements in OSF it is necessary to include in computations the physical parameters defining the real flow such as fluid surface tension, the contact angle and eventually to initialize the flow into a geometry in which the free surface shape is not linear but it approximates the real free surface observed experimentally.

For the present study surface tension has been included into computations but the convergence of the computation has not been archived. Different simulations have been performed in order to obtain computation convergence: the use of high resolution schemes as CICSAM with implicit and explicit formulations, a refined mesh with a unitary aspect ratio, the reduction of time step from $2e^{-5} \text{ s}$ to $1e^{-6} \text{ s}$.

Despite all measures taken the convergence of the computation has not been obtained; very large values of velocity are obtained for both fluid phases in the vicinity of the interface, as well as in the surrounding air phase, especially near to the pressure outlet areas.

Velocity increases abruptly form zero to almost 100 mm/s at the first displacement of the interface and the propagation of surface tension gradients and dynamic contact angle from the walls towards the center of the gap. Truncation errors increase form one iteration to another leading to unrealistic values of velocity vectors and the deformation of the free

surface (see Figure 4.25). A solution might be a further reduction of the computational time step until values of $1e^{-7} \div 1e^{-8} s$, in this case, the necessary time to obtain a single oscillation of the plate is too long considering the available hardware resources.

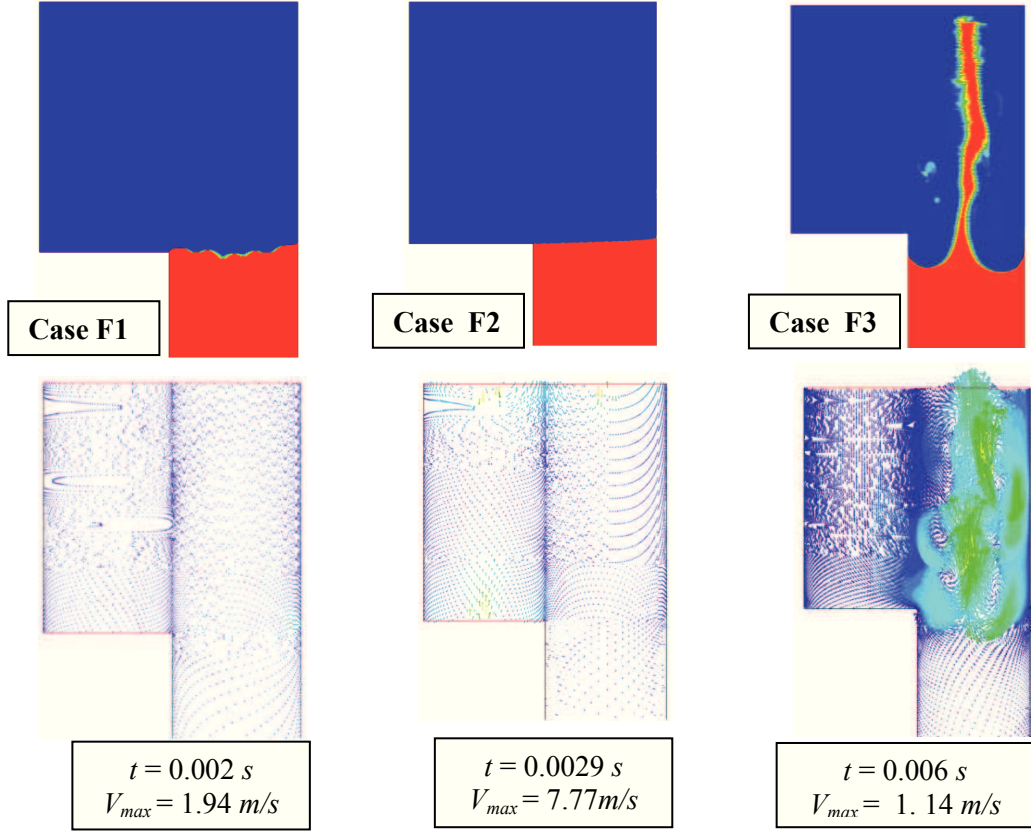


Fig. 4.25. Oil-air interface and velocity vector distributions obtained for oscillatory squeezing flow in the presence of surface tension and liquid-solid contact angle ($h_0 = 150 \mu m$, $\omega = 10 Hz$, $\varepsilon_0 = 0.90 \mu m$). Case F1: Solver GGCB, GR scheme for interface tracking; Case F2: Solver GGNB, GR scheme for interface tracking; Case F3: Solver GGNB, CICSAM scheme for interface tracking.

Hence, the continuation of investigations in this direction is found inefficient for this thesis. However a correlation can be made between the shapes of the interface obtained through numerical simulations (Figure 4.23) and the deformed pressure isolines obtained in single phase numerical simulations (Figure 4.22). Thus the shape of the free surface may be emphasized through single phase simulations, at least qualitatively.

As conclusion, the modeling of the free surface for oscillatory squeezing flow in the presence of superficial tension or contact angle could not be archived. In the absence of end effects, numerical solutions indicate good representation of the squeezing phenomenon and a fair correlation between the computed values and the experimental measurements. Moreover, at small film thickness the numerical solution corresponds qualitatively and quantitatively with the analytical solution, thus the influence of possible end effects or inertial term can be neglected.

4.4. NUMERICAL MODELING OF CONSTANT VELOCITY SQUEEZE FLOW

For constant velocity squeeze flow the simulations were performed (as mentioned before) using two methods: (i) a transient unsteady solution (with deformable mesh) and (ii) a quasi-steady approximation (fixed mesh, different gaps). Unlike for oscillatory squeezing flow, the force is computed on the upper wall of the geometry accordantly to the performed experimental investigations (see Chapter 5). For single phase simulations the investigations were performed for three different squeezing velocities ($\dot{h} \in [0.01, 0.1, 1] \text{ mm/s}$) using the rheological parameters of the mineral oil investigated in the previous paragraph ($\eta_0 = 0.11 \text{ Pas}$; $\rho_{oil} = 877 \text{ kg/m}^3$). In the case of the quasi-steady approximation, force distribution has been obtained by performing a simulation for each pair of (h_0, \dot{h}) . During experimental investigations the evolution of the free surface has been found to vary depending on the squeezing velocity, therefore, the free surface evolution and its influence on the squeezing force has been analyzed numerically.

4.4.1. Qualitative and quantitative analysis between transient and quasi-steady approximations

Squeeze force variation obtained using both solutions are presented in Figure 4.26 for three squeezing velocities. The geometries used to perform the simulations are presented in Paragraph 4.2 (Figure 4.4 and Figure 4.5).

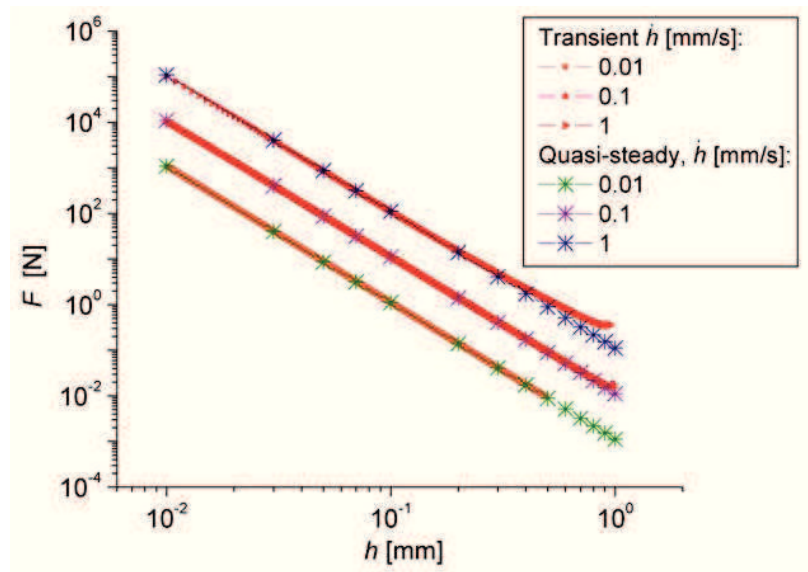


Fig. 4.26. Normal force dependence on film thickness and squeeze velocity obtained numerically using transient and quasi-steady approximations of the constant velocity squeeze motion of mineral oil.

Normal force variation indicates a very good correlation between the transient and quasi-steady approximations, except the high film thickness domain, where, in the case of transient unsteady approximation the flow is not fully developed and the residuals have not yet reached the convergence limit. To analyze the development of the flow in the gap the radial and axial velocity components are extracted at different radii for the case where the squeezing velocity is $\dot{h} = 0.01 \text{ mm/s}$, all results being compared with the analytical predictions.

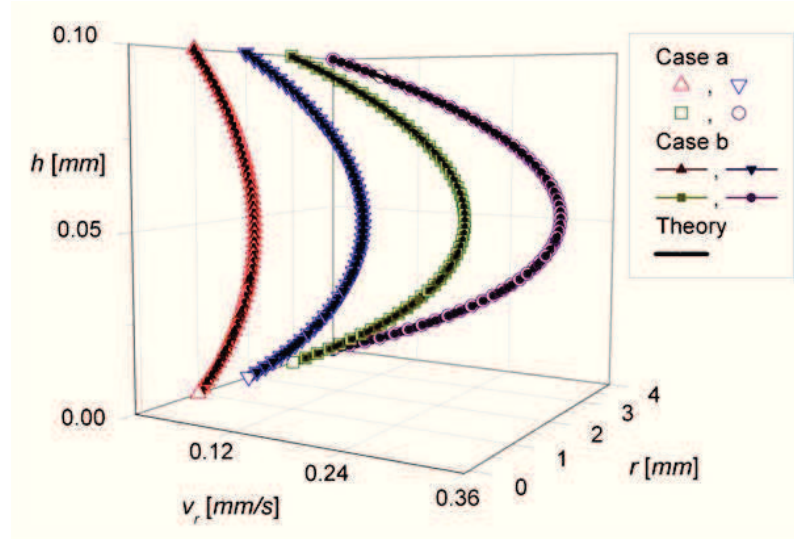


Fig. 4.27. Radial velocity distribution in the gap, for the mineral oil sample, at a constant squeezing velocity of $\dot{h} = 0.01 \text{ mm/s}$ and $h = 0.1 \text{ mm}$. Comparison between analytical solution and the numerical simulations using a quasi-steady approximation (case a) and a transient approximation (case b).

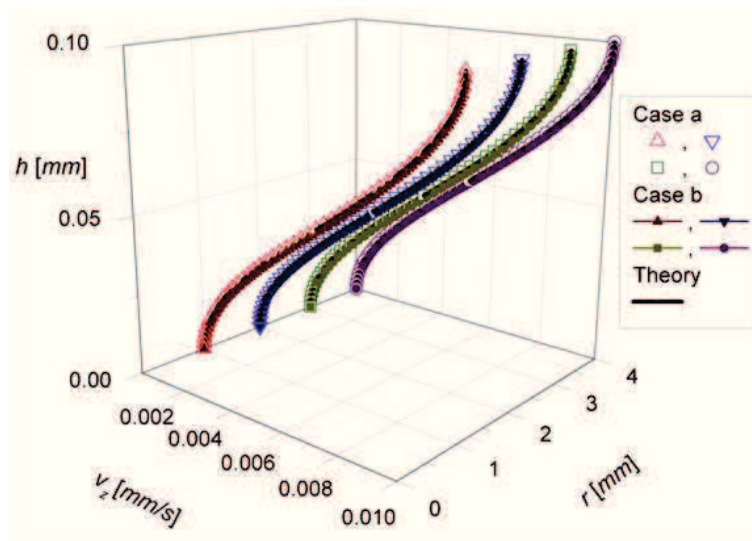


Fig. 4.28. Axial velocity distribution in the gap, for the mineral oil sample, at a constant squeezing velocity of $\dot{h} = 0.01 \text{ mm/s}$ and $h = 0.1 \text{ mm}$. Comparison between analytical solution and the numerical simulations using a quasi-steady approximation (case a) and a transient approximation (case b).

The coherence of the results is found also for the radial and axial velocity distributions in the gap (at different radii) and for the pressure distribution on the upper wall, the results being identical for both approximations used (see Figures 4.27-4.28). Moreover the numerical simulation results fit perfectly the analytical distributions. Radial velocity varies along plate radius, increasing gradually once approaching the exit of the gap (see Figure 4.27). Axial velocity distribution is constant along the plate radius because the fluid is moving with constant velocity on the axial direction (Figure 4.28), accordingly to the theoretical hypothesis that the radial flow is dominating the squeezing motion. The results indicate a good correlation between both numerical approximations used and the analytical model as showed in Figures 4.26 – 4.29.

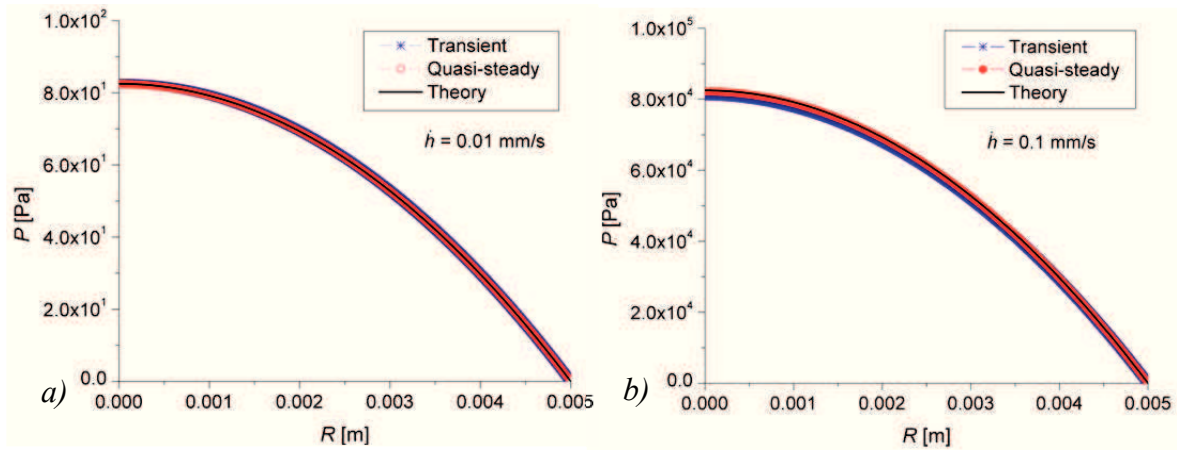


Fig. 4.29. Pressure distribution on the upper wall for the mineral oil sample at a constant squeezing velocity of $\dot{h} = 0.01 \text{ mm/s}$ and $\dot{h} = 0.1 \text{ mm/s}$. Comparison between analytical solution and the numerical simulations using a quasi-steady approximation (case a) and a transient approximation (case b).

Making a comparison between the necessary time to simulate the motion by using the two methods and considering the good correlation between the results, both from qualitative and quantitative point of view, we consider that the quasi-steady approximation may be successfully used to model the constant velocity squeeze flow. Moreover the quasi-steady approximation requires a much smaller computational time being more efficient than the transient approximation, for whom there are needed between two and seven days of computations depending on the squeezing velocity, the initial gap and the hardware resources.

However, the quasi-steady method requires a different geometry for each film thickness, thus its use is recommended only for simple geometries. These results prove that for the simple squeeze flow inertia hasn't got a significant influence, and thus the inertial term may be neglected for the studied film thickness and squeeze velocities domains. In conclusion in the absence of end effects the numerical simulations of the analyzed transient squeezing gives identical results with the quasi-steady classical analytical solution.

4.4.2. End effects in single phase constant velocity squeeze flow

The investigation of free surface influence through numerical simulations is motivated by the evolution of the free surface observed experimentally for different Newtonian and non-Newtonian fluids. Firstly, [Figure 4.30](#) presents a schematic representation of different shapes of the free surface observed experimentally or found in literature (red curve) and the linear shape of the free surface as it is considered by the analytical model and most of numerical solutions (blue line).

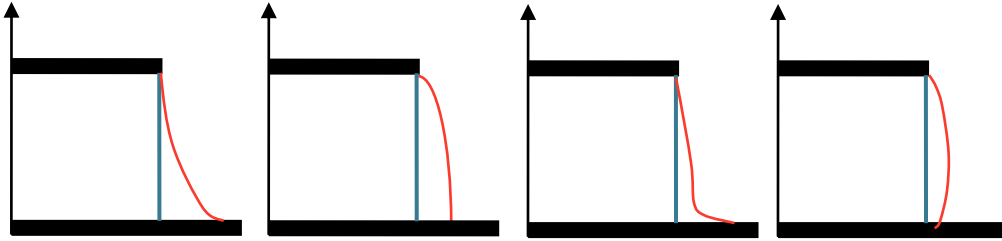


Fig. 4.30. Different shapes of the free surface in squeeze motion, observed experimentally (red curve) and as considered by most of the numerical solutions and analytical model.

For single phase simulations free surface influence is neglected, being included only for multiphase simulations (by using VOF model) where surface tension, contact angle, adherence properties and gravity may be considered. Unlike for the oscillatory squeeze flow, for the simple squeeze flow, both pressure distribution and pressure isolines do not indicate the presence of end effects when using the transient approximation (see. [Figures 4.31 – 4.33](#)). A very good correlation is found between the upper and lower wall pressure distributions and the pressure isolines are not deformed. For constant velocity squeeze flow the influence of free surface shape has been investigated also by using the quasi-steady approximation and geometries with different shapes of the pressure outlet zone ([Annex 5](#)).

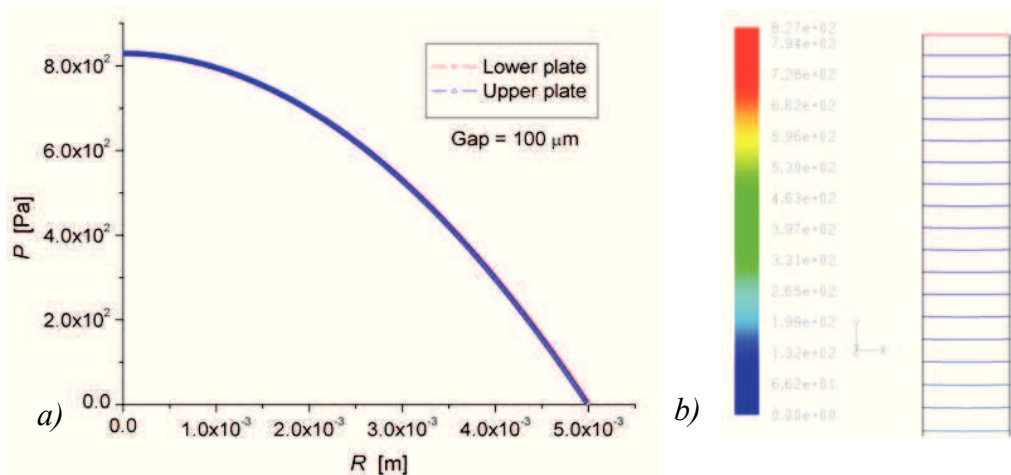


Fig. 4.31. Pressure distribution on upper and lower walls (a) and pressure isolines in the gap (b) for the transient numerical solution of constant velocity squeeze flow, mineral oil sample at $\dot{h} = 0.1 \text{ mm/s}$, $h = 0.1 \text{ mm}$.

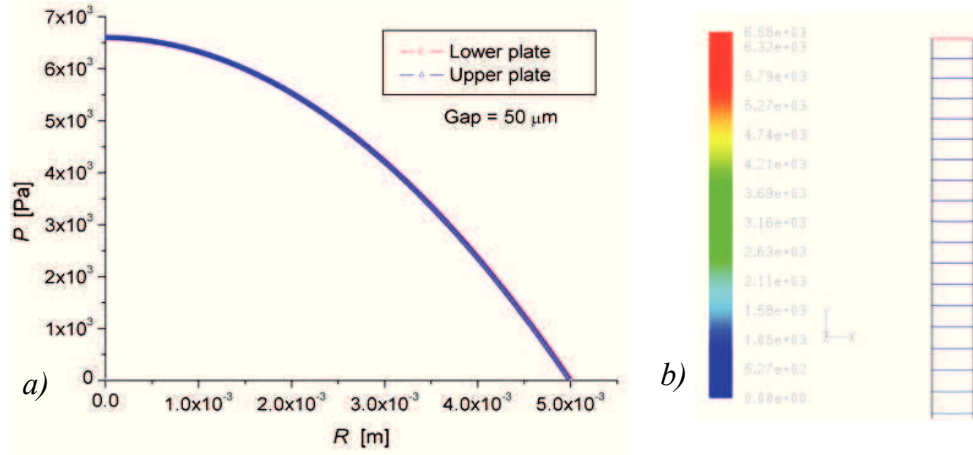


Fig. 4.32. Pressure distribution on upper and lower walls (a) and pressure isolines in the gap (b) for the transient numerical solution of constant velocity squeeze flow, mineral oil sample at $\dot{h} = 0.1 \text{ mm/s}$, $h = 0.05 \text{ mm}$.

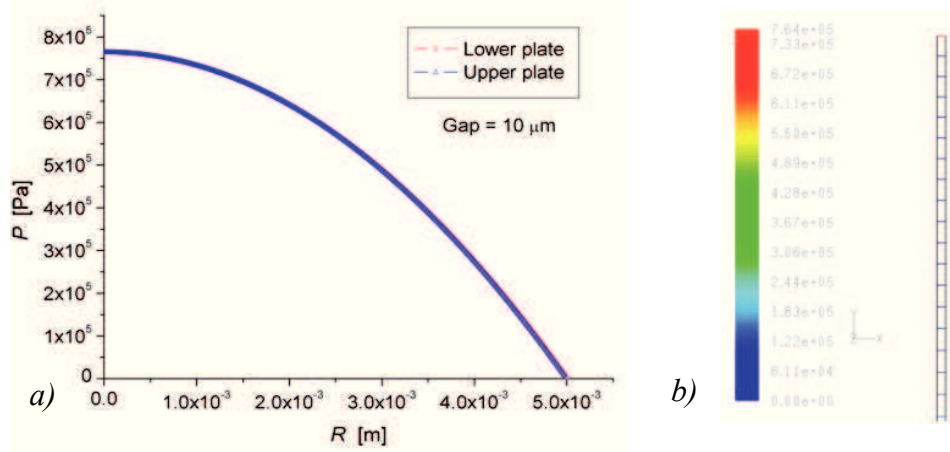


Fig. 4.33. Pressure distribution on upper and lower walls (a) and pressure isolines in the gap (b) for the transient numerical solution of constant velocity squeeze flow, mineral oil sample at $\dot{h} = 0.1 \text{ mm/s}$, $h = 0.01 \text{ mm}$.

The end effects influence cannot be analyzed using a single fluid phase in this case, neither a quasi-steady approximation (Annex 5), for this investigations being necessary a multiphase simulation of the motion. The computed force values and pressure distribution on the upper plate are not affected by the slopes of the imposed free surfaces.

4.4.3. Multiphase modeling of simple squeeze flow

Starting with a geometry with imposed boundary conditions which corresponds exactly with the real experimental model (Figure 4.34.a), in which the surrounding area of the gap has two pressure outlet zones (boundary condition p_0) the flow give rise to an abnormal flow direction of the air phase between the two outlet zones, even at very small squeezing velocities ($\dot{h} = 0.01 \text{ mm/s}$). In the absence of gravitational effect or surface tension, the increase of velocity magnitude of the phases (reaching 3.91 m/s) and the unrealistic

deformation of the interface, requires the change of the initial imposed boundary conditions. The simulation was repeated using a geometry with a surrounding domain (air phase volume) that has only a single outlet area, increasing also the squeezing velocity to minimize the capillary effects and to induce a principal direction of the flow. Also in this case the limitations of the GR scheme leads to very large values of the *Courant Number* (CN) and the convergence is not obtained (Figure 4.34.b1).

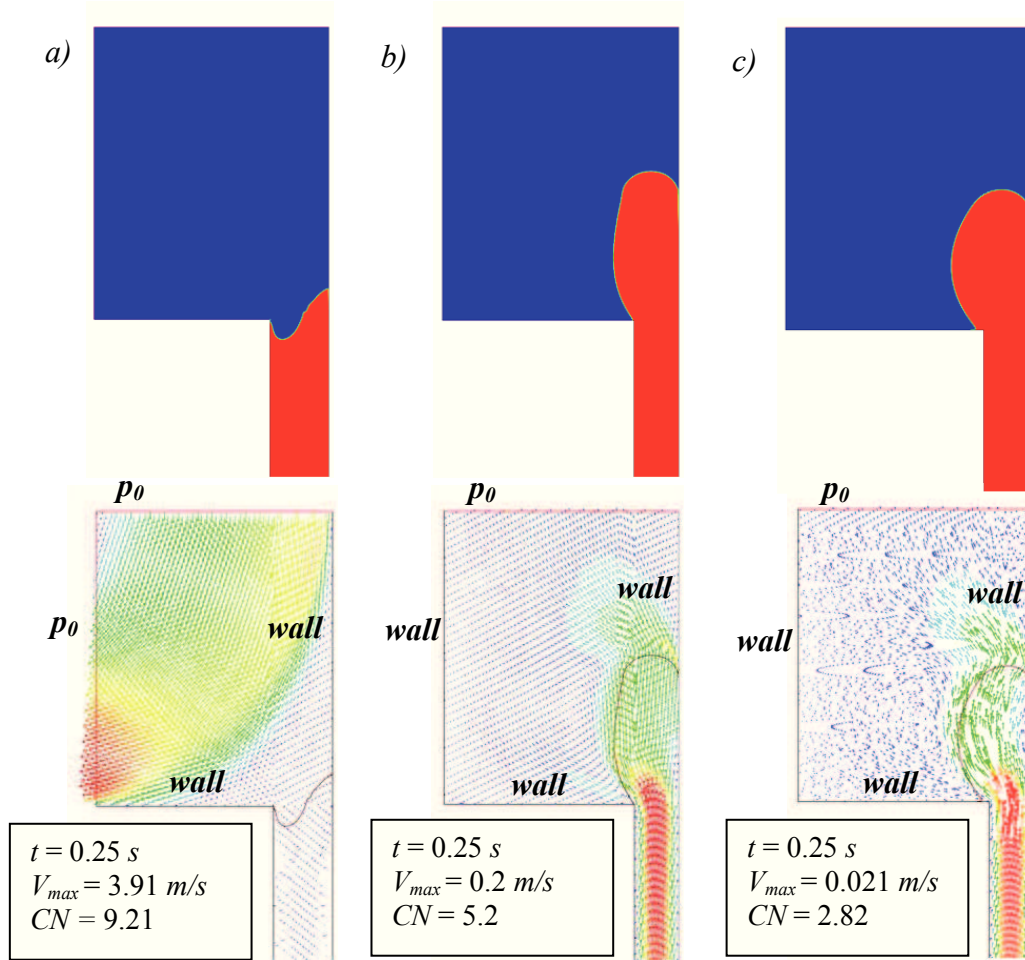


Fig. 4.34. Oil-air interface and velocity vectors obtained numerically for the constant velocity squeeze flow using VOF2 geometry with different boundary conditions: two pressure outlet zones - red line (a) and a single outlet zone (b, c). The simulation settings imply the use of Pressure-Based solver with GGNC model and GR (a, b) and CICSAM (c) interface tracking methods. The simulation is performed without taking into account gravity, surface tension or contact angle.

However by using the CICSAM scheme for interface tracking the convergence is obtained (this scheme supports larger values of the CN), the shape of the free surface and velocity vectors for both of fluid phases being presented in Figure 4.34.b2. Thus, for all numerical simulations presented in this paragraph the high resolution scheme (CICSAM) has been used, with the *Pressure-Based* solver and the GGNB method for computing the local gradients.

In [Figure 4.35](#) the influence of different contact angle values on the evolution of the interface is presented, for the simple squeeze flow, at different simulation times corresponding to a reduction of the film thickness. The results are obtained in the absence of the gravitational effects and surface tension (case 1) and in the presence of gravity and surface tension (cases 2 - 4), with different imposed contact-angle values on the boundaries.

For the simulations that include the presence of the fluid surface tension ($\sigma_s = 0.01 \text{ N/m}$), the dynamic contact angle imposed for each solid wall are presented in [Table 4.3](#). The variation of imposed contact angle aims the investigation of the free surface evolution during the squeeze flow and the advance of the fluid interface on the solid boundaries, considering the important applications of a possible control of the wetting properties (the no-slip or adherence condition is considered).

Table 4.3. Imposed values for the dynamic contact angle at solid-fluid interface (θ), used for the multiphase numerical simulation of constant velocity squeeze flow.

Case	C2	C3	C4
Boundary Description	θ [°]	θ [°]	θ [°]
Lower wall	30	30	30
Upper Wall	30	30	30
Lower external wall	90	30	30
Margin	90	90	30
External Wall	90	90	90

A first comparison between cases C1 and C2 evidenced that, in the absence of gravity and surface tension the fluid accumulates at the edge of the testing gap. Under gravitational effects the interface starts to wet the lower wall, its advance being limited by the imposed boundary condition on the lower wall.

Meanwhile the surface tension leads to a rise of the squeezed fluid on the margin (corresponding to the real plate edge), the fluid actually wets this surface due to capillary action and plate displacement. By imposing a lower contact angle on the lower external wall (case C3) we notice a faster onward motion of the interface towards the exit of the flow domain without a decrease of the film ascension on the margin.

The shape of the free surface and its development in time completely changes when the contact angle is also reduced to 30° (case C4). The shape obtained trough the C4 simulation can be correlated with the one observed during experimental investigations ([Paragraph 5.4.3](#)).

For D1-D3 simulations the parameters used for the C4 case were kept, but the slip condition on the lower wall and lower external wall has been changed in order to investigate the influence of slip phenomena on the force distribution and on free surface's evolution.

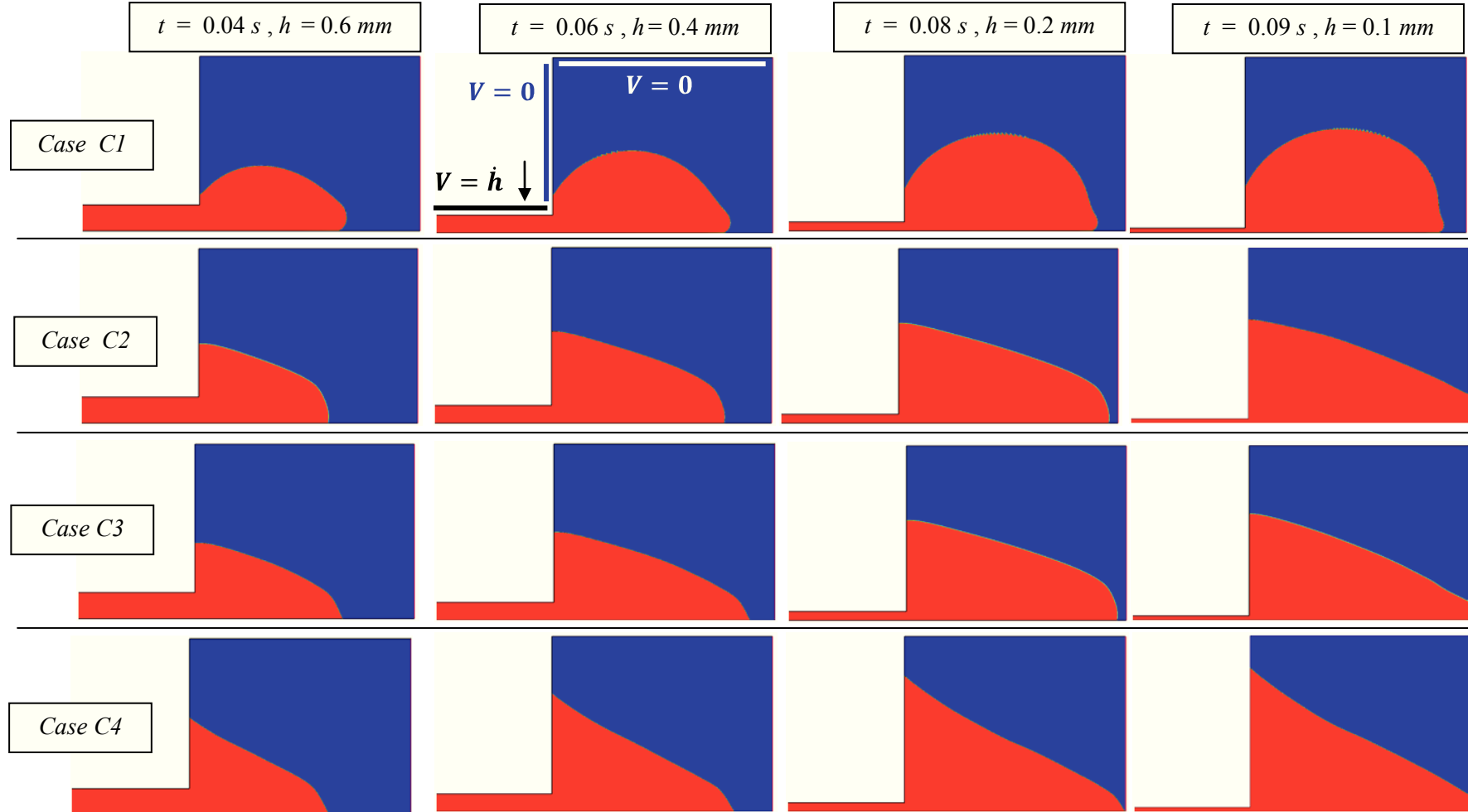


Fig. 4.35. The development of oil-air interface obtained trough numerical simulation of constant velocity squeeze flow ($\dot{h} = 1 \text{ mm/s}$) without gravitational effects and surface tension (case 1) and in their presence, using different values of the imposed contact angles (case 2,3,4).

Thus for case D1 the no-slip condition is imposed, for case D2 the a slip condition is imposed for the external lower wall by imposing a very small value of the wall shear stress ($\sigma^* = 0.0001 \text{ N/m}$), inducing a partial slip condition for the entire domain, and for case D3 the slip condition is extended on the whole lower surface (lower wall and external lower wall) inducing almost a perfect slip condition of the fluid at the wall.

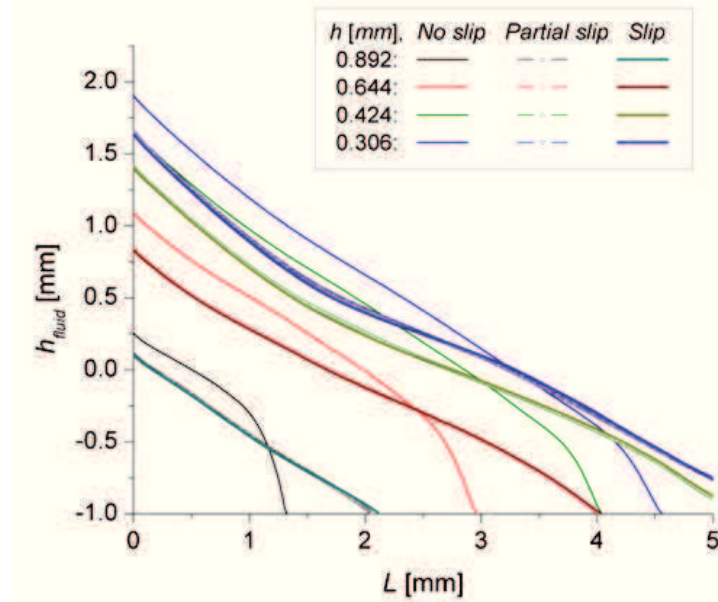


Fig. 4.36. Development of oil-air interface obtained trough numerical simulation of constant velocity squeeze flow ($\dot{h} = 1 \text{ mm/s}$) for different wetting conditions imposed on the lower walls, (corresponding to case D1, D2 and D3 – see [Figure 4.37-4.38](#)).

By tracking the development of the interface and the onward motion of the fluid on the lower wall, respectively fluid ascension on the margin it can be noticed that the presence of the slip condition leads to a significant change of the interface shape and a quicker advance of the fluid towards the exit of the flow domain. Equally the maximum height reached by the fluid rising on the margin is reduced once the partial-slip or perfect slip conditions are imposed (see. [Figures 4.36 - 4.38](#)).

The shape of the interface obtained trough numerical simulations (especially for the partial slip condition) corresponds to the one observed during experimental investigations ([Figures 4.37-4.38](#)). The differences may due to the dimensions of the external lower wall used in the numerical simulation (which is shorter than for the experimental geometry, see [Paragraph 4.2](#)) but also to the limitation of fluid surface tension $\sigma_s = 0.01 \text{ N/m}$.

The analytical expression of the maximum height of a liquid column rising on a wall (see [Paragraph 2.5.1](#)) assumes that the lifting velocity id due exclusively to the surface tension force that act on the interface.

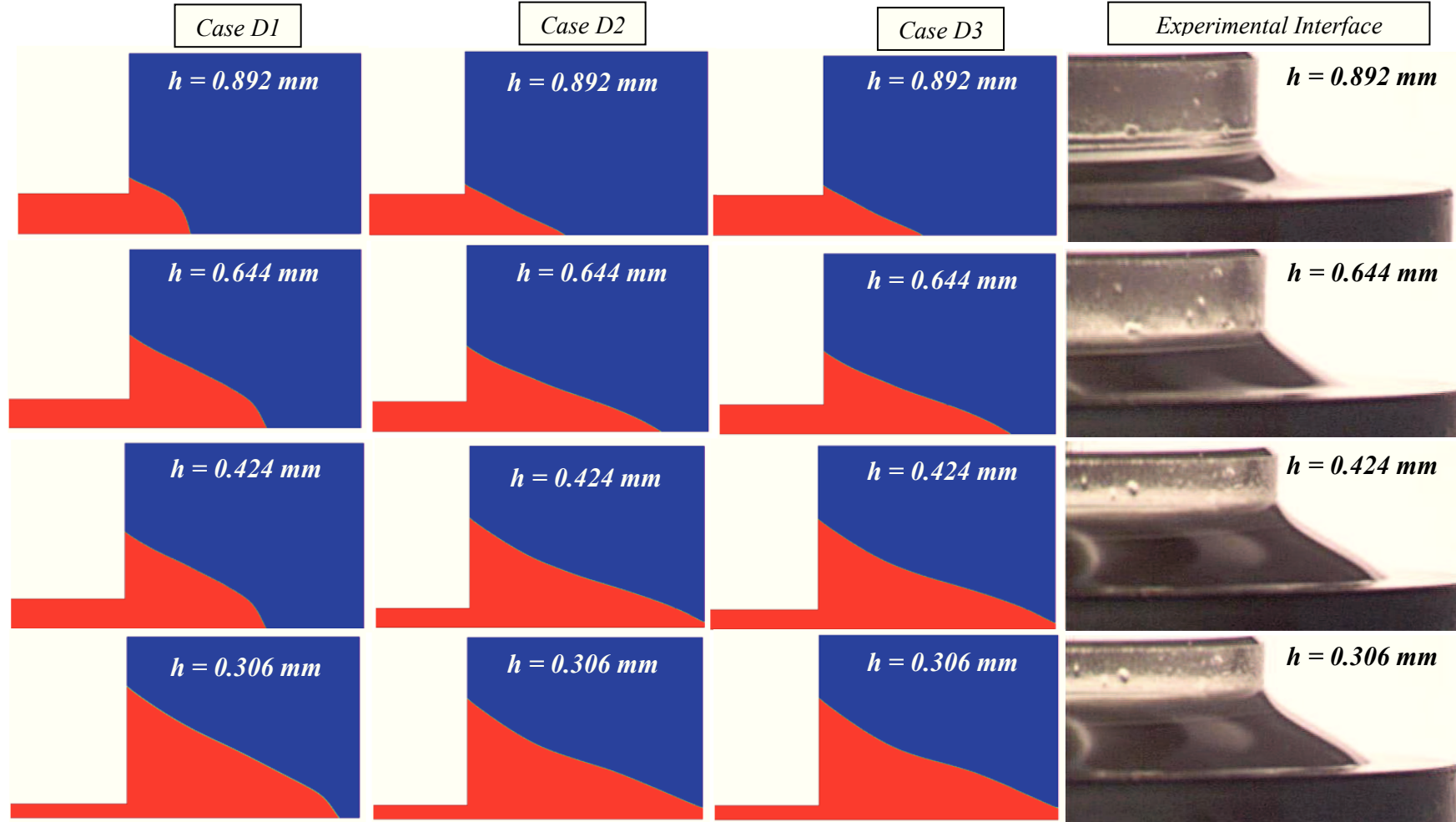


Fig. 4.37. The development of oil-air interface obtained trough numerical simulation of constant velocity squeeze flow ($\dot{h} = 1 \text{ mm/s}$), in the presence of gravity and surface tension, using different slip conditions: no slip condition on all walls (case D1); partial slip, only on the external lower wall (case D2); almost perfect slip on the entire lower surface (case D3). Comparison with the experimental visualizations for $h \in [0.892 \div 0.306] \text{ mm}$.

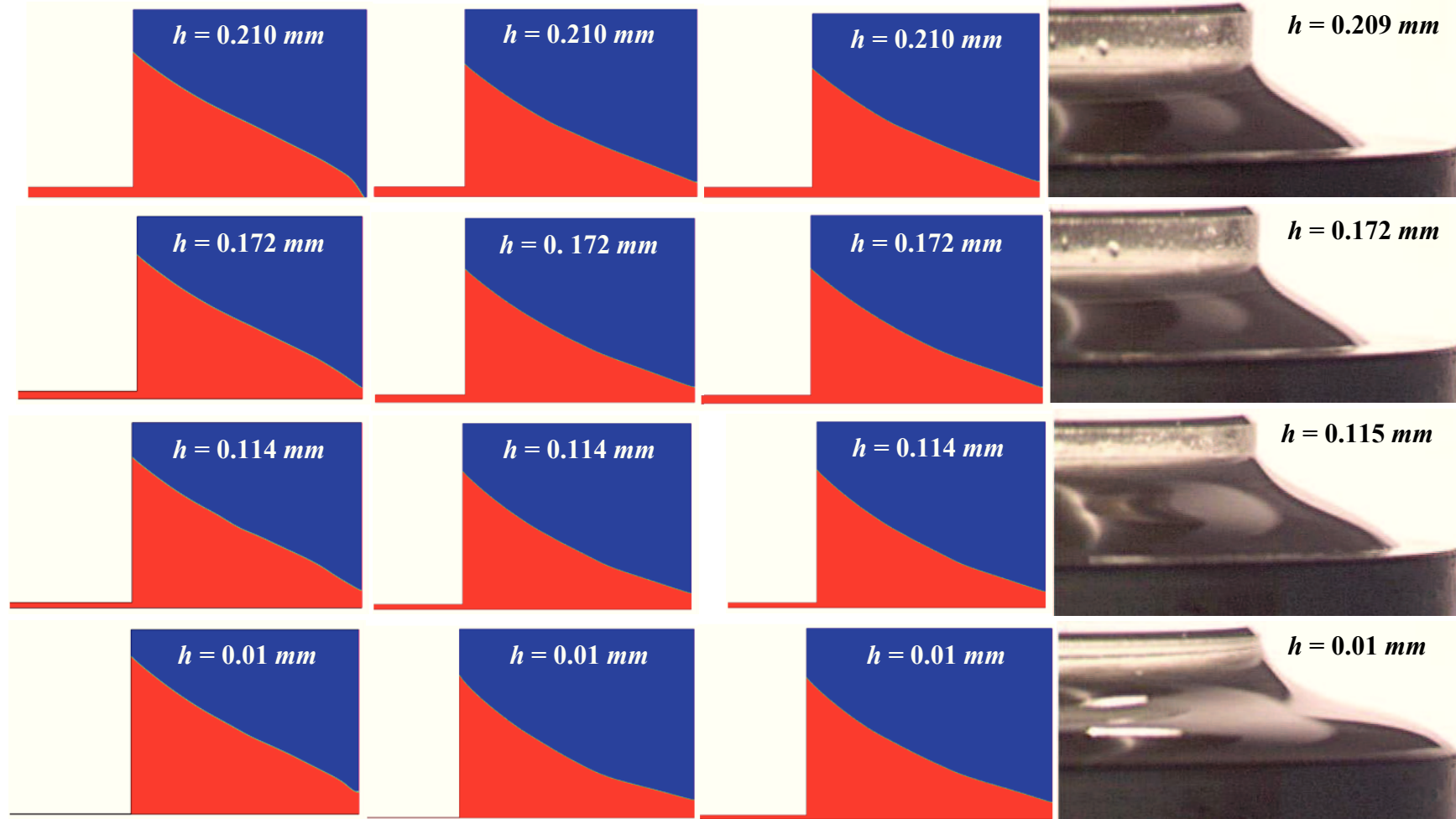


Fig. 4.38. The development of oil-air interface obtained trough numerical simulation of constant velocity squeeze flow ($\dot{h} = 1 \text{ mm/s}$), in the presence of gravity and surface tension, using different slip conditions: no slip condition on all walls (case D1); partial slip, only on the external lower wall (case D2); almost perfect slip on the entire lower surface (case D3). Comparison with the experimental visualizations for $h \in [0.210 \div 0.01] \text{ mm}$.

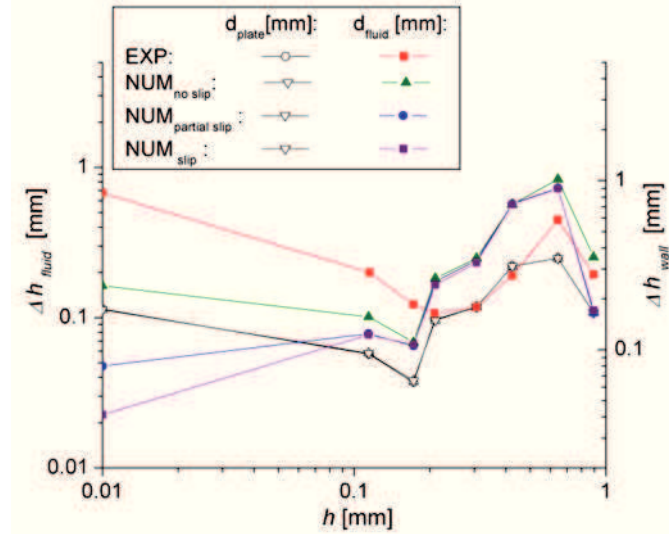


Fig. 4.39. The variation of the upper plate displacement Δh_{wall} and the advance of the fluid column on the margin Δh_{fluid} with fluid film thickness. Comparison between experimental measurements and numerical simulation results for the constant velocity squeeze flow ($\dot{h} = 1 \text{ mm/s}$), using different wetting conditions (see case D1, D2 and D3).

In comparison with the analytical formulation of the free surface that wets the margin, the simulations are always indicating superior values of the maximum height of the liquid column, regardless the wetting property of the lower walls (see Figure 4.39 – 4.40). This fact may due to the descending displacement of the upper wall that induces a supplementary rising velocity of the fluid, during the squeeze motion.

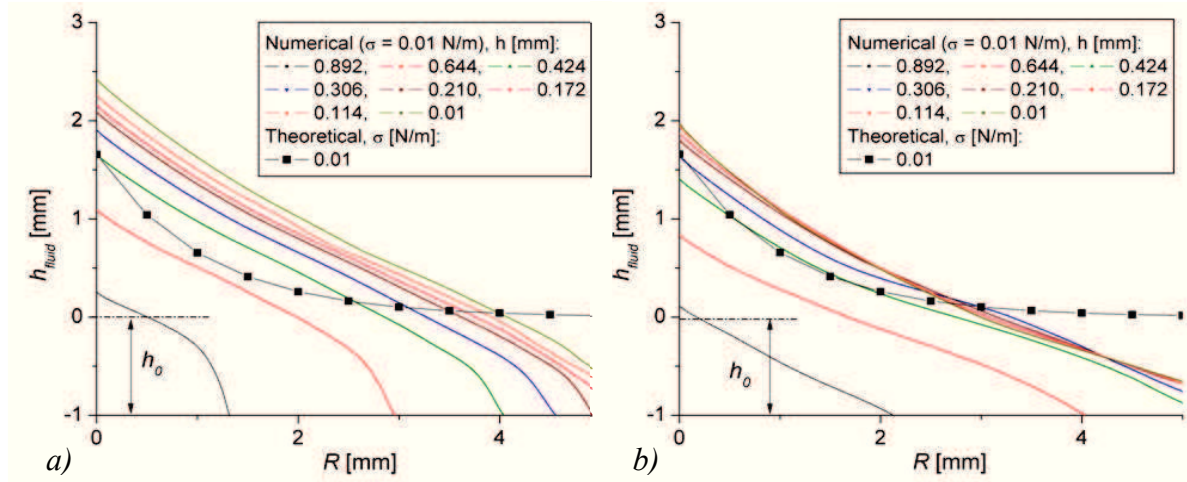


Fig. 4.40. The development of oil-air interface obtained trough numerical simulation of constant velocity squeeze flow ($\dot{h} = 1 \text{ mm/s}$) in comparison with the analytical predictions. Results are obtained in the presence of gravity and surface tension, using different adherence conditions: perfect adherence (a); almost no adherence (b).

Moreover the radial and axial velocity distributions (Figure 4.41, respectively 4.42) in the gap are influenced by the presence of the perfect slip condition. Normal force variation with fluid thickness is presented in Figure 4.43.

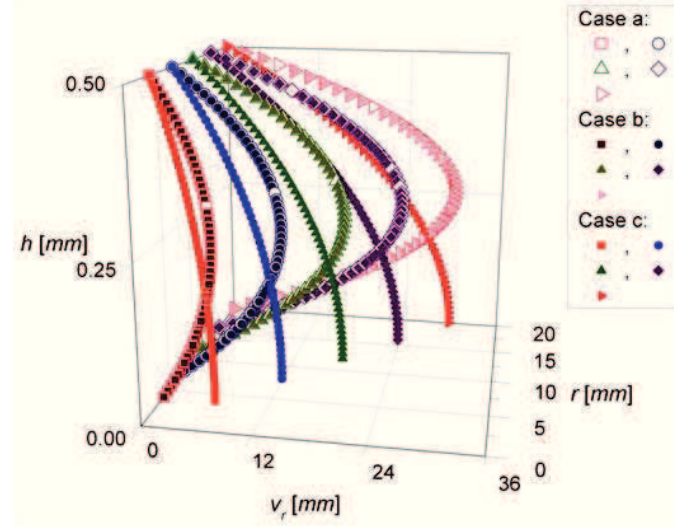


Fig. 4.41. Radial velocity distribution in the gap, for the mineral oil sample, at a constant squeezing velocity of $\dot{h} = 0.01 \text{ mm/s}$ and $h = 0.1 \text{ mm}$. Comparison between numerical simulations: single phase quasi-steady approximation (case a); transient multiphase approximation with no slip condition (case b), transient multiphase approximation with perfect slip condition (case c).

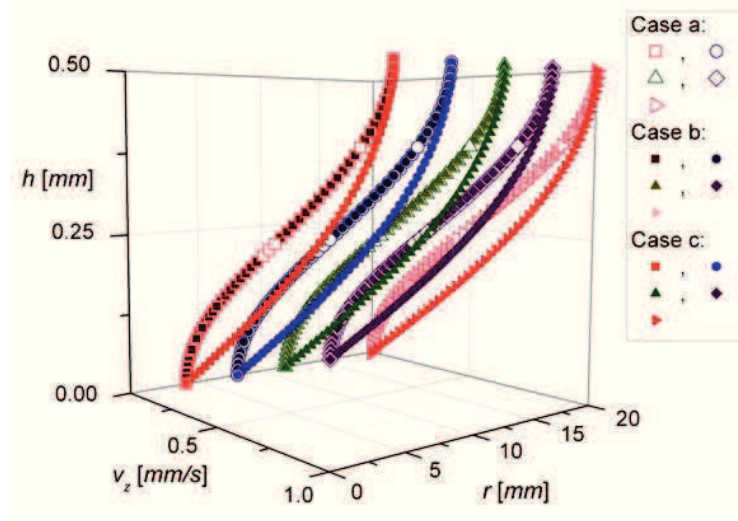


Fig. 4.42. Axial velocity distribution in the gap, for the mineral oil sample, at a constant squeezing velocity of $\dot{h} = 0.01 \text{ mm/s}$ and $h = 0.1 \text{ mm}$. Comparison between numerical simulations: single phase quasi-steady approximation (case a); transient multiphase approximation with no slip condition (case b), transient multiphase approximation with perfect slip condition (case c).

It can be observed that the presence of both gravity and surface tension during multiphase numerical simulations leads to a decrease of the force values in comparison with the single phase simulation of the phenomenon.

The computed values however are in concordance with the ones measured during experimental investigations. By imposing a no slip condition on the entire lower surface defining the geometry leads to a significant decrease of the normal force values, framing the experimental measurements somewhere between no slip and almost perfect slip conditions.

This may disclose the occurrence of a partial slip of the oil at the plate during experimental investigations. It must be also considered that the numerical simulations were

performed with a imposed surface tension smaller than the real one ($\sigma_{simulation} = 0.01 \text{ N/m}$; $\sigma_{oil} \sim 0.04 \text{ N/m}$) due to the numerical code limitations. The difference between theoretical results (analytical formulation and numerical simulations) and the experimental measurements can due also to a limitation of the force transducer.

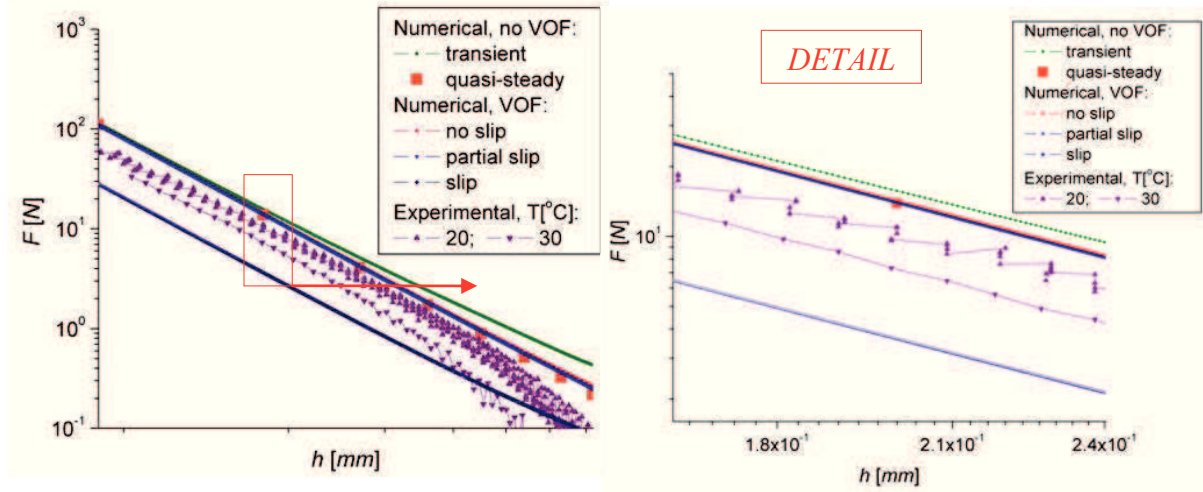


Fig. 4.43. Normal force distribution for constant velocity squeeze flow ($\dot{h} = 1 \text{ mm/s}$) of mineral oil sample. Comparison between numerical simulations results in both single and multi phase modes and the experimental measurements performed at different testing temperatures.

However, normal force distribution, fluid column height on plate margin, the onward motion of the interface on the lower plate and even the velocities distributions are being influenced by the initial shape of the free surface. Therefore, in order to obtain a better correlation between numerical simulations and experimental measurements of visualizations it is necessary to initialize the simulation with a geometry for which the free surface shape must correspond to the one observed experimentally.

4.5. COMPARISON BETWEEN NUMERICAL SOLUTIONS: GENERALIZED REYNOLDS EQUATION AND NAVIER-STOKES EQUATIONS FOR OSCILLATORY SQUEEZE FLOW

The most common analytical formulation of squeezing phenomenon (pressure distribution, squeeze force, velocity distributions) derives from the *Reynolds Approximation for Lubrication*, as shown in Paragraph 3.2. However the commercial CFD code *Fluent* solves *Navier-Stokes Equations* in order to determine squeeze flow parameters.

In Paragraph 4.3.1 a comparison has been made between numerical simulation results and analytical prediction, comparison that disclose a significant influence of the inertial term, that is included by the *Navier-Stokes Equations* but neglected by the analytical formulation. In this paragraph a second numerical code is used to compute squeeze flow parameters

(especially squeezing force), by using a *Generalized Reynolds Equation* to solve the oscillatory squeeze flow for both Newtonian and Generalized-Newtonian fluids.

The finite elements numerical code is written in **Fortran 95, v. 5.7** software and the simulations are preformed by using a dedicated computational platform named **Winteracter 7.10**, which allows the compilation, linking and simulation of the code.

The *Generalized-Reynolds Equation* used is [28]:

$$\frac{\partial}{\partial r} \left(r \frac{\partial p}{\partial r} G_e \right) = -r \dot{h} \quad (4.10)$$

with fluid velocity given by

$$v_r = \frac{\partial p}{\partial r} \left(I_1 - \frac{J_1}{J_0} \cdot I_0 \right) \quad (4.11)$$

where $G_e = J_2 - \frac{J_1^2}{J_0}$ and $I_0 = \int_0^h \frac{d\xi}{\eta(z)}$; $I_1 = \int_0^z \frac{\xi \cdot d\xi}{\eta(z)}$; $J_0 = \int_0^h \frac{dz}{\eta(z)}$; $J_1 = \int_0^h \frac{z \cdot dz}{\eta(z)}$; $J_2 = \int_0^h \frac{z^2 \cdot dz}{\eta(z)}$.

The determination of this equation form *Navier-Stokes System* is detailed in [Annex 6](#). The flow domain is meshed using finite elements (and shape functions) and the “meshed” equations use a first order finite elements discretization.

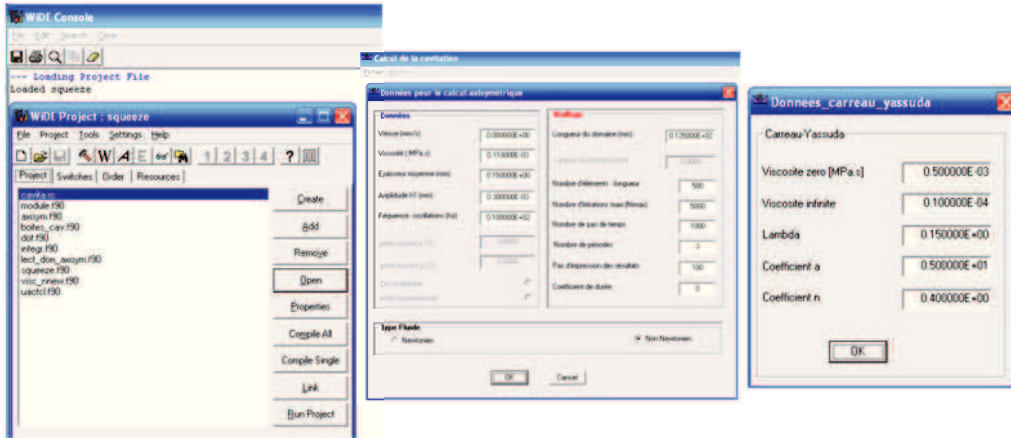


Fig. 4.44. Winteracter console and the affichage of input data for numerical simulations with the personalized code created in Fortran.

Multiple simulations have been performed for both *Newtonian* and *Generalized-Newtonian* fluids, the results being compared with the analytical formulations and numerical simulations results obtained with *Fluent* code in previous paragraphs

.The initialization parameters are stored in a data file, that is read (and modified if necessary) at the beginning of each simulation (see [Figure 4.44](#)). The data file contains various information such as: (i) geometry definition (initial film thickness, plate radius); (ii) displacement profile (frequency, amplitude, number of oscillating periods); (iii) computational parameters (maximum number of iterations, number of time steps); (iv) fluid properties (Newtonian viscosity or *Carreau-Yasuda* parameters).

The computational algorithm is the following:

Run (start the program)

Reading simulation parameters: the data file

Computation initialization

Start time step

For every time step

If “Newtonian” then call “Newtonian module”

Solve Reynolds for Newtonian viscosity given

End if

For “non-Newtonian” do

Solve Reynolds for η_0 given

Compute complete integrals I_1, I_2, J_1, J_2 on film thickness

Compute viscosity

End do

Solve Reynolds with the new viscosity

Compute: pressure distribution, squeezing force

Write results files: pressure, computed force, film thickness variation

End time step

Repeat for the imposed number of time steps

End

4.5.1. Results obtained for Newtonian fluids

The simulations were performed by using the rheological properties of mineral oil sample ($\eta_0 = 0.15 \text{ Pa.s}$) at different input parameters (film thicknesses, oscillatory frequencies and oscillatory amplitudes).

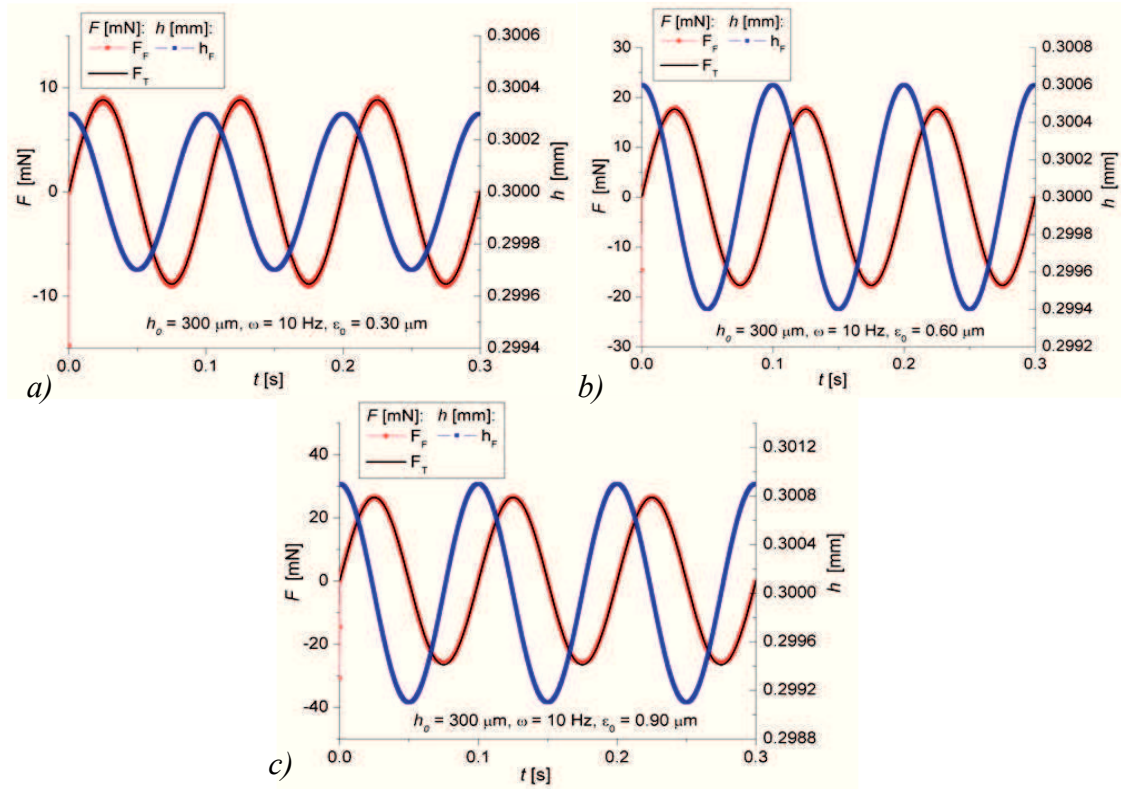


Fig. 4.45. Comparison between numerical simulations results obtained with FORTRAN code and analytical predictions. Oscillatory squeeze flow of mineral oil sample, $h_0 = 300 \mu\text{m}$, $\omega_s = 10 \text{ Hz}$ and: $\varepsilon_0 = 0.30 \mu\text{m}$ (a); $\varepsilon_0 = 0.60 \mu\text{m}$ (b); $\varepsilon_0 = 0.90 \mu\text{m}$ (b).

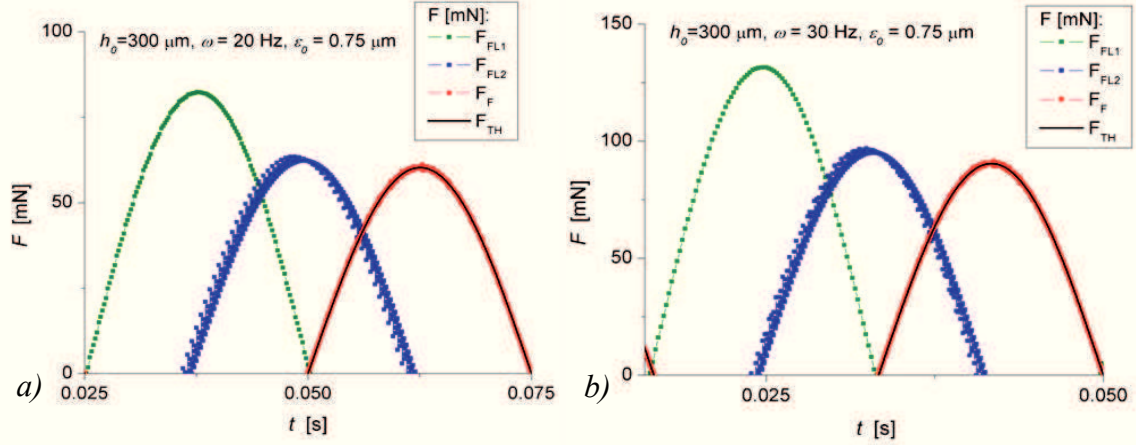


Fig. 4.46. Comparison between numerical simulations results obtained with FORTRAN code (red dots), analytical predictions (black line) and numerical simulations obtained with FLUENT code for a larger (green dots) and a smaller time step (blue dots). Oscillatory squeeze flow of mineral oil sample, $h_0 = 300 \mu\text{m}$, $\varepsilon_0 = 0.75 \mu\text{m}$, and $\omega_s = 20 \text{ Hz}$ (a); $\omega_s = 30 \text{ Hz}$ (b).

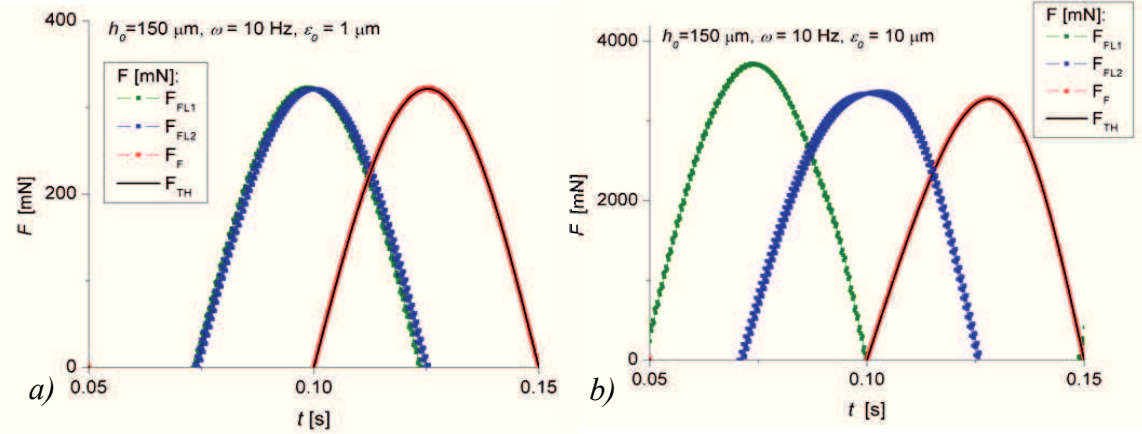


Fig. 4.47. Comparison between numerical simulations results obtained with FORTRAN code (red dots), analytical predictions (black line) and numerical simulations obtained with FLUENT code for a larger (green dots) and a smaller time step (blue dots). Oscillatory squeeze flow of mineral oil sample, $h_0 = 150 \mu\text{m}$, $\omega = 10 \text{ Hz}$ and: $\varepsilon_0 = 1 \mu\text{m}$ (a); $\varepsilon_0 = 10 \mu\text{m}$ (b).

A first comparison between numerical results and analytical predictions disclose a very good agreement, regardless the input parameters (as shown in Figure 4.45). the computed phase angle corresponds to a pure viscous behavior. By comparison with the numerical simulations presented in Paragraph 4.3.1 (simulations performed with Fluent code), the results obtained with *Fortran* code are smaller. Actually, being almost identical with the analytical predictions, the relative errors presented in Figures 4.9 – 4.13 between *Fluent* simulations results and analytical model, can be considered, as the same, between *Fluent* simulation results and *Fortran* simulation results.

4.5.2. Results obtained for Carreau-Yasuda model

When using the *Generalised Reynolds Equation* to predict the behavior of a *Carreau-Yasuda* fluid, (see Table 4.2, PAA3 parameters), in oscillatory squeeze flow (Figure 4.48),

PAA3 parameters), the results are indicating a phase angle characteristic to pure viscous fluids (as predicted by Fluent).

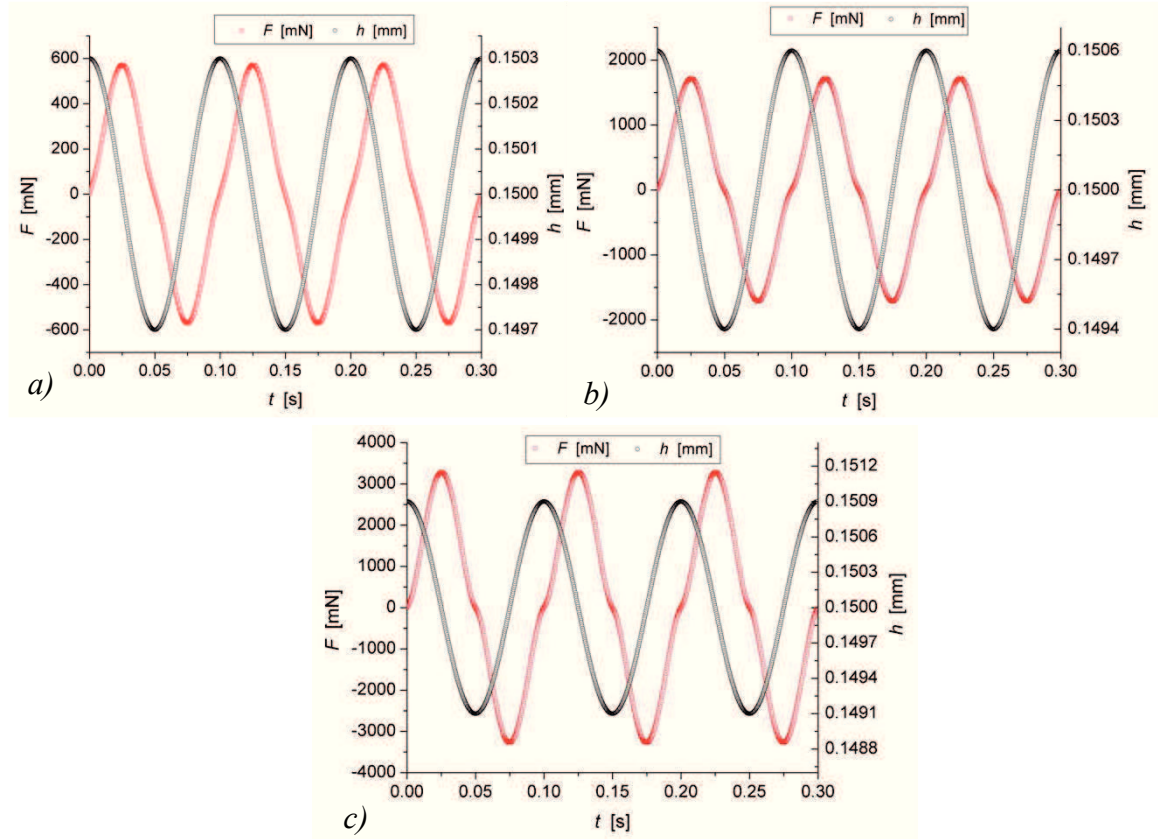


Fig. 4.48. Results obtained with Fortran Code, for a Carreau-Yasuda fluid in oscillatory squeezing flow ($h_0 = 150 \mu\text{m}$, $\omega_s = 10 \text{ Hz}$ and different ε_0). The parameters (PAA3) are indicated in Table 4.2.

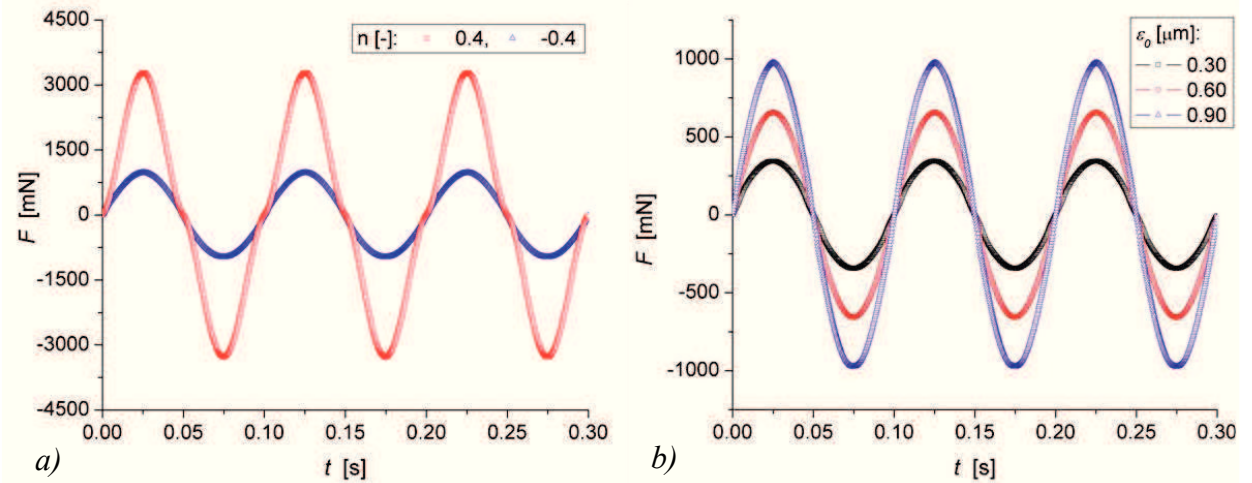


Fig. 4.49. Results obtained with Fortran Code, for a Carreau-Yasuda fluid in oscillatory squeezing flow ($h_0 = 150 \mu\text{m}$, $\omega_s = 10 \text{ Hz}$). The parameters (PAA3 and PAA 4) are indicated in Table 4.2. Comparison between a positive and negative flow index of the constitutive model, at $\varepsilon_0 = 0.90 \mu\text{m}$ (a) and force signals obtained for a negative flow index and different oscillatory amplitudes.

However the deformation of the signal can be observed, due to the pseudoplastic character of the model. Also, the deformation of the signal increases with oscillatory amplitude (similar to the results obtained with *Fluent* code). In comparison with the numerical

results obtained with *Fluent* code, *Fortran* code predicts much larger values of the normal squeezing force. The differences between the force signal deformations obtained using the two numerical codes, may be due to inertial effects that are only taken into account by the Navier-Stokes equations (used by *Fluent* code).

The non-monotonous behavior, given by the *Carreau-Yasuda* model with a negative flow index (Figure 4.49), is not emphasized when using *Fortran* code. The force signal is less deformed for a negative flow index and force amplitude is smaller (when keeping the same parameters of the constitutive model and changing only the flow index, see Table 4.2, PAA4 parameters).

4.6. CONCLUSIONS

Numerical investigations of squeeze flow have been performed using commercial code *Fluent* using rheological parameters of some fluids which have been also investigated experimentally in order to obtain a correlation of the results. In the case of oscillatory squeezing flow the correlation between numerical simulation results with the analytical predictions lead to the determination of a limited validity domain for the analytical expression of squeeze force, depending on film thickness, the oscillatory frequency and the oscillatory amplitude of the imposed displacement profile.

The differences between the two theoretical solutions may be due to the dynamics of the complex squeeze motion, especially the inertial term, taken into account by the *Navier-Stokes* system of equations solved by *Fluent* but neglected when determining the analytical formulation (from *Reynolds Lubrication Approximation*). Furthermore, the influence of computational time step imposed by the user was investigated. For smaller time steps used in simulation, the values of the computed force decreased, approaching the theoretical predictions but being always superior to them.

The differences between the *Navier-Stokes* formulation for squeezing phenomena and the *Reynolds Approximation for Lubrication* are emphasized in Paragraph 4.5.1, where a second code is used for the computation of normal force in oscillatory squeeze flow. The results obtained with the code using a *Generalized-Reynolds Equation* are almost identical with the analytical predictions therefore all the affirmations made above are valid also in this case.

In the case of constant velocity squeeze flow there were used two numerical methods to solve the unsteady motion: a transient deformable-mesh solution and a quasi-steady approximation of the flow. A very good correlation was found between the two

approximations from both qualitative (velocity distributions on radial and axial directions) and quantitative (force values, pressure distribution) point of view. Cause of the good agreement with the analytical predictions and the reduced necessary time of computation, the quasi-steady approximation is recommended for numerical investigations of such complex flow in simple geometries.

End effects were investigated through multiphase flows by using *Volume of Fluids* module of the numerical code. In oscillatory squeezing flow the computations disclose that by considering the influence of gravity and the presence of a fluid-air interface, force values are being reduced in comparison with single phase simulations.

By comparing the single phase and multiphase simulations it has been showed that the free surface shape or the end effects influence on the pressure fields can be emphasized through the deformation of pressure isolines obtained in single phase simulations which correspond to the shape of the interface obtained in multiphase VOF simulations for the same testing conditions. For the multiphase constant velocity simulations the influence of contact angle and adherence conditions were investigated.

The contact angle plays a significant role on interface dynamics, controlling the onward motion of the interface on the lower wall and also the rising height of the fluid column on the geometry margin. By changing adherence conditions from no-slip to an almost perfect slip condition the numerical modeling of the interface can be correlated to the observed experimental free surface.

Normal force distribution, free surface development and also fluid velocity distribution in the gap are influenced by the wetting conditions. The experimental measurements were proved to be framed between numerical results obtained in perfect slip and no slip conditions, therefore a partial-slip at the plate during experimental testing may be considered.

The limitations of the numerical code impose the finding of different methods which can allow the convergence of numerical computations for modeling conditions closer to the real experimental ones.

Therefore this study may continue by initializing the computations in a geometry that free surface corresponds to the free surface observed experimentally, by using larger values of the superficial tension and different architecture of the solid walls by imposing multiple wetting conditions.

Chapter 5. EXPERIMENTAL INVESTIGATIONS OF SQUEEZE FLOW

5.1. EXPERIMENTAL SETUPS AND TESTING PROCEDURES

5.1.1. Devices and procedures for oscillatory squeezing flow

Experimental investigations were performed with a controlled frequency rheometer-MFR 2100 (*Micro Fourier Rheometer*), prototype designed by GBC Scientific Australia. The rheometer's mechanism is based on impressing a multi-frequency signal by upper plate motion in the normal direction. The device is usually capable to give amplitudes up to $25\ \mu\text{m}$, in a frequency range $\omega \in [0.1 \div 50]\text{Hz}$, as long as the force magnitude, located at the lower plate, is kept in a range of force sensor measuring domain $\pm 44\ \text{N}$ [75], [76], [77], [78], [97], [98]. The sample is placed between the two plates, which are assumed to be parallel. The oscillatory motion imposed by the upper plate induces the squeezing of the sample, the corresponding normal force being measured at the lower plate (see. Figure 5.1)

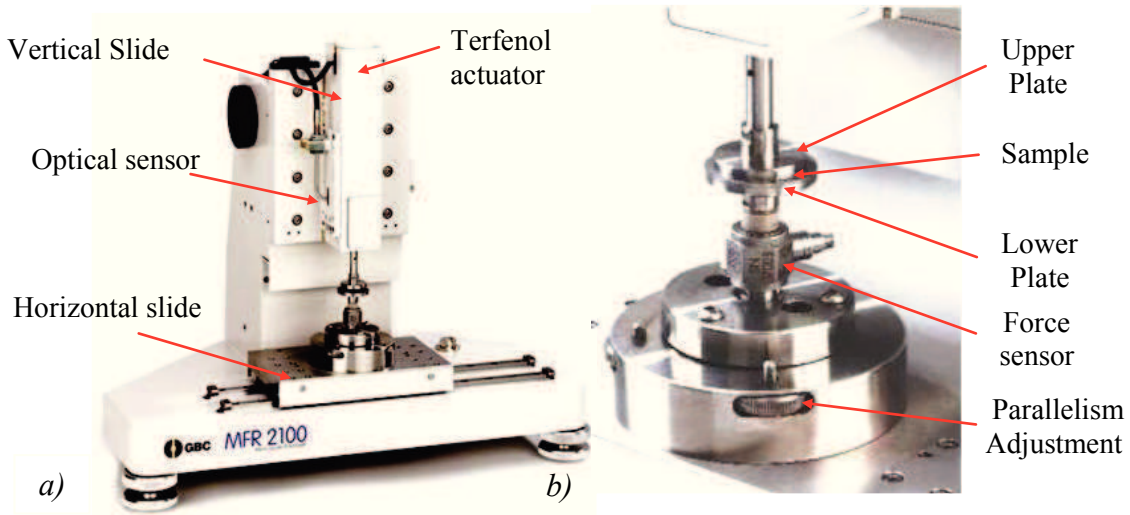


Fig. 5.1. Micro Fourier Rheometer- MFR 2100 (a) and the parallel plate geometry used (25 mm diameter) (b).

5.1.1.1. Mechanism and components

The rheometer has an axially symmetric design that has been chosen to increase its rigidity and eliminate or reduce flexing of the system that could lead to errors in the measured viscoelastic properties of the fluid. All body parts are constructed from stainless steel (see

Figure 5.1). The rheometer mechanism consists of a vertical column (3), mounted on a rigid heavy cast steel base (1), supported all by four leveling feet (2). For an easy adjustment of the base the instrument has a spirit level (17) incorporated on the base upper face (Figure 5.2). A precision motorized slide is provided on both the base and column slides. Geared stepper motors drive both the vertical slide (6) and the horizontal slide (14). The vertical slide mechanism, contained in the vertical column case has also a hand wheel (18) connected to the motor allowing the vertical slide to be moved with a step of $\pm 0.625 \mu m$ manually, or otherwise be controlled automatically through the rheometer's own software.

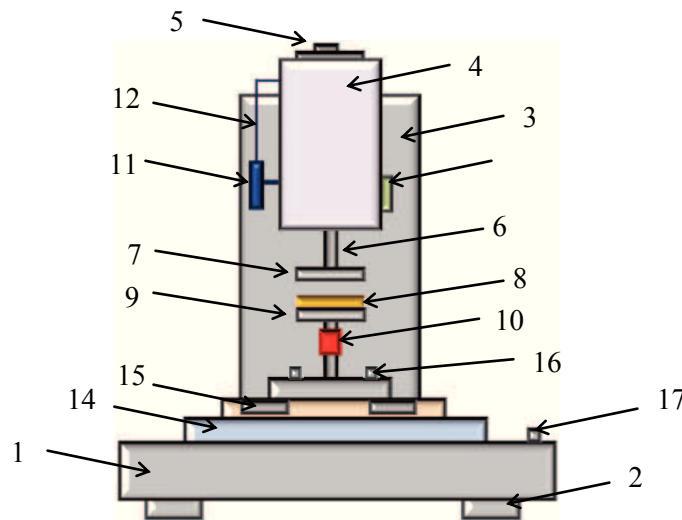


Fig. 5.2. MFR 2100 rheometer – schematic representation.

On the horizontal slide is mounted the lower plate (9) with the load cell (10) beneath it, the parallelism adjustment being possible due to the carriage (6) that has an incorporated universal joint, which allows the inclination of the plate in four direction, by using two little turning wheels (15). Once the plate is considered to be well adjusted, its position is fixed through three fixing screws (16). The vertical column contains the rheometer head mechanism, mounted on the upper plate (7), which can be raised or lowered so that the sample (8) can be placed between the two testing plates and the testing gap set precisely.

A load is generated by a magneto restrictive transducer known as the Terfenol-D driver (4) and its displacement is monitored using an optical sensor (11). The top end of the Terfenol transducer is set to a fixed position by way of a set screw (5). When it is driven its bottom end vibrates and transmits its motion to the leaf spring suspended top plate assembly. The top plate assembly comprises a bush on which a small mirror is mounted. The fiber optic displacement sensor detects the motion of the mirror which is identical to the rheometer upper plate displacement.

The load is measured by the load cell (or strain gauge) located under the lower measuring plate. The lower plate is mounted on a stage that can be slid across the base to permit observation and imaging using a microscope. The load cell supplied with the instrument is a piezoelectric type (PCB 208B01) with an integrated FET impedance transducer to extend its low frequency response. The electronic unit provides for both piezoelectric and strain gauge load cells. Since the sockets carry excitation voltages reference should be made to the technical information before using a load cell other than the one supplied. The load cell supplied is rated for a maximum load of ± 10 lb (± 44.5 N) and may be selected for AC or DC coupling. The load cell is attached to the parallelism device.

Measurements precision is directly dependent on the parallelism between the two plates. The parallelism is adjusted by performing small angular adjustments to the bottom plate. The bottom plate is mounted on a movable ball, which is part of the parallelism adjustment assembly. The ball is normally immobilized by way of a plate secured to the base by three parallelism lock screws. Loosening the front lock screw allows the operator to change the angular position of the ball using the two thumb wheels located on the front of the parallelism assembly. Note that no adjustment is possible while the three lock screws are tight. Loosening one screw frees the adjustments. The aim of the adjustment is to set the gap between the plates precisely using the *ruby spacer* provided with the instrument at four predetermined locations on the rheometer bottom plate [22], [96], [97], [98], [200]. Despite the control loop systems, the rheometer functioning was not satisfactory during the work at this thesis, the measurements being limited both for the range of test frequency and in the range of signal amplitude.

5.1.1.2. The experimental setup

The *MFR D/A-A/D Control* is connected to the MFR computer on which its own software is installed and the instrument motions are controlled (both Terfenol Actuator and vertical/horizontal slides). A laptop is connected to *MFR D/A-A/D Control* through a *National Instruments Data Acquisition Board*, allowing the storage of measured values in simple text files. All measured values are filtered through the *MFR D/A-A/D Control* from both displacement and force sensor (see. [Figure 5.3](#)).

Data acquisition was performed using *National Instrument's* software **Lab View 8.5** and then processed by using **Origin Pro 8.0** software, which allows users to analyze, compute and represent the measured data. Both force (output) and displacement signals (input) were captured through the acquisition setup.

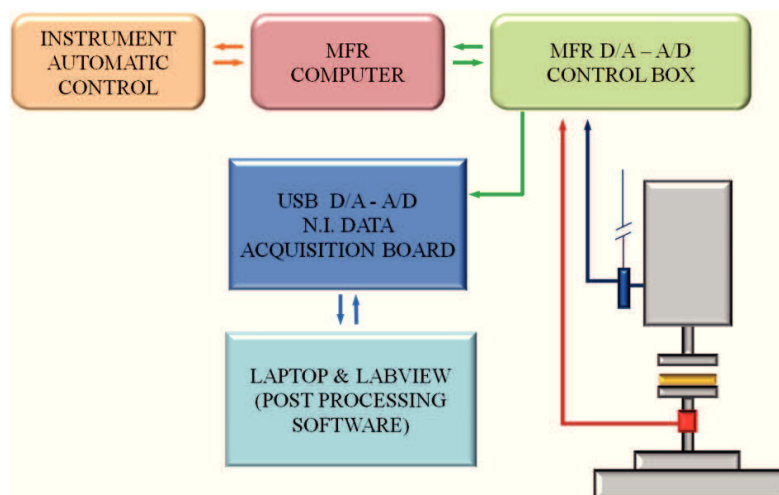


Fig. 5.3. Experimental scheme of the setup used for oscillatory squeezing flow.

5.1.2. Instrumentation and procedures for constant velocity squeezing flow

5.1.2.1. Experimental instrumentation

The simple squeeze motion (constant velocity squeeze flow) has been investigated experimentally using *Physica Anton Paar MCR 301* rheometer with various parallel-plate testing geometries. The experimental setup has been adjusted in order to allow flow visualizations during performed investigations (see Figure 5.4).

Rheometers control is accomplished through *Rheoplus 32* dedicated software, version 3.41, installed on the MCR computer. The rheometer's design allows the investigation of fluids rheology in various shearing tests (simple strain or stress controlled shear tests, oscillatory shear tests, waveform analysis, temperature sweep tests et al.) but also in constant velocity squeeze flow, performed by imposing a constant descending velocity (vertical motion) of the upper plate.

The rheometer's exclusive features include also: (i) the TruGap™ system used for measuring the gap; (ii) a TruRate™ adaptive controller of the sample in rotation and step strain; (iii) the TruStrain™ system used for the accurate control of the imposed deformation or strain due to improved real-time position control oscillation (formerly DSO); (iv) Toolmaster™ system for the automatic recognition of measuring system and accessories; (v) QuickConnect coupling that assures a very easy (one-hand) connection of the measuring geometry on the vertical slide; (vi) variate measuring systems for all kinds of applications (parallel plate of glass or metal, cone-plate, Couette cylinders, double cone for interfacial measurements, et al.); (vii) the T-Ready™ system that reduces waiting times by detecting and

signaling sample temperature equilibration [252][253]. The technical specifications of the rheometer are presented in Table 5.1.

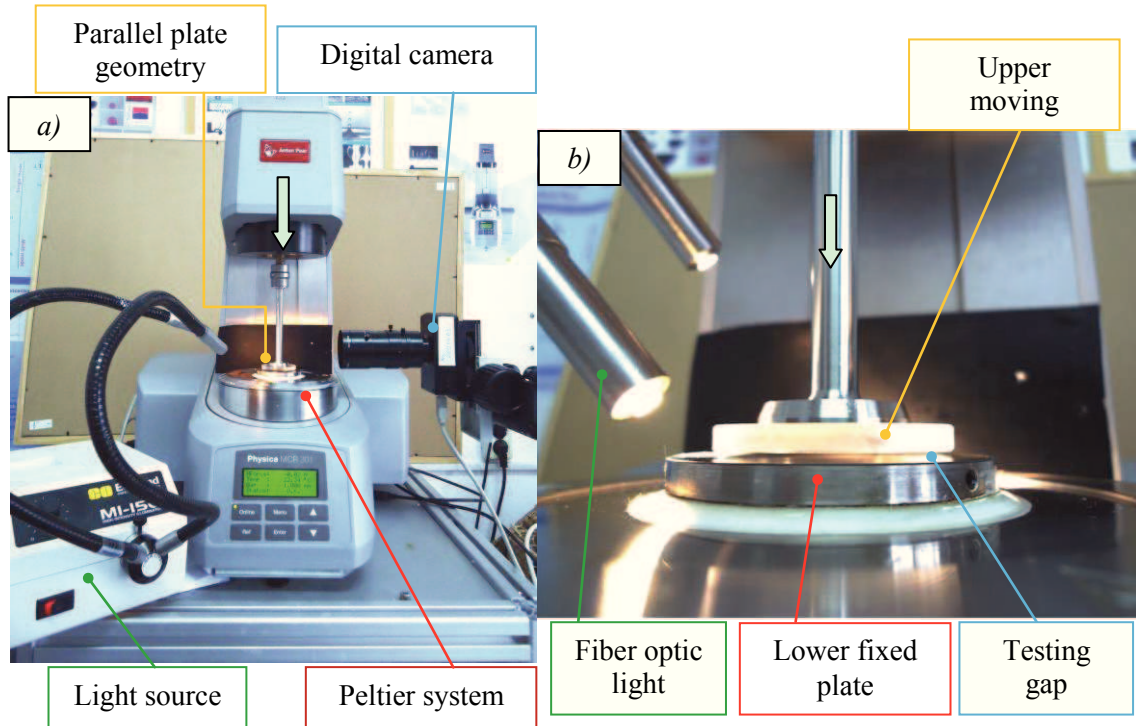


Fig. 5.4. Physica MCR 301 Rheometer: experimental setup (a) and the parallel plate glass geometry (43 mm diameter) (b).

Table 5.1. Technical specifications of Physica MCR 301 Rheometer [252][253].

Technical Data	Unit	Physica MCR 301
Min. torque rotation	μNm	0.05
Min. torque oscillation	μNm	0.01
Max. torque	mNm	200
Torque resolution	nNm	0.1
Angular deflection (set value)	μrad	0.1 to ∞
Angular resolution	μrad	0.01
Min. angular frequency	rad/s	10-5
Max. angular frequency	rad/s	628
Normal force range	N	0.01-50
Normal force resolution	N	0.002
Max. temperature range	$^{\circ}\text{C}$	-150 to +1000

The measuring precision of the normal force sensor is very good 0.002 N, yet the force transducer is limited at a maximum force of 50 N. The experimental setup (Figure 5.4) includes a visualization system composed of a light source with fiber optic light-guiding wires and a Lumenera CCD digital camera, with a frame rate of up to 15 fps. For the experimental investigations of constant velocity squeeze flow there were use various parallel plate geometries (plate-plate glass geometry with 43 mm diameter; plate-plate steel geometry with 25 mm diameter; plate-plate steel geometry with 50 mm diameter) each being adapted at the consistency of the analyzed material: (i) at low viscosity values the use of large diameter

plates is recommend to obtain an increase of the force measuring range at high gaps where the low values of normal force are difficult to record; (ii) for highly viscous fluids smaller diameter plates are use in order to limit the actual contact area on which the force is measured in order to capture the force variation on a larger domain of the film heights (at low heights the force strongly increases ant it's value is limited by the force transducer at 50 N) . Temperature control is archived for the lower fixed plate through the peltier system (based on rhe recirculation of cooling/heating liquid through a special chamber mounted under the lower plate) on a temperature domain of -150 to +1000 °C (see [Figure 5.4 - 5.5](#) and [Table 5.1](#))

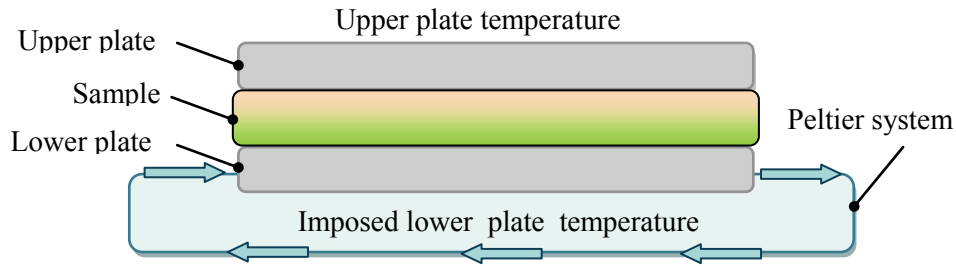


Fig. 5.5. Schematic representation of the Peltier system used temperature control.

The upper plate temperature is not controlled, remaining in contact with the surrounding environment (air temperature). Therefore, even tough film thickness is relatively small ($h_0 < 1\text{ mm}$) the presence of a temperature gradient in the gap may be considered to influence the normal force measurements (implicitly the viscosity measurements in shear testing). However temperature influence is not studied in this thesis but is considered as a possible influence on the performed squeeze measurements. The testing temperature for all performed experimental investigations of the simple squeeze motion is considered to be equal to one imposed for the lower plate.

5.1.2.2. Testing procedure for constant velocity squeeze flow

The fluid is being placed on the lower plate (whom temperature is controlled) and the upper plate is descended until reaching the initial film thickness from which the squeeze test starts. For low viscous fluids, such as mineral oils, glycerin, low concentrated polymer solution et al., the initial film thickness is smaller ($h_0 = 1\text{ mm}$) than the one for high viscous fluids, like honey, cosmetic cream, polysiloxane, gel and other soft solids ($h_0 = 2 - 3\text{ mm}$).

Before reaching h_0 , the upper plate stops its descent to allow the user to trim the excess sample in order to avoid the occurrence of possible end effects. When starting the test the plate descends with the imposed velocity, during a imposed time period correlated with film thickness. During the constant velocity squeeze test the fluid occupying the gap is deformed

and forced outside the decreasing space between the solid plates. The fluid resistance is materialized in the squeezing force acting normally to the plates recorded through the force transducer mounted at the end of upper plate rod on the vertical column.

In this setup both measurements of input (velocity, displacement) and output (force) are performed on the upper plate. Several experiments were performed in order to establish a correlation between the dynamics of the system, force sensor sensitivity and the influence of plates parallelism. The working domain for squeeze tests was established in the range of measured force $F < 20 \text{ N}$ and gaps $h > 50 \mu\text{m}$.

5.2. PURE VISCOUS FLUIDS RHEOLOGY IN OSCILLATORY SQUEEZING TESTS

The rheological characterization was performed for multiple Newtonian fluids with different viscosity coefficients. Initially the tests were performed for a Newtonian mineral oil ($\eta_0 = 0.11 - 0.15 \text{ Pa.s}$ at 20 degrees), in order to establish a valid testing domain where the experimental and theoretical results can be correlated.

This correlation assumes the initial determination of fluids shear viscosity, necessary to approximate analytically the squeezing force (see eq. 3.10 – 3.13). Therefore the fluids were characterized firstly through shear tests by using *Physica MCR 301 rheometer* presented in Paragraph 4.3. The input signal for the displacement of the upper plate was chosen to be a sine wave, as it is easy to compute and is the most stable input signal types of the rheometer. Experiments were carried out at different frequencies ($\omega \leq 50 \text{ Hz}$), amplitudes ($\varepsilon \leq 1 \mu\text{m}$) and different nominal gaps, at a temperature of 20°C . A first result discloses a 90° phase angle between the input (displacement) and output signal (force), characteristic to dynamic response of a pure viscous fluid (Figure 5.6).

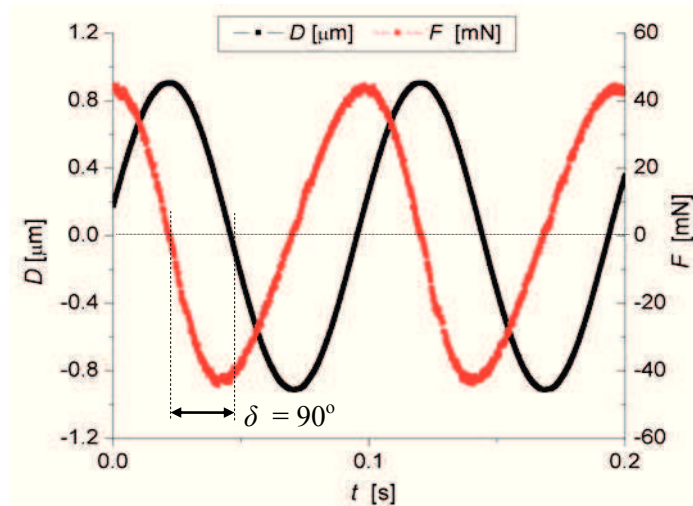


Fig. 5.6. Experimental force and displacement signals obtained in oscillatory squeezing flow of mineral oil sample at $\varepsilon_0 = 0.30 \mu\text{m}$, $\omega_s = 10 \text{ Hz}$, $h_0 = 300 \mu\text{m}$.

Due to technical limits and environmental influences, the signals captured with the data acquisition board are slightly noisy, especially in the case of the force signal. However, the disturbances are quite small compared to the base signal, so after a low pass filter (Fourier) was applied, the measured signal became a uniform wave (Figure 5.7).

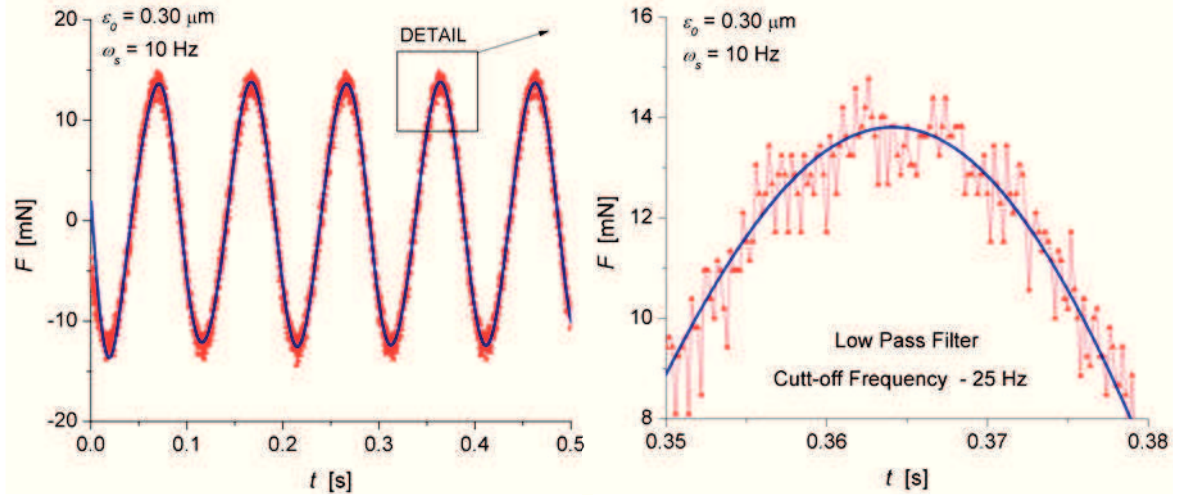


Fig. 5.7. Filtered force signal obtained in oscillatory squeezing flow of mineral oil sample at $\omega_s = 10 \text{ Hz}$, $\varepsilon_0 = 0.45 \mu\text{m}$, $h_0 = 300 \mu\text{m}$.

Comparing the theoretical and experimental values, we observe a phase difference (δ) between the two signals and an offset which is due to improper data acquisition with *Lab View*. Looking at the input displacement signal $D = \varepsilon(t)$, we find the same phase difference between experimental measurements and theoretical sine prediction, see Figure 5.8.

This phenomenon indicates that the rheometer, cannot maintain a constant input signal frequency in time, or it has an odd calibration of the optical displacement sensor. This problem can be solved only trough the re-calibration of the displacement sensor and the plate displacement mechanism, facts that weren't totally achieved during this study.

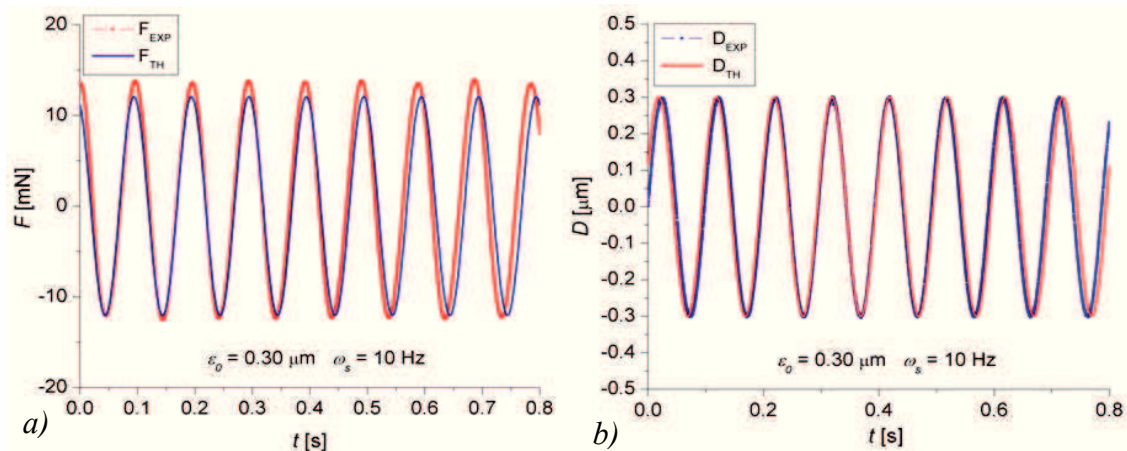


Fig. 5.8. Comparison between experimental and theoretical force (a) and displacement (b) signals obtained in oscillatory squeezing flow of mineral oil sample at $\varepsilon_0 = 0.75 \mu\text{m}$, $\omega_s = 10 \text{ Hz}$, $h_0 = 300 \mu\text{m}$.

The solution adopted was to include registered phase shift in the analytical expression of displacement and to determine a correction value (δ_c) for the experimental sine signal, which depends on the input parameters (amplitude, frequency), for the present case the value being $\delta_c = 2.59599^\circ$ (see Figure 5.8).

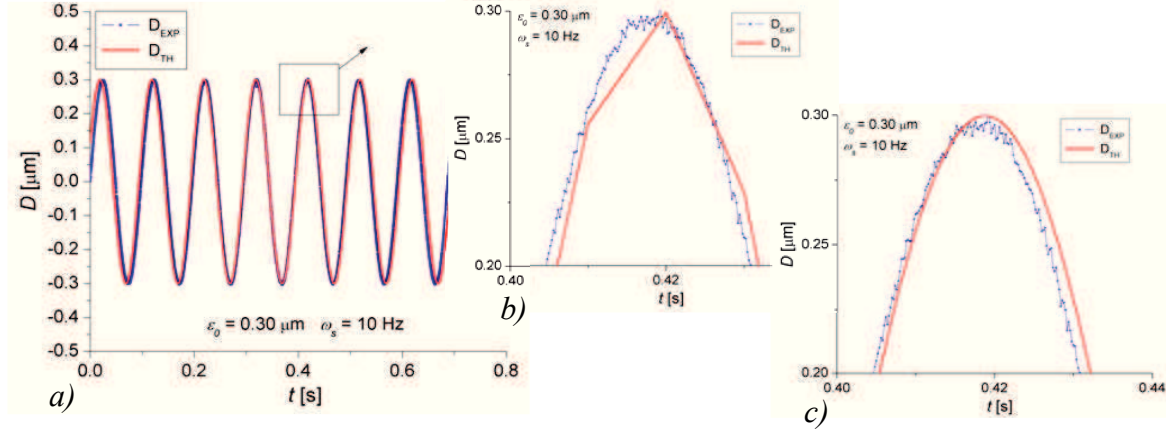


Fig. 5.9. Displacement signal fitting (a), by using 5000 (b) or 10.000 points (b) for the interpolation. The results correspond to an oscillatory squeezing test of mineral oil sample at $\epsilon_0 = 0.75 \mu\text{m}$, $\omega_s = 10 \text{ Hz}$ and $h_0 = 300 \mu\text{m}$.

The correction procedure used to determine δ_c shows the importance of choosing an appropriate number of points to approximate the shape of a signal. If the number of points is not large enough result may be wrong or irrelevant. In a first approximation we used 5000 points of approximation, a number that has proven to be insufficient to outline a sinusoidal profile (see Figure 5.9.a). The duplication of approximation points leads to a correct fitting of the signal (Figure 5.9.c).

In Figure 5.10 are presented the experimental results for the force signal of the mineral oil obtained at two values of h_0 in comparison with the values predicted by the theoretical model. It can be seen that the experimental values are always higher than the theoretical ones, the difference between them increasing at low film thicknesses. This effect is probably caused by the lack of parallelism between the plates, which affects the experimental results especially for small film thickness and low viscosities [72], [77], [78]. Considering the inherent inertia of the measuring system, it is possible that the calibration factor of the force transducer to modify with the force magnitude. Frequency influence on the measured values is emphasized in Figure 5.11, for an initial film thickness of $h_0 = 300 \mu\text{m}$. The experimental results indicate a linear dependence on the oscillatory force amplitude of the displacement signal. The differences between experimental measurements and theoretical predictions increase with both oscillatory frequency and oscillatory amplitude (Figure 5.11). This fact may be correlated to the dynamics of the squeezing motion: at high frequencies the inertia becomes

important; therefore it is normal for the force measured values to be superior comparing to the analytical computed ones (for which the acceleration is not considered).

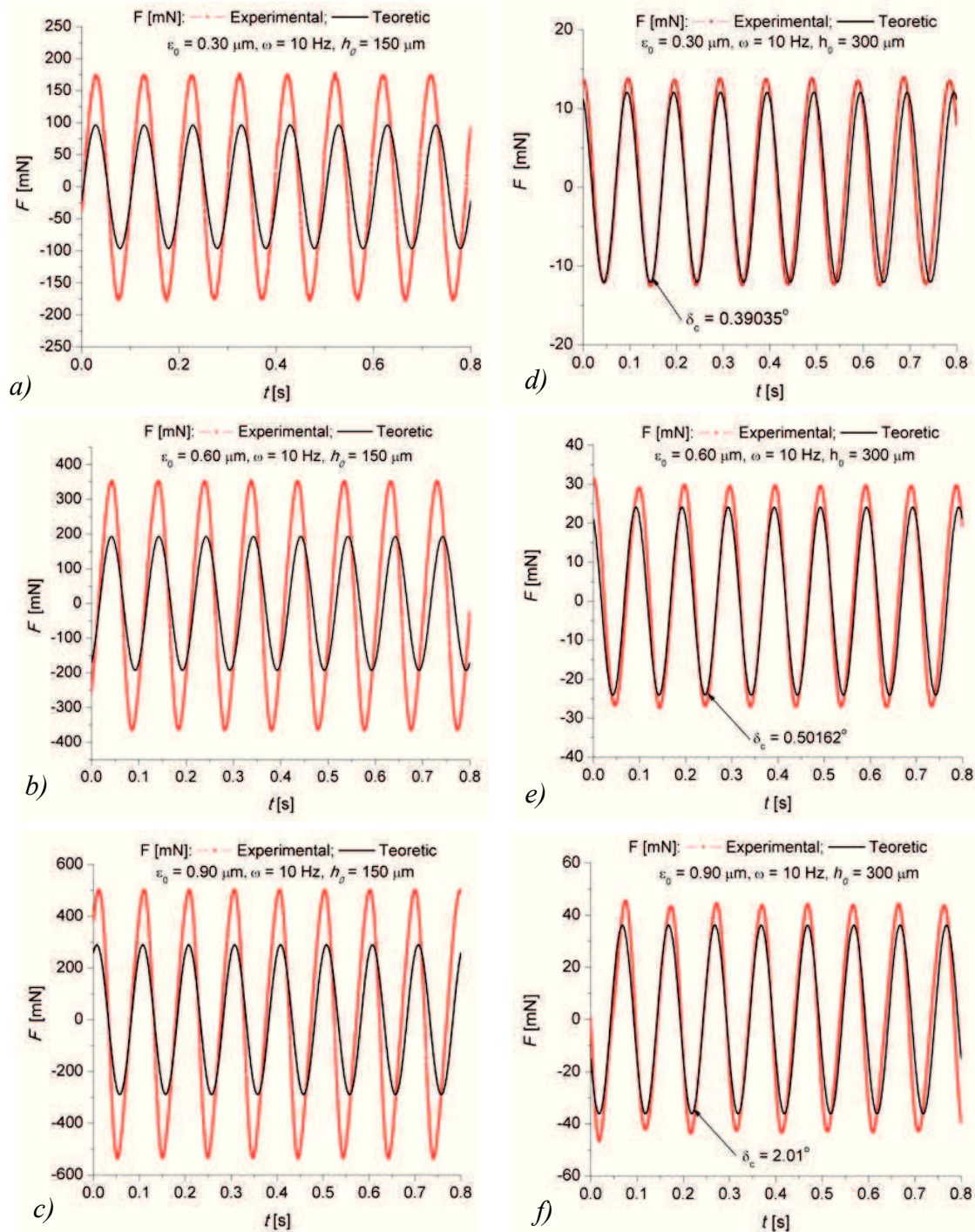


Fig. 5.10. Comparison between theoretical and experimental force signals for mineral oil sample in oscillatory squeezing flow: different initial film thickness, $h_0 = 150 \mu\text{m}$ (a, b, c) and $h_0 = 300 \mu\text{m}$ (d, e, f); different values of oscillatory displacement amplitude, $\varepsilon_0 = 0.30 \mu\text{m}$ (a, d), $\varepsilon_0 = 0.60 \mu\text{m}$ (b, e), $\varepsilon_0 = 0.90 \mu\text{m}$ (c, f) and $\omega_s = 10 \text{ Hz}$.

This assumption is sustained by the results obtained experimentally for the glycerin sample ($h_0 = 300 \mu\text{m}$, $\omega_s < 10 \text{ Hz}$ and $\varepsilon_0 < 1 \mu\text{m}$), where by applying a correction factor a good agreement was found between theory and experimental measurements.

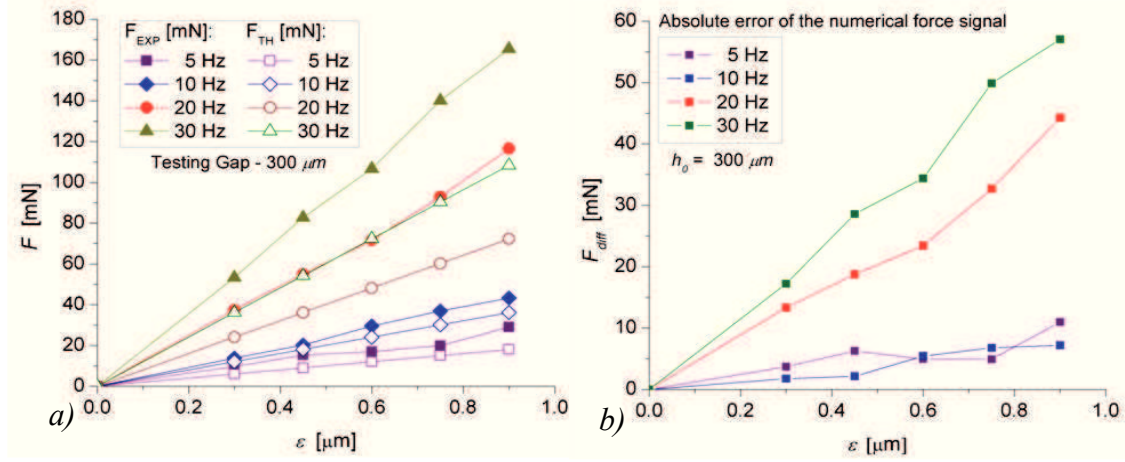


Fig. 5.11. Experimental and corresponding theoretical force magnitude (a) and force amplitude difference (b), as function of ω_s and ε_0 at $h_0 = 300 \mu m$. Values extracted from the signals for mineral oil sample investigations in oscillatory squeezing flow tests.

The tests were repeated for a glycerin solution ($\eta_0 = 0.9 Pa.s$) at a initial film thickness of $h_0 = 300 \mu m$. By applying a unique correction factor on the measured values (eq. 5.1) we improve the correlation between of the measured force signal and the theoretical prediction (see Figure 5.12).

$$F_{EXP_CR} = C_f \cdot F_{EXP} \quad (5.1)$$

Force amplitude values and the apparent viscosity computed from this values by using (ec. 3.16) are presented in Table 5.2. The results are indicating a good agreement with the shear predicted viscosity of the sample, keeping the relative error between the shear viscosity and the one obtained in squeeze flow in an acceptable range.

All the measurements indicate a phase angle of 90° between the displacement and the force signals, accordingly to the Newtonian rheological behavior of the samples. At small values of displacement oscillatory amplitude is observed an underestimation of the viscosity coefficient.

Table 5.2. Corrected force amplitude, apparent viscosity and relative error of measured viscosity (in comparison with shear viscosity) for the glycerin sample in oscillatory squeezing flow.

$\varepsilon_0 [\mu m]$	$F [N]$	$\eta_a [Pa.s]$	$\Delta \varepsilon [\%]$
0.3	0.07134	0.88821	1.31025
0.45	0.10301	0.85501	4.99924
0.6	0.15264	0.95021	5.57894
0.75	0.18881	0.9403	4.47778
0.9	0.23001	0.95457	6.06312
1	0.25976	0.97023	7.8034
2	0.5043	0.94181	4.64517

However the relative errors are small enough to consider a good correlation between the results obtained trough the oscillatory squeeze test and the ones predicted in shear flow tests.

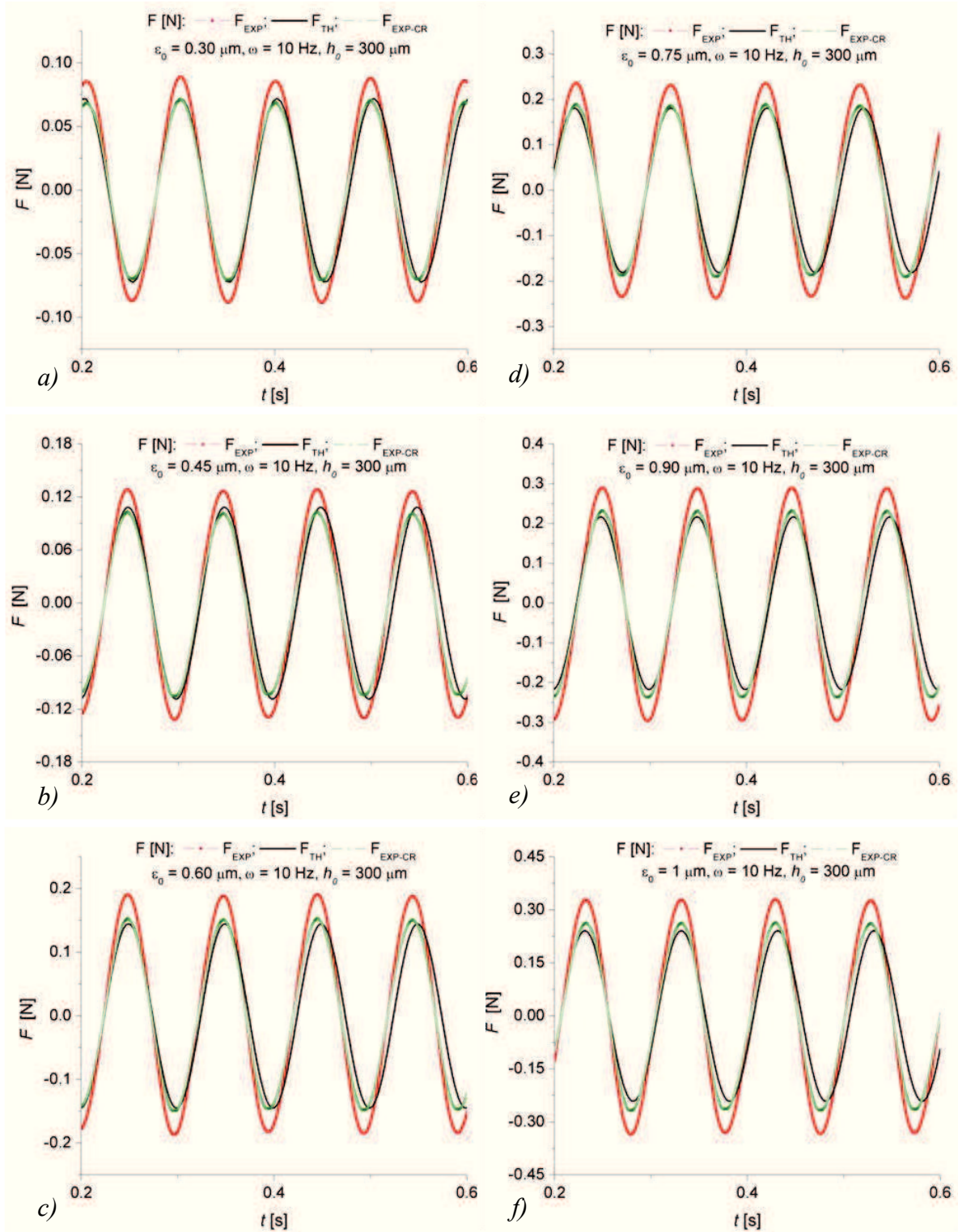


Fig. 5.12. Comparison between theoretical and experimental force signals (measured and corrected) for glycerin sample in oscillatory squeezing flow at $h_0 = 300 \mu\text{m}$; $\omega_s = 10 \text{ Hz}$, and different values of oscillatory displacement amplitude: $\varepsilon_0 = 0.30 \mu\text{m}$ (a), $\varepsilon_0 = 0.45 \mu\text{m}$ (b), $\varepsilon_0 = 0.60 \mu\text{m}$ (c), $\varepsilon_0 = 0.75 \mu\text{m}$ (d), $\varepsilon_0 = 0.90 \mu\text{m}$ (e), $\varepsilon_0 = 1 \mu\text{m}$ (f).

.The phenomena presented in this paragraph disclose some technical issues (dysfunctions) of the MFR 2100 rheometer:

- (i) The limited control of the displacement signal which cannot be kept constant for a sufficiently long observation time;
- (ii) The nonlinear response of the force transducer, and, consequently the difficulty of its calibration;
- (iii) The lack of an appropriate parallelism between the plates.

These issues could not be completely eliminated mainly due to lack of appropriate technical assistance (service) from the manufacturer. The negative impact of these problems is seen especially in small film thicknesses h_0 , high inertia of the measuring system and low viscous samples ($\eta_0 \leq 0.1 \text{ Pa.s}$). These issues do not affect the measurements from the qualitative point of view: the linear dependence of measured force on the oscillatory frequency (for $\omega_s \leq 10 \text{ Hz}$) and the 90° phase angle measured for pure viscous fluids.

For samples with high viscosity ($\eta_0 \geq 0.5 \text{ Pa.s}$) the measurements performed for initial film thickness $h_0 \geq 250 \mu\text{m}$ are not affected by the mentioned issues, the correlation between measurements and theoretical predictions being adequate from both qualitative and quantitative points of view (see Paragraph 4.3).

5.3. THE RHEOLOGY OF COMPLEX FLUIDS IN OSCILLATORY SQUEEZING FLOW

The present section presents the rheological characterization of two complex fluids in oscillatory squeezing flow: a polymer solution – PAA (Polyacrilamye in water, used also in Paragraph 4.3.3) and a low consistency impression material (ISO 4823), based on condensation-curing addition silicon or polydimethylsiloxane - PS (polimerized silicone – polysiloxane). The chemical structure of PS consists of alternating silicon and oxygen atoms connected through sigma bonds, having side chains attached to the silicon atoms, as presented in Figure 5.13 [255]. The complete analysis of the shear rheology of this material is presented in Chapter 6. PAA is a viscoelastic liquid with a shear thinning behavior and the polysiloxane is a complex fluid with yield stress.

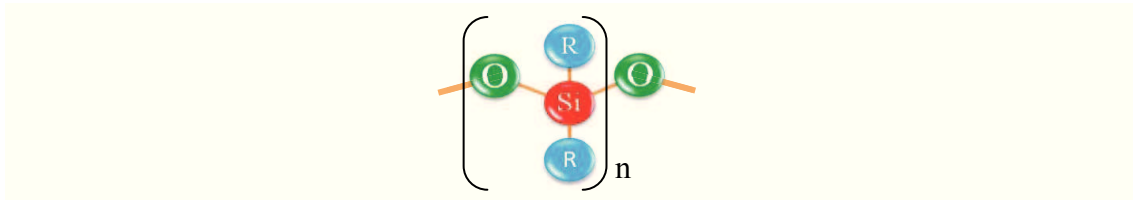


Fig. 5.13. Chemical structure of polysiloxane (PDMS).

The investigations covered a frequency domain of $1 \text{ Hz} \leq \omega_s \leq 20 \text{ Hz}$, with oscillatory displacement amplitude of $\varepsilon_0 \leq 1 \mu\text{m}$ and initial film thickness $h_0 \in [150 \div 300] \mu\text{m}$, all measurements being performed at $T = 20^\circ \text{ C}$.

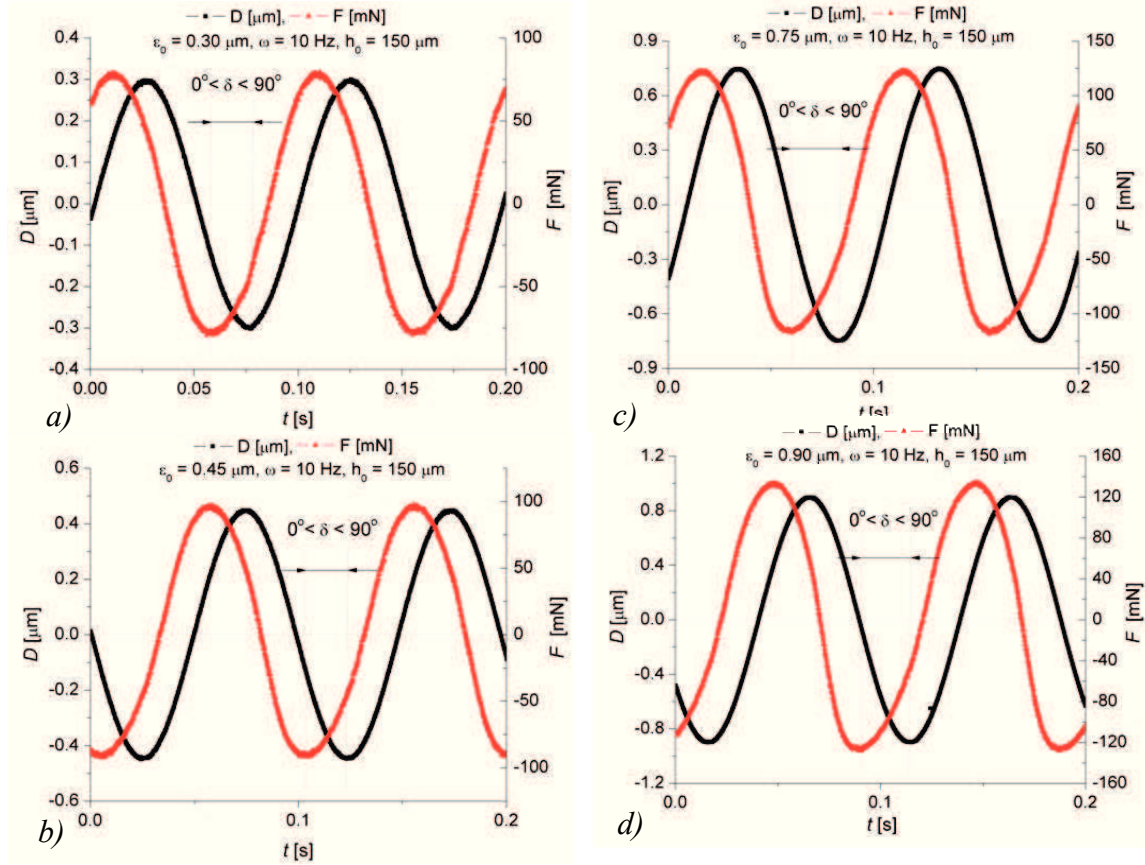


Fig. 5.14. Time dependent displacement and force signals obtained in oscillatory squeezing flow of PAA sample at $h_0 = 300 \mu\text{m}$, $\omega_s = 10 \text{ Hz}$ and different oscillatory amplitudes: $\varepsilon_0 = 0.30 \mu\text{m}$ (a), $\varepsilon_0 = 0.45 \mu\text{m}$ (b), $\varepsilon_0 = 0.75 \mu\text{m}$ (c) and $\varepsilon_0 = 0.90 \mu\text{m}$ (d).

For the PAA sample the results (displacement and force signals) obtained in oscillatory squeezing flow are presented in Figure 5.14 and for the polysiloxane in Figure 5.15. In both cases the phase angle between force and displacement signal is smaller than 90° indicating a viscoelastic behavior of the samples.

For the PAA solution the deformation of force signal depends on the oscillatory amplitude of the input (at constant frequency) as found also in the numerical simulations. For the polysiloxane sample at $\omega_s = 1 \text{ Hz}$ the phase angle is almost equal to 90° indicating a weakly elastic behavior, thus a strong viscous behavior. At higher frequencies $\omega = 5 \div 10 \text{ Hz}$ the results are indicating a more pronounced elastic behavior but the signal deformation is not observed.

The Lissajous figures corresponding to the performed measurements (shown above) are presented in Figure 5.16 - 5.18. Lissajous curves disclose the parametric dependency between the measured force and imposed deformation, usually the dependence between the applied deformation and the material response, and are often used for the characterization of both linear and nonlinear behavior of complex fluids in shear flows (see. Paragraph 2.4).

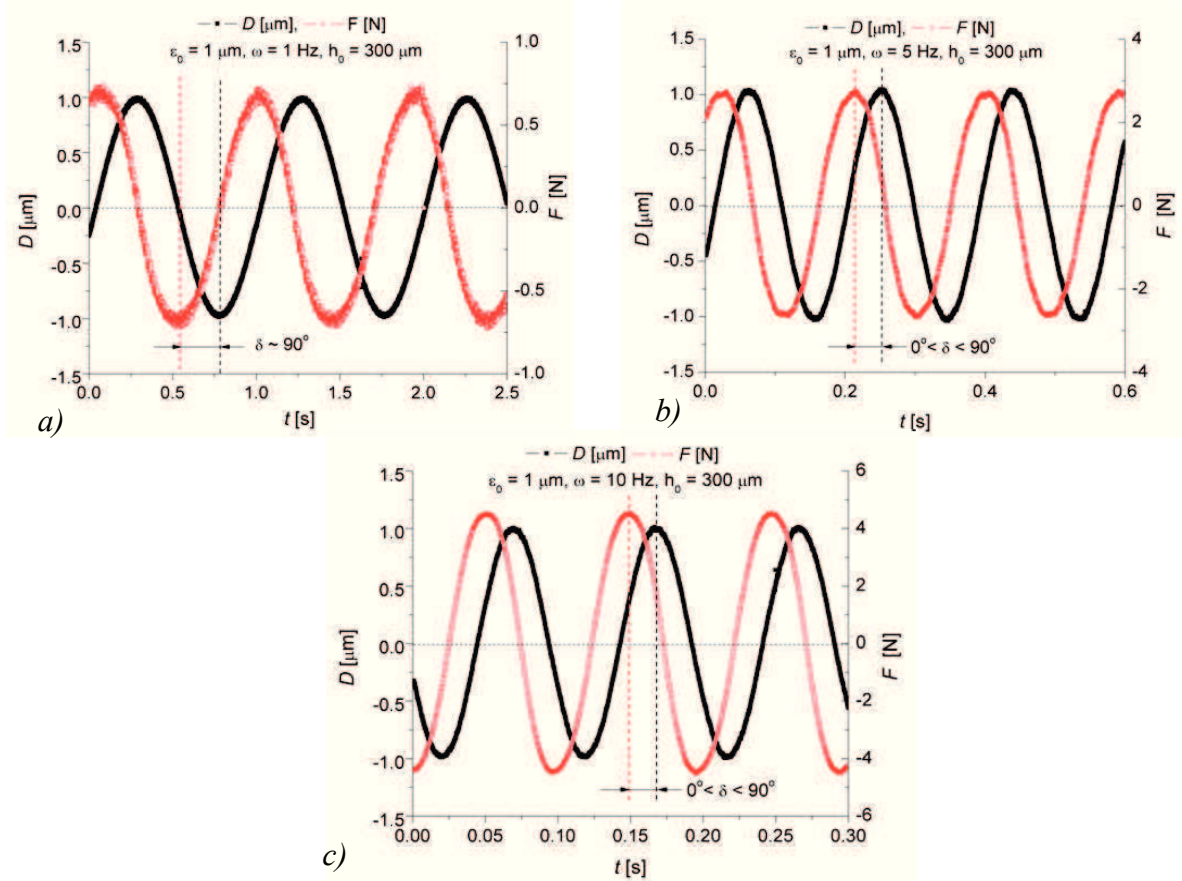


Fig. 5.15. Time dependent displacement and force signals obtained in oscillatory squeezing flow of PS sample at $h_0 = 300$ μm, $\varepsilon_0 = 1$ μm and different oscillatory frequencies: $\omega_s = 1$ Hz (a), $\omega_s = 5$ Hz (b) and $\omega_s = 10$ Hz (c).

For the mineral oil and the glycerin samples measurements (presented in the previous paragraph) the Lissajous curves are indicating, as expected a pure viscous rheological behavior (see Figure 5.16). The deviations from a perfectly circular form are due exclusively to the limitations errors of the force transducer and displacement sensor.

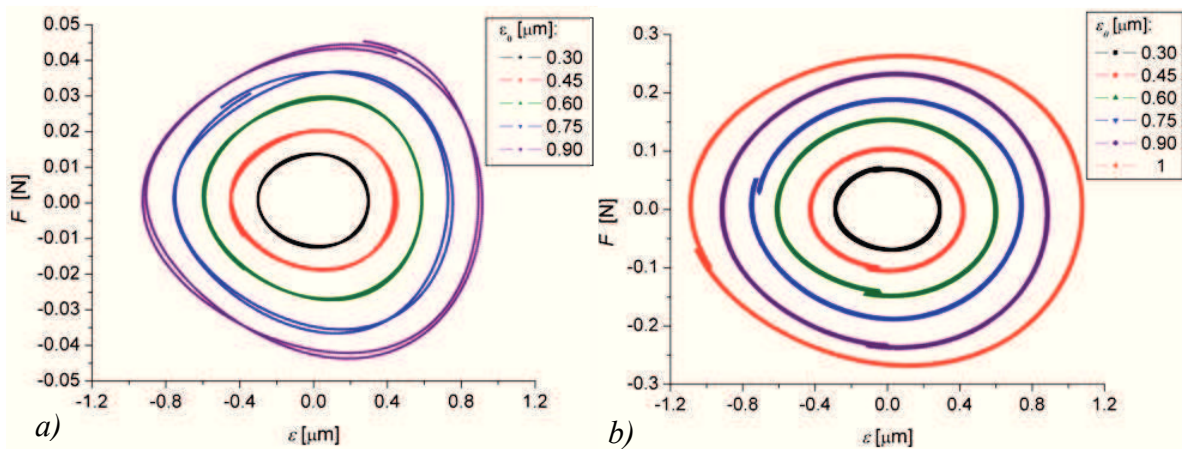


Fig. 5.16. Lissajous figures obtained in oscillatory squeezing flow for the mineral oil (a) and glycerin sample (b) at $h_0 = 300$ μm, $\omega_s = 10$ Hz and different oscillatory amplitudes.

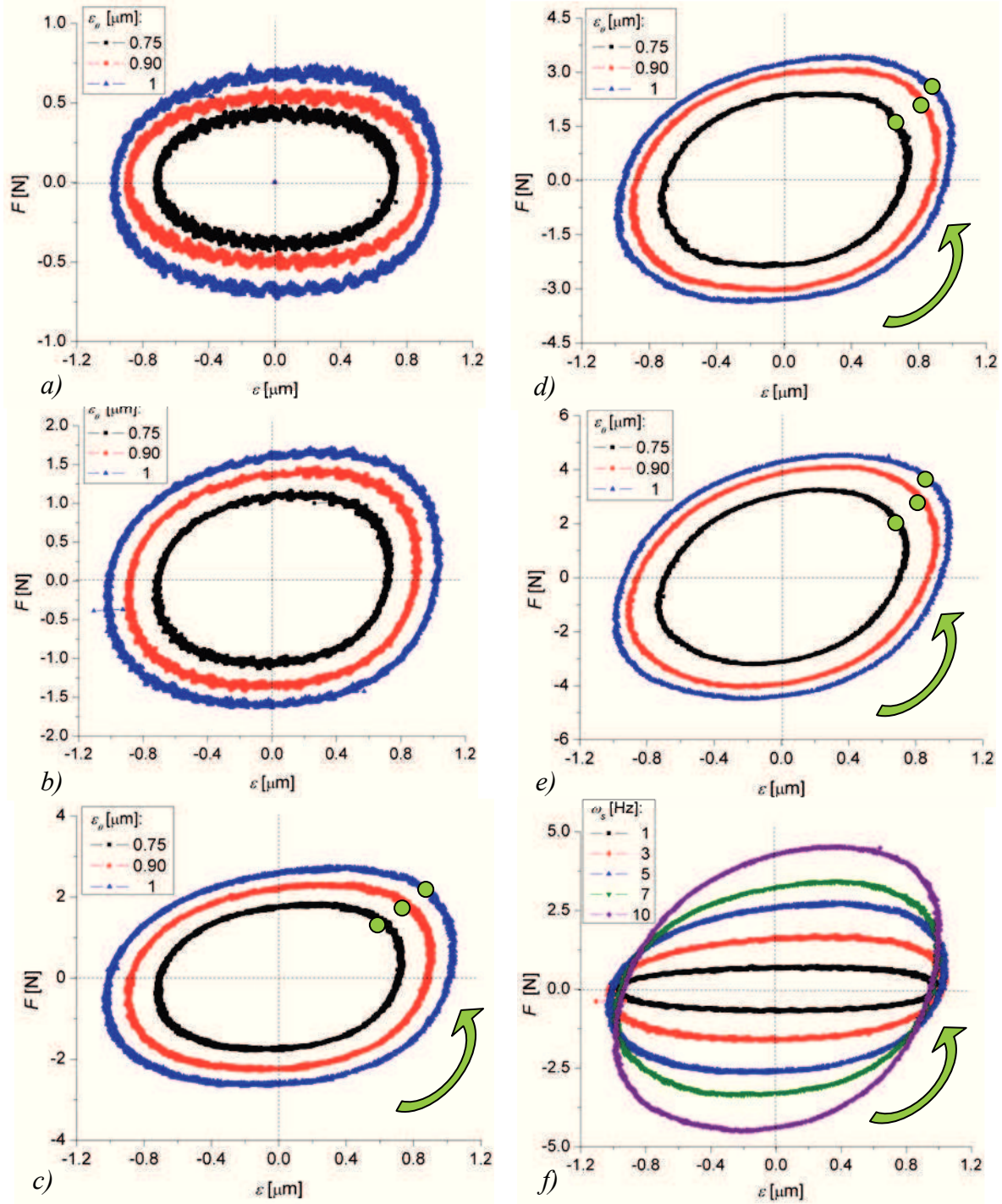


Fig. 5.17. Lissajous figures obtained in oscillatory squeezing flow for the PS sample. The curves correspond to $h_0 = 300 \mu\text{m}$, $\varepsilon_0 \in [0.75 \div 1] \mu\text{m}$ and different oscillatory frequencies, $\omega_s = 1 \text{ Hz}$ (a), $\omega_s = 3 \text{ Hz}$ (b), $\omega_s = 5 \text{ Hz}$ (c), $\omega_s = 7 \text{ Hz}$ (d), $\omega_s = 10 \text{ Hz}$ (e) and to $h_0 = 300 \mu\text{m}$, $\varepsilon_0 = 1 \mu\text{m}$ at different oscillatory frequencies ω_s (f).

In the case of PS sample the deformation of Lissajous curve is increasing with oscillatory amplitude ε_0 .

The flattening and elongation of the curve at high frequencies indicates an increase of elasticity component and therefore disclose a viscoelastic behavior of the material (Figure 5.17).

The curves are rotating counter-clockwise (irregardless the dependency on ω_s or ε_0) indicating in this case a swelling behavior with increasing the applied deformation.

By comparison, the ellipsoidal shape of the Lissajous curves obtained for the PAA sample (Figure 5.18) discloses a viscoelastic rheological behavior with a strong elastic component at small deformations. The clockwise rotation of the curves reveals a shear thinning behavior, accordingly to the sample characterization performed in shear tests (see Paragraph 4.3.3).

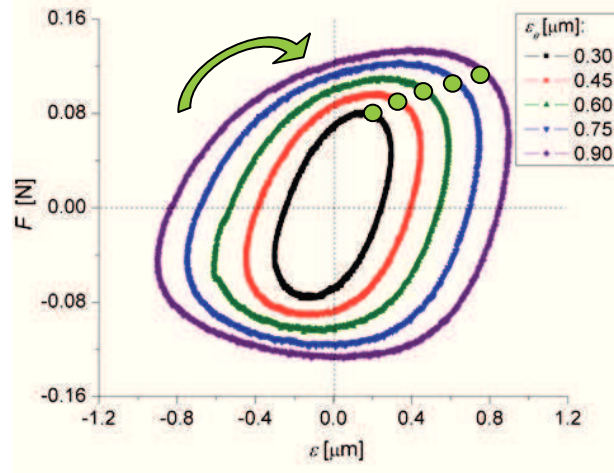


Fig. 5.18. Lissajous figures obtained in oscillatory squeezing flow for the PAA sample at $h_0 = 150 \mu\text{m}$, $\omega_s = 10 \text{ Hz}$ and different oscillatory amplitudes.

One has to notice that the presented analysis is based on the nonlinear viscoelasticity theory for shear motions (see Paragraph 2.4 and Chapter 6), because the scientific literature offers poor resources regarding nonlinear rheology analyze in squeezing flows [122], [187].

5.4. THE RHEOLOGICAL BEHAVIOR OF NEWTONIAN FLUIDS IN CONSTANT VELOCITY SQUEEZE FLOW

The simple squeeze flow was analyzed for three Newtonian fluids (mineral oil, glycerin, honey) with various viscosities $\eta_0 \in (0.05 \div 20) \text{ Pa.s}$ at different squeezing velocities and temperatures. The testing parameters and the initial film thickness are presented in Table 5.3 for each tested sample.

Table 5.3. Testing parameters for different Newtonian samples in constant velocity squeeze flow.

Tested Sample	h_0 [mm]	\dot{h} [mm/s]	T [°C]
Mineral Oil	1	{0.01; 0.1; 1}	{1, 10, 20, 30}
Glycerin	1	{0.01; 0.1; 1}	{10, 20}
Honney	2	{0.001; 0.01; 0.1}	{5, 10, 20, 30}

Measured parameters were than postprocessed with **Origin 8.0** software and represented graphically in both dimensional and dimensionless ways.

5.4.1. Establishing the reliability domain depending on the fluid film thickness

The first tested sample is the mineral oil, a pure viscous fluid with a minimum viscosity of $0.07 \text{ Pa}\cdot\text{s}$ measured at 30° . Figure 5.20 presents the experimental measurements of the normal force for a constant velocity squeeze flow of mineral oil sample at $\dot{h} = 0.01 \text{ mm/s}$ and $T \in [1 \div 30]^\circ\text{C}$ in comparison with the theoretical predictions (numerical and analytical).

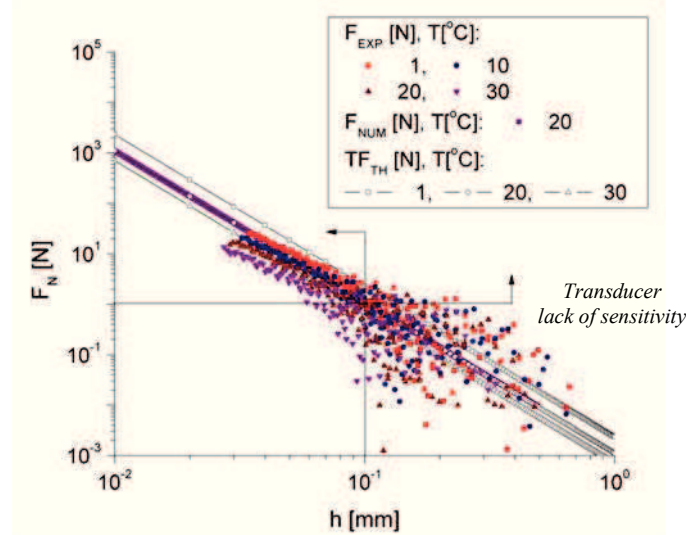


Fig. 5.19. Comparison between experimental measurements and theoretical predictions for mineral oil sample in constant velocity squeeze flow ($\dot{h} = 0.01 \text{ mm/s}$) at different temperature values. Establishing the reliability domain depending on the fluid film thickness.

It can be observed that at a constant squeezing velocity the measured force values decrease once increasing temperature and that the lower limit of the reliability domain of fluid film thickness increases with temperature (since the measured values decrease and are found in the limits of the force transducer).

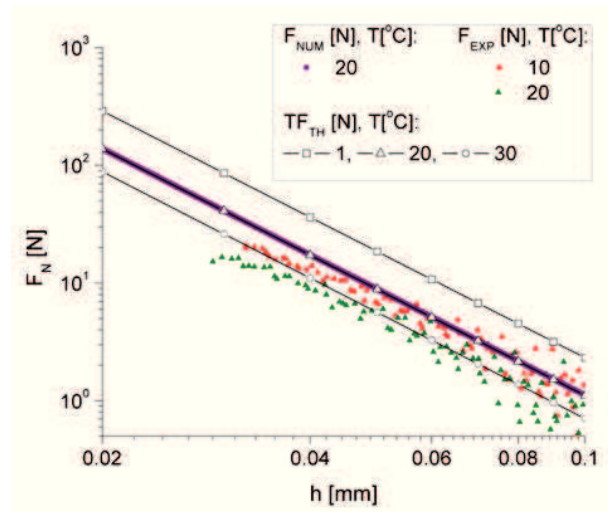


Fig. 5.20. Comparison between experimental measurements and theoretical predictions for mineral oil sample in constant velocity squeeze flow ($\dot{h} = 0.01 \text{ mm/s}$) and $T = [10 \div 20]^\circ\text{C}$.

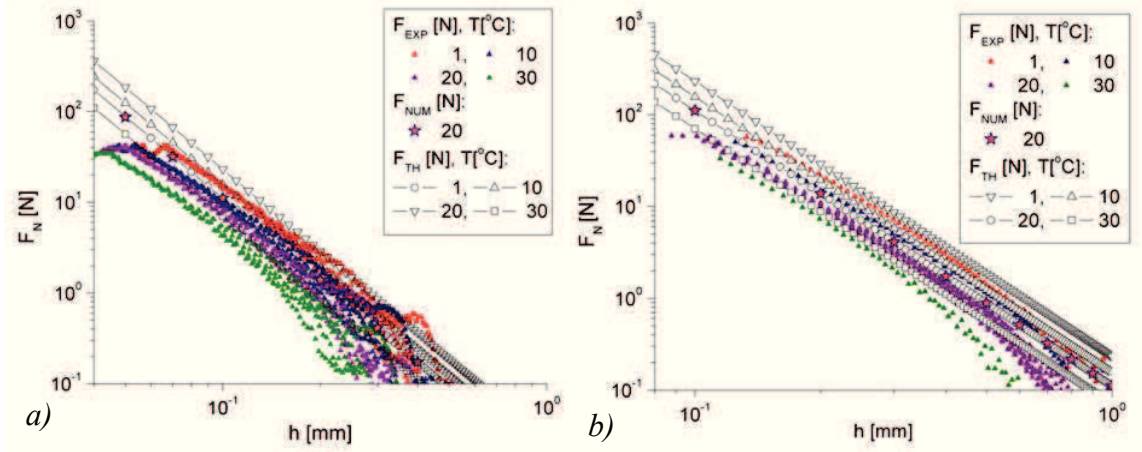


Fig. 5.21. Comparison between experimental measurements and theoretical predictions for mineral oil sample in constant velocity squeeze flow at different temperature values: $\dot{h} = 0.1 \text{ mm/s}$ (a); $\dot{h} = 1 \text{ mm/s}$.

At high film thickness force distribution disclose a spreading due to the lower values of the force that cannot be properly captured by the sensor (Figure 5.19). At $T = [10 \div 20]^\circ\text{C}$, see Figure 5.21 the measurements disclose a linear distribution of the squeezing force, characteristic to a Newtonian behavior, but the values are smaller than the ones predicted by theory (numerical results, analytical predictions). Same phenomena is observed when increasing squeezing velocity ($\dot{h} \geq 0.1 \text{ mm/s}$), see. Figure 5.22. The difference between experimental and theoretical values, and also a slightly change from the exponent -3 of the theoretical dependence $F = F(h)$, may be due to different factors like: viscosity variation with temperature in the gap, improper parallelism between the plates, inertia influence and possible wall depletion phenomena (lack of adherence).

In our study, a dimensionless force expression is used to represent the measured values in order to build a “master curve” for all data (different samples, temperatures and testing geometries).

5.4.2. Dimensionless force formulation

The dimensionless representation uses the following expressions:

$$\bar{h} = \frac{h}{R}, \quad (5.2)$$

the force being expressed by

$$\bar{F} = \frac{F}{\eta RV} = -\frac{3\pi}{2} \cdot \bar{h}^{-3} \quad (5.3)$$

The measurements for mineral oil are represented in dimensionless form by using different values of the viscosity coefficient (see Figure 5.22). Viscosity values were chosen from shear test rheology of the sample, being temperature dependent as shown in Paragraph 4.4. It is noticed that even a slight change of the viscosity value has an important effect on the squeezing force: at smaller values the force approaches the theoretical predictions.

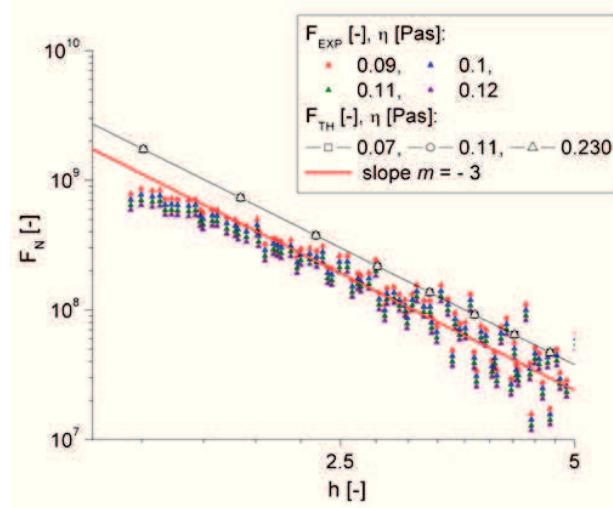


Fig. 5.22. Dimensionless experimental values (using different viscosity coefficients) and theoretical predictions for mineral oil sample in constant velocity squeeze flow at $\dot{h} = 0.01 \text{ mm/s}$ and $T = 20^\circ\text{C}$.

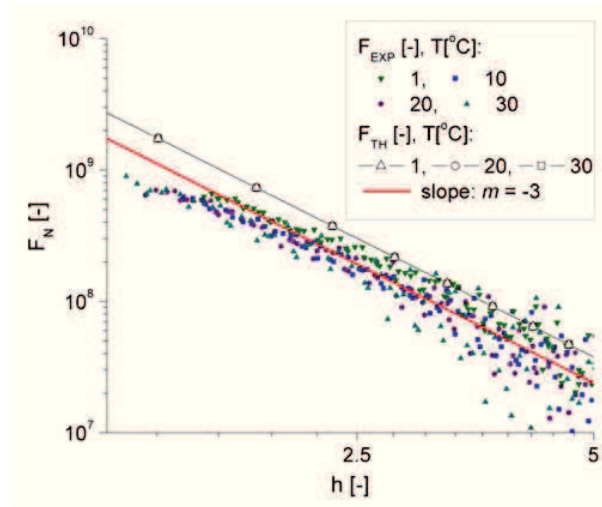


Fig. 5.23. Dimensionless experimental values and theoretical predictions for mineral oil sample in constant velocity squeeze flow at $\dot{h} = 0.01 \text{ mm/s}$ and different temperatures.

At small squeezing velocities the dimensionless measured values are smaller than the theoretical ones as emphasized in Figure 5.23. Once increasing velocity the experimental results approach the theoretical predictions and are almost identical at large speeds, $\dot{h} = 1 \text{ mm/s}$ (Figure 5.24.b). For the second sample, the glycerin solution, the dimensionless results are presented in Figure 5.25. In this case a nonlinear distribution of the normal force is found especially at small squeezing velocities ($\dot{h} = 0.01 \text{ mm/s}$), the phenomena being probably due to a partial slip at the wall. This deviation is diminished once increasing the

squeezing velocity but the experimental values overcome the theoretical ones especially at high film thickness. This may be due to the inertial effects that occur when the velocity increases.

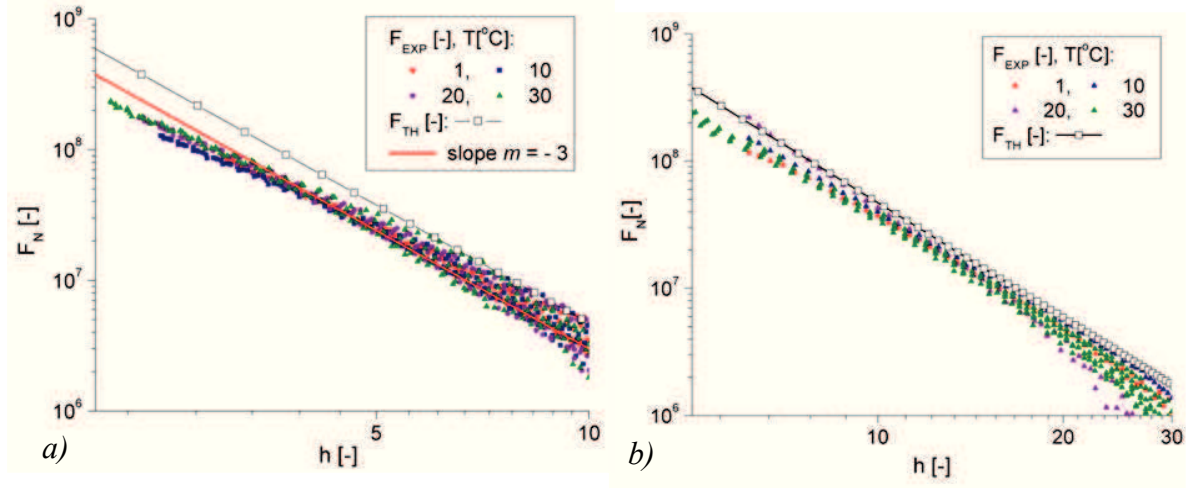


Fig. 5.24. Dimensionless experimental values and theoretical predictions for mineral oil sample in constant velocity squeeze flow at different temperatures and: $\dot{h} = 0.1$ mm/s (a), $\dot{h} = 1$ mm/s (b).

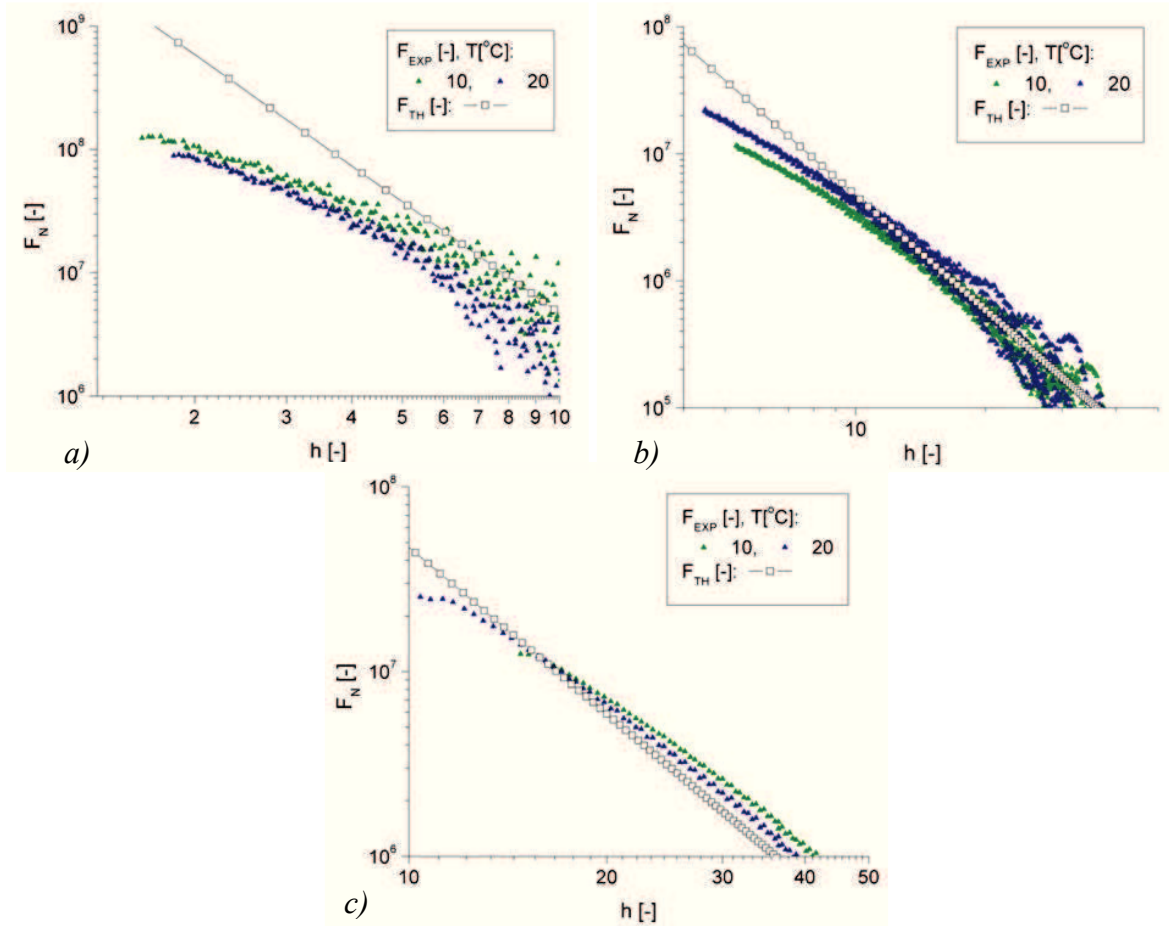


Fig. 5.25. Dimensionless experimental values and theoretical predictions for glycerin sample in constant velocity squeeze flow at different temperatures and: $\dot{h} = 0.01$ mm/s (a), $\dot{h} = 0.1$ mm/s (b), $\dot{h} = 1$ mm/s (c).

The glycerin sample is almost ten times more viscous than the mineral oil sample. Therefore an accumulation of the squeezed fluid on the lower plate, in the vicinity of the outlet zone may cause an additional pressure in the gap, giving rise to an increase of the measured force (see also Paragraph 4.3)

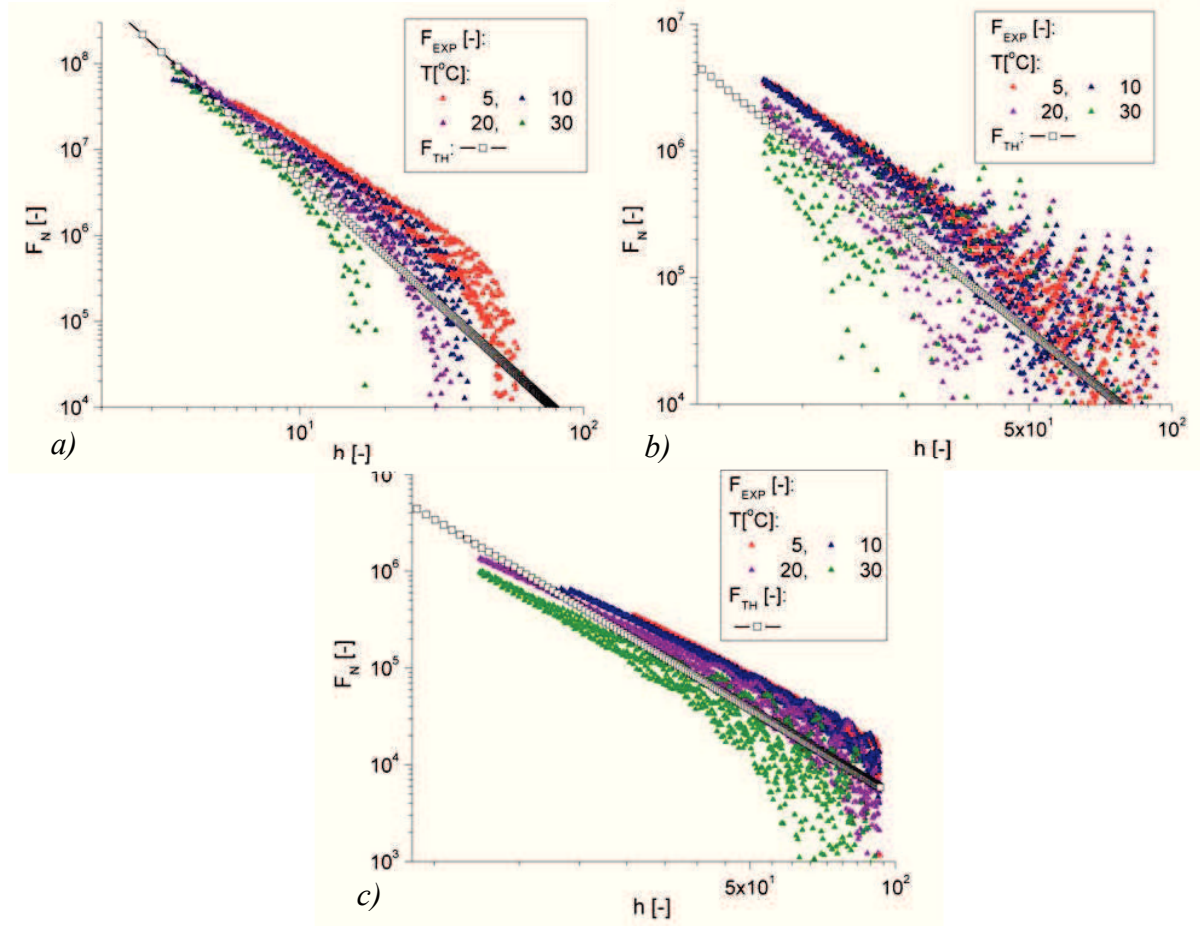


Fig. 5.26. Dimensionless experimental values and theoretical predictions for honey in constant velocity squeeze flow at different temperatures and: $\dot{h} = 0.001 \text{ mm/s}$ (a), $\dot{h} = 0.01 \text{ mm/s}$ (b), $\dot{h} = 0.1 \text{ mm/s}$ (c).

For the third sample (honey) the results disclose the same behavior: a linear distribution is found only if increasing squeezing velocity and the measured values are superior in comparison with the theoretical ones.

For this sample, the influence of testing temperature (viscosity coefficient) is more obvious: at small temperatures (therefore high viscosity) the measured force is always larger than the ones predicted by the theoretical formulation (see Figure 5.26). This may due, as mentioned before, to the presence of end effects.

The master curve for all samples is presented in Figure 5.27, and discloses a good agreement between the experimental measurements and the theoretical values. The results disclose more consistency at higher squeeze velocity (if we are limited at the optimal range for the thrust) which is also an indication of the theoretical expression validity domain.

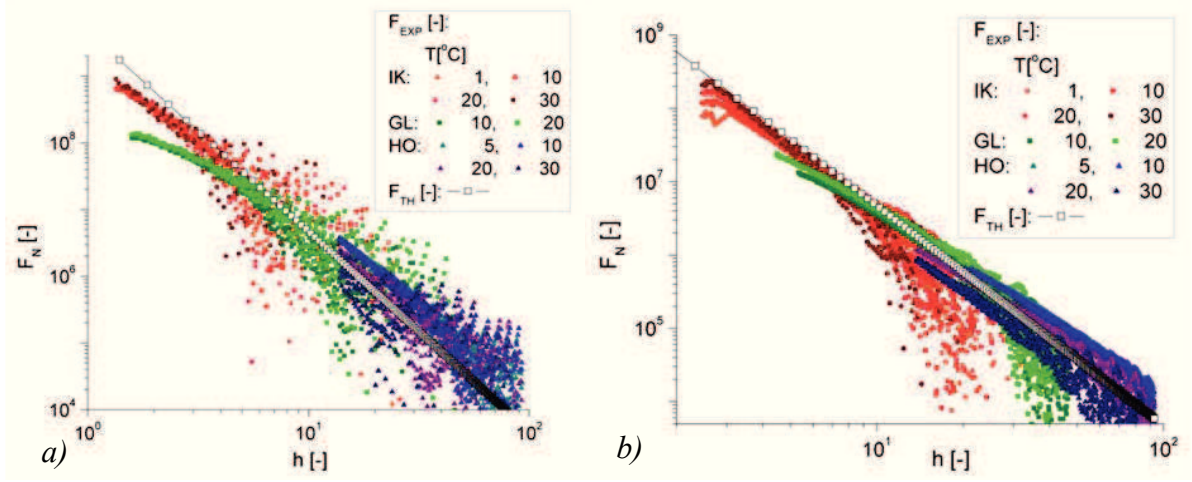


Fig. 5.27. Master curve representing the dimensionless experimental and theoretical force distribution for all investigated Newtonian samples in constant velocity squeeze flow at different temperatures:

$\dot{h} = 0.01 \text{ mm/s}$ (a), $\dot{h} = 0.1 \text{ mm/s}$ (b).

5.4.3. Free surface influence in constant velocity squeeze flow

In the previous section there were presented some experimental measurements obtained for Newtonian fluids in constant velocity squeeze flow. For low viscous fluids (mineral oil, IK, $\eta = 0.11 \text{ Pa.s}$ at $T = 20^\circ\text{C}$) the measured normal force is smaller than the one predicted analytically for the whole film thickness domain $h(t)$ and at all testing squeezing velocities. When increasing viscosity (glycerin solution, GL, $\eta = 0.9 \text{ Pa.s}$ at $T = 20^\circ\text{C}$) the measurements disclose larger values in comparison with the theoretical predictions at high gap values (corresponding to the beginning of the squeezing test). These effects are more obvious for honey sample (HO, $\eta = 16 \text{ Pa.s}$ at $T = 20^\circ\text{C}$). Since all samples were investigated using the same testing procedures and the same rheometer these differences may be explained by the different evolution of the free surface for each sample.

The experimental setup allows the visualization of the free surface during the squeezing flow and its correlation with the measured force. Therefore during each test the interface evolution was tracked and recorded in video files (avi format) from which there were extracted successive images using *Movie Maker* software, correlated with different observation times and the measured force. Figure 5.28 presents free surface evolution for the glycerin solution at constant squeeze velocity $\dot{h} = 1 \text{ mm/s}$ at $T = 20^\circ\text{C}$. The images are marked with a notation P1 - P8 which corresponds to the points indicated on the measured force distribution. The free surface between P1 and P2 discloses a flow resistance of the material through the agglomeration of the fluid on the lower plate in the vicinity of the outlet area of the testing gap.

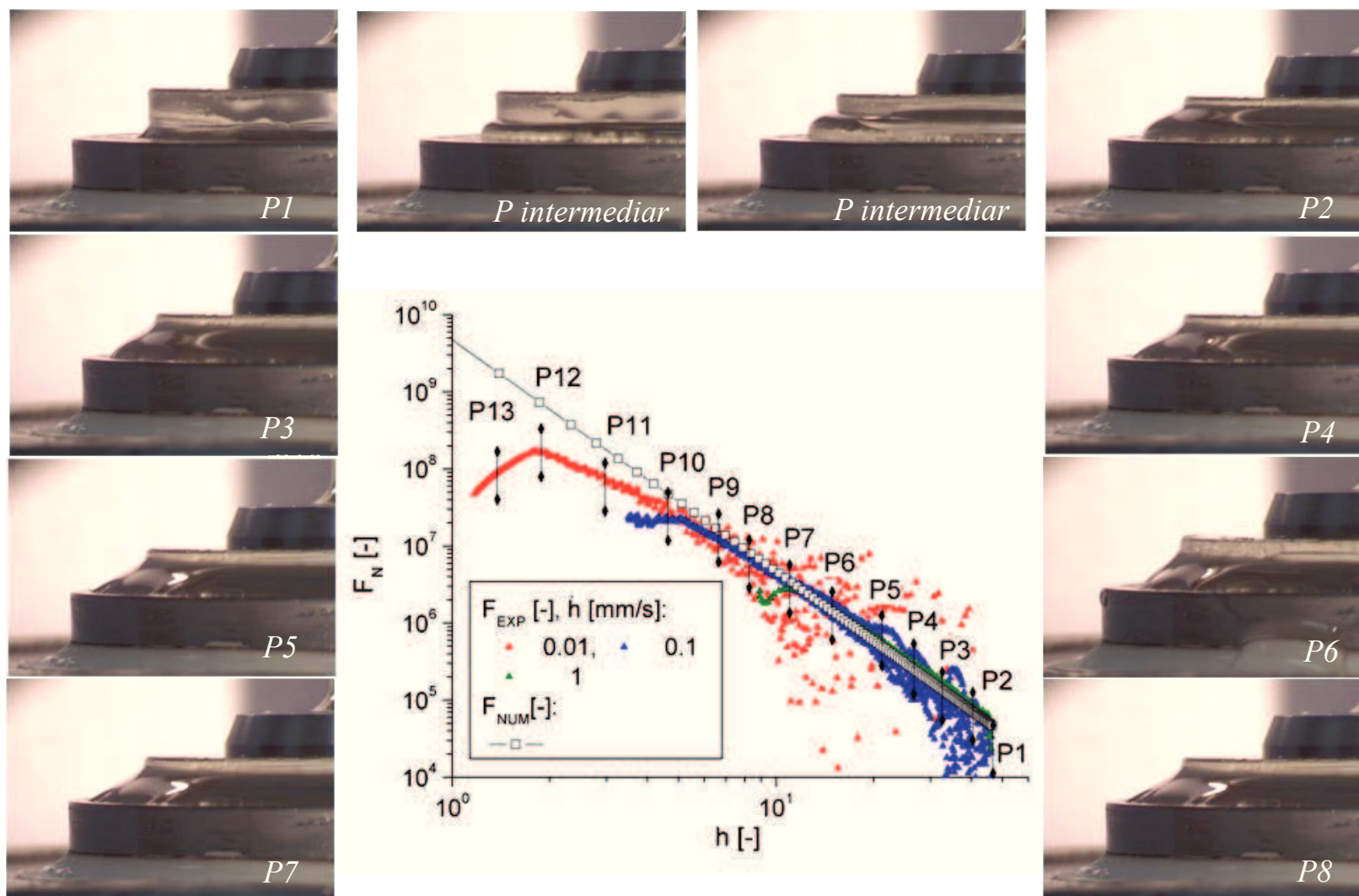


Fig. 5.28. Free surface evolution depending on film thickness (h) for the glycerin solution in constant velocity squeeze flow, $\dot{h} = 1$ mm/s.

The onward motion of the fluid on the lower plate and the rise of the fluid on the plate's edge are determined by the surface tension of the fluid and the contact angle at the fluid-solid interface. The fact that experimental values of force are superior to the theoretical ones might be given by the initial resistance of the fluid at the onset of the squeezing, especially at high squeeze velocities. Consecutive images, P3 - P8, are following the interface evolution during the squeeze motion until the end of the test. The evolution suggests a lower flow resistance; the interface has a rapid advance on the lower plate once the flow (particularly on radial direction) is developed.

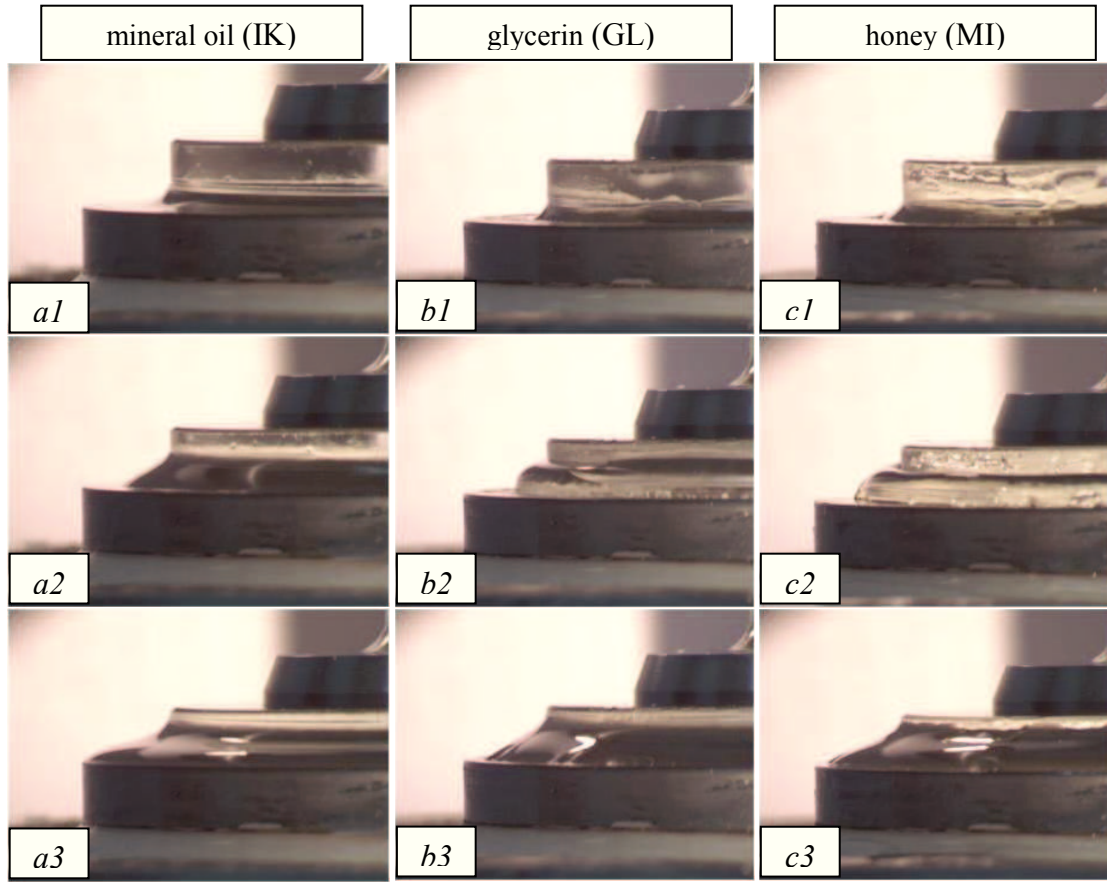


Fig. 5.29. Free surface evolution during constant velocity squeeze flow ($\dot{h} = 0.1 \text{ mm/s}$) for mineral oil (a), glycerin (b) and honey (c). The captured images correspond to the beginning of the test (a1, b1, c1); an intermediate observational time (a2, b2, c2) and the end of the test (a3, b3, c3).

The evolution of the free surface is shown for all Newtonian samples in constant velocity squeeze flow, at all speeds in [Annex 7](#). [Figure 5.29](#) presents the shape of fluid-air interface for the analyzed samples at the beginning of a test, at a intermediate observation time and at the end of the test, for a constant velocity of $\dot{h} = 1 \text{ mm/s}$. It may be observed that the oil samples wets both the lower plate and upper plate margin since the beginning of the test ([Figure 5.29.a1](#)), behavior that is not disclosed by the other samples. The interface keeps its shape during the whole test, advancing on surfaces of both plates. Free surface

dynamics discloses a reduced flow resistance of the sample, due to a small contact angle (20 - 30° for mineral oils) and a small surface tension (0.4-0.5 N/m). For the glycerin solution the shape of the interface at the beginning of the test resembles the one observed for the mineral oil sample. However an intermediate observation time, it discloses an agglomeration of the squeezed material at the end of the testing gap, probably due to the fact that glycerin has a larger contact angle than the mineral oil.

At the end of the test the shape of the free surface approximates again the behavior of the mineral oil sample, even though the fluid interface does not reach the border of the lower plate. At small squeezing velocities, the glycerin samples behavior resembles completely the one observed for the mineral oil (see Annex 7). For the third sample, the honey, the behavior observed for glycerin is more pronounced, the flow resistance increasing accordingly to the viscosity and the contact angle (see Annex 7). As a conclusion the normal force variation may be influenced by the dynamics of the flow process, exclusively dependent on the squeezing velocity but also on the rheological properties of the fluid: viscosity, surface tension and contact angle.

5.5. COMPLEX FLUIDS RHEOLOGY IN SIMPLE SQUEEZE FLOW

This section is dedicated to the characterization of three complex fluids through simple squeeze flow: a cosmetic cream (CR), a hair gel sample (GEL) and an impression material, polysiloxane based (PS). The rheological properties of these samples were also investigated in shear motions (see. Chapter 6). The tests were performed at different squeezing velocities, the consistency of these materials allowing initial gaps of 2 or 3 mm.

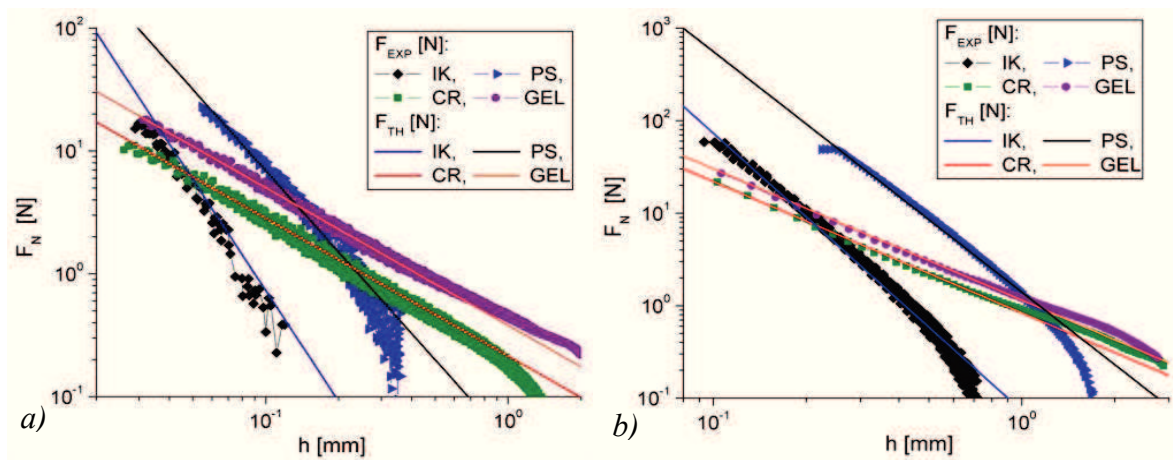


Fig. 5.30. Comparison between experimental measurements and analytical predictions (Power-Law model) of squeezing force for the analyzed samples (IK, PS, CR and GEL) at different squeezing velocities $\dot{h} = 0.01 \text{ mm/s}$ (a), $\dot{h} = 1 \text{ mm/s}$ (b).

Unlike pure viscous fluids (mineral oil, IK) the distribution of the normal force disclose a change in slope due exclusively to the viscoelastic shear thinning component of this materials. For the PS sample the variation of normal force values disclose the presence of the elastic component through a small change in the slope but the flow is obviously dominated by the pure viscous components (see Figure 5.30). The experimental values were fitted using *Power Law* force expression (eq. 3.43) for all the samples. It may be noticed that for the PS sample the flow index is smaller then unit (where unit indicates a Newtonian behavior, as for IK) [72], [127], [202]. Unlike PS, the results obtained for CR and GEL samples disclose the presence of elasticity in materials internal structure and a shear thinning behavior, both trough the significant change in slope and the presence of low values of the flow indexes of the analytical expression. The parameters used for the approximation of the curves are presented in Table 5.4. The influence of squeezing velocity on the viscoelastic behavior of CR and GEL samples is presented in Figure 5.31. In both cases the increase of squeezing velocity leads to a progressive increase of the slope and respectively the flow index.

Table 5.4. Parameters used for the approximation of experimental force distribution of analyzed samples in constant velocity squeeze flow, by using Power-Law force expression.

Fluid	\dot{h} [mm/s]			
	0.01		1	
	k [-]	n [-]	k [-]	n [-]
IK	40	1	40	1
PS	95	0.8	150	0.6
CR	12	0.06	24	0.21
GEL	14.5	0.06	26	0.21

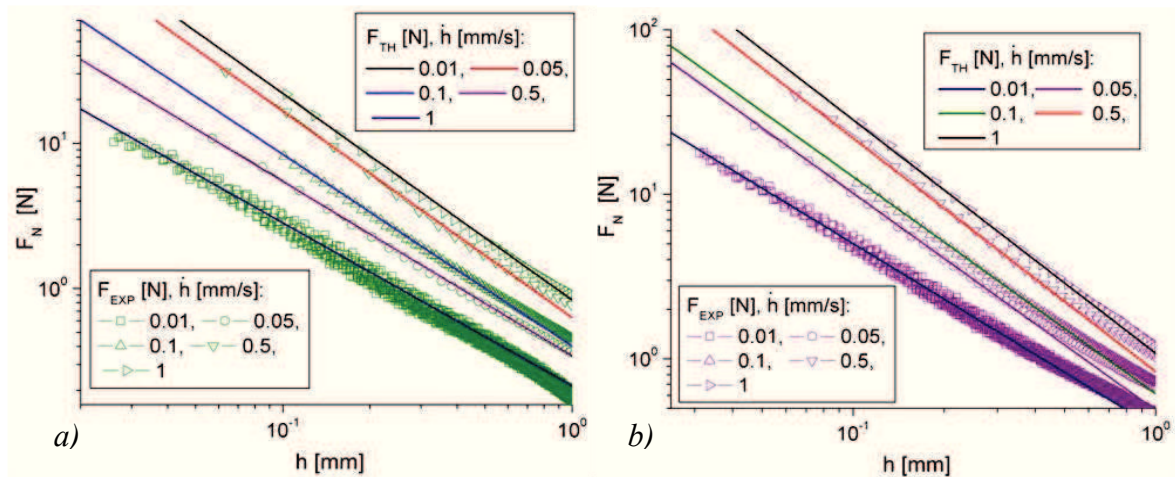


Fig. 5.31. Comparison between experimental measurements and analytical predictions (Power-Law model) of squeezing force for the CR (a) and PS (b) samples at different squeezing velocities.

Both the flow index n and the consistency index k are exclusively dependent on the squeezing velocity. The increase of the consistency index suggests that the elastic structure of the samples responds stiffer at high velocities (see Table 5.5).

Table 5.5. Parameters used for the approximation of experimental force distribution for CR and GEL samples in constant velocity squeeze flow by using Power-Law force expression.

\dot{h} [mm/s]	CR		GEL	
	k [–]	n [–]	k [–]	n [–]
0.01	12	0.06	14.5	0.06
0.05	15	0.1	18.6	0.16
0.1	17.5	0.16	20	0.16
0.5	22	0.21	24	0.21
1	24	0.21	26	0.21

Flow index increase with velocity (strain rate) it is also o indication that viscosity curve (which disclose a shear thinning/pseudoplastic behavior) approach the plateau region (at η_{∞}). It can be also considered the presence of a lubricating film exuded by the samples during the squeezing test, which may lead to a partial slip and thus a change in slope of the force distribution. Even if the elasticity cannot be quantified exactly in a simple squeeze test, it can be showed that at least qualitatively, this motion can be use to obtain some information on the complex rheology of the samples.

5.6. CONCLUSIONS

In this chapter were presented experimental investigations of squeezing motions performed in oscillatory and constant velocity flows on Newtonian and viscoelastic/complex fluids. All tests were performed in controll strain mode, the input being the oscillatory displacement and the constant velocity of the upper plate. Squeezing is not a flow with a simple kinematics (as the shear is), therefore the corresponding formula for the thrust is valid only in thin film approximation, which is not always fullfiled in experiments. The analitic formula corresponding to the normal force, for a given motion of the upper plate is the only available expression for computing the viscosity which does not explicitly contain the expression for the strain rate.

One main conclusion of this chapter is the following: squeezing is an experimental technique able to differentiate the rheological behavior of materials (from pure viscous to viscoelastic, from Newtonian to shear thinning/pseudoplastic character) and to emphasis qualitatively the corresponding rheology. Still, it is not the proper procedure to determine qualitative informations about the material functions. Our investigations also showed that the end effects and wall depletion phenomena might have a relevant influence on the results. Their control is difficult, and normally rise the the price of the equipment. A solution to use squeeze flow as a rheometrical technique is to include the measurements in a CFD procedure, i.e. to couple the experiments with direct numerical simulations. We called this procedure **Computational Rheometry** (see [Chapter 1](#) and [8](#)). A flow can used in “*applied rheometry*”

only if it exists a single definition of a material function, which can be easily computed from the measurements. Based on formula (3.10) we can define the squeeze viscosity function as:

$$\eta_{SQ} = K_{SQ} \frac{F}{\dot{\gamma}_{SQ}} \quad (5.4)$$

where $\dot{\gamma}_{SQ} = V_0/h$ is an apparent squeeze strain rate (for $V_0 = \dot{h}$) and $K_{SQ} = 2h^2/3\pi R^4$ is a geometrical parameter. The material squeeze viscosity is respresented in Figure 5.32, for the tested samples. The results for Newtonian fluids are qualitativley consistent with the data from shear experiments. The squeeze function for non-Newtonian fluids disclose a shear thinning behavior more relevant for cream and gel samples which is also consistent with the computed shear flow index.

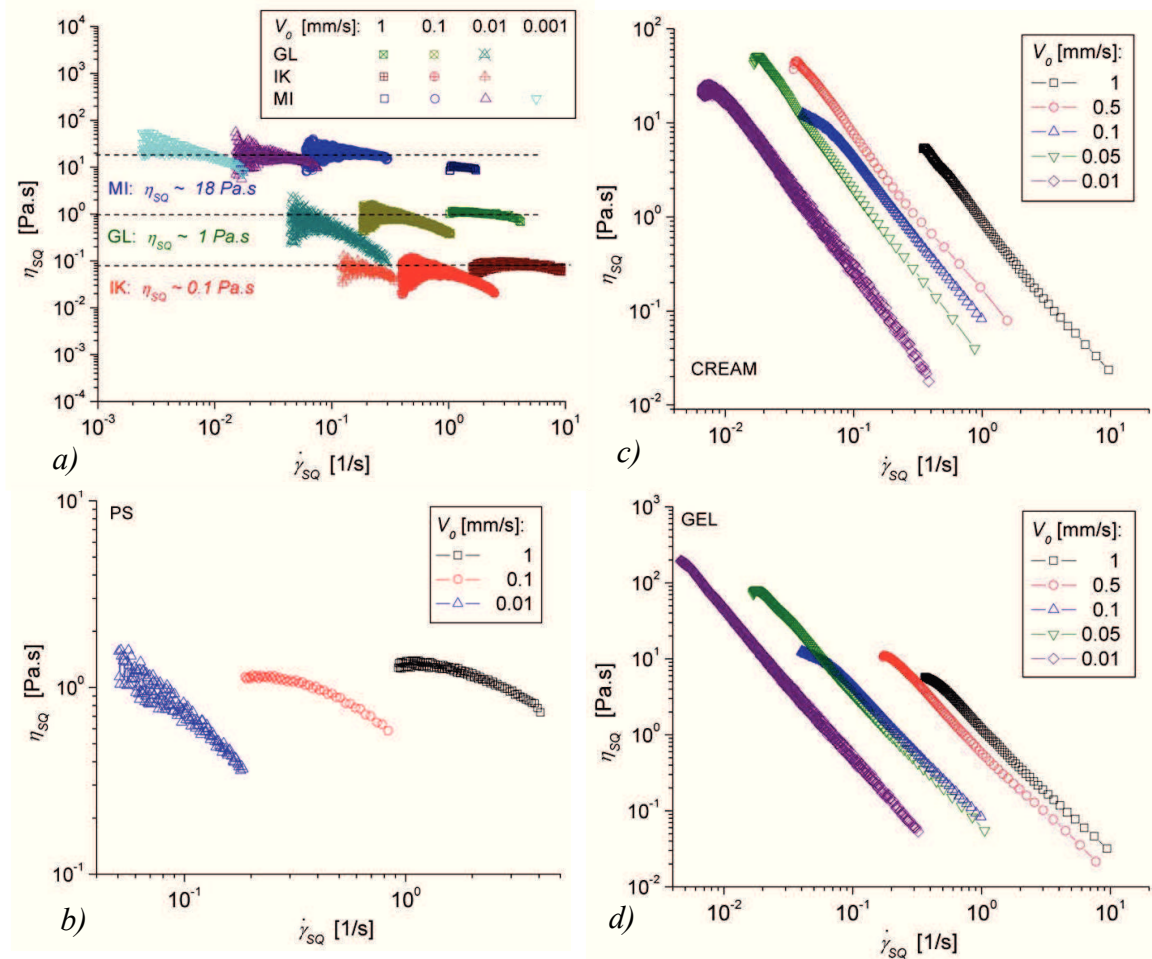


Fig. 5.32. Squeeze viscosity for: Newtonian fluids (honey - MI, glycerin - GL, oil - IK),(a); PS sample (b); cosmetic cream sample CR (c) and gel sample (d).

However the squeeze viscosity (eq. 5.4) is dependent also on the value of squeeze velocity. The proposed relation is just an example of a new material function determined in a flow with complex kinematics which might be taken into consideration when complex fluids must be characterized.

Chapter 6. NONLINEAR BEHAVIOR OF COMPLEX FLUIDS IN SHEAR TESTS

During the last decade, the analysis of nonlinear viscoelastic material behavior has become one of the main research issues in rheology. The understanding and the correction of shear testing procedures; correlations between macroscopic response of fluids under different applied deformations (viscosity curves, flow curves, dynamic moduli variation) and the changes in their microstructure (chemical reactions, particle dynamics); the classification of materials based on their nonlinear rheology, all these aspects represent important steps of establishing a basis of the nonlinear viscoelasticity theory.

The present chapter aims the rheological characterization of some complex fluids in the nonlinear viscoelastic domain and the correlation between different shear testing procedures in order to determine materials parameters that can be used to distinguish the areas of linear and nonlinear viscoelasticity. The analyze also aims to establish a connection between the non-monotonic behavior of yield stress fluids in the transition zone (MAOS regime, dependent on a critical deformation amplitude) in dynamic tests and the critical yield point (critical yield stress or critical rate) which is usually determined in simple shear tests.

In this chapter are characterized the CR and PS samples investigated in squeeze flow (see [Paragraph 5.5](#)). One objective of this study is to correlate both types of experiments and to establish qualitative correspondences between the two sets of data.

6.1. MATERIALS AND METHODS

The samples used in the present work are colloidal systems and suspensions: cosmetic cream (CR) and impression material (polysiloxane - PS), respectively. Lanolin and glycerin have been also tested as reference samples for a typical soft solid rheology (lanolin), respectively for a dominant viscous Newtonian behavior (glycerin).

Cosmetic cream composition of is a mixture of various solvents (water, glycerin, oils), emulsifiers, preservatives solutions (Imidazolidinyl Urea, Propylparaben, Methylparaben), surfactants (Cetyl Alcohol, Cetareth-20), and pigments (CI 47005, CI 14700). Surfactant components of our sample (especially urea) can form in combination with water and oil

phase's different molecular assemblies (micelles, liquid crystals)⁷ and some of its components (antistatic ingredients, pigments) are solid particles. Considering the complexity of sample's structural network, the occurrence of non-linearity is expected during experimental investigations in both simple shear and dynamic testing modes.

The impression material sample is a condensation-curing addition silicone with low consistency used in dental applications (ISO 4823). Corresponding to standard description the sample is a light body material with low consistency and viscosity, containing polydimethylsiloxane, organic peroxide and surfactants.

Lanolin sample is a waxy raw material with a complex micro-structure, predominantly composed of long chain waxy esters, considered generally as emulsion, with a similar rheological behavior as lubricating greases.

The measurements were carried out with a commercial *Physica Anton Paar MCR 301* rheometer using plate-plate (25 mm diameter) and cone-plate (50 mm diameter) geometries at a nominal gap of 0.3 mm; the upper tool is rotated and the lower is at rest, the measurements of torque and angular rotation angle being performed at the upper tool (see [Paragraph 5.1.2.1](#) for description). In order to investigate the possibility of slip phenomena during the tests a gap of 1 mm was also used for dynamic stress/strain sweep tests.

All measurements were performed at constant temperature of 20 °C in both controlled strain and controlled stress mode. Shear stress sweep tests were used to determine transient flow curves for the cream sample.

Multiple creep, stressing and stress relaxation tests were carried out for the PS sample in order to build a steady state flow curve for this material. Elastic and viscous components were determined for all analyzed samples through multiple dynamic amplitude sweep tests performed at different frequency values.

No rough surfaces or special techniques were used to avoid a possible slip of samples during the experiments. Each test presented and discussed in this paper was performed at least two times, both qualitative and quantitative measured data being almost identical.

Of course, we also obtained sometimes results which disclose spurious or wall depletion effects, but they are not taken into consideration in the present work. Moreover for a better understanding of materials behavior and the possible changes that may appear in their microstructure they were observed with a microscope in their initial state and after a simple shear deformation ($\dot{\gamma} = 1 [s^{-1}]$ for 300 s). After applying the deformation there weren't observed important changes of materials structure (see. [Annex 8](#)).

6.2. NONLINEAR VISCOELASTIC BEHAVIOR IN DYNAMIC SHEAR TESTS

The investigation started with multiple dynamic strain amplitude sweep tests performed for all of our samples at different angular frequencies, $\omega \in [1 \div 50 \text{ rad/s}]$. The first two figures show the materials elastic (G') and viscous (G'') moduli obtained at $\omega = 1 \text{ rad/s}$ and $\omega = 10 \text{ rad/s}$ (Figures 6.1.a and b). The glycerin sample discloses a pure Newtonian behavior (constant G'' and no elasticity, i.e. $G' = 0$). The lanolin sample has a solid-like behavior ($G' > G''$) for small strain amplitudes and a liquid-like behavior ($G' < G''$) after the crossing point at very low strain amplitude ($\gamma_0 \cong 0.03$). However, the high values of both moduli is a typical rheological behavior of soft solids (type 1), in comparison with the non-monotonous distribution of G' and G'' observed in the case of cream (CR) and polysiloxane (PS), samples considered complex fluids belonging to soft matter materials thinning (see. Paragraph 2.4), [114], [116], [117].

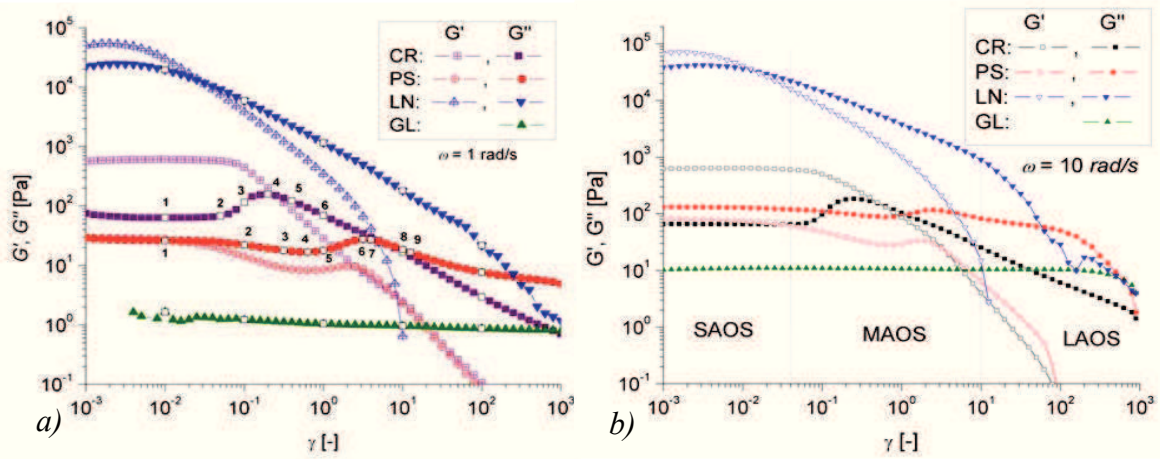


Fig. 6.1. Dynamic strain sweeps at constant angular frequency, $\omega = 1 \text{ rad/s}$ (a) and $\omega = 10 \text{ rad/s}$ (b): cosmetic cream (CR), polysiloxane (PS), lanolin (LN) and glycerin (GL). Hollow marks indicate the points where the Lissajous figures were extracted.

An unusual increase of viscous modulus is found for CR sample in the vicinity of the crossing point ($\gamma_0 \cong 0.25$) between solid-like and liquid-like behavior. The relatively maximum (called also „peak”) appears at a strain value of $\gamma_0 \cong 0.2$ which indicates a non-monotonous rheological behavior, classified in literature as a weak strain overshoot behavior (type 3).

In the case of PS sample, both G' and G'' disclose a peak. It is easily observed that PS sample has a pronounced viscous behavior in comparison with CR sample ($G' \leq G''$) for almost the whole tested strain amplitudes. At a critical strain of $\gamma_0 \cong 0.012$ the elastic modulus starts to decrease and the sample behavior changes from a weak elastic behavior (G'

and G'' have almost same value) to a liquid dominated one. However this transition seems to be unstable since for both viscous and elastic components present fluctuations before the onset of fluid behavior (where both moduli begin to decrease monotonically). The relative peak is present for G' at a strain of $\gamma_0 \cong 2.50$ and after his occurrence an abrupt decrease is found for this component. In the case of G'' the peak occurs at a strain value of $\gamma_0 \cong 3.15$ and its decrease is smoother on the strain domain. This type of behavior is less met in literature being specific to associative polymers; it is classified as a strong strain overshoot behavior (type 4) [114], [116], [117]. The numbers shown in Figure 6.1 indicate the points on G'' curve selected for a further more complex analyze in terms of Lissajous figures (Figures 6.6 – 6.8) and raw stress signals (Figure 6.2), in order to obtain a better understanding and characterization of this complex rheological behavior of transition.

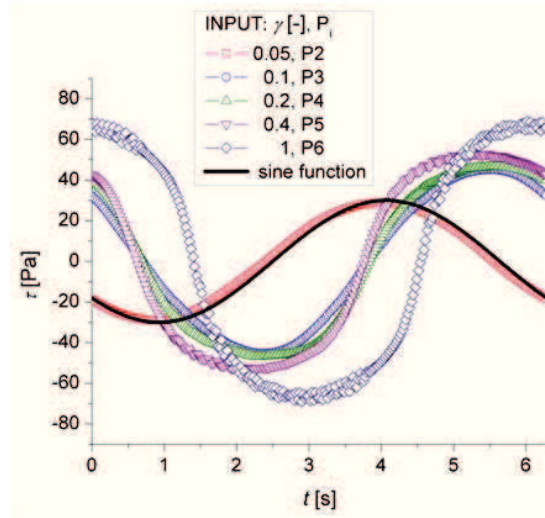


Fig. 6.2. Oscillatory shear stress output for CR sample as function of the strain amplitude input $\omega = 1 \text{ rad/s}$, corresponding to the points selected in Figure 6.1.

Applying a sinusoidal deformation (input) to a sample, material's stress response (output) is expected to have also sine waveform, at least at small applied deformations. Figure 6.2 shows the output raw data of the amplitude strain test for CR sample. The stress signal wave is starting to deform from its sinusoidal form (linear regime – SAOS) as the strain increases and leads the sample in the transition zone (MAOS). At a strain amplitude of only $\gamma_0 \cong 0.05$, corresponding to the second point (P2) marked in Figure 6.1, the stress signal begins to deform from the pure sine waveform (represented by the solid black-line).

This indicates the onset of a non-linear regime. As the input strain increases, the output signal becomes more deformed changing its shape when passing from small to medium and from medium to large amplitudes (LAOS), where it has a tendency to have a rectangular form specific to hard gel solutions [114]. It is important to remark that the same phenomena,

deformation of the output signal beyond a critical strain amplitude, was observed also in squeezing (see Paragraph 5.3).

Figure 6.3 presents shear stress distribution for CR and PS samples. The dynamic moduli against strain amplitude for multiple frequencies are presented in Figure 6.4 for both samples, in the range of $\omega \in [1 \div 30 \text{ rad/s}]$. The delimitation of the three regimes is easily observed and independent on frequency value. For CR sample we define a linear regime for small amplitude oscillatory shear strain values (SAOS) where $\gamma_0 < 0.05$; a medium amplitude oscillatory shear (MAOS) for $0.05 < \gamma_0 < 5$ (where the transition from solid-like to liquid-like behavior is made and the instability in material structure is pronounced) and a large amplitude oscillatory shear domain (LAOS) for $\gamma_0 > 5$ (see Figure 6.3.a).

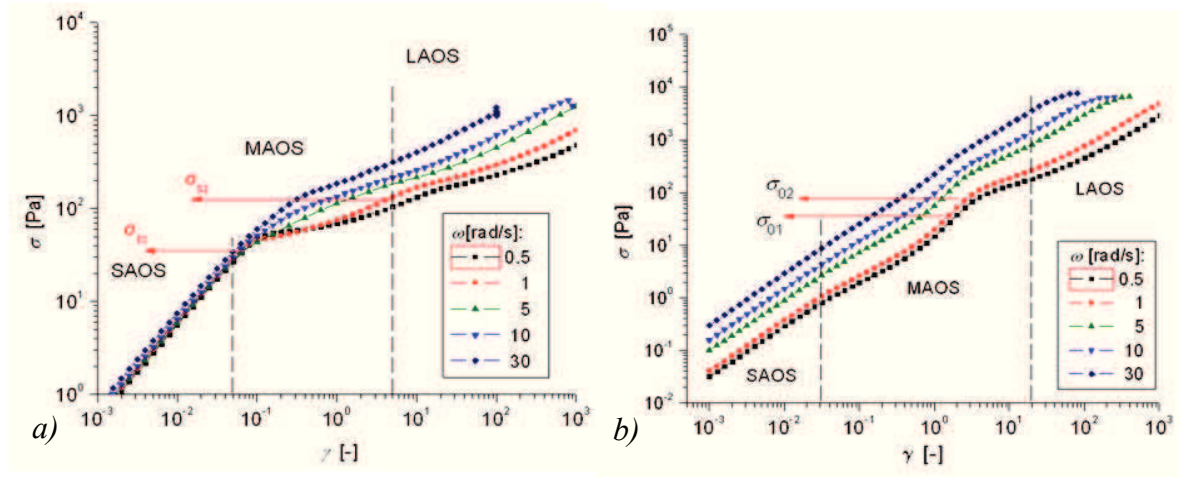


Fig. 6.3. Dynamic strain sweeps at various angular frequency values for CR (a) and PS (b) sample. The delimitation of the flow regimes as function of the input strain amplitude and shear stress variation.

In the case of CR sample frequency dependence is manifested only in MAOS and LAOS zones, in SAOS the stress amplitude being a function of only of strain amplitude $\sigma_0 = \sigma_0(\gamma_0)$, with almost a linear dependence.

This behavior is typical for gel-like material structures and the shape of the signal places our CR sample somewhere between soft and hard gel behavior. When entering MAOS region shear stress amplitude starts to manifest a dependency on the applied frequency $\sigma_0 = \sigma_0(\gamma_0, \omega)$ (σ_0 is increasing with ω at constant γ_0 , see Figure 6.3.a, the dependence becomes more sensitive approaching the LAOS domain).

This behavior is well emphasized by the loss modulus distribution, which discloses in MAOS region a remarkable peak at the value of strain amplitude in the range of $\gamma_0 \in (0.2 \div 0.3)$ for all applied frequencies (see Figure 6.4.b). Furthermore, the G'' values found in the SAOS regime and the maximum value reached in MAOS region increases with oscillatory

frequency, this dependence being well marked for $\gamma_0 > 5$, where the onset of LAOS regime is considered (see Figure 6.4.c).

In comparison to CR material, the PS sample responds like a visco-elastic material, with shear stress amplitude increasing directly with both strain amplitude and frequency $\sigma_0 = \sigma_0(\gamma_0, \omega)$, see Figure 6.3.b. In the MAOS region, $\gamma_0 \in (0.03 \div 20)$, stress response fluctuates, the moduli decreasing and increasing with strain amplitude, passing through a relatively peak before to enter the LAOS domain.

The presence of this instability and the peaks in G' and G'' are more relevant at low values of angular frequency ($\omega \leq 10 \text{ rad/s}$, the phenomena being diminished once increasing angular frequency. Both storage (Figure 6.4.c) and loss moduli (Figure 6.4.d) decrease once entering the unstable zone until they reach a critical strain amplitude ($\gamma_0 \cong 0.5$) and start to increase. The peaks (G'' peaks appearing earlier than for G') are present at strain amplitude of $\gamma_0 \in (2.5 \div 3)$, shifted to lower values in this range by increasing frequency.

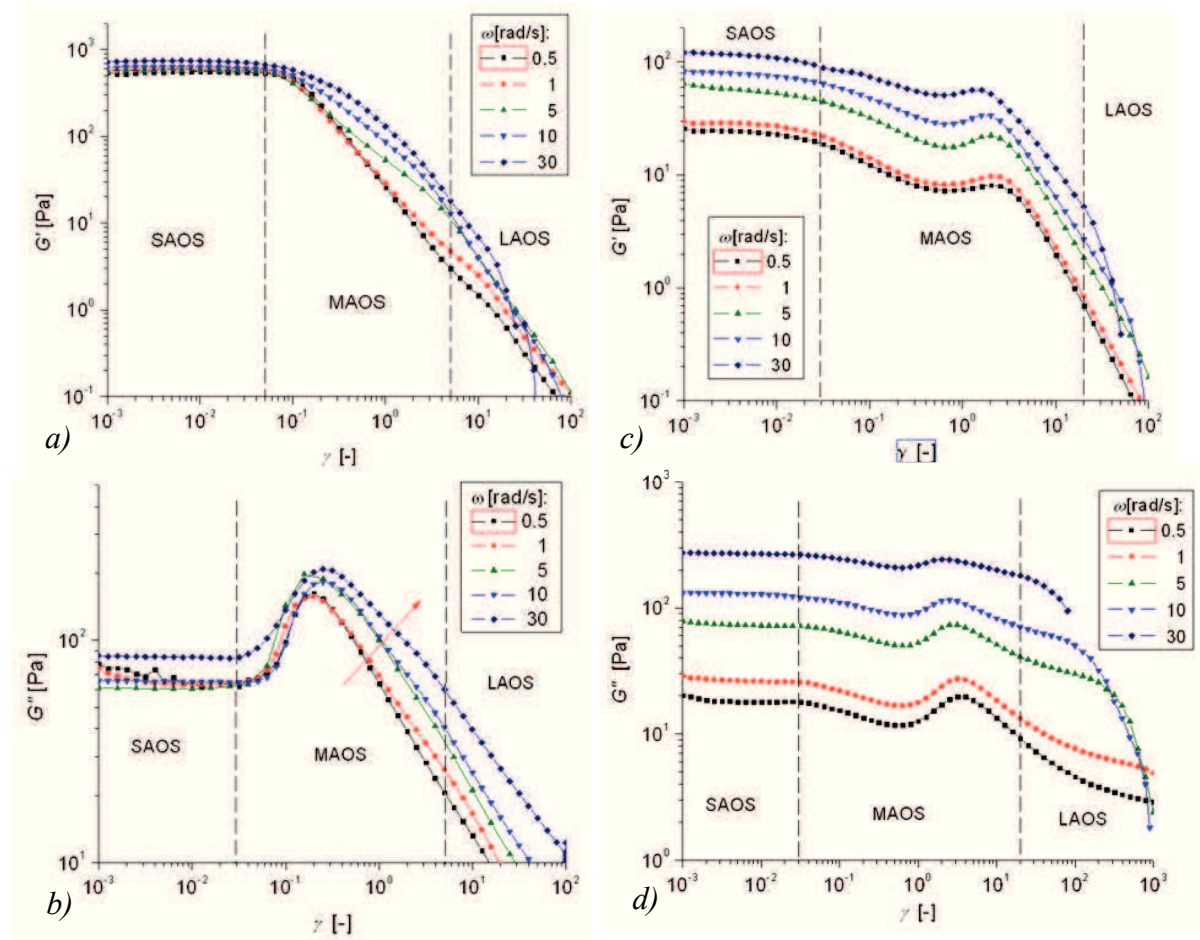


Fig. 6.4. Dynamic strain sweeps at various angular frequency values for CR (a,b) and PS (c,d) sample. The delimitation of the flow regimes as function of the input strain amplitude: storage modulus (a,c) and loss modulus (b,d).

The Lissajous figures are representations of raw stress response vs. strain (or shear rate) for the whole period of oscillation. For visco-elastic materials in the non-linear regime (MAOS, LAOS) the shape of Lissajous loop deforms from its original ellipsoidal shape due to the deformation of the stress output signal (see Figure 6.2).

Therefore, it is expected that the shape and area of Lissajous figures contain value information on the change in material rheology with the increasing of the input magnitude. Figure 6.5 and Figure 6.5 show the Lissajous loops for CR and respectively PS samples at a constant frequency $\omega = 1 \text{ rad/s}$, corresponding to the points indicated in Figure 6.1.

When strain increases at the end of SAOS domain the visco-elastic behavior of CR sample, showed by the ellipsoidal shape of the loop (P1), starts to change. The area of loop increases with strain amplitude and its shape deforms, stretches horizontally and flattens vertically tending to a square-like shape at high strains (Figure 6.5).

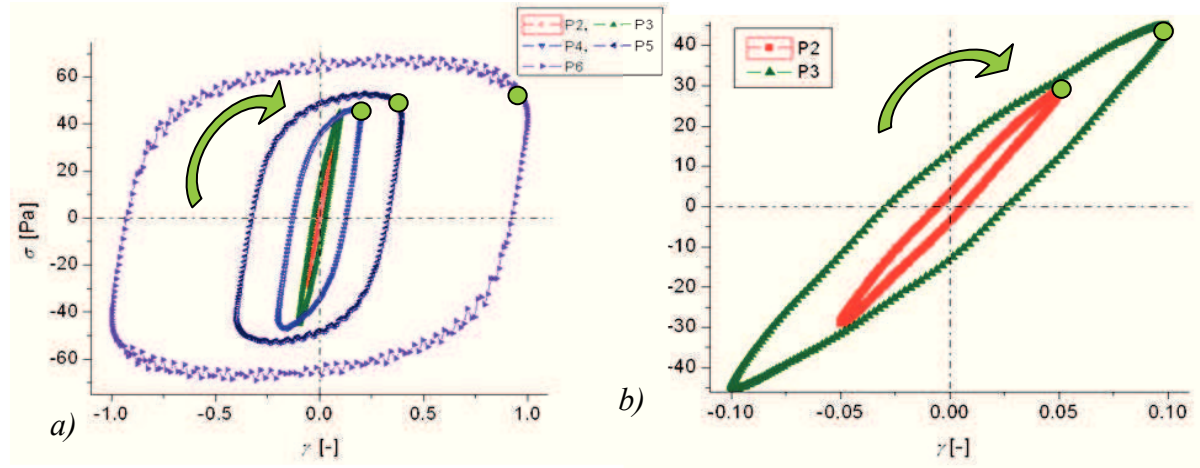


Fig. 6.5. Lissajous figures, oscillatory stress vs. oscillatory strain, for CR sample corresponding to the points indicated in Figure 6.1, $\omega = 1 \text{ rad/s}$. (a); the detail P3 point marks the onset of non-linearity (b).

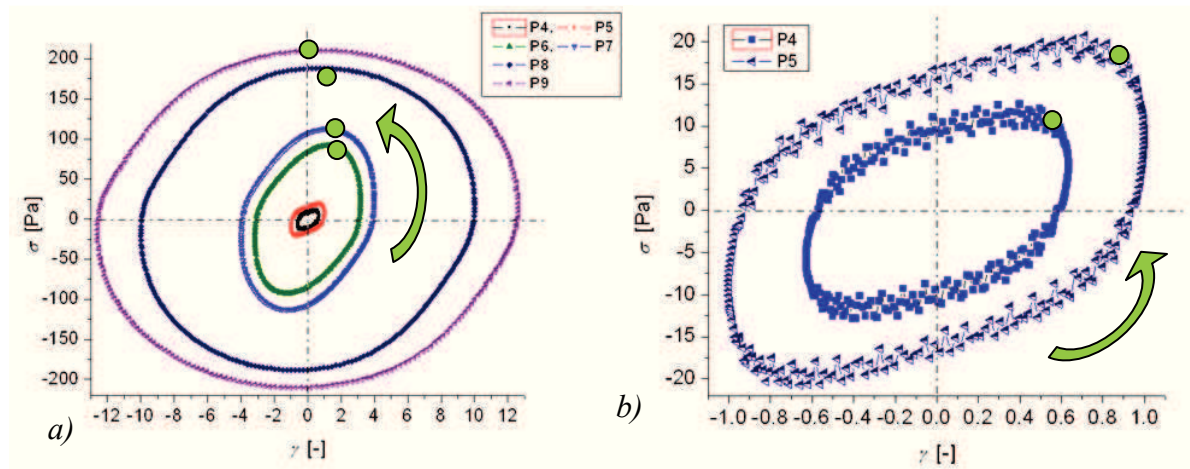


Fig. 6.6. Lissajous figures, oscillatory stress vs. oscillatory strain, for PS sample corresponding to the points indicated in Figure 6.1, $\omega = 1 \text{ rad/s}$. (a). And a detail on P4 and P5 points (b).

The clockwise rotation of the loops indicates a gradual softening of the material with increasing strain amplitude [81], [82], [83]. The elongated distorted shape of the curves disclose a weak strain-stiffening behavior and as approaching larger strains (in LAOS region) the rectangular shape indicates a shear-thinning behavior and a gel-like structure of our sample [82], [114].

In the case of PS sample (Figure 6.6), as entering the MAOS region the Lissajous figures deform with the similar evolution as for the cream sample. The shape elongates horizontally and flattens vertically (P4, P5) but then it rotates counter-clockwise and takes almost an oval shape (P6, P7) tending to a circle shape in LAOS region (P8, P9). PS sample discloses also a weak strain-stiffening behavior with increasing strain amplitude but unlike CR sample, PS has a more pronounced viscous character in MAOS and LAOS zones [82], [114]. If we make comparison between Lissajous figures in shear (Figure 6.6) and squeezing (Figure 5.18) we observe the same qualitative rheological behavior, so both experiments are consistent.

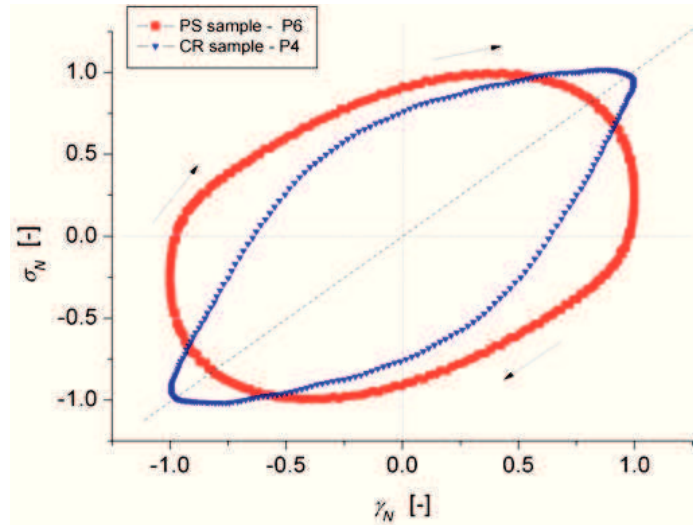


Fig. 6.7. Normalized Lissajous figures corresponding to the maximum of G'' for CR and PS samples at $\omega = 1 \text{ rad/s}$ (see Figure 6.1).

The differences between the structure and evolution of the two tested soft matters are evidenced in Figure 6.7, where the normalized Lissajous loops are plotted for the peak points of viscous modulus G'' , see Figure 6.1.

The cream sample tends to a strain stiffening gel behavior, the elongation of the loop showing also a weak strain overshoot, given only by the viscous component. In the case of the PS sample the loop tends to an oval shape, stretching and widening in the same time because of the contribution of both viscous and elastic components. The informations extracted from the Lissajous curves correspond to the materials behavior in SAOS region. As it can be seen in Figure 6.8 the two tested samples disclose a different behavior in frequency sweep

experiment performed in SAOS. Within the small amplitude domain CR exhibit a gel-like behavior with G' and G'' almost parallel and the PS sample has a shear-thinning visco-elastic behavior, passing from solid-like ($G' > G''$) to liquid-like ($G' < G''$) behavior at a frequency value almost equal to unit.

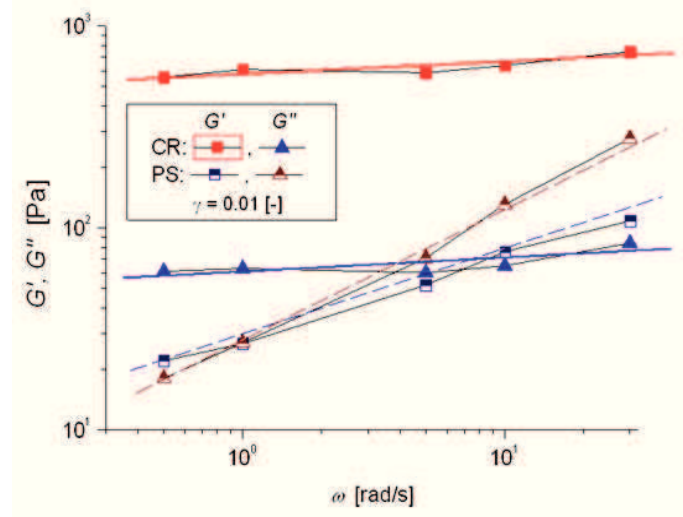


Fig. 6.8. Dynamics moduli vs. angular frequency in SAOS regime for CR and PS samples: gel structure for CR, respectively transition region for PS.

The area of stress/strain Lissajous figure is proportional with the viscous energy dissipated by the system materialului [81], [114], [196], whereas the area of stress/strain rate shows the energy stored by the material structure [143].

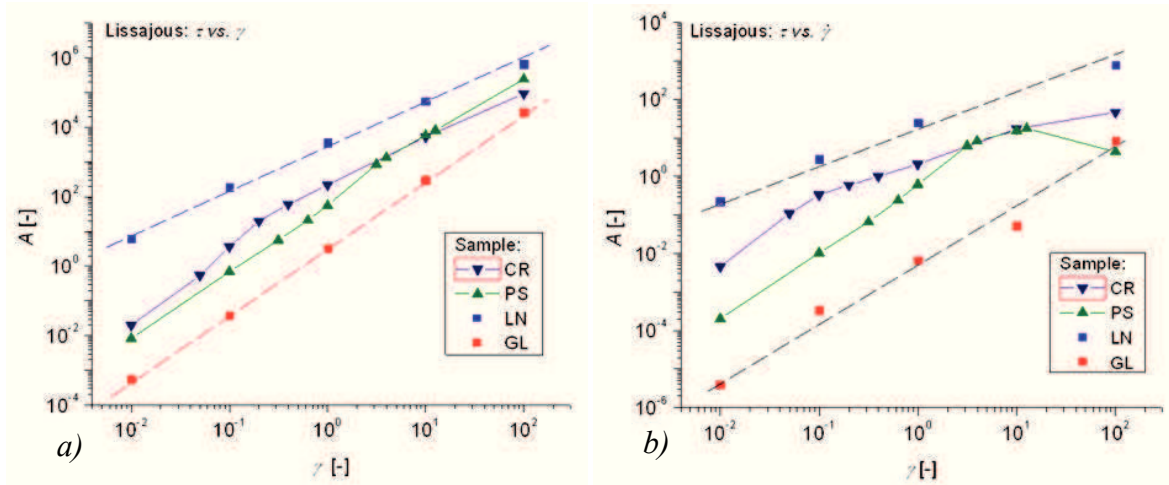


Fig. 6.9. Area of Lissajous figures vs. strain amplitude for the tested sample, oscillatory stress vs. oscillatory strain (a) and oscillatory stress vs. oscillatory shear rate (b) at $\omega = 1 \text{ rad/s}$.

Looking at the evolution of Lissajous loops areas, corresponding to the points marked in Figure 6.1, a first notice is the monotonic increasing in the case of GL and LN samples, as expected since they disclose a simple and predictable rheological behavior (see Figure 6.9). In the case of CR sample the area of stress vs. strain loop increases at higher rate once entering

MAOS region (corresponding to the peak in G''), meaning the viscous energy is dissipated probably due to the breakup of the network microstructures that had already stored tension at the beginning of the flow, as indicated by the increase of stress vs. rate curve area.

In the case of PS sample, the area of loops increase higher as reaching the peaks observed in both moduli. During the transition zone the dissipated energy seems to be increase with a smaller rate than the stored one, indicating a strong strain overshoot in MAOS region (accumulating tension in the structure) and a strain thinning at large strains where the system dissipates more energy but it stops accumulating (from the decrease of area stress vs. rate). As is expected, for both samples the maximum of the rate areas increasing is reached at the critical values of the strains already found in the previous experiments.

6.3. NONLINEAR VISCOELASTICITY IN SIMPLE SHEAR FLOWS

This section introduces a new highlighting procedure of the nonlinear viscoelastic behavior of complex fluids by using simple shear tests and by correlating the simple shear response with the dynamic one (presented in the previous paragraph). In Figure 6.10 are shown flow curves of CR sample obtained through multiple stress-controlled tests at imposed shear stress that increases (filled points) or decreases (open points) in the range $\sigma \in [1 \div 400 \text{ Pa}]$, with different slopes in time.

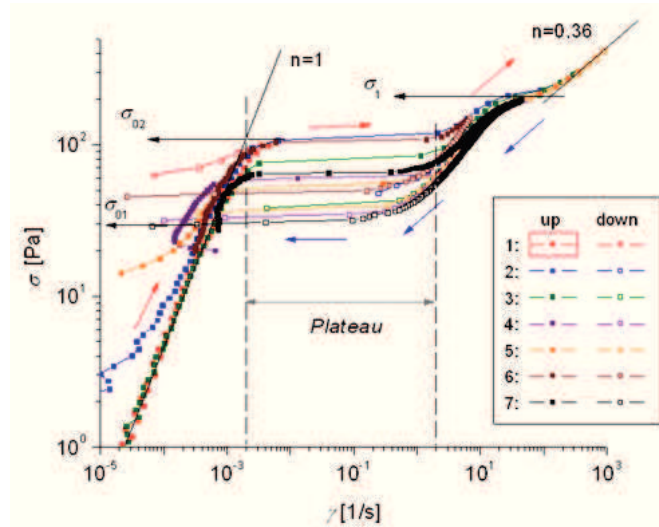


Fig. 6.10. Transient up (filled points) and down (hollow points) flow curves (shear stress vs. shear rate) for CR sample (stress controlled experiments at $\sigma \in [1 \div 400] \text{ Pa}$).

The flow curves exhibit a “plateau” zone for shear rates $\dot{\gamma} \in (0.002 \div 2) \text{ s}^{-1}$ and $\sigma \in [30 \div 110 \text{ Pa}]$, depending of the history of imposed load, respectively deformation. We have to notice that limit stress values of this instability/jump zone are found delimiting also the MAOS domain at low frequencies, σ_{01} and σ_{02} in Figure 6.3.a. At $\sigma_1 \cong 210 \text{ Pa}$ shear

stress distribution tends to form a second (smaller) plateau before entering LAOS region and changing its slope from almost Newtonian one, previous to the jump, to a strong shear thinning behavior. Hence, the sample discloses a well defined zero shear viscosity.

The observed jump in shear rate under a constant applied shear stress is associated either with intrinsic instability of the constitutive relation [13], [16], [45], or to the slip of the sample at one plate. In the first case we can speak about a real yield stress which determines a “kink” in the velocity distribution within the gap, keeping valid the adherence conditions at the walls [13], [16], [68], [95], [170], [171].

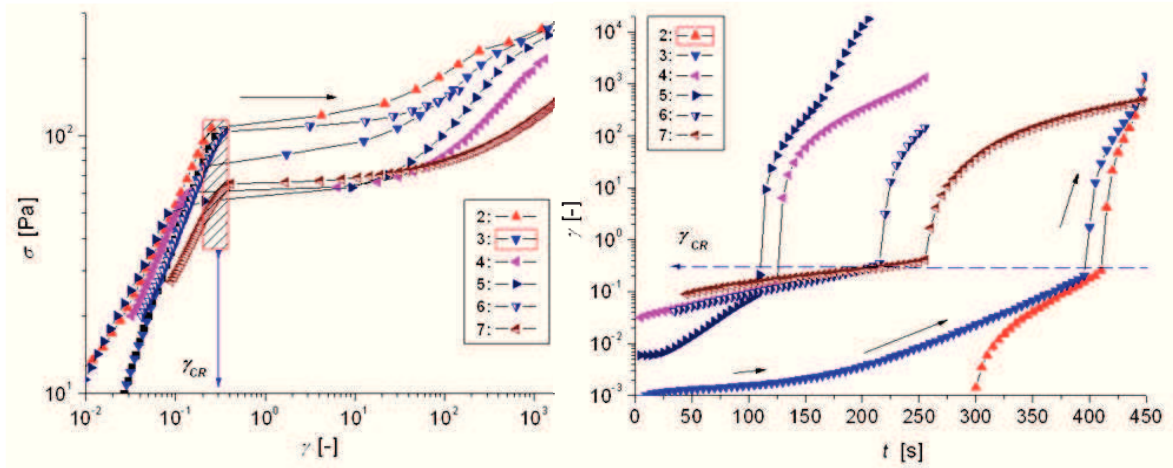


Fig. 6.11. Critical strain value emphasized for CR sample in shear experiments (see Figure 6.10): applied shear stress vs. strain (a) and strain vs. time (b).

This definition of yield stress associates its value with the corresponding shear stress of the jump. Although the jump has not a very precise location on the flow curve - $\sigma(\dot{\gamma})$, one can observe that the critical point of the plateau onset is well defined by a unique strain value γ_{cr} (see Figure 6.11). As can be observed from Figure 6.11.b the value of strain associated with the jump in rate from the flow curves is well established at $\gamma_{cr} = 0.28$, which corresponds to the interval where the peak in G'' is observed (see Figure 6.4.b).

Multiple creep, stressing and relaxation tests were performed for the PS sample in order to determine the viscosity variation in time (Figure 6.12), the viscosity transient curve (Figure 6.13) and to build up a quasi-steady flow curve (Figure 6.14).

At small imposed shear stresses, $\sigma < 50 \text{ Pa}$, viscosity tends to increase reaching a steady state value η_0 and for $\sigma > 50 \text{ Pa}$ it decreases towards a second steady state value, η_∞ .

For $\sigma = 50 \text{ Pa}$ the viscosity strives to reach η_0 , but the observational time (4000 s) is not enough for the curve to attend the steady state value hence it remains in the unstable zone corresponding to S2 solution (see Figure 6.12). The critical value indicated by viscosity distribution in time is an indicator of the instability domain as it will be shown furtheron.

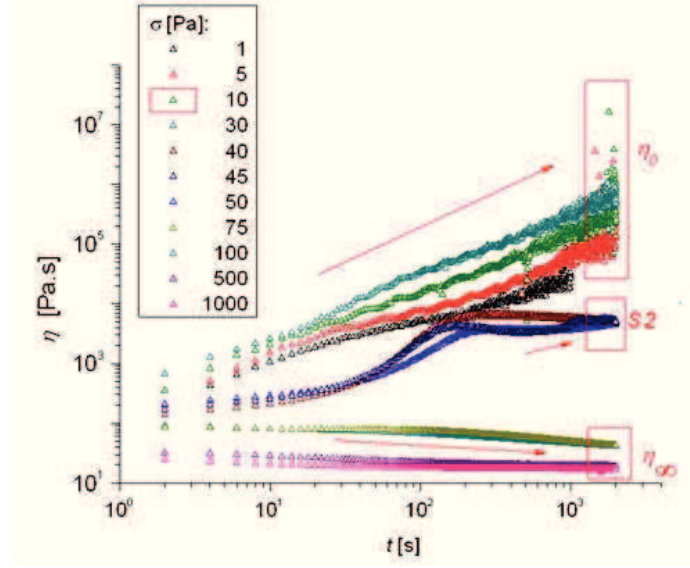


Fig. 6.12. Time dependent viscosity curves obtained through multiple Creep tests for PS sample.

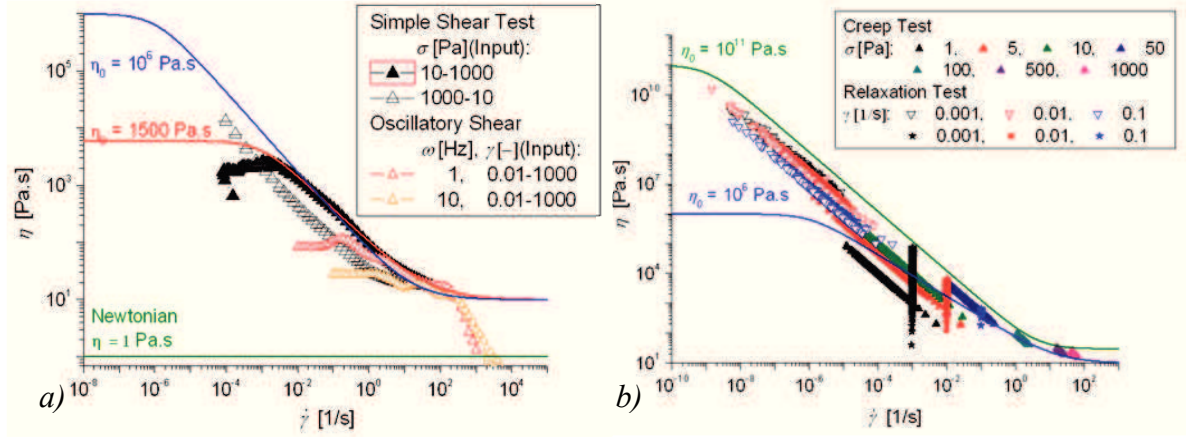


Fig. 6.13. Viscosity dependence on shear rate for PS sample and the interpolation of the measured values using Carreau-Yasuda model: comparison between dynamic shear tests (strain controlled) and simple shear tests (stress controlled), (a); construction of a transient flow curve from multiple Creep and Stress Relaxation tests (b).

Results coherence is emphasised in Figure 6.13 by the correspondence between simple shear and dynamic shear measurements performed in both control stress and control strain modes. The measured values can be interpolated using Carreau-Yasuda model. Additionally, the result discloses the need of performing multiple types of test in order to get a good representation of the viscosity curve, hence a proper approximation of sample rheology. In Figure 6.13.a, dynamic measurements indicate a zero shear viscosity of $\eta_0 = 1500 \text{ Pa.s}$. When correlating the dynamic measurements with the simple shear tests (Figure 6.13.b), we can interpolate the results using a higher value of the zero viscosity $\eta_0 = 10^5 \text{ Pa.s}$.

However, if relaxation domains are taken into consideration, see Figure 6.13.b, a much larger zero shear viscosity is observed $\eta_0 = 10^{11} \text{ Pa.s}$. Such values are characteristic to complex fluids with a pronounced and well defined yield stress. This value is not a real steady

state since for the relaxation domain, the upper plate is at rest, so the measurement is performed in transition to rest.

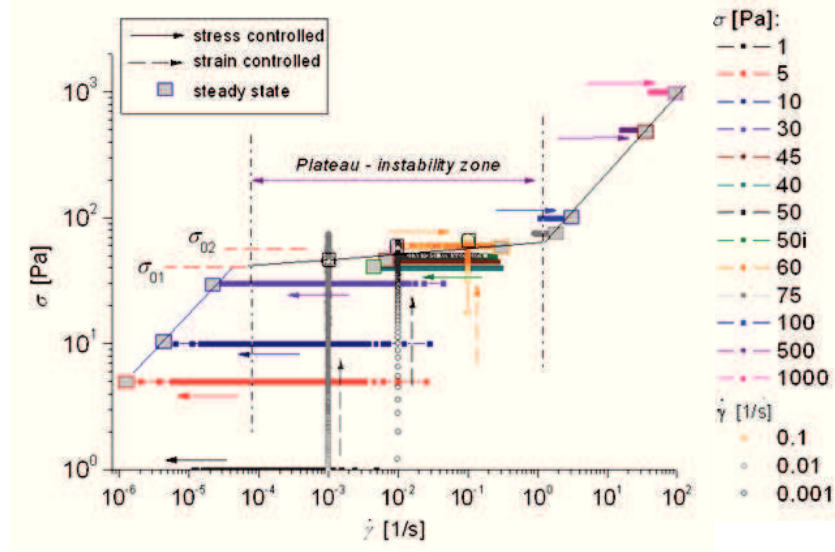


Fig. 6.14. Quasi-steady flow curve for PS sample (multiple stress and strain controlled shear tests).

Under different values of the applied shear stress the dynamics of the samples disclose around the value $\sigma \cong 50 \text{ Pa}$ a plateau behavior in the quasi-steady flow curve (Figure 6.14). A shear stress domain of $\sigma \in [40 \div 60] \text{ Pa}$ is established, for $\dot{\gamma} \in (10^{-4} \div 10^0) [1/s]$, where the material presents a less predictable behavior, zone which corresponds to the MAOS region. In the instability domain, the shear stress vs. shear rate variation changes direction from “towards left” to “towards right”, similar to the variation in time of viscosity distribution showed in Figure 6.12.

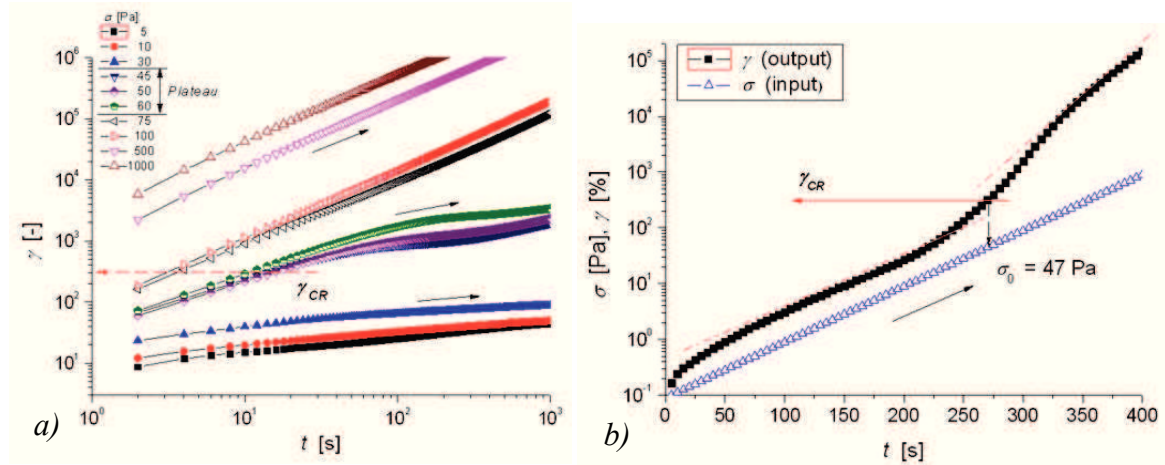


Fig. 6.15. Creep curves performed for the PS sample: a) constant shear stress, see Fig. 7; b) shear stress sweep. In both experiments is emphasis the same value of critical strain, i.e. $\gamma_{cr} \cong 3 [-]$.

Also, like for CR sample, there is critical strain amplitude $\gamma_{cr} \cong 3 [-]$ that seems to mark the onset of the jump in shear rate from simple shear tests (Figure 6.15), which can be correlated to the maximum of G'' distribution presented in Figure 6.4.d.

6.4. FOURIER ANALYSIS AND INVESTIGATION OF SLIP OCCURRENCE

One conclusion is that tested soft matter samples (complex fluids with yield stress) discloses in a shear flow a critical strain value, γ_{cr} , which define the onset of the liquid-like behavior. This value is associated to the existence of a plateau in flow curve and the relatively maximum of viscous modulus in strain amplitude sweep experiment. The plateau might be also related to the jump in strain rate at a constant value of shear stress, σ_0 . In this case, the yield state is given by the pair (σ_0, γ_{cr}) , the strain value γ_{cr} being the characteristic measure of the critical yield point. Since the plateau in flow curve is directly related to a jump in shear rate, it is important to make difference between the existence of the yield state and possible slip at the boundary. Some “wall depletion phenomena” might generate in shear flows similar experimental findings and the distinguish between them is not trivial in the absence of a quality visualization system, at which our laboratory has not access at this moment (as we already mentioned, the present experiments are considered related to intrinsic material rheology and not with boundary effects).

The rheometry performed in the non-linear domain (MAOS and LAOS regimes), corroborated with sets of strain and stress controlled shear experiments, might be a solution to find a proper answer to this intrigue “rheological question”: is the deformation process of soft matter samples characterized by a yield state, or the material is subject to slip at the boundary due to specific microscopic architecture?

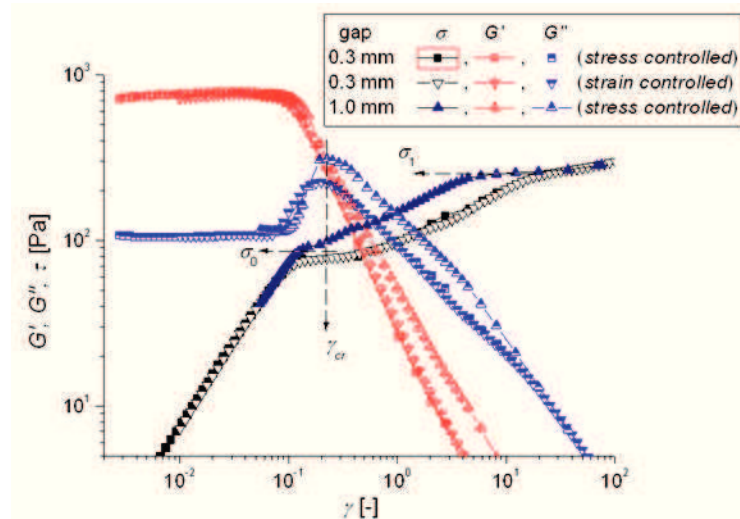


Fig. 6.16. Answers of CR sample in oscillatory tests under different experimental conditions (strain/stress amplitude sweep $\omega = 1 \text{ rad/s}$), see also [Figure 6.1](#).

However, the present experiments prove that observed macroscopic phenomena is characterized by the same value of the strain, which make sense if that critical strain value is a well defined material property. If what we observe is a manifest of slipping, it means that slip

at the boundary (for a given boundary geometry) is independent on the type of applied test and on the history of deformation. We consider the first explanation more plausible.

The experiments were completed for CR sample by several strain and stress controlled tests. In Figure 6.16 are shown three amplitude sweeps with very similar qualitative/quantitative results: same location of the yield point as the previous findings, i.e. $\gamma_{cr} \cong 0.23$ and $\sigma_0 \cong 80 \text{ Pa}$. Here is also present the second plateau corresponding to a stress value of $\sigma_1 \cong 250 \text{ Pa}$, see also Figure 6.10.

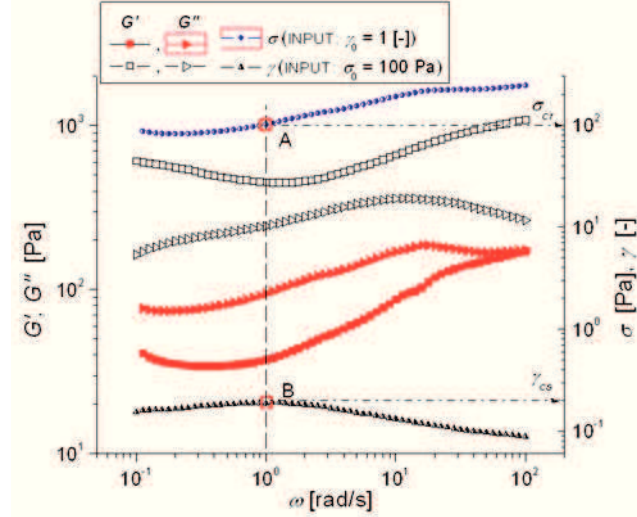


Fig. 6.17. Frequency sweep (controlled strain and controlled stress experiments) for CR sample. The corresponding values of loss tangent are: $\tan\delta = 2.6$ (point A – controlled strain), respectively $\tan\delta = 0.52$ (point B – controlled stress), see Figure 6.16.

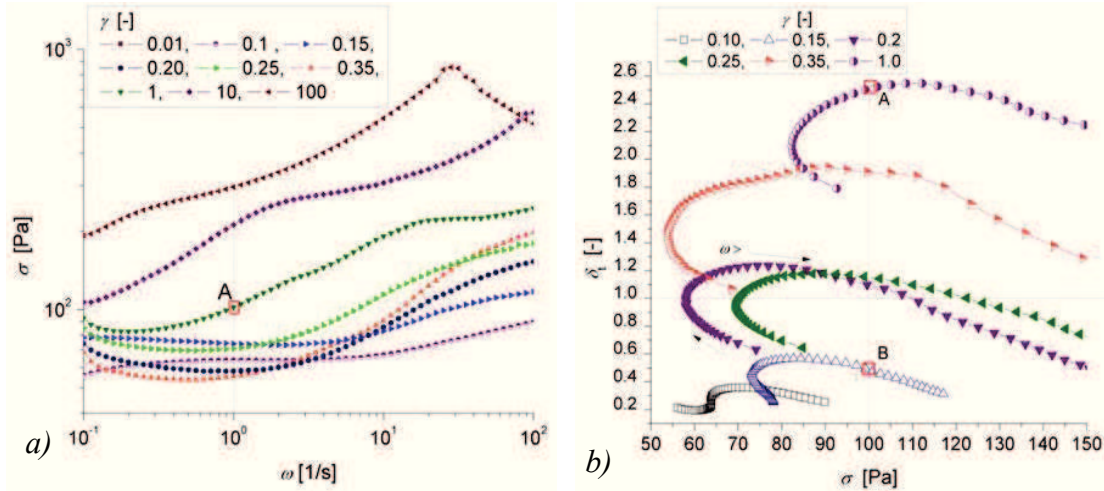


Fig. 6.18. Shear stress amplitude and loss tangent in frequency sweep test at different input strain amplitudes (CR sample). It is important to remark that rheological characteristics recorded in the stress controlled experiment from Figure 6.17 are also found in the strain controlled test, see location of point B in the two graphs.

Figure 6.17 presents frequency sweeps performed in MAOS domain. The correlation between test is very good if you assume the existence of a plateau in shear stress amplitude vs. strain amplitude: at $\sigma_0 = 100 \text{ Pa}$ the strain controlled test is characterized by $\gamma_0 = 1$ and

the stress controlled gives a deformation amplitude of $\gamma_0 = 0.2$, data which are consistent with results from Figure 6.16. Moreover, the strain controlled impose a flow within the sample (point A is after the peak in G'' , $G' < G''$), whereas the stress controlled keeps the sample as a solid-like (point B is before the peak in G'' , $G' > G''$), see also Figure 6.18.

The decompositions of the output signal using the FT-rheology are shown in Figure 6.19. The tests were performed with and without the DSO system, using for the stress input test (Figure 19.a) the wave analysis modulus of *Physica MC 301 rheometer*. There are observed: (i) the sharp increasing of the third harmonic ones the MAOS regime is established (more than 10% from A1 at strain amplitudes higher than γ_{cr}), (ii) the maintaining of the second harmonic generally below 1% from A1 for all regimes (with exception of the data extracted from the frequency sweep test in Figure 19.b).

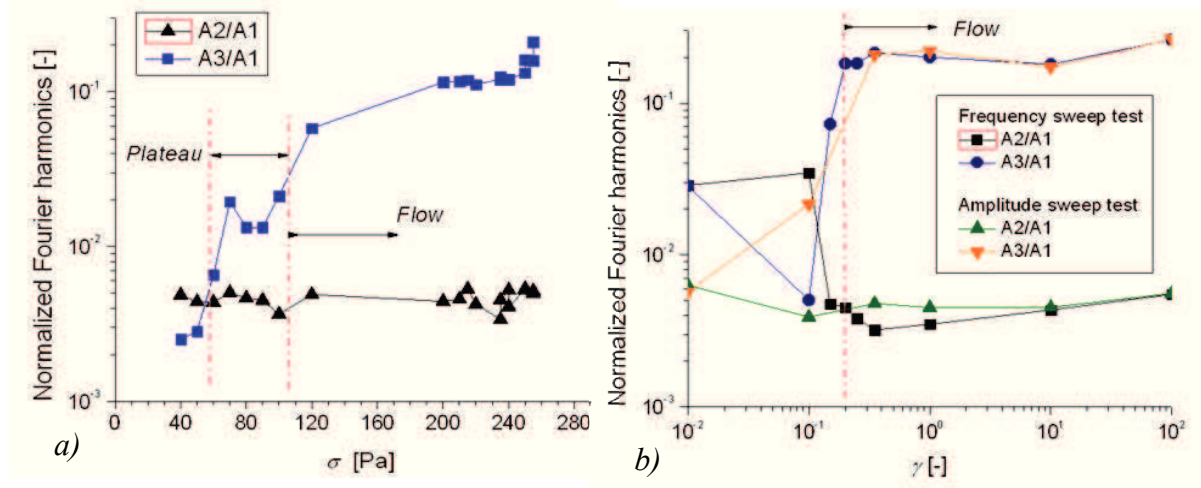


Fig. 6.19. The normalized Fourier harmonics extracted from stress input (a) and strain input (b) tests at $\omega = 1 \text{ rad/s}$. The results mark the same interval for critical values of strain, respectively stress, amplitudes from which the materials start to flow.

The increasing of the third harmonic is not monotonous in MAOS regime, which suggest the existence of the plateau in the flow curve. The existence of the second harmonic at relative amplitudes lower than 1% is normal for measurements performed with standard equipment. However, the data at low values for frequency sweep conditions (Figure 19.b) might suggest not necessary the existence of slip [101], especially if the material is characterized by non-monotonic constitutive relation [10], [11], [13], [16], [45], [132].

6.5. CONCLUSIONS

The present chapter was concerned with rheological investigations of two soft matter samples in oscillation and simple shear flows. The tested materials, a cosmetic cream (CR) and polysiloxane (PS), disclose a well defined yield state characterized by a critical value of

strain deformation, γ_{cr} , which corresponds to the peak of G'' in the strain sweep amplitude experiments and with the onset of the plateau in the shear flow curve. Oscillatory testes performed in MAOS and LAOS regimes offer value information about the rheology of soft matter, in particular the measurement of γ_{cr} which defines the onset of material fluid behavior.

The present experiments prove very good quantitative correlations of the data measured in shear and oscillation. At the same time the results are consistent with the existence within the soft matter samples of a yield state which defines the materials rheology at the onset of the fluid behavior, an important parameter for many practical applications in varied domains [156], [236], [242]. The yield state is direct associated with the existence of the plateau in quasi-steady flow curve, which is in many cases the consequence of a non-monotonic constitutive relation [13], [16], [45], [132], [250].

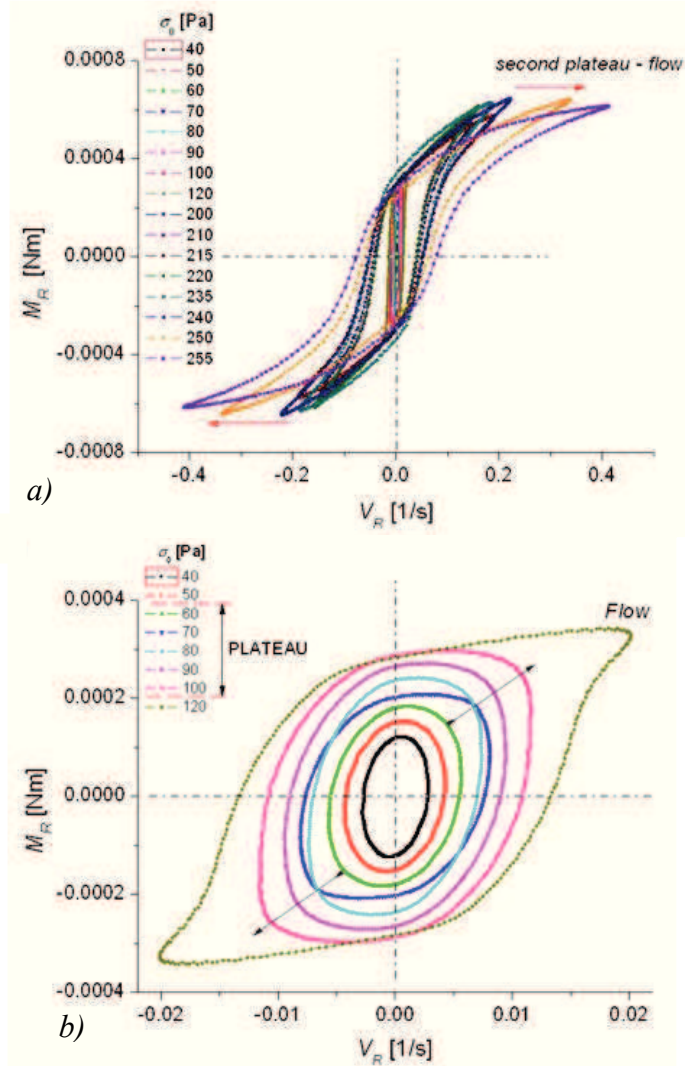


Fig. 6.20. The evidence of plateau behavior in the topology of Lissajous figures shear stress vs. shear rate for CR sample: a) well defined flow behavior at $\sigma_0 > 120$ Pa , b) detail with the transition/plateau domain (input stress amplitude tests at $\omega = 1$ rad/s).

This constitutive relation is unstable and normally generates shear bandings or kinks in the velocity distribution, phenomena which is not trivial to be distinguished from the real slip of the sample at the wall (especially if the slipping is located at nano- or micro-distances from the wall) [27], [36], [84], [85], [150]. We consider oscillatory rheology an useful technique to investigate not only the existence of plateau behavior and yield state, but also the presence of slip [82], [114].

For example, in Figure 6.20 the topology evolution of the Lissajous figures disclose clear the plateau region, i.e. the transition from visco-elastic behavior to the fluid one (Figure 6.20.b). The existence of wall depletion phenomena or possible slip can be observed in the same oscillatory test, if for each imposed stress amplitude we perform several oscillations cycles (with the same sample) and record the differences in the maximum rate magnitude, see Figures 6.21 – 6.22.

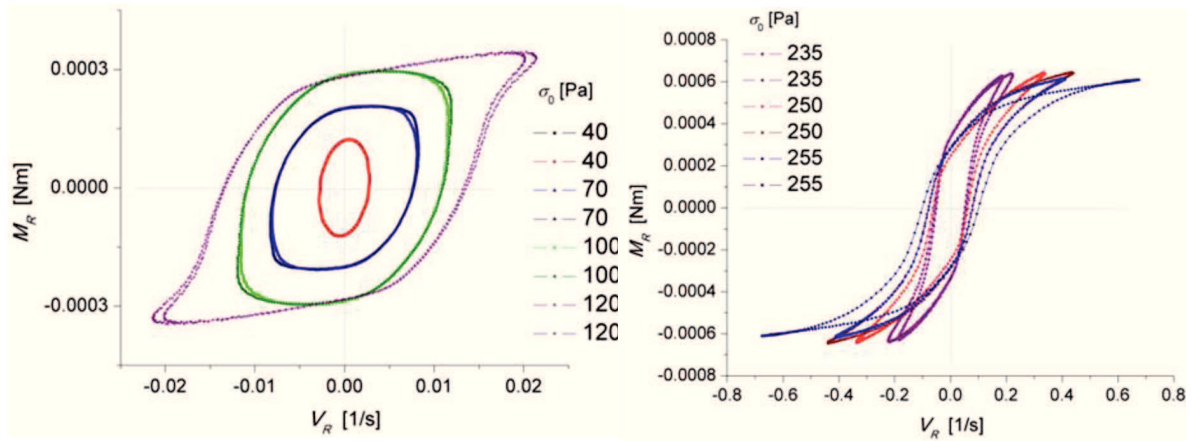


Fig. 6.21. Doubled Lissajous figures for different imposed stress magnitude. In the flow domain the difference between two consecutive tests is sharp increasing, see Figure 22, which suggest possible existence of slip.

By extracting the difference of the maximum rate magnitude (Figure 6.22) one can highlight both the critical shear stress value (corresponding to all results presented in Paragraphs 6.2-6.4 for CR sample) which marks out the onset of the instability domain (the plateau zone) but also the possibility of slip occurrence (between sample and plate) at very large shear stresses.

The results of this study demonstrated that for soft matter materials in which the yield state is present the correspondence between the simple shear and oscillatory tests in MAOS and LAOS domains can be established. Consequently, the onset of the flow behavior (marked by the critical yield stress) in simple shear motions can be detected also in dynamic shear tests. Its location coincides with the strain amplitude corresponding to the peak in the viscous

modulus, so the yielding behavior is better characterized by a critical value of strain, rather than a unique value of the yield stress.

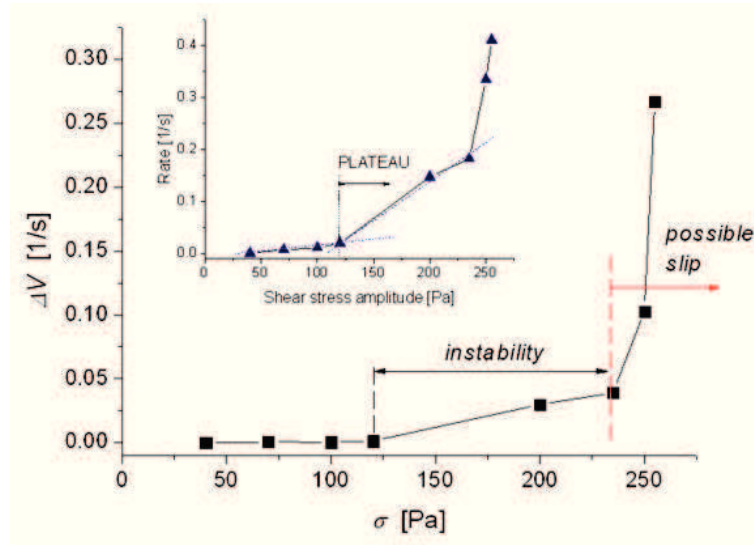


Fig. 6.22. The difference in maximum rate magnitude between two consecutive cycles of oscillatory tests performed at imposed stress amplitude. In detail is shown the variation of maximum rate amplitude with the shear stress. The region where possible slip can be observed follows the instability domain, which is associated with the plateau.

The existence of material instabilities or/and slip in shear flows of soft matter systems is still an open subject and also a challenge for developing novel techniques in rheometry and flow visualizations. If we make now correspondance between the investigations – squeezing and shearing of complex fluids (as CR and PS) we find consistent results. In both tests the samples disclose the elastic component, the shear thinning character and same dynamics in oscillation.

One important remark is that present squeeze results are exclusively characterizing the process beyond the yield stress, while the flow field is completely developed. To analyze the onset of the flow, and to determine the yield stress in squeezing, there are necessary controlled stress measurements (the corresponding of creep in shear) which at the moment are not available in our laboratory.

Chapter 7. THE INFLUENCE OF SURFACE MICROSTRUCTURE ON THE SQUEEZING FORCE

7.1. THE INFLUENCE OF SURFACE MICROSTRUCTURE ON NEWTONIAN FLUIDS ADHESION PROPERTY

As shown in Paragraphs 2.52 and 6.5 the solid-liquid contact, i.e. the adherence conditions, has a significant influence on flow dynamics and it represents a key factor in rheometry. The presence of slip at solid surface and wall depletion phenomena, already mentioned in Paragraph 2.5.2 and all over the thesis, can induce major effects on the flow dynamics and, of course, on the measurements of force, respectively torque. In this last chapter we shall not focus on these phenomena.

The investigations are driven by the latest application in fluid mechanics: the influence of patterned surfaces on the flow field, a major subject for research in lab on a chip domain of microfluidics [15], [47], [147], [238]. The influence of surface microstructure on the normal force variation in simple squeeze test is being analyzed experimentally in Paragraph 7.2 and numerically in Paragraph 7.3. This study is novel in rheometry and we believe in its potential application in developing a new procedure to investigate the rheology of complex fluids in the vicinity of solid surfaces.

7.1.1. The experimental setup

The investigations were performed within REOROM laboratory using a visualization system presented in Figure 7.1 and using three silica disks with different surface microstructures. The setup includes a Lumenera CCD camera for video recording, a light source and a computer. The drops were placed on the solid surface with a syringe mounted on a vertical slide, keeping constant the distance between syringe nozzle and the surfaces. The development of the drop and the tracking of fluid-solid contact angle were recorded using Blueberry Flash Recorder and stored in avi files. As previously mentioned, the surfaces used for this analysis are three silica plates with different microstructures: a smooth plate, a plate with a micro textured surface (see Figure 7.1.b) and plate with micro-spirals (see Figure 7.1.c). Surface micro architecture dimensions are presented in Annex 9.

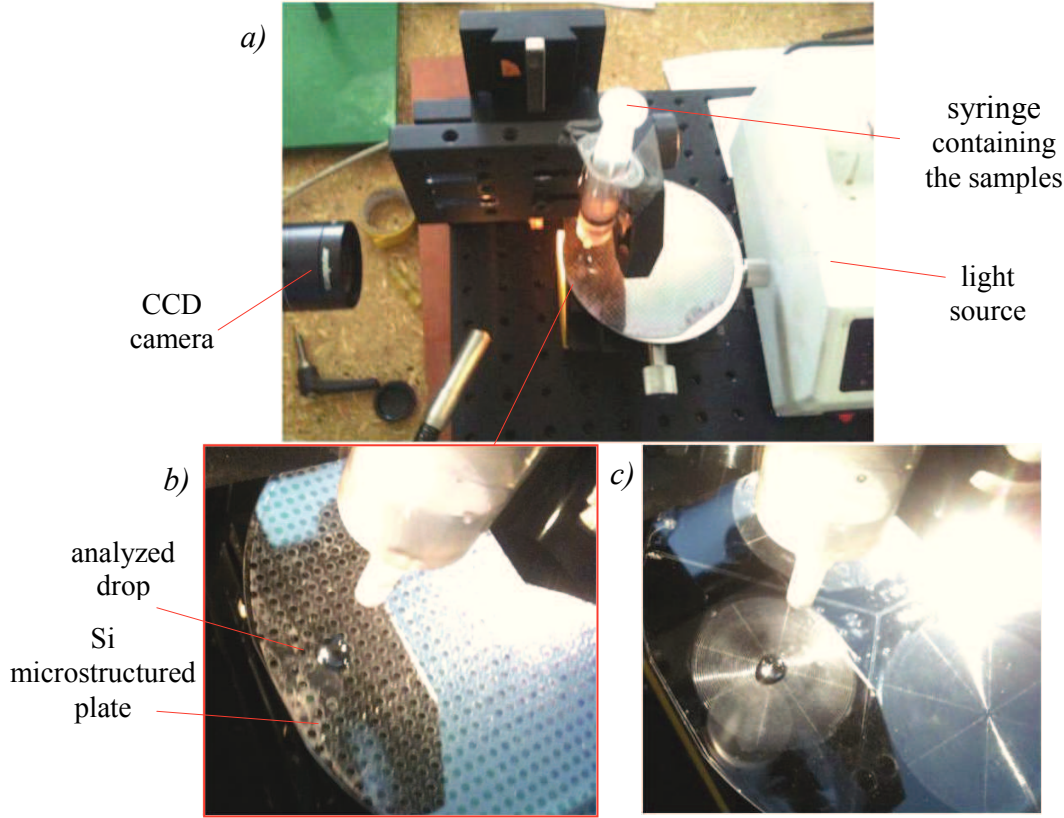


Fig. 7.1. Video acquisition system used to determine the influence of surface microstructure on Newtonian fluids contact angle: experimental assembly (a) silicon surface micro textured (b) and micro-spiral (c).

After recording droplet evolution in video files, successive images were extracted by using *Movie Maker* software. The comparison was made between images corresponding at an observation time of 80 s, at which it is considered that each drop has reached steady state contact with the solid surface.

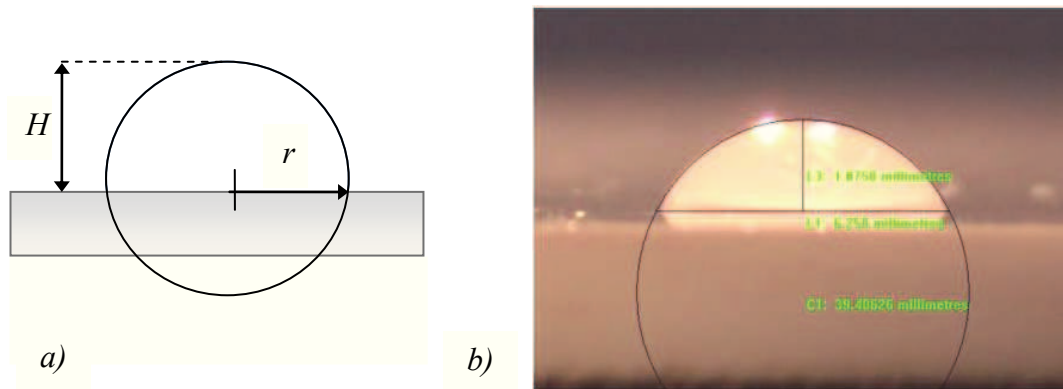


Fig. 7.2. Contact angle determination by measurements of the droplet height and the radius of circle segment corresponding fluid-solid contact, performed using *Image-Pro* software.

Contact angle determination was made by measuring droplet height and the radius of a circle segment corresponding fluid-solid contact using *Image-Pro* software. After extracting this information, the contact angle θ was calculated using the following expressions [255]:

$$H = r - r \cdot \cos\left(\frac{\alpha}{2}\right) \quad (7.1)$$

$$\alpha = \arccos\left(2 * \left(\frac{r-h}{r}\right)^2 - 1\right) \quad (7.2)$$

$$\theta = 180^\circ - \alpha/2. \quad (7.3)$$

7.1.2. Contact angle between various Newtonian sample and micro-structured surfaces

Figure 7.3 presents the influence of surface microstructure on different Newtonian fluids contact angle: water ($\eta_0 = 10^{-3} Pa.s$), glycerin ($\eta_0 = 0.9 Pa.s$), honey ($\eta_0 = 16 Pa.s$), mineral oil ($\eta_0 = 0.11 Pa.s$). These results are showed in Table 7.1.

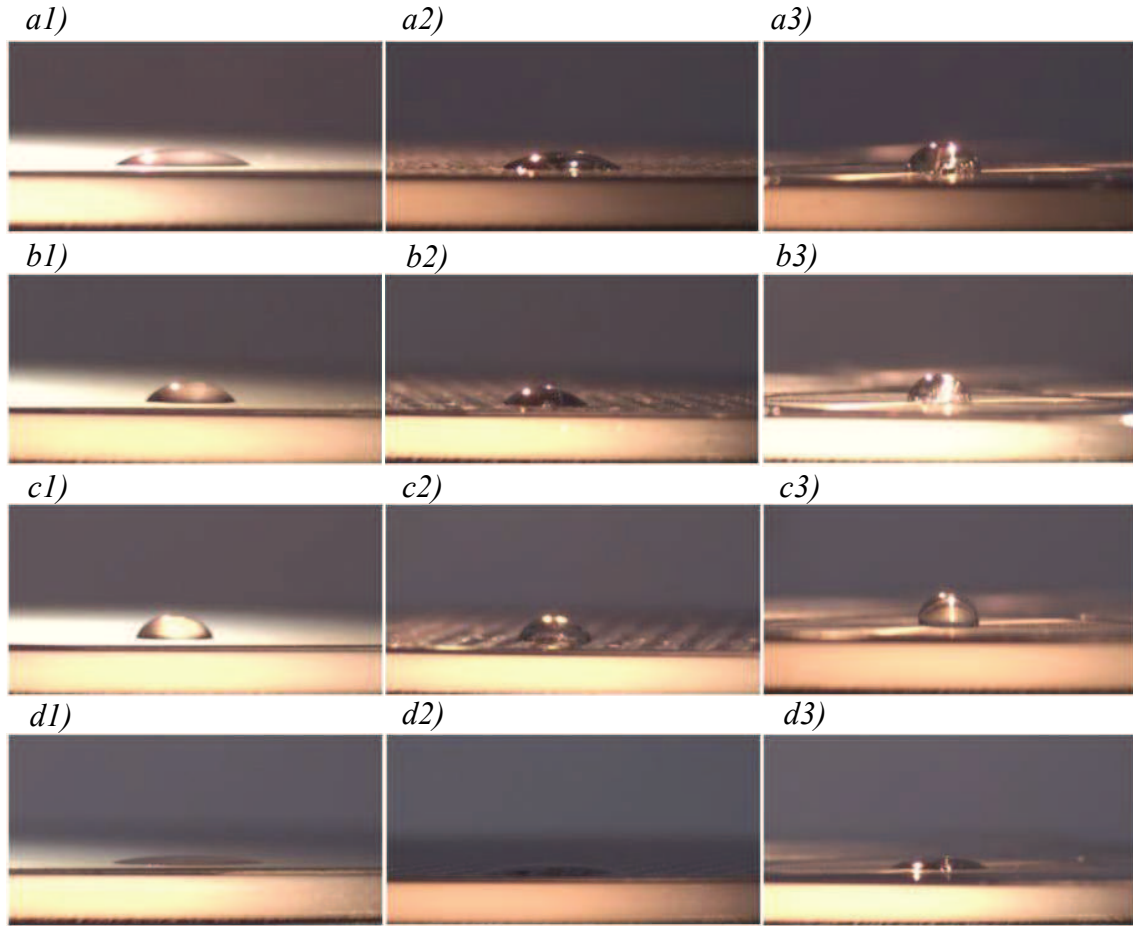


Fig. 7.3. Influence of surface microstructure on Newtonian fluids contact angles: water (a1, a2, a3), glycerin (b1, b2, b3), honey (c1, c2, c3), mineral oil (d1, d2, d3). The contact surfaces have different micro architectures: plane surface (a1, b1, c1, d1); micro-textured surface (a2, b2, c2, d2); micro-spiral surface (a3, b3, c3, d3). All images correspond to an observational time of 80 s at which the drop is considered to have reached steady state value.

Using micro-textured and micro-spiral surfaces, the contact angle increases significantly in comparison with the plane surface for all tested samples. The micro-spiral surface brings an

increase of more than 150% (170%) for water contact angle in comparison with the plane surface, for mineral oil the increase being of almost 63%. For glycerin and honey, the micro-spiral surface brings a reduced increase of contact angle, 46% and respectively 26 %.

Table 7.1. Measured contact angles for all tested samples in contact with different silica micro structured surfaces: plane surface, micro textured surface, micro—spiral surface.

Surface	Plane plate	Micro-textured plate	Micro-spiral plate
Fluid	$\theta [^\circ]$		
Water	28.35	31.3	76.73
Glycerin	51.54	55.9	75.51
Mineral Oil	14.92	18.49	24.28
Honey	69.94	72.54	88.015

Besides the influence of the surface patterns, the contact angle increase seems is dependent on the samples viscosity. The increase of the contact angle and the change of the adherence condition is significant for less viscous fluids (like water and mineral oil) and less obvious for high viscous fluids (glycerin, honey). Within this paragraph the influence of surface micro architecture on pure viscous samples contact angle was proven, hence on the adherence propriety at fluid-solid contact.

Changing surface micro architecture from plane to micro-textured give rise to a increase of the fluid-solid contact angle (in some cases the surface being transformed from hydrophilic to almost hydrophobic). Moreover when the surface presents a micro-spiral the contact angle increases significantly, this phenomenon being favored for low viscous fluids.

7.2. CONSTANT VELOCITY SQUEEZE FLOW IN THE PRESENCE OF MICRO-STRUCTURED SURFACES

In the previous section the influence of surface microstructure on fluid adherence and wetting proprieties has been proven. Considering the importance of a possible control of fluid-solid adherence conditions, the present paragraph presents a study on the influence of microstructure on the normal force measured in constant velocity squeeze tests and implicitly on the Newtonian viscosity coefficient measured in this type of tests.

A series of measurements were performed by using *Physica Anton Paar MCR 301* rheometer, presented before in [Paragraph 5.2.1](#) with parallel-plate glass geometry (43 mm). On the lower plate of the rheometer the silica surfaces were placed successively in order to modify gap architecture during squeeze flow.

The plates were fixed by adding a small amount of glue on the lower surface of the rheometer and by pressing the silica plates on this adhesive. After fixing each plate the nominal gap was set through the automatic gap setting option of *MCR 301*, *Tru gap* option.

The analysis was performed on two Newtonian samples with different viscosities, mineral oil ($\eta_0 = 0.11 \text{ Pa}\cdot\text{s}$) and honey ($\eta_0 = 16 \text{ Pa}\cdot\text{s}$), at a constant temperature of 20C and squeezing velocities of $\dot{h} \in (0.001 \div 2) \text{ mm/s}$. The dimensionless Re number (eq. 3.1, Paragraph 3.2.1) that expresses the influence on inertial and viscous forces is exclusively dependent on film thickness variation as shown in Figure 7.4.

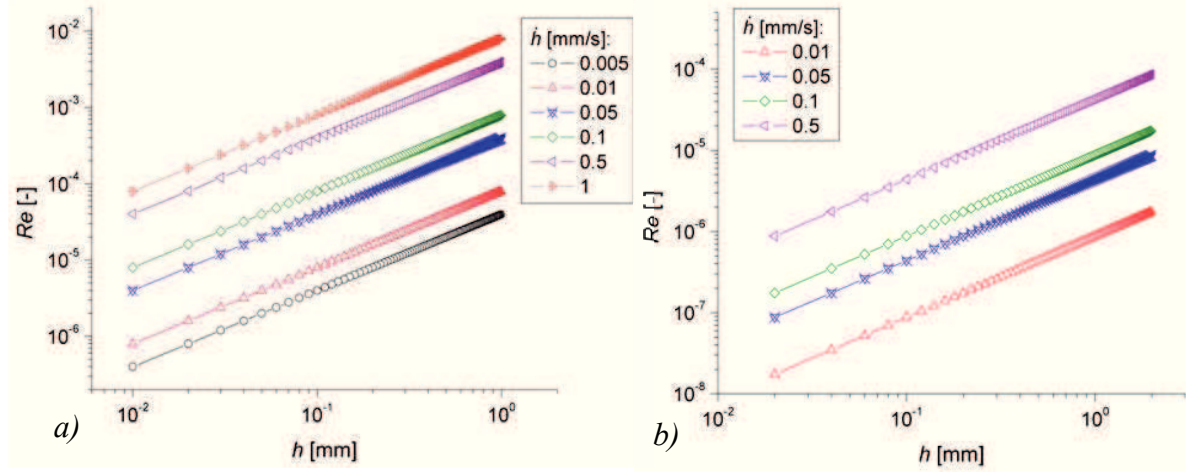


Fig. 7.4. Re number variation in constant velocity squeeze flow of mineral oil (a) and honey (b) at $\dot{h} \in (0.001 \div 2) \text{ mm/s}$.

At high values of film thickness, corresponding to the beginning of squeezing tests, the flow is dominated by the inertial forces (large Re). Once decreasing film thickness Re values decrease and the flow becomes dominated by viscous forces. For the investigated squeezing motion, Re values may be considered small in comparison with other flow motions (as for example shear flows): $Re < 10^{-2}$ for mineral oil sample, $Re < 10^{-4}$ for honey sample in the film thicknesses and squeezing velocities frame used for measurements.

Figure 7.5 presents the results obtained for the mineral oil sample at different squeezing velocities in the presence of micro structured surfaces. For all velocities there can be distinguished two gap dependent zones in which the influence of surface microstructure acts differently: (i) a large thickness domain characterized by the onset of the flow; (ii) a low film thickness domain where the flow is fully developed (especially on the radial direction).

The superior limit of this domain depends exclusively on the squeezing velocity: as example for the mineral oil sample it starts at a value of $h \sim 0.2 \text{ mm}$ at small squeezing velocities $\dot{h} = 0.005 \text{ mm/s}$ and it increases at $h \sim 0.55 \text{ mm}$ for larger velocities ($\dot{h} = 1 \text{ mm/s}$). Surface microstructure influences the motion, this can be firstly observed in the change of slope of normal force distribution (respectively of the flow index). This phenomenon is obvious at small squeezing velocities and is being diminished once the velocity is increased. At very small velocities $\dot{h} < 0.005 \text{ mm/s}$, the presence of

microstructure brings an increase of measured force values is on the whole thickness domain (in comparison with the plane surface). At large values of film thickness, the presence of microstructure increases the force.

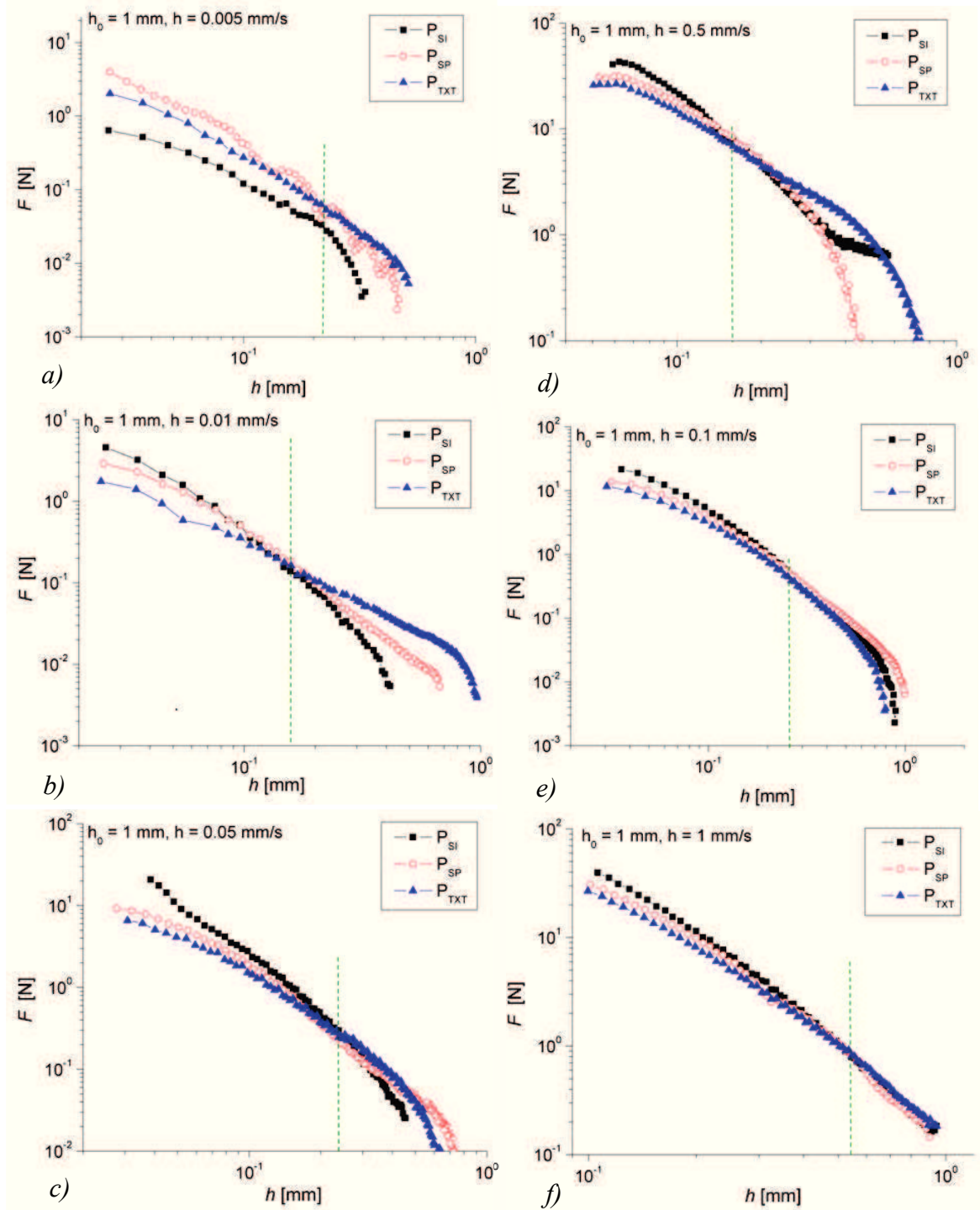


Fig. 7.5. Normal force dependency on film thickness for a mineral oil sample during simple squeeze tests at $\dot{h} \in [0.005 \div 1]$ mm/s, $T = 20^\circ\text{C}$ and $h_0 = 1$ mm. Surface microstructure influence on the normal force: plane plate (P_{SI}), micro-textured plate (P_{TXT}), micro-spiral plate (P_{SP})

At small values of film thickness the force values decrease in the presence of the microstructure the influence being manifested oppositely. It can also be noticed that the

micro-texture surface has a more pronounced influence than the micro-spiral surface in squeezing motion, even though the measurements of fluid-solid contact angle disclose a more pronounced influence of the micro-spiral surface.

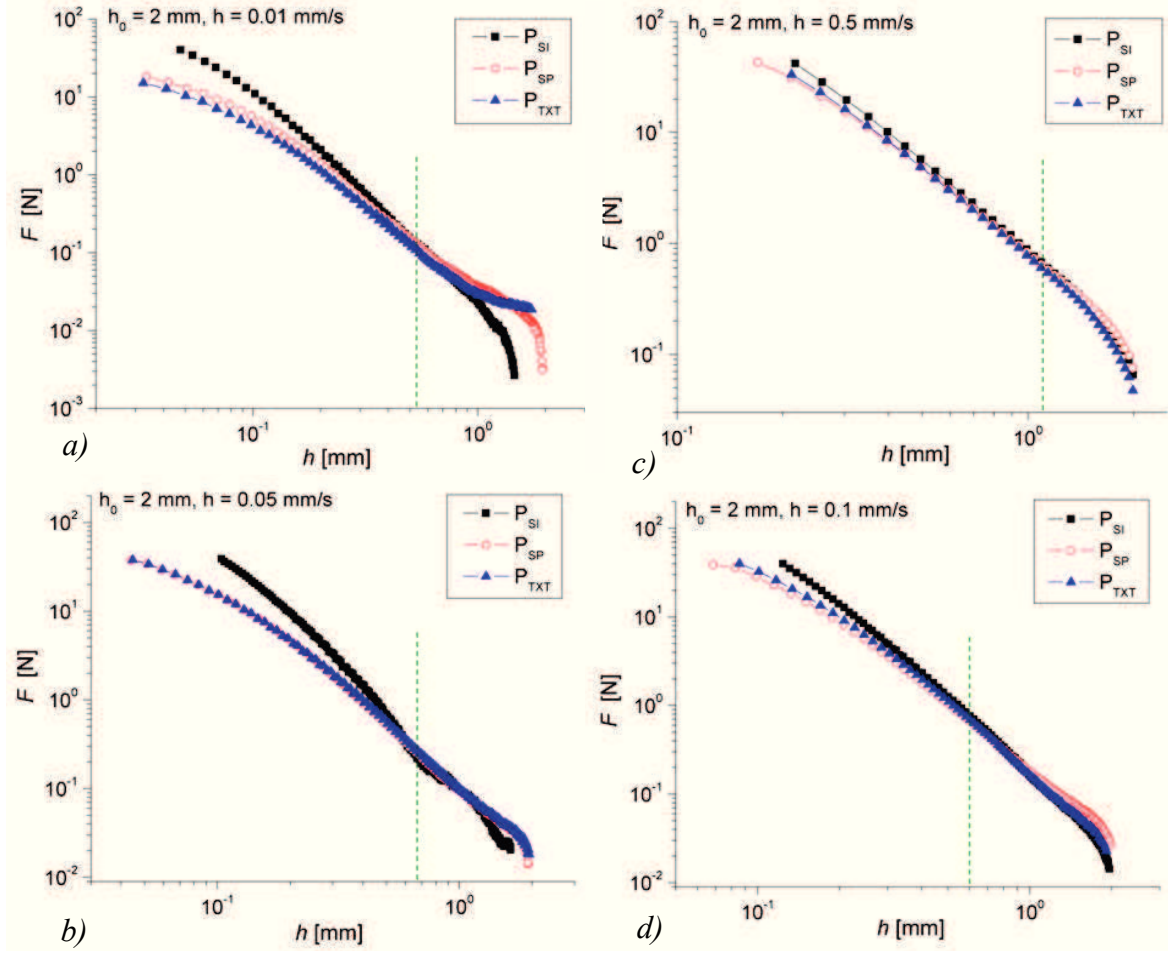


Fig. 7.6. Normal force dependency on film thickness for a honey during simple squeeze tests at $\dot{h} \in [0.01 \div 0.1]$ mm/s, $T = 20^\circ\text{C}$ and $h_0 = 2$ mm. Surface microstructure influence on the normal force: plane plate (P_{SI}), micro-textured plate (P_{TXT}), micro-spiral plate (P_{SP})

The same behavior is observed for honey sample (Figure 7.6) even though the phenomenon is diminished due to the higher value of viscosity coefficient of the sample. Also in this case the presence of microstructure brings an increase of normal force values on the large film thickness domain and a reduction of the force at small film thicknesses. Similar to the mineral oil sample, the results obtained for honey indicate a different behavior of the sample when using a micro structured surface in comparison with the case where a plane surface is used in comparison with the plane surface.

This behavior has been observed also in simple and dynamic shear tests [15], [47], [147]. For Newtonian fluids (i.e. mineral oil sample – IK), viscosity values decreased significantly in the presence of micro-textured (patterned) surfaces as seen in Figure 7.7, [15].

In the case of viscoelastic fluids, with higher viscosities this effect is diminished, accordingly to the squeeze measurements presented above (Figures 7.5-7.6).

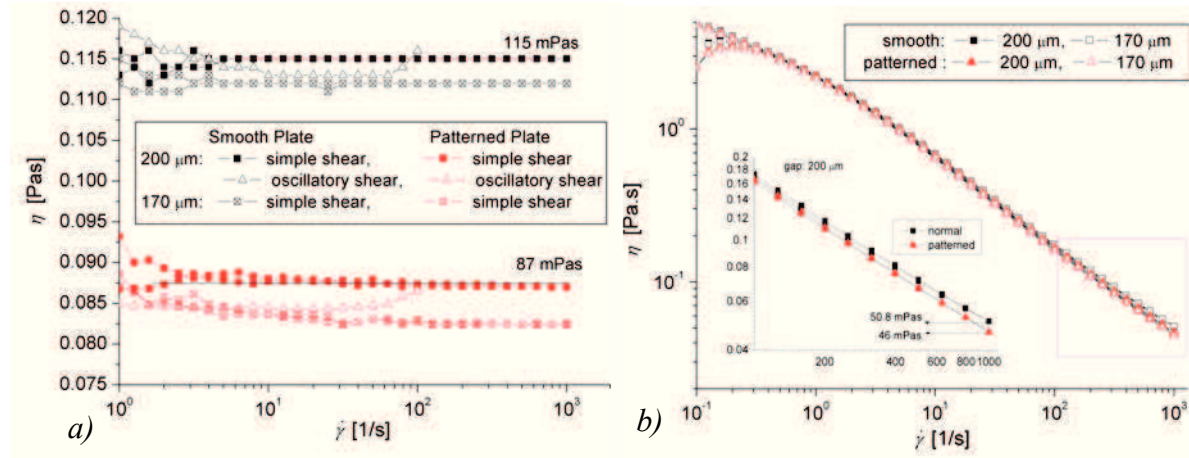


Fig. 7.7. Influence of patterned surfaces on shear viscosity of pure viscous, mineral oil sample (a) and viscoelastic, PAA solution (b) in simple and oscillatory shear tests [15].

One concludes that in the presence of microstructures the Newtonian fluid discloses a lower friction at the wall (for small gaps) in comparison with the smooth surface. This phenomenon is generated by a partial slip of the patterned surface, which can be considered as wall depletion phenomena. On the base of such measurement we can compute the wall slip velocity, and relate this velocity with material/fluid rheometry.

7.3. NUMERICAL SIMULATION OF CONSTANT VELOCITY SQUEEZE FLOW IN THE PRESENCE OF MICRO-STRUCTURED SURFACES

In the absence of a visualisation system that may allow an analysis of the flow in the gap, the numerical simulation of the phenomenon in the presence of modified surfaces may be a very useful tool of investigation, as already proven in Chapter 4. The numerical investigations were performed using the spiral geometry as a model in *Fluent* software with a quasi-steady approximation of the squeezing motion.

7.3.1. The construction and meshing of the flow domain

The lack of symmetry of this particular geometry doesn't allow the reduction of geometry dimensions (as for the simulations performed in Chapter 4), in this case being necessary the use of a 3D flow domain. The complexity of surface microstructure has led to its construction with different software, *Solid Works*. After building up the geometry, the flow domain was meshed using *Gambit* preprocessor software.

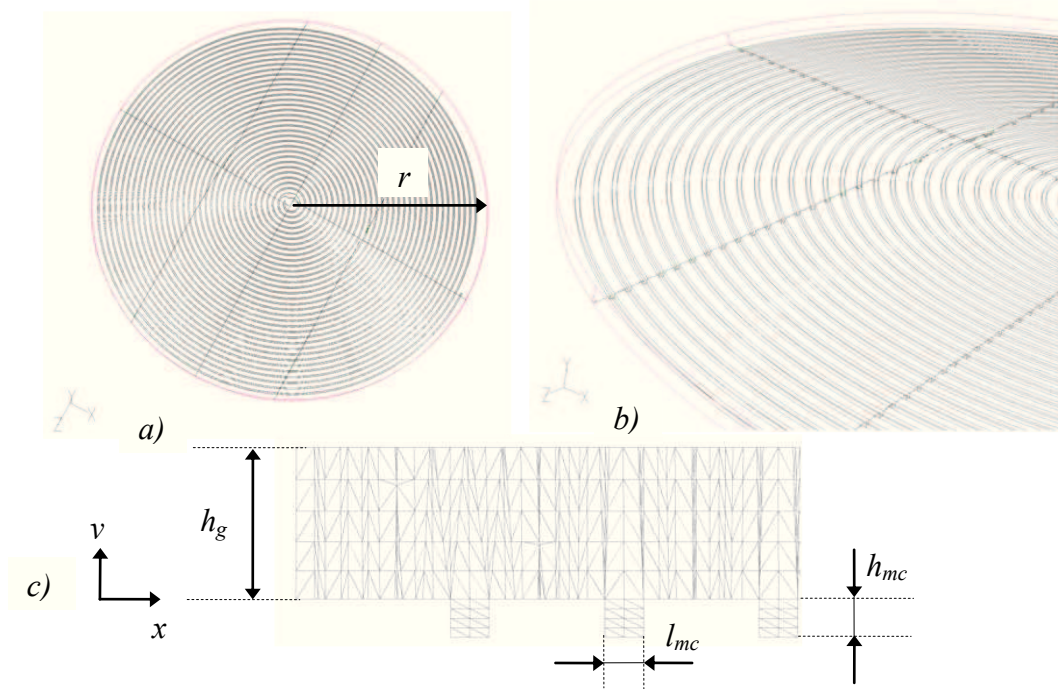


Fig. 7.8. Construction of geometries and meshing of floe area for the micro-spiral geometry: top view of the lower plate (a); 3D arbitrary view of the geometry (b); transversal section of the mesh at $z=0$ with detail on the outlet zone (c)

The virtual geometry reproduces closely the real model containing 63 semicircles on the lower wall, semicircles that are connected to form the micro-spiral channel that has a width of $l_{mc} = 0.1 \text{ mm}$ and a $h_{mc} = 0.1 \text{ mm}$ height. The virtual geometry has a radius of $r = l_{mc} = 14.2 \text{ mm}$ the total film thickness is defined as a sum of the height of the flow domain $h_g = 0.4 \text{ mm}$ and the height of the micro-spiral channel $h_{mc} = 0.1 \text{ mm}$ as shown in Figure 7.8. The mesh was made using 3D tetrahedral elements, the final geometry having almost 3.000.000 cells. For comparison there were build two other parallel-plates 3D geometries corresponding to film thicknesses of $h_0 = 0.4 \text{ mm}$ and $h_0 = 0.5 \text{ mm}$. The simulations were performed using the rheological parameters of mineral oil sample in constant velocity squeeze flow at $\dot{h} \in [0.01, 1] \text{ mm/s}$, the motion being considered steady. The convergence criterion is reached after 200 iterations but the results presented are however obtained for 400 iterations.

7.3.2. Simulation results for mineral oil sample

In order to represent the flow field a transversal iso-surface was created, in (x, o, y) plane, at $z = 0$ (Figure 7.9.a). The presence of microstructure leads to a decrease of the wall shear stress values from $\sigma = 35.1 \text{ Pa}$ in the case of plane surfaces at $\sigma = 27.9 \text{ Pa}$ for the micro structured ones (see Figure 7.10). Also it can be noticed that in the vicinity of the microchannel, and especially inside the spiral, the wall shear stress is naught, which leads to

modified adherence conditions and implicitly changes of flow dynamic in the gap (see also Figure 7.10.b). Figure 7.11 presents the velocity distribution in the gap. For the micro structured geometry the maximum velocity decreases but its distribution seems to be more uniform in comparison with the smooth plate geometry.

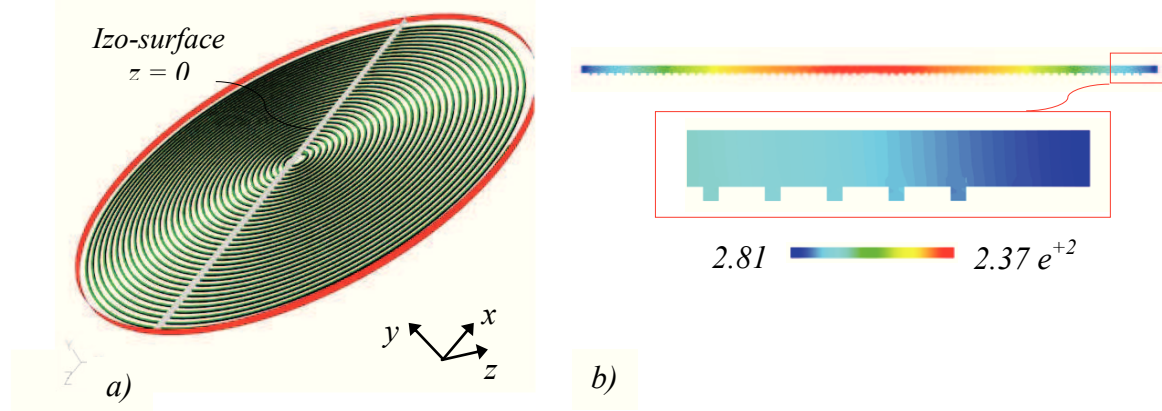


Fig. 7.9. Transversal iso-surface construction (at $z = 0$) for numerical results representation of the simple squeeze flow of mineral oil (a), pressure distribution in the gap for a squeezing velocity of $\dot{h} = 1 \text{ mm/s}$.

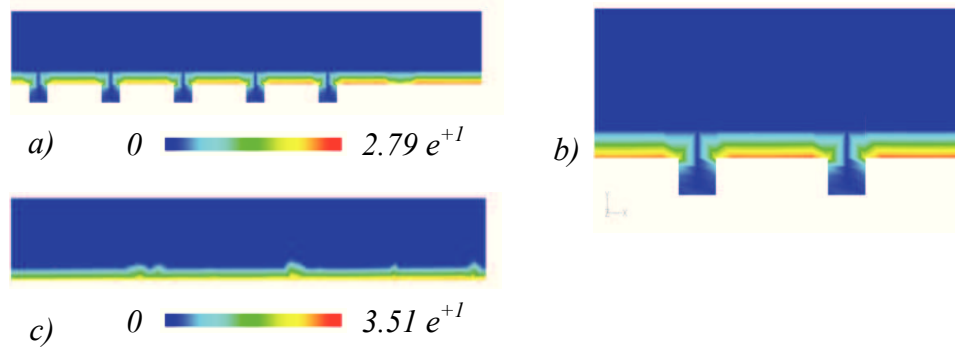


Fig. 7.10. Wall shear stress distribution in the gap obtained from the numerical simulation of constant velocity squeeze flow ($\dot{h} = 1 \text{ mm/s}$) of mineral oil sample for: micro-spiral geometry (a) with detain on the last two microchannels near the outlet area (b) and the parallel plane plate geometry (c).

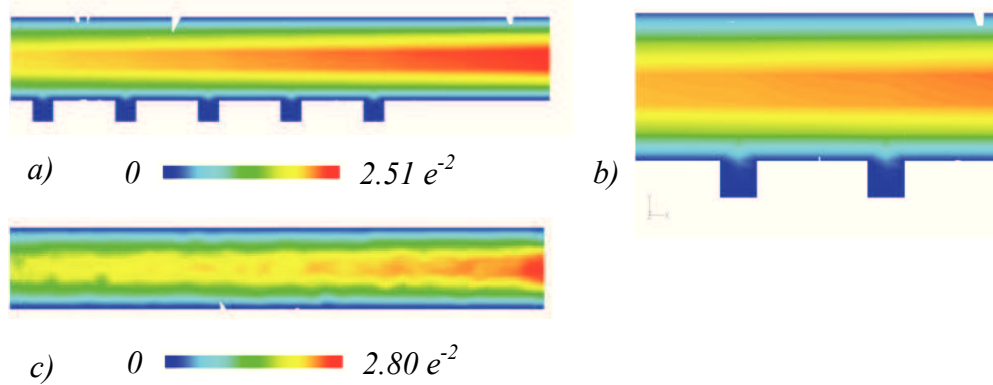


Fig. 7.11. Velocity distribution in the gap obtained from the numerical simulation of constant velocity squeeze flow ($\dot{h} = 1 \text{ mm/s}$) of mineral oil sample for: micro-spiral geometry (a) with detain on the last two microchannels near the outlet area (b) and the parallel plane plate geometry (c).

Moreover a recirculation zone is observed in the micro-chanel (see Figure 7.12), where the velocity is very small. According to the velocity distribution, the characteristic Re number is very small in the microchanel and increases in the outlet zone, see Figure 7.13.

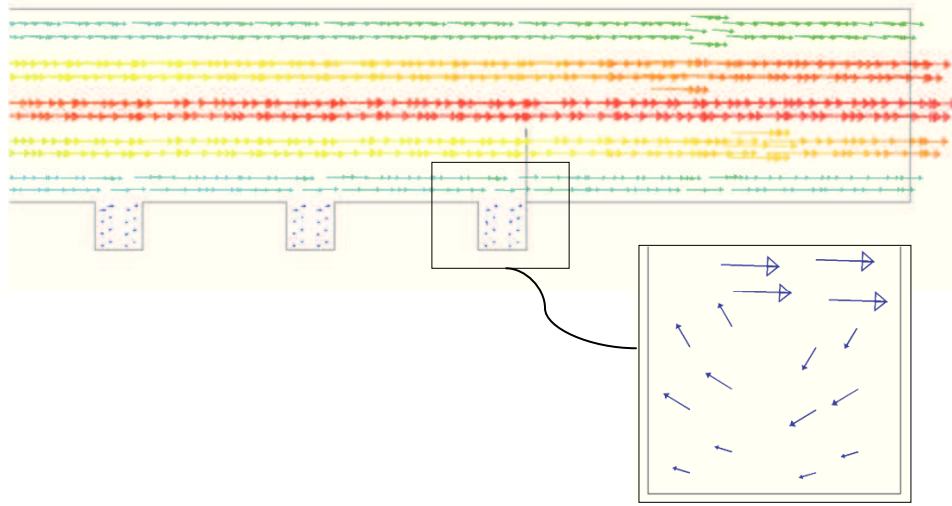


Fig. 7.12. Velocity vectors in the gap obtained from the numerical simulation of constant velocity squeeze flow ($\dot{h} = 1 \text{ mm/s}$) of mineral oil sample for the micro-spiral geometry. Fluid recirculation in the microchannel.

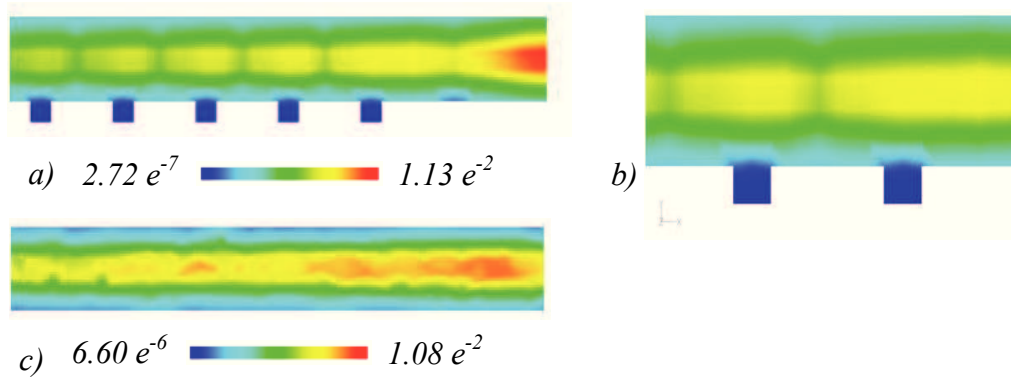


Fig. 7.13. Cells Re number distribution in the gap obtained from the numerical simulation of constant velocity squeeze flow ($\dot{h} = 1 \text{ mm/s}$) of mineral oil sample for: micro-spiral geometry (a) with detain on the last two microchannels near the outlet area (b) and the parallel plane plate geometry (c).

Table 7.2. Normal force values obtained through the numerical simulations at constant velocity squeeze flow of mineral oil sample, using the quasi-steady approximation of the flow. Surface microstructure influence on force values; Comparison with the theoretical prediction for parallel smooth plate geometries.

$\dot{h} \text{ [mm/s]}$	Suprafață	Gap [mm]	$F_{NU} \text{ [N]}$	$F_{TH} \text{ [N]}$
1	Microspiral	0.4	0.2959	
	Smooth	0.4	0.3360	0.3292
	Smooth	0.5	0.1722	0.1686
0.01	Microspiral	0.4	0.004219	
	Smooth	0.4	0.0044710	0.0032931
	Smooth	0.5	0.00310672	0.0016861

Computed normal force values are presented in Table 7.2 a small decrease is found for a squeezing velocity of $\dot{h} = 1 \text{ mm/s}$. Since constant velocity squeeze flow is a complex

unsteady motion, the tracking of the micro structured surfaces influence on the normal force may be possible by using a transient unsteady approach. Such simulations may be performed only in the presence of performant hardware resources that may allow a reduction of the computational time, taking into consideration geometry dimensions and the increased number of cells that are needed to obtain a good approximation of the real phenomenon.

7.4. CONCLUSIONS

In this chapter the influence of surface microstructure on the fluid-liquid contact angle, on the adherence properties and the dynamics of the constant velocity squeeze flow was investigated. It has been showed that the presence of microstructures on the solid surfaces can lead to an increase of almost 170 % of the contact angle, especially for low viscous fluids, microstructure influence being exclusively dependent on viscosity coefficient value.

For the simple squeeze flow the presence of micro structured surfaces disclose two opposite actions depending on the film thickness: an increase of normal force at high film thicknesses, where the flow is governed by the inertial forces; a decrease of normal force values at low gaps, where the flow is governed by the viscous forces.

The numerical simulations, performed using a quasi-steady approximation, disclose a modified adherence property in the presence of micro-spiral surface trough the reduction of wall shear stress values and a modified velocity distribution the gap. However, in order to analyze numerically the microstructure influence on normal force values it is necessary to perform unsteady transient simulations (deformable mesh) using a more refined mesh, such simulations requiring performant hardware resources that are not yet available in ***Reorom Laboratory***.

The present numerical simulations are qualitatively consistent with experiments and bring a new insight on the flow dynamics in the presence of such patterned surfaces. The results are encouraging and prove the capabilities of ***Computational Rheometry*** to be used as an efficient tool for material testing.

Chapter 8. FINAL CONCLUSIONS

8.1. GENERAL ASPECTS

This thesis was dedicated exclusively to the rheological characterization of simple and complex fluids in squeezing and shear flows using available rheometric testing procedures. The main objective of the study was to analyze if the squeezing process might be used as a feasible procedure to test fluids rheology.

The thesis includes a consistent experimental and numerical study of the squeezing phenomenon in simple and dynamic motions, concerning mainly two issues: (i) free surface influence on flow dynamics and normal force distribution; (ii) the analysis of linear and nonlinear viscoelasticity of complex fluids in oscillatory squeeze flow. The results obtained from numerical simulations show a good correlation with the experimental measurements.

Experimental investigations of oscillatory squeeze flow disclose the necessity of introducing a correction factor for normal force measurements and also a calibration factor of the force transducer. The investigation of complex fluids using oscillatory squeeze motion was performed for both linear and nonlinear domains, the measurements being compared with those obtained for purely viscous fluids. Due to the lack of data on complex fluids rheology in squeezing flow corroborated with the technical limits of our rheometer, the results presented have mainly a qualitative relevance.

The study of constant velocity squeeze flow was focused on two subjects: (i) the modeling of free surface at the edge of the gap and its influence on measured thrust; (ii) investigations of the imposed boundary conditions influence on the pressure distribution in the gap. In relation with the latest subject,

Chapter 7 presents a fundamental problem encountered in the literature: the fluid-solid adherence conditions and their control. It has been demonstrated that surface microstructure influences the contact angle formed by purely viscous fluids. By performing a series of constant velocity squeeze tests in the presence of different micro structured surfaces, the influence of micro texture and micro-spiral architecture on the measured normal force was proven.

Chapter 8. Final Conclusions

In addition to the detailed study of Newtonian and complex fluids in squeeze motions, the thesis includes an extensive chapter dedicated to the nonlinear behavior of complex fluids in simple and dynamic shear motions.

The nonlinear rheology of complex fluids was determined by linking simple and dynamic shear tests, the response recorded macroscopically (flow curves, dynamic modules, Lissajous curves) with the micro structural changes in the samples.

One main conclusion of the thesis is the necessity of coupling experimental measurements with numerical simulations in order to obtain a feasible testing procedure for fluid rheology in squeezing flows. For rheometry the squeeze flows within thin film approximation are attractive due to their apparently experimental simplicity.

Our investigations proved that fluid dynamics in squeeze flow is influenced by many factors as inertia, edge effects, wall depletion. Still, two major problems were encountered during the experimental investigations: (i) at large gaps the use of a high sensitivity force transducer is imperative to obtain qualitative data, but this rise the costs of experimental equipment; (ii) at low gaps a small lack of plates parallelisms and the edge effects have a large influence on the measured data and yet the available analytical solutions are valid only for very low gaps and pure viscous fluids. Under these conditions a “trusty measurements domain” was established for which the data was analyzed.

The coupling of experimental and numerical investigations is obviously necessary to have at hand consistent data with the theoretical framework of squeezing motion. Therefore, one concludes that squeezing might be an alternative motion used in rheometry (apart shear flows) but only for a well defined range of imposed strain amplitudes and frequencies (chosen in concordance with force transducer’s working domain).

Due to the complexity of flow and the high costs of devices involved we do not expect that commercial rheometers based on oscillatory squeezing flow to be available in the near future. Squeezing flow remains a very useful measuring technique and it is very indicated for laboratory experiments and research, where complex fluids have to be analyzed and characterized in complex flows.

We also recommend squeezing as the most indicated testing procedure for the determination of slip and wall depletion phenomena in the presence of microstructured surfaces.

8.2. PRACTICAL APPLICATIONS OF SQUEEZE FLOW MOTION

The interest shown to this complex flow is due to the numerous applications in varied fields (mechanic engineering and tribology, rheology, biology, geology, constructions), to the presence of motion in numerous industrial processes of production or processing (hot stamping, gluing with adhesives, lithography by nano-printing, compression of construction materials, food industry) and in natural, biologic processes (mastication, joints, valves, biofluids, earth settling), as specified in [Paragraph 3.1.1](#).

Various applications are found in the engineering field, the most obvious being fluid lubrication in bearings, gear couplings, machines, car engines, naval engines, the fluid film preventing the solid-solid contact and the surface deterioration. Also, squeeze motion is found in the fluid damping mechanism often encountered in the car building industry. The elasto-hydrodynamic contact of car tyres with the wet asphalt supposes the squeezing of the fluid among the skid-proof grooves of the tyre.

The reduction of devices dimensions gave rise to nano or microscopic scale applications of squeeze flow, in the so-called *Micro-Electro-Mechanical Systems - MEMS* such as: fluid micro-dampers, sensors, actuators, the manufacturing process of lithography by nano-printing of micro and nano-devices.

One of the most important field of applications for the squeeze motion is found in biology and medicine: human articulations - squeeze motion between porous layers; blood micro-circulation; closing of human cardiac valves and mechanical cardiac valves.

Nevertheless, rheology and rheometry are part of these application domains since squeeze phenomenon supposes a complex motion which includes both shear components (in the vicinity of solid walls defining the squeeze process) and elongation components (in the middle of the gap). Due to these kinematic features, the squeeze flow has been intensely used along the years to determine the rheological properties of simple and complex fluids.

8.3. ORIGINAL CONTRIBUTIONS

The innovative character of the thesis can be found throughout all its contents, by linking conventional experimental test methods with numerical simulations of real flows, supporting a new concept in rheology: ***Computational Rheometry in Rheology*** (see. [Figure 1.1](#)). Hence, all experimental investigations carried out in this study for the squeezing flows were accompanied by numerical simulations.

Chapter 8. Final Conclusions

The original contributions were focused on the following aspects:

- (i) The constant velocity squeeze flow was investigated also using a quasi-steady approximation of the motion, which brings a significant reduction of the computational time, and a very good correlation with the transient (deformable mesh) approximation and the analytical predictions. The results obtained for the variation of normal force, pressure distributions on fluid film thickness, radial distributions and axial velocity distribution are almost identical for all three methods mentioned previously (the analytical model, transient numerical modeling and numerical modeling in a quasi-steady approximation).
- (ii) Investigation of free surface influence and slip/no slip conditions on the distribution of normal force in both constant velocity and oscillatory squeeze flow. In the case of constant velocity squeeze flow, the numerical simulations coupled with the free surface evolution and measured normal force during experimental investigations are suggesting the presence of a partial slip during the experiments between the mineral oil and rheometers plates.
- (iii) Moreover, by defining the squeezing viscosity function and its dependence on the apparent squeezing rate some representation of measured viscosity variation in squeeze flow has been made. The results for Newtonian fluids are qualitatively consistent with the data from shear experiments. The squeeze function for non-Newtonian fluids disclose a shear thinning behavior more relevant for cream and gel samples which is also consistent with the computed shear flow index.
- (iv) The approach itself of the oscillatory squeezing motion in order to establish a procedure for rheological characterization of simple and complex fluids is innovative, studies of these procedures being used only in a few laboratories around world. The rheological characterization of pure viscous and complex fluids in both simple and oscillatory squeeze motion (on linear and nonlinear viscoelasticity domains) correspond qualitatively with the shear rheology of these samples.
- (v) Another major contribution of this work is the correlation between simple and dynamic shear motions for analysis of nonlinear viscoelastic behavior of complex fluids. Chapter 6 introduces a new method to determine and define the yield state of complex fluids by establishing a critical strain that defines the state of yield stress, or the onset of the flow in these materials.
- (vi) Finally, [Chapter 7](#) brings another original contribution by investigating the influence of surface microstructure on fluid-solid contact angle and on the dynamics of complex flows, namely the complex squeezing motion.

8.4. FURTHER DEVELOPMENT OF THE STUDY

The limited resources available throughout the completion of this study, which may include experimental instrumentation, hardware resources available for the numerical simulations and not at least the most important resource of all - time- has led to complete this thesis in the present format. However, after addressing important issues of flow dynamics, with applications in many areas (rheology, tribology, hydraulics, food and cosmetics industry, bioengineering, microfluidic) the further development of this study is encouraged in the following directions:

- (i) the introduction of viscoelasticity in numerical simulations of complex motions like squeeze flow;
- (ii) free surface modeling for complex fluids in squeeze flow by using both simple and more complex geometries;
- (iii) the construction of more performant experimental setups that may allow microscopical flow visualizations during shear motion of complex fluid in order to better understand their behavior on the nonlinear viscoelastic domain;
- (iv) further studies of surface microstructure influence on the flow dynamics and measured rheological properties of simple and complex fluids;
- (v) introduction of nano and micro structures in microfluidic applications to improve flow dynamics and mixing.

BIBLIOGRAPHY

- [1] Acrivos, A., Khusid, B., Koplik, J., & Drazer, G. (2002) *Squeezing flow of particles and large molecules suspended in a liquid through nanochannels*. International Conference on Computational Nanoscience and Nanotechnology - ICCN 2002, (2pp).
- [2] Adams, M. J., Aydin, I., Briscoe, B. J., & Sinha, S. K. (1997) *A finite element analysis of the squeeze flow of an elasto-viscoplastic paste material*. J. Non-Newtonian Fluid Mech., 71, 41-57.
- [3] Adams, M. J., Biswas, S. K., & Briscoe, K. M. (1991) *The effects of interface constraints on the deformation of pastes*. Powder Technol., 65 (1-3), 381-392.
- [4] Adams, M. J., Briscoe, B. J., & Kamjab, M. (1993) *The deformation and flow of highly concentrated dispersions*. Adv. Colloid Interface Sci., 44, 143-182.
- [5] Adams, M. J., Briscoe, B. J., Corfield, G. M., & Lawrence, C. J. (1998) *The wall yield of rate-dependent materials*. Dynamics of complex fluids, Imperial College Press, 394-398.
- [6] Ajiboye, A. T., & Ahaneku, I. E. (2012) *Design and Construction of Compressive Force Measuring Device for Engineering and Biomaterials*. Int. J. of Biological Eng , 2 (1), 1-4.
- [7] Altmann, N., Cooper-White, J. J., Dunstan, D. E., & Stokes, J. R. (2004) *Strong through to weak 'sheared' gels*. J. Non-Newtonian Fluid Mech., 124, 129-136.
- [8] Ancy, C. (2009) *Lecture notes - Fluid dynamics and rheology*. Lausanne: École Polytechnique Fédérale de Lausanne.
- [9] Assis, F., (2003) *PhD. Thesis: Etude de la dynamique non linéaire d'amortisseurs du type squeeze film*. Ecole Centrale de Lyon.
- [10] Atalik, K., & Keunings, R. (2004) *On the occurrence of even harmonics in the shear stress response of viscoelastic fluids in large amplitude oscillatory shear*. J. Non-Newtonian Fluid Mech., 122, 107-116.
- [11] Bălan, C. (2001) *Experimental and numerical investigations on the pure material instability of an Oldroyd's 3-constant model*. Continuum. Mech. Thermodyn., 13, 399-414.
- [12] Bălan, C. (2003) *Lecții de mecanica fluidelor*. București: Ed. Tehnică SA.
- [13] Bălan, C. (1999) *Pure material instability and the concept of yield stress*. Appl. Rheol., 9 (2), 58- 63.
- [14] Bălan, C. (2000) *The Rheology of Lubricating Greases*. Amsterdam: ELGI.
- [15] Bălan, C., Broboană, D., Ionescu, E., Riedel, R., (2012) *Influence of hydrophobic surfaces on the measured rheological properties of complex fluids*. Proceedings of the XVIth International Congress on Rheology, Lisbon, Portugal.
- [16] Bălan, C., & Fosdick, R. (2000) *Constitutive relation with coexisting strain rates*. Int. J. Non-Linear Mech., 35 (6), 1023-1043.
- [17] Bălan, C., & Hutter, K. (1995) *A procedure to determine the material constants and the viscosity function for a yield shear stress*. Acta Mech., 109, 65-79.
- [18] Bălan, M. C. (2011) *PhD. Thesis: Modeling and control of viscous and viscoelastic fluids flows in microchannels*. Bucharest: Politehnica University of Bucharest.
- [19] Barnes, G., & Gentle, I. (2011) *Interfacial Science: An Introduction, 2nd ed*. Oxford, U. K.: Oxford University Press.
- [20] Barnes, H. A. (1999) *The yield stress - a review or 'παντα ρει' – everything flows?* J. Non-Newtonian Fluid Mech., 81, 133-178.
- [21] Bechert, D. W., Bruse, M., Hage, W., & Meyer, R. (2000) *Fluid mechanics of biological surfaces and their technological application*. Naturwissenschaften , 87, 157-171.
- [22] Bell, D., Binding, D. M., & Walters, K. (2006) *The oscillatory squeeze flow rheometer: comprehensive theory and a new experimental facility*. Rheo. Acta, 46, 111-112.

Bibliography

- [23] Bhattacharjee, R. C., Das, N. C., & Pal, A. K. (1999) *Analysis of an unsteady squeezing flow of dusty fluids*. Tribology International, 32, 427–434.
- [24] Bird, J. C., Ruiter, R., Courbin, L., & Stone, H. A. (2010) *Daughter bubble cascades produced by folding of ruptured thin films*. Nature (doi:10.1038/nature09069), 759-762.
- [25] Bird, R. B. (1987) *Dynamics of Polymeric Liquids*. New York.
- [26] Bird, R. B. (1976) *Useful Non-Newtonian Models*. Annual Review of Fluid Mechanics , 8, 13-34.
- [27] Bocquet, L., & Barrat, J. L. (2007) *Flow boundary conditions from nano- to micro-scales*. Soft Matter, 3, 685–693.
- [28] Bonneau, D., Fătu, A., Souchet, D., (2011) *Paliers hydrodynamiques I'équations, modelés numériques isothermes et lubrification mixte*. Lavoisier.
- [29] Bower, C., Gallegos, C., Mackley, M. R., & Madiedo, J. M. (1999) *The rheological and microstructural characterisation of the non-linear flow behavior of concentrated oil-in-water emulsions*. Rheol. Acta, 38, 145-159.
- [30] Brackbill, J., Kothe, D., & Zemach, C. (1992) *A continuum method for modeling surface tension*. Journal of Computational Physics, 100, 335-354.
- [31] Brader, J. M., Siebenburger, M., Ballau, M., Reinheimer, K., Wilhelm, M., Frey, S. J., et al. (2010) *Nonlinear response of dense colloidal suspensions under oscillatory shear: Mode-coupling theory and FT-rheology experiments*. Phys. Rev. E., 061401.
- [32] Brindley, G., Davies, J. M., & Walters, K. (1976) *Elasto-viscous squeeze films. Part I*. J. Non-Newtonian Fl. Mech., 1, 19-37.
- [33] Broboană D, M. T. (2005) *Mecanica fluidelor cu Fluent*. București: Ed. Politehnica Press.
- [34] Bujurke, N. M., Basti, D. P., & Kudenatti, R. B. (2008). *Surface roughness effects on squeeze film behavior in porous circular disks with couple stress fluid*. Transp. Porous Med., 71, 185-197.
- [35] Burbidge, A. S., & Servias, C. (2004) *Squeeze flow of apparently lubricated thin films*. J. Non-Newtonian Fluid Mech., 124, 115-127.
- [36] Buscall, R. (2010). *Letter to the Editor: Wall slip in dispersion rheometry*. J. Rheol., 54, 1177–1183.
- [37] Caba, A. C. (2005) *Characterization of carbon mat thermoplastic composites: Flow and mechanical properties* . Blacksburg, Virginia: Virginia Polytechnic Institute and State University.
- [38] Călin, A. (2008) *PhD. Thesis: Modeling the flow of polymeric fluids in complex geometries*. Bucharest, Politehnica University of Bucharest.
- [39] Campanella, O. H., & Corvalan, C. M. (2007) *Squeezing and elongational flow*. G. V. Barbosa-Canovas, Food Engineering. Oxford, UK: Encyclopedia of Life Support Systems (EOLSS), Eolss Publishers.
- [40] Campanella, O. H., & M, P. (1987) *Lubricated squeezing flow of a newtonian liquid between elastic and rigid plates*. Rheologica Acta, 26 (4), 396– 400.
- [41] Campanella, O. H., & Peleg, M. (1987a) *Determination of the yield stress of semi-liquid foods from squeezing flow data*. J. Food Science, 52, 214-217.
- [42] Campanella, O. H., & Peleg, M. (1987b) *Squeezing flow viscometry of peanut butter*. J. Food Science, 52, 180-184.
- [43] Campanella, O. H., Pelleg, M., Poppewell, L. M., & Rosenau, J. R. (1987) *Elongational viscosity measurements of melting American processed cheese*. J. Food Science, 52, 180-184.
- [44] Carrier, V. (2009) *Nonlinear rheology of colloidal glasses of soft thermosensitive microgel particles*. J. Rheol., 53 (2), 245-273.

Bibliography

- [45] Caton, F., & Baravian, C. (2008) *Plastic behavior of some yield stress fluids: from creep to long-time yield*. Rheol. Acta, 47, 601–607.
- [46] Chartei, S., Macosko, C. W., & Winter, H. H. (1981) *Lubricating squeezing flow: a new biaxial extensional rheometer*. J. Rheology, 25, 433-443.
- [47] Choi, W. (2009) *PhD Thesis: Micro-textured surfaces for omniphobicity and drag-reduction*. Massachusetts Institute of Technology.
- [48] Cheneler, D., Bowen, J., Ward, M. C., & Adams, M. J. (2011) *Micro squeeze flow rheometer for high frequency analysis of nano-litre volumes*. Microelectron. Eng. , 4.
- [49] Chorin, A. (1968) *Numerical solution of Navier-Stokes equations*. Mathematics of Computation, 22:745-762.
- [50] Chow, L. C., & Pinnivgton, R. J. (1989) *Practical industrial method of increasing structural damping in machinery, ii: squeeze-film damping with liquids*. Journal of Sound and Sound Vibration, 128 (Z), 333-347.
- [51] Chow, L. G., & Pinnington, R. J. (1987) *Practical industrial method of increasing structural damping in machinery*. Journal of Sound and Vibration, 119 (I), 123-139.
- [52] Citerene, G. P., Carreau, P. J., & Moan, M. (2001) *Rheological properties of peanut butter*. Rheol. Acta, 40, 86-96.
- [53] Clasen, C., & McKinley, G. (2004) *Gap-dependent microrheometry of complex liquids*. J. Non-Newtonian Fluid Mech., 124, 10.
- [54] Coblaș, D., Broboană, D., & Bălan, C. (2011) *Viscosity function of materials characterized by steady non-monotonous flow curve*. The 7th Int. Symp. Advanced Topics in Electric. Eng. (pp. 30-40). Bucharest.
- [55] Coblaș, D., Fătu, A., & Rădulescu, A. (2009) *Slip/no-slip influence on the behavior of a radial bearing*. Tehnologia Inovativă - Revista Construcțiilor de Mașini, 61 (2-3), 51-54.
- [56] Coblaș, D., Hajjam, M., & Rădulescu, A. (2009) *Slip/no-slip influence on the behavior of a radial bearing with a static load EHD analyzes*. Tehnologia Inovativă, Revista Construcțiilor de Mașini, 61 (2-3), 55-58.
- [57] Cohen, I., Davidovich, B., Schofield, A. B., Brenner, P., & Weitz, D. (2006). *Slip, yield, bands in colloidal crystals under oscillatory shear*. P.R.L., 97, 21552(4).
- [58] Collomb, J., Chaari, F., & Chaouche, M. (2004) *Squeeze flow of concentrated suspensions of spheres in Newtonian and shear-thinning fluids*. J. of Rheology, 48 (2), 405-416.
- [59] Collyer, A., & Clegg, D. (1988) *Rheological Measurement*. Barking, England: Elsevier Applied Science Publishers LTD.
- [60] Constantinescu, V. (1987) *Dinamica fluidelor vâscoase în regim laminar bucuresti (Dynamics of viscous fluids in laminar flow)*. București: Ed. Academiei Române.
- [61] Corradini, M. G., Stern, V., Suwonsichon, T., & Peleg, M. (2000) *Squeezing flow of semi liquid foods between parallel teflon coated plates*. Rheologica Acta, 39, 452-460.
- [62] Crassous, J. J., Régisser, R., Ballauff, M., & Willenbacher, N. (2005) *Characterization of the viscoelastic behavior of complex fluids using the piezoelastic axial vibrator*. J. Rheol., 49, 851-863.
- [63] Darwish, M., & Moukalled, F. (2006) *Convective schemes for capturing interfaces of free-surface flows on unstructured grids*. Numerical Heat Transfer Part B: Fundamentals, 49 (1): 19-42.
- [64] Davies, G. A., & Stokes, J. R. (2008) *Thin film and high shear rheology of multiphase complex fluids*. J. Non-Newtonian Fluid Mech., 148, 73-87.
- [65] de Gennes, P. G., Brochard-Wyart, F., & Quere, D. (2004). *Capillary and wetting phenomena: drops, bubbles, pearls, waves*. New York: Springer Verlag.
- [66] Debbaut, B. (2001) *Non-isothermal and viscoelastic effects in the squeeze flow between infinite plates*. J. Non-Newtonian Fluid Mech., 98, 15-31.

Bibliography

- [67] Delhaye, N., Pitou, A., & Chaouche, M. (2000) *Squeeze flow of highly concentrated suspensions of spheres*. J. Non-Newtonian Fluid Mech., 94, 67-74.
- [68] Divoux, T., Barentin, C., & Manneville, S. (2011) *From stress-induced fluidization processes to Herschel-Bulkley behavior in simple yield stress fluids*. Soft Matter, 7 (DOI: 10.1039/c1sm05607g).
- [69] Doraiswamy, D. (2000) *Chapter 35. The rheology of non-newtonian fluids*. R. Dorf, *The Engineering Handbook*, CRC Press, 16pp .
- [70] Doraiswamy, D. (2002) *The origins of rheology: A short historical excursion*. Rheology Bulletin, 71 (1), 9.
- [71] Dusschoten, D. v., & Wilhem, M. (2001) *Increased torque transducer sensitivity via oversampling*. Rheol. Acta, 40, 395-399.
- [72] Engman, J., Servias, C., & Burbidge, A. S. (2005) *Squeeze flow and applications to rheometry: A review*. J. Non-Newtonian Fluid Mech., 132, 1-27.
- [73] Erbil, H. Y. (2006) *Surface Chemistry Of Solid and Liquid Interfaces*. Oxford: Blackwell Publishing Ltd.
- [74] Erişmiş, M. A. (2004) *PhD Thesis: Mems accelerometers and gyroscopes for inertial measurement units* . Ankara, Turkey: Middle east technical university.
- [75] Esmonde, H., See, H., & Swain, M. V. (2009) *Cavitation in an oscillatory squeeze film rheometer*. Meas. Sci. Technol., 20, 8.
- [76] Esmonde, H. (2011) *On the use of non-planar geometry to improve squeeze film rheometry*. Meas. Sci. Technol., 22, 9.
- [77] Esmonde, H., See, H., & Swain, M. V. (2008) *Dynamic squeeze film rheometry for flat and spherical geometries using nonlinear spectral analysis*. Meas. Sci. Technol., 19, 10.
- [78] Esmonde, H., See, H., & Swain, M. V. (2009) *Modelling of ER squeeze films at low amplitude oscillations*. J. Non-Newtonian Fluid Mech., 161, 101-108.
- [79] Estellé, P., Lanos, C., & Mélinge, Y. S. (2003) *Squeezing flow for rheological characterisation of food materials*. 3rd International Symposium on Food Rheology and Structure, Zurich, 115-119.
- [80] Estellé, P., Mélinge, Y., Perrot, A., & Lanos, C. (2008) *Energy distribution in the squeezing of particles in concentrated suspension*. Granular Matter, 10, 81–87.
- [81] Ewoldt, R. H. (2006) *Msc disertation: Rheology of complex fluid films for biological and mechanical adhesive locomotion*. Massachusetts: M.I.T.
- [82] Ewoldt, R. H., Hosoi, A. E., & McKinley, G. H. (2007) *Rheological fingerprinting of complex fluids using large amplitude oscillatory shear (LAOS) flow*. Annual transactions of the nordic rheology society, 15, 6.
- [83] Ewoldt, R. H., Winter, P., Maxey, J., & McKinley, G. H. (2010) *Large amplitude oscillatory shear of pseudoplastic and elastoviscoplastic materials*. Rheol. Acta, 49, 191–212.
- [84] Fardin, M. A., Divoux, T., Guedeau-Boudeville, M. A., Buchet-Maulien, I., Browaeys, J., McKinley, G. H., et al. (2012) *Shear-banding in surfactant wormlike micelles: elastic instabilities and wall slip*. Soft Matter (DOI: 10.1039/c2sm06992).
- [85] Fardin, M. A., Ober, T. J., Gay, C., Gregoire, G., McKinley, G. H., & Lerouge, S. (2012) *Potential “ways of thinking” about the shear-banding phenomenon*. Soft Matter, 8, 910-922.
- [86] Farjoud, A., Ahmadian, M., Mahmoodi, N., Zhang, X., & Craft, M. (2011) *Nonlinear modeling and testing of magneto-rheological fluids in low shearrate squeezing flows*. IOP Smart Mater. Struct. 20 , 14.
- [87] Fătu, A., Hajjam, M., & Bonneau, D. (2008) *Wall Slip in EDH Journal Bearings*. International Joint Tribology Conference. Miami, Florida.

Bibliography

- [88] Ferec, J., Heuzey, M. C., Ausias, G., & Carreau, P. J. (2008) *Rheological behavior of fiber-filled polymers under large amplitude oscillatory shear flow*. J. Non-Newtonian Fluid Mech., 151, 89–100.
- [89] Ferguson, J., & Kemblowski, Z. (1991) *Applied Fluid Rheology*. New York: Elsevier Science Publishers LTD.
- [90] Field, J. S., Swain, M. V., & Phan-Thien, N. (1996) *An experimental investigation of the use of random squeezing to determine the complex modulus of viscoelastic fluids*. J. Non-Newtonian Fluid Mech., 65, 177-194.
- [91] Fielding, S. (2007) *Complex dynamics of shear banded flows*. Soft Matter, 3, 1262–1279.
- [92] Fielding, S. M., & Wilson, H. J. (2010) *Shear banding and interfacial instability in planar Poiseuille flow*. J. Non-Newton Fluid Mech., 165, 196–202.
- [93] Fluent 6.3, D. (2008) *User's Manual*.
- [94] Flügge, W. (1967) *Viscoelasticity*. Waltham, MA: Blaisdell Publishing Company.
- [95] Ganapathy, R., & Sood, A. K. (2008) *Nonlinear flow of wormlike micellar gels: Regular and chaotic time-dependence of stress, normal force and nematic ordering*. J. Non-Newtonian Fluid Mech., 149 (1-3), 78-86.
- [96] Garwood Grey, R., Condick, G. M., & Svendsen, D. (2007) *Patent No. US 7,194,895 B2*. United States.
- [97] GBC, S. (2001) *MFR 2100 Rheometer - Operation Manual*. Dandenong, Victoria, Australia: GBC Scientific Equipment Pty. Ltd.
- [98] GBC, S. (2001) *MFR 2100 Rheometer - Service Manual*. Dandenong, Victoria, Australia: GBC Scientific Equipment Pty. Ltd.
- [99] Gertzog, K. P., Nikolakopoulos, P. G., & Papadopoulos, C. A. (2008) *CFD analysis of journal bearing hydrodynamic lubrication by Bingham lubricant*. Tribology International, 41, 1190-1204.
- [100] Gopala, V., & van Wachem, B. (2008) *Volume of fluid methods for immiscible-fluid and free-surface flows*. Chemical Engineering Journal, 141: 204–221.
- [101] Graham, M. D. (1995) *Wall slip and the nonlinear dynamics of large amplitude oscillatory shear flows*. J. Rheol., 39 (4), 697-712.
- [102] Granick, S., Zhu, Y., & Lee, H. J. (2003) *Slippery questions about complex fluids flowing past solids*. Nature Materials, 2, 221-227.
- [103] Grimm, R. J. (1976) *Squeezing flows of newtonian liquid films - an analysis including fluid inertia*. Appl. Sci. Res., 32, 149-166.
- [104] Grosshans, D., Knaebel, A., & Lequeux, F. (1995) *Plasticity of an amorphous assembly of elastic gel beads*. J. Physics II France, 5, 53-62.
- [105] Guadarrama-Medina, T., Shiu, Y., & Venerus, D. C. (2009) *Direct comparison of equibiaxial elongational viscosity measurements from lubricated squeezing flow and the MultiAxiales Dehnrheometer*. Rheol. Acta, 48, 11–17.
- [106] Ham, M., Neild, A., Ng, T. W., Sze, S., & Ng, C. (2010) *Particle movement with squeezing flow of liquid films*. Sensors and Actuators, 151 (B), 297–303 .
- [107] Hashizaki, K., Chiba, T., Taguchi, H., & Saito, Y. (2009) *Highly viscoelastic reverse worm-like micelles formed in a lecithin/urea/oil system*. Colloid. Polym. Sci., 287, 927–932.
- [108] Hoffman, F. M. (1997) *An Introduction to Fourier Theory*. San Diego : University of California.
- [109] Hoffner, B., Gerhards, C., & Peleg, M. (1997) *Imperfect lubricated squeezing flow viscometry for foods*. Rheol. Acta , 36, 686-693.
- [110] Hsu, C. J., Lai, C., Lu, R. F., & Lin, J. R. (2009) *Combined effects of surface roughness and rotating inertia on the squeeze film characteristics of parallel circular disks*. J. of Marine Sci. and Teh., 17 (1), 60-66.

Bibliography

- [111] Hu, Y. T. (2010) *Steady state shear banding in entangled polymers?* J. Rheol., 54 (6), 1037-1323.
- [112] Huang, T. A. (2008) *Utility of squeeze flow in the food industry*. The XVth International Congress on Rheology, Monterey, California: A.I.P., 1280-1282.
- [113] Huang, W., Li, H., Xu, Y., & Lian, G. (2006) *Hydrodynamic force between two hard spheres tangentially translating in a power-law fluid*. Chemical Engineering Science, 61, 1480-1488.
- [114] Hyun, K. A., Wilhelm, M., Klein, C. O., Cho, K. S., Nam, J. G., Ahn, K. H., et al. (2011) *A review of nonlinear oscillatory shear tests: Analysis and application of large amplitude oscillatory shear (LAOS)*. Prog. Polym. Sci. (doi:10.1016/j.progpolymsci.2011.02.002).
- [115] Hyun, K., & Wilhelm, M. (2010) *Non-linear rheology of entangled linear and branched polymer melts under large amplitude oscillatory shear*. Kautsch. Gummi Kunstst , 123 – 129.
- [116] Hyun, K., Nam, J. G., Wilhelm, M., Seung, A., & Lee, J. (2006) *Large amplitude oscillatory shear behavior of PEO-PPO-PEO triblock copolymer solutions*. Rheol. Acta, 45, 239–249.
- [117] Hyun, K., Nam, J. G., Wilhelm, M., Ahn, K. H., & Lee, S. J. (2003) *Nonlinear response of complex fluids under LAOS (large amplitude oscillatory shear) flow*. Korea-Australia Rheology Journal, 15 (2), 97-105.
- [118] T.A. Instruments (2000) *AR 500-1000 Rheometers Hardware Manual*.
- [119] Ionescu, D. G. (2004) *Introducere in mecanica fluidelor*. București: Editura Tehnică.
- [120] Jenkins, J. T., & Koenders, M. A. (2005) *Hydrodynamic interaction of rough spheres*. Granular Matter, 7, 13-18.
- [121] Jeong, J. H., Choi, Y. S., Shin, Y. J., Lee, J. J., Park, K. T., Lee, E. S., et al. (2002) *Flow behavior at the embossing stage of nanoimprint lithography*. Fibres and polymers, 3 (3), 113-119.
- [122] Jiang, P., See, H., Swain, M. V., & Phan-Thien, N. (2003) *Using oscillatory squeezing flow to measure the viscoelastic properties of dental composite resin cements during curing*. Rheol. Acta, 42, 118-112.
- [123] Kaci, A., Racineux, G., & Chaouche, M. (2009). *Study of flow and blockage of highly concentrated granular suspensions under squeeze test conditions*. Annual transactions of the nordic rheology society, 17, 6.
- [124] Karapetsas, G., & Tsamopolous, J. (2006) *Transient squeeze flow of viscoplastic materials*. Journal of Non-Newtonian Fluid Mechanics, 133: 35-56.
- [125] Karis, T. E., Kono, R. N., & Jhon, M. S. (2003) *Harmonic analysis in grease rheology*. J. Appl. Polym. Sci., 90, 334–343.
- [126] Karis, T. E., Kono, R. N., Lim, C. A., Jhon, M. S., & Choi, H. J. (2003) *Nonlinear rheology for a grease*. J. Inf. Eng. Chem., 9 (4), 419-425.
- [127] Kaylon, D. M., & Tang, H. S. (2007) *Inverse problem solution of squeeze flow for parameters of generalized Newtonian fluid and wall slip*. J. Non-Newtonian Fluid Mech., 143, 133-140.
- [128] Kim, S. H., Sim H. G., Hyun, K. A., & Lee, S. J. (2002) *Large amplitude oscillatory shear behavior of the network model for associating polymeric systems*. Korea-Australia Rheology Journal, 14 (2), 49-55.
- [129] Klein, C. O., Spiess, H. W., Calin, A., Balan, C., & Wilhelm, M. (2007) *Separation of the nonlinear oscillatory response into a superposition of linear, strain hardening, strain softening, and wall slip response*. Macromolecules, 40, 4250-4259.
- [130] Klein, C., Venema, P., Sagis, L., & van der Linden, E. (2008) *Rheological discrimination and characterization of carrageenans and starches by Fourier transform-rheology in the non-linear viscous regime*. J. Non-Newtonian Fluid Mech., 151, 145–150.

Bibliography

- [131] Kolenda, F., Retana, P., Racineux, G., & Poitou, A. (2003) *Identification of rheological parameters by the squeezing test*. Powder Technology, 130, 56–62.
- [132] Kolkka, R. W., Malkus, D. S., Hansen, M. G., Ierley, G. R., & Worthing, R. A. (1988) *Spurt phenomena of the Johnson-Segalman fluid and related models*. J. Non-Newtonian Fluid Mech., 29, 303–335.
- [133] Kompani, M., & Venerus, D. C. (2000) *Equibiaxial extensional flow of polymer melts via lubricated squeeze flow I. Experimental analysis*. Rheologica Acta, 39, 441–451.
- [134] Kouassi-Koffi, J. D., Launay, B., Davidou, S., Kouamé, L. P., & Michon, C. (2010) *Lubricated squeezing flow of thin slabs of wheat flour dough: comparison of results at constant plate speed and constant extension rates*. Rheol Acta, 49, 275–283.
- [135] Kramb, R. C., & Zukoski, C. F. (2011) *Nonlinear rheology and yielding in dense suspensions of hard anisotropic colloids*. J. Rheol., 55 (5), 1069–2084.
- [136] Krotov, V., & Rusanov, A. (1999) *Physicochemical Hydrodynamics of Capillary Systems*. London: Imperial College Press.
- [137] Kung, K. Y., Hsu, C. H., Chen, P. C., & Lin, J. R. (2004) *Effects of surface roughness on dynamic squeeze behavior of partial journal bearings with finite width*. Math'04 Proceedings of the 5th WSEAS International Conference on Applied Mathematics, Stevens Point, Wisconsin, USA: ACM, Inc., 6pp.
- [138] Kuzhir, P., López-López, M. T., Vertelov, G., Pradille, C., & Bossis, G. (2008) *Shear and squeeze rheometry of suspensions of magnetic polymerized chains*. Rheol. Acta., 47, 179–187.
- [139] Kuzma, D. C. (1968) *Fluid inertia effects in squeeze films*. Appl. Sci. Res., 18 (1), 15–20.
- [140] Langlois, W. (1964) *Slow Viscous Flow*. New York: MacMillan Co.
- [141] Larson, R. G. (1998) *Constitutive equations for polymer melts and solutions*. Boston: Butterworths.
- [142] Larson, R. G. (1999) *The structure and rheology of complex fluids*. New-York: Oxford University Press.
- [143] Lauger, J., & Stettin, H. (2010) *Differences between stress and strain control in the non-linear behavior of complex fluids*. Rheol. Acta (DOI 10.1007/s00397-010-0450-0).
- [144] Laun, H. m., Rady, M., & Hassager, O. (1999) *Analytical solutions for squeeze flow with partial wall slip*. J. Non-Newtonian Fluid Mech., 81, 1–15.
- [145] Lawal, A., & Kalyon, M. (2000) *Compressive squeeze flow of generalized newtonian fluids with apparent wall slip*. Intern. Polymer Processing XV, 63–71.
- [146] Leblanc, J. L. (2008) *Large amplitude oscillatory shear experiments to investigate the nonlinear viscoelastic properties of highly loaded carbon black rubber compounds without curatives*. J. of Appl. Poly. Sci., 109, 1271–1293.
- [147] Lee, D. J., Cho, K. Y., Jang, S., Song, Y. S., Youn, J. R. (2012) *Liquid slip on a nanostructured surface*. Langmuir, 28 (28), pp 10488–10494
- [148] Lee, S. J., Denn, M. M., Crochet, M. J., Metzner, A. B., & Riggins, G. J. (1984) *Compressive flow between parallel disks II: Oscillatory behavior of viscoelastic materials under a constant load*. J. of Non-Newtonian Fl. Mech., 14, 301–325.
- [149] Leonov, A. I., & Prokunin, A. N. (1994) *Nonlinear phenomena in flows of viscoelastic polymer fluids*. London: Chapman & Hall.
- [150] Lettinga, M. P., & Manneville, S. (2009) *Competition between shear banding and wall slip in wormlike micelles*. Phys. Rev. Lett., 103, 248302.
- [151] Ling, G. H., & Shaw, M. T. (2011) *Interparticle interaction and gel characterization of PE microgels using small- and large-strain viscoelastic response*. Rheol Acta, 50, 243–255.
- [152] Lu, R. F., & Lin, J. R. (2007) *A theoretical study of combined effects of non-Newtonian rheology and viscosity-pressure dependence in the sphere- plate squeeze-film system*. Tribology International, 40, 125–131.

Bibliography

- [153] Ma, G. J., Wu, C. W., & Zhou, P. (2006) *Squeeze fluid film of spherical hydrophobic surfaces with wall slip*. Tribology International, 39, 863-872.
- [154] Ma, G. J., Wu, C. W., & Zhou, P. (2007) *Wall slip and hydrodynamics of two-dimensional journal bearing*. Tribology International, 40, 1056-1066.
- [155] Macosko, C. (1994) *Rheology. Principles, Measurements and Applications*. Minnesota: VCH Publishers Inc.
- [156] Majumdar, S., Krishnaswamy, R., & Sood, A. K. (2011) *Shear banding in a yield stress bearing Langmuir monolayer*. Soft Matter, 7, 7805-7812.
- [157] Malkin, A. Y. (1994) *Rheology Fundamentals*. Canada: ChemTech Publishing.
- [158] Malkin, A., Ilyin, S., Semakov, A., & Kulichikhin, V. (2012) *Viscoplasticity and stratified flow of colloid suspensions*. Soft Matter (DOI: 10.1039/c2sm06950d).
- [159] Mărculescu, C. (2009) *PhD Thesis: Studiul hidrodinamicii unui reactor chimic de polimerizare cu aplicatii in tehnologia polimerilor pre-ceramici*. București.
- [160] Masciaa, S., Patel, M. J., Rougha, S. L., Martinb, P. J., & Wilson, D. I. (2006) *Liquid phase migration in the extrusion and squeezing of microcrystalline cellulose pastes*. European Journal of Pharmaceutical Sciences , 29, 22-34.
- [161] McIntyre, E. C. (2008) *PhD. Thesis, Compression of smart materials: squeeze flow of electrorheological and magnetorheological fluids*. Michigan: The University of Michigan.
- [162] McKinley, G. H. (2005) *Dimensionless groups for understanding free surface flows of complex fluids*. S.O.R. Rheology Bulletin, 74, Lubbock: The Society of Rheology, 9pp.
- [163] Meeten, G. H. (2001) *Squeeze flow between plane and spherical surfaces*. Rheol. Acta, 40, 279-288.
- [164] Meeten, G. H. (2002) *Constant-force flow of soft solids*. Rheol. Acta, 41, 557-566.
- [165] Meeten, G. H. (2004) *Squeeze flow of soft solids between rough surfaces*. Rheol. Acta, 43, 6-16.
- [166] Mezger, T. G. (2006) *The rheology handbook 2nd Ed*. Hannover, Germany: Vincentz Network GmbH & Co.
- [167] Mitsoulis, E., & Matsoukas, A. (2005) *Free surface effects in squeeze flow of Bingham plastics*. J. Non-Newtonian Fluid Mech., 129, 182-187.
- [168] Mittal, K. L. (2008) *Contact angle, wettability and adhesion, Vol. 5*. The Netherlands: VSP.
- [169] Miyazaki, K., Wyss, H. M., Weitz, D. A., & Reichman, D. R. (2006) *Nonlinear viscoelasticity of metastable complex fluids*. Europhys. Lett., 75 (6), 915-921.
- [170] Møller, P. C., Fall, A., Chikkadi, V., Derks, D., & Bonn, D. (2009) *An attempt to categorize yield stress fluid behavior*. Phil. Trans. R. Soc., A (367), 5139-5155.
- [171] Møller, P. C., Rodts, S., Michels, M. A., & Bonn, D. (2008) *Shear banding and yield stress in soft glassy materials*. Phys. Rev. E., 77, 041507.
- [172] Moore, D. F. (1965) *A review of squeeze films*. Wear, 8, 245-263.
- [173] Munch, A., Wagner, B., & Witelski, T. P. (2005) *Lubrication models with small to large slip lengths*. Journal of Engineering Mathematics, 53 , 359–383.
- [174] Naduvanamani, N. B., & Siddangouda, A. (2007) *Combined effects of surface roughness and couple stresses on squeeze film lubrication between porous circular stepped plates*. J. of Eng. Trib., 221 (J), 525-534.
- [175] Nam, J. G., Hyun, K., Ahn, H. K., & Lee, S. J. (2008) *Prediction of normal stresses under large amplitude oscillatory shear flow*. J. Non-Newtonian Fl. Mech., 150, 1-10.
- [176] Noresson, V., & Ohlson, N. G. (2001) *A critical study of the Bingham model in squeeze-flow mode*. Materials and Design, 22, 651-658.
- [177] Oliver, D. R., & Huang, X. (2000) *Squeeze film testing of ceramic pastes*. Br. Cream. Trans., 99, 101-108.

Bibliography

- [178] Ouyang, T. (2010) *Phd thesis: Investigation, modeling and optimization of the pre-ceramic polymer melt fiber spinning process*. Bucharest.
- [179] Padua, G. W., & Whitney, R. M. (1982) *Application of the instron tester for investigation of rheology of corn dough*. Cereal Chem. , 59, 361-36.
- [180] Panahi, R., Jahanbakhsh, E., & Seif, M. (2005) *Comparison of interface capturing methods in two phase flows*. Iranian Journal of Science & Technology, Transaction B, Engineering, 29 (B6): 539-548.
- [181] Panahi, R., Jahanbakhsh, E., & Seif, M (2006). *Developement of a numerical hydrodynamic tank for ship motion simulation*. ECCOMAS CFD 2006, Egmond Aan Zee, Netherlands: TU Delft, The Netherlands, 6pp.
- [182] Pascovici, D., & Cicone, T. (2001) *Elemente de Tribologie*. Bucuresti: Editura BREN.
- [183] Phan-Thien, N. (2000) *Squeezing flow of a viscoelastic solid*. J. Non-Newtonian Fl. Mech., 95, 343-362.
- [184] Phan-Thien, N., & Dudek, J. (1985) *Squeeze film flow of ideal elastic liquids*. Journal of Non-Newtonian Fluid Mechanics, 227-254.
- [185] Phan-Thien, N., & Low, H. T. (1988) *Squeeze flow of a viscoelastic fluid a lubrication model*. J. of Non-Newtonian Fl. Mech., 28, 129-148.
- [186] Phan-Thien, N., & Tanner, R. I. (1983) *Viscoelastic squeeze-film flows - Maxwell fluids*. J. Fluid Mech., 129, 265-281.
- [187] Phan-Thien, N., Nasser, S., & Bliston, L. E. (2000) *Oscillatory squeezing flow of a biological material*. Rheol. Acta, 39, 409-417.
- [188] Ping, H., Jianbin, L., & Shizhu, W. (1999) *Theoretical study on the lubrication failure for the lubricants with a limiting shear stress*. Tribology International, 32 (7), 421-426.
- [189] Pipe, C. J., Majmudar, T. S., & McKinley, G. H. (2008) *High shear rate viscometry*. Rheol. Acta , 47, 621-642.
- [190] Poitou, A., & Racineux, G. (2001) *A squeezing experiment showing binder migration in concentrated suspensions*. J. Rheology, 45, 609-625.
- [191] Purwar, S., Lim, J. K., & Mauger, J. W. (1988) *Measuring viscosity of pharmaceutical nd cosmetic semisolids using normal stress*. J. Soc.Cosmect., 39, 241-258.
- [192] Putz, A. M., & Burghilea, T. I. (2009) *The solid-fluid transition in a yield stress shear thinning physical gel*. Rheol. Acta, 48, 673-689.
- [193] Rabideau, B. D., Lanos, C., & Cussot, P. (2009) *An investigation of squeeze flow as a viable technique for determining the yiel stress*. Rheol. Acta , 48, 517-526.
- [194] Raphaelides, S. N., & Gioldasi, A. (2004) *Elongational flow studies of set yogurt*. Journal of Food Engineering, 70 (4), 538-545.
- [195] Rădulescu, A., V., Bălan, C., Rădulescu, I., (2009) *Analytical model for lubricant squeeze film between tilted circular surfaces*. 17th International Colloquium Tribology, Stuttgart, Germany.
- [196] Renou, F., Stellbrink, J., & Petekidis, G. (2010) *Yielding process in a colloidal glass of oft star-like micelles under large amplitude oscillatory shear (LAOS)*. J. Rheol., 54 (6), 1219-1242.
- [197] Rogers, S. A., & Vlasopoulous, D. (2010) *Frieze group analysis of asymetric response to large-amplitude oscillatory shear*. J. Rheol., 54 (4), 859-880.
- [198] Roussel, N., & Lanos, C. (2004) *Particle fluid separation in shear flow of dense suspensions: experimental measurements on squeezed clay pastes*. Appl. Rheol., 14 (5), 256-265.
- [199] Ruttgers, A. (2010) *PhD. Thesis: Multiscale modelling of dilute polymeric fluids with stochastic and Fokker-Planck-based methods*. Kerpen: Rheinischen Friedrich-Wilhelms-Universität Bonn.

Bibliography

- [200] Sakai, S. (2004) *Improvements of an oscillatory squeezing flow rheometer for small elasticity measurements of liquids*. Rheol. Acta, 44, 16-28.
- [201] Sánchez, A. M., Prieto, R., Laso, M., & Riesgo, T. (2008) *A piezoelectric minirheometer for measuring the viscosity of polymer microsamples*. IEEE Trans. on Industrial Electronics, 55 (1).
- [202] Scott, J. R. (1931) *Theory and application of the parallel-plate plastimeter*. Trans. Int. Rubber. Ind., 7, 169-175.
- [203] Servais, C., Luciani, A., Anders, J., & Manson, E. (2002) *Squeeze flow of concentrated long fibre suspensions: experiments and model*. J. Non-Newtonian Fluid Mech., 104, 165–184.
- [204] Seth, J. R., Locatelli-Champagne, C., Monti, F., Bonnecaze, R. T., & Cloitre, M. (2012) *How do soft particle glasses yield and flow near solid surfaces?* Soft Matter, 8, 140-148.
- [205] Shaukat, A., Sharma, A., & Joshi, M. Y. (2012) *Squeeze flow behavior of (soft glassy) thixotropic material*. J. Non-Newtonian Fluid Mech., 167-168, 9-17.
- [206] Sherwood, J. D. (2002) *Liquid–solid relative motion during squeeze flow of pastes*. J. Non-Newtonian Fluid Mech., 104.
- [207] Sherwood, J. (2003) *Squeeze flow of a dry foam*. Journal of Non-Newtonian Fluid Mechanics, 115–128.
- [208] Sherwood, J., & al., e. (1991) *Squeeze-film rheometry of non-uniform mudcakes*. Journal of Non-Newtonian Fluid Mechanics, 311-334.
- [209] Sherwood, J., & Durban, D. (1998) *Squeeze-flow of a Herschel–Bulkley fluid*. Journal of Non-Newtonian Fluid Mechanics, 115-121.
- [210] Shukla, M. (2002) *Roughness effect on squeeze film pressure*. Sadhana, 27 (5), 577–583.
- [211] Smyrniotis, D. N., & Tsamopoulos, J. A. (2001) *Squeeze flow of Bingham plastics*. J. Non-Newtonian Fluid Mech., 100, 165–190.
- [212] Sneddon, I. N. (1961) *Fourier Series*. London: Latimer, Trend & Co. Ltd, Plymouth.
- [213] Soskey, P. R., & Winter, H. H. (1985) *Equibiaxial extension of two polymer melts: polystyrene and polyethylene*. J. Rheology, 29, 493-517.
- [214] Stefan, J. (1874) *Versuche uber die scheinbare adhesion*. Sitz. Kais. Akad. Wiss. Math., 69, 713-735.
- [215] Stolarski, T. A., & Chai, W. (2008) *Inertia effect in squeeze film air contact*. Tribology International, 41, 716-723.
- [216] Tanas, R. (2002) *Squeezing and squeezing-like terms in the master equation for a two-level atom in strong fields*. IOP, J. of Optics B, 4, 142–152.
- [217] Tanner, R., & Walters, K. (1998) *Rheology: An Historical Perspective*. Amsterdam, Netherlands: Elsevier Science B V.
- [218] Tiang, Y., Meng, Y., Mao, H., & Wen, S. (2002) *Mechanical property of electrorheological fluid under step compression*. J. of App. Phys., 92 (11), 5.
- [219] Tichy, J. A. (1982) *Effects of fluid inertia and viscoelasticity on squeeze film bearing forces at large vibration amplitudes*. Wear, 76, 69-89.
- [220] Tipei, N. (1957) *Hidrodinamica Lubrificației*. București: Ed. Academiei Române.
- [221] Toutoua, Y., Roussela, N., & Lanos, C. (2005) *The squeezing test: a tool to identify firm cement-based material's rheological behavior and evaluate their extrusion ability*. Cement and Concrete Research, 35, 1891– 1899.
- [222] Tropea, C., Yarin, A. L., & Foss, J. F. (2007) *Springer Handbook of Experimental Fluid Mechanics*. Berlin: Springer-Verlag Berlin Heidelberg.
- [223] Ubbink, O. (1977) *PhD Thesis: Numerical prediction of two fluid systems with sharp interfaces*. London.

Bibliography

- [224] Vadher, P. A., Dehri, G., & Patel, R. M. (2008) *The effect of surface roughness on the performance of hydromagnetic squeeze films between two conducting rough porous elliptical plates*. Turkish J. Eng. Env. Sci., 32, 219 – 227.
- [225] Venerus, D. C., Kompani, M., & Berenstein, B. (2000) *Equibiaxial extensional flow of polymer melts via lubricated squeeze flow II. Flow modeling*. Rheol. Acta, 39, 574-582.
- [226] Venkatesh, K. P., Patil, N., Pandey, A. K., & Pratap, R. (2009) *Design and characterization of in-plane MEMS yaw rate sensor*. Sadhana, 34 (4), 633–642.
- [227] Versteeg, H., & Malalasekera, W. (1995) *An introduction to Computational Fluid Dynamics*. Harlow: Longman Scientific & Tehnical.
- [228] Versteeg, H., & Malalasekera, W. (1998) *An introduction to Computational Fluid Dynamics 2nd Ed*. Harllow: Longman Scientific & Tehnical.
- [229] Waclawczyk, T., & Koronowicz, T. (2008) *Comparison of CICSAM and HRIC high-resolution schemes for interface capturing*. Journal of theoretical and applied mechanics, 46 (2): 325-345.
- [230] Walicki, E., & Walicka, A. (2001) *Inertia effects in squeeze flows of viscoplastic fluids*. Mech. of Composite Mat., 37, 347-356.
- [231] Weeks, E. R., Crocker, J. C., Levitt, A. C., Schofield, A., & Weitz, D. A. (2000) *Three-dimensional direct imaging of structural relaxation near the colloidal glass transition*. Science, 287, 627-631.
- [232] Whicker, D., Browne, A. L., & Rhode, S. M. (1976) *Some effects of inclination on elastohydrodynamic squeeze film problems*. J. Fluid Mechanics, 72 (2), 247-260.
- [233] Wilhem, M. (2002) *Fourier-Transform Rheology*. Macromol. Mater. Eng , 287, 83-205.
- [234] Wu, C. W., & Ma, G. J. (2005) *Abnormal behavior of a hydrodynamic lubrication journal bearing caused by wall slip*. Tribology International, 38, 492–499.
- [235] Xing, C., Braun, M. J., & Li, H. (2010) *Damping and added mass coefficients for a squeeze film damper using the full 3-D Navier–Stokes equation*. Tribology International, 43, 654–666 .
- [236] Xu, W., Tang, H., Lv, H., Li, J., Zhao, X., Li, H., et al. (2012) *Sol–gel transition of poly(3-hexylthiophene) revealed by capillary measurements: phase behaviors, gelation kinetics and the formation mechanism*. Soft Matter, 8, 726-733.
- [237] Xu, Y., Li, H., & Huang, W. (2005) *Viscous forces between two spheres colliding trough interstitial power-law fluid*. China Particulology, 3 (1-2), 52-57.
- [238] Yan, Y., Zhang, Z., Cheneler, D., Stokes, J. R., & Adams, M. J. (2009) *The influence of flow confinement on the rheological properties of complex fluids*. Rheol. Acta, 12.
- [239] Yang, F. (1998) *Exact solution for compressive flow of viscoplastic fluids under perfect slip wall boundary conditions*. Rheol. Acta , 37, 68-72.
- [240] Yang, I. J., Gretillat, M. A., & Senturia, S. D. (1997) *Effect of air damping on the dynamics of nonuniform deformations of microstructures*. Solid State Sensors and Actuators, 2, 1093-1096.
- [241] Yang, S. P., & Zhu, K. Q. (2006) *Analytical solutions for squeeze flow of Bingham fluid with Navier slip condition*. J. Non-Newtonian Fluid Mech., 138, 173–180.
- [242] Yao, N. Y., Becker, D. J., Chase, P., Broedersz, C. P., Depken, M., MacKintosh, F. C., et al. (2011) *Nonlinear viscoelasticity of actin transiently cross-linked with mutant α -Actinin-4*. J. Mol. Biol., 411, 1062–1071.
- [243] Yesilata, B., Clasen, C., & McKinley, G. H. (2006) *Nonlinear shear and extensional flow dynamics of wormlike surfactant solutions*. J. Non-Newtonian Fluid Mech., 133, 73–90.
- [244] Yingxi, Z., & Granick, S. (2002) *Limits of the hydrodynamic no-slip boundary condition*. Phys Rev Lett., 88 (10), 4.
- [245] Yingxi, Z., & Granick, S. (2001) *Rate-dependent slip of Newtonian liquid at smooth surfaces*. Phys. Rev. Lett., 87 (9), 4.

Bibliography

- [246] Yu, W., Wang, P., & Zhou, C. (2009) *General stress decomposition in nonlinear oscillatory shear flow*. J. Rheol., 53 (1), 215-238.
- [247] Zahorski, S. (1978) *Viscoelastic properties in plane squeeze-film flows*. J. Non-Newtonian Fl. Mech., 4, 217-228.
- [248] Zarbane, K., (2009) *PhD. Thesis: Etude numérique et expérimentale du comportement d'un film lubrifiant soumis a un chargement périodique*. Université de Poitiers.
- [249] Zhang, M., Xing, S., Xiao, L., Bao, P., Liu, W., & Xin, Q. (2008) *Design process parameteres for direct squeeze casting*. J. of Univ. Sci. and Tehnol. Beijing, 15 (3), 339-343.
- [250] Zhou, L., Cook, L. P., & McKinley, G. H. (2010) *Probing shear-banding transitions of the VCM model for entangled wormlike micellar solutions using large amplitude oscillatory shear (LAOS) deformations*. J. Non-Newtonian Fluid Mech., 165, 1462–1472.
- [251] Zwick, K. J., Ayyaswamy, P. S., & Cohen, I. M. (1997) *Oscillatory enhancement of the squeezing flow of yield stress fluids: a novel experimental result*. J. Fluid Mech. , 339, 77.
- [252] *** <http://www.anton-paar.com>.
- [253] *** Anton-Paar, G. G. *Technical Notes MCR Rheometers*. Graz, Germany: Anton Paar GmbH.
- [254] *** Brookfield n.d., *Brookfield R/S-Cps+ Rheometer, Operating Instructions Manual*, No. M/01-213-A0706 . Brookfield Engineering Laboratories, Inc.
- [255] *** <http://en.wikipedia.org>

ANNEXES

ANNEX 1. Rheological models dependency on their constitutive parameters

Viscosity vs. shear rate curve is dependent on constitutive parameters (also called the material parameters) value used for the rheological model. In this annex the influence of constitutive parameters on the variation of viscosity function for three rheological models (*Carreau-Yassuda*, *Bingham*, *Oldroyd*) is presented. For each model, the influence of each parameter is determined successively, whereas the other parameters are kept constant.

The Carreau Yassuda Model (eq. 2.16)

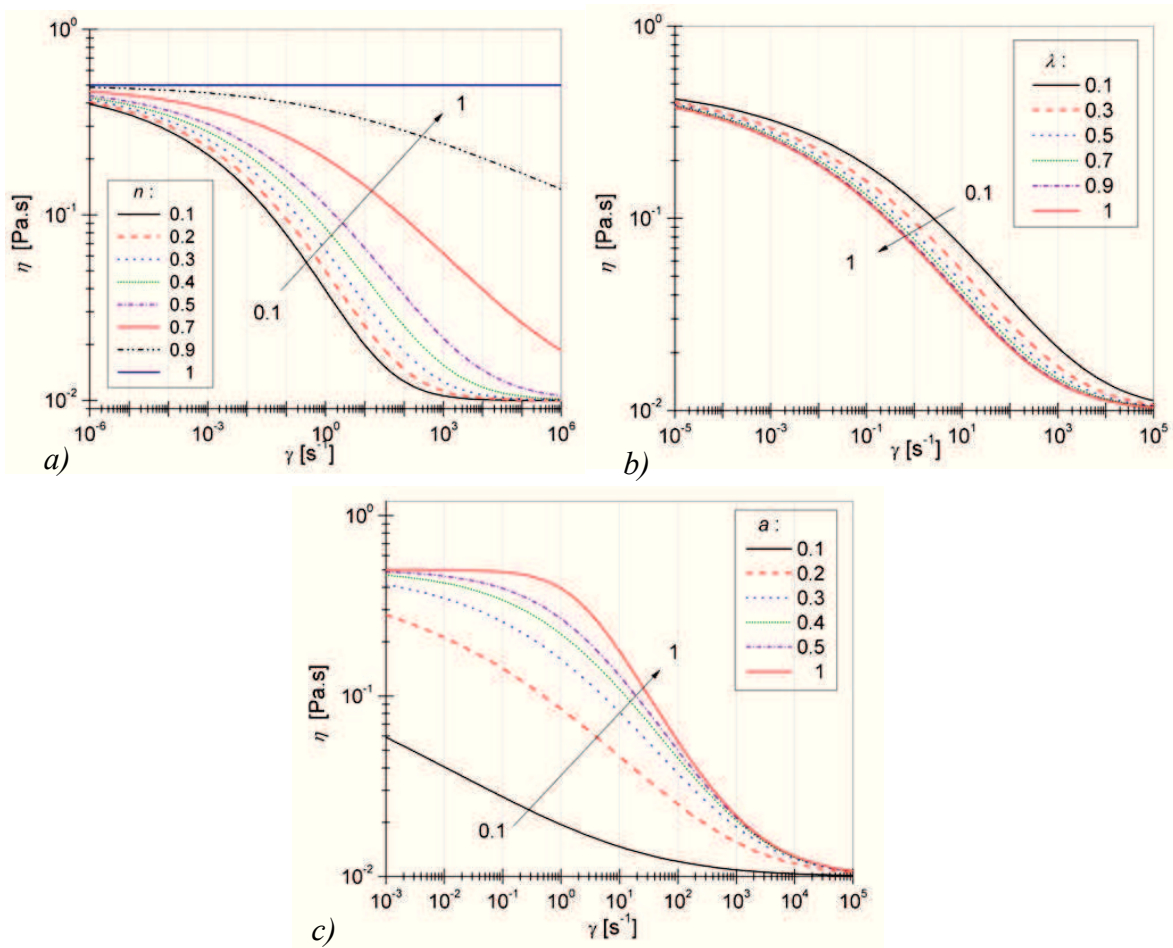


Fig. A. 1. Viscosity curve variation for Carreau-Yassuda model, depending on constitutive parameters: n (a), k (b), a (c).

In the case of Carreau-Yassuda model, the curves disclose a significant dependence of the viscosity curve of n and a , whereas λ doesn't have a significant influence (Figure A.1).

Table. A. 1. Parameters used for the representation of Careau-Yasuda model dependency on constitutive parameters.

η_0 [Pa.s]	η_∞ [Pa.s]	λ [-]	a [-]	n [-]
0.5	0.01	0.5	0.2	{0.1, 0.2, 0.3, 0.4, 0.5, 0.7, 0.9, 1}
0.5	0.01	{0.1, 0.5, 0.7, 0.9, 1}	0.2	0.4
0.5	0.01	0.5	{0.1, 0.2, 0.3, 0.4, 0.5, 1}	0.4

The Bingham model (eq. 2.18)

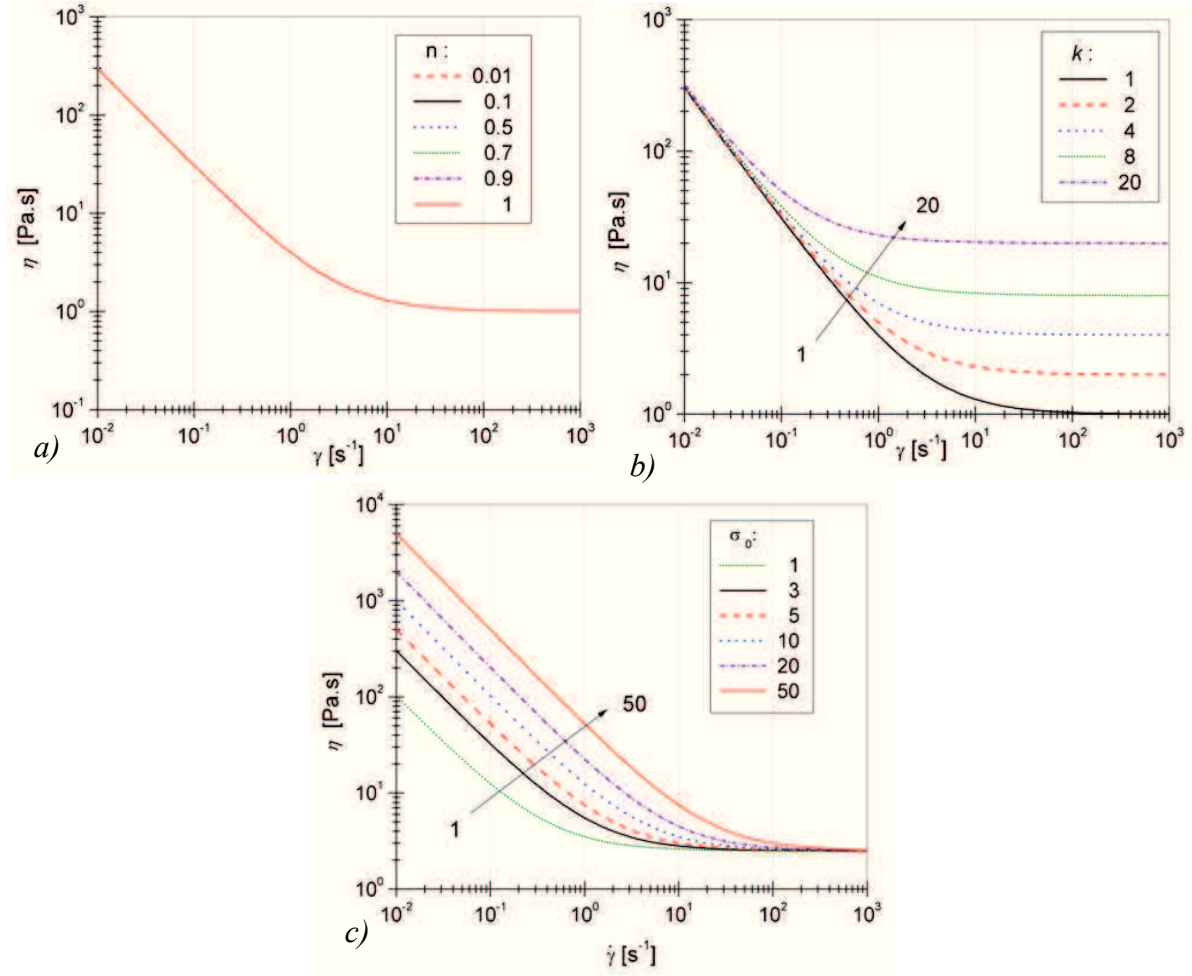


Fig. A. 2. Viscosity curve variation for Bingham model, depending on constitutive parameters: n (a), k (b), σ_0 (c).

Table. A. 2. Parameters used for the representation of Bingham model dependency on constitutive parameters.

σ_0 [Pa]	n [—]	k [—]
3	{0.01, 0.1, 0.5, 0.7, 0.9, 1}	1
3	1.2	{1, 2, 4, 8, 20}
{1, 3, 5, 10, 20, 50}	1.2	2.5

In the case of Bingham model, the curves disclose a significant dependence of the viscosity curve on σ_0 and k , whereas n doesn't have a significant influence.

ANNEX 2. Approximation of the experimental modules of a viscoelastic fluid by a *Maxwell* model with 8 elements

Figure 2.9 (Paragraph 2.3) presents the approximation of the experimental modules G' and G'' for a viscoelastic fluid (shampoo) with the *Maxwell* model with 8 elements, with variable relaxation time steps, at different amplitudes of the applied strain: $\gamma_0 = 0.01$ [—] (a); $\gamma_0 = 0.1$ [—] (b) și $\gamma_0 = 1$ [—] (c).

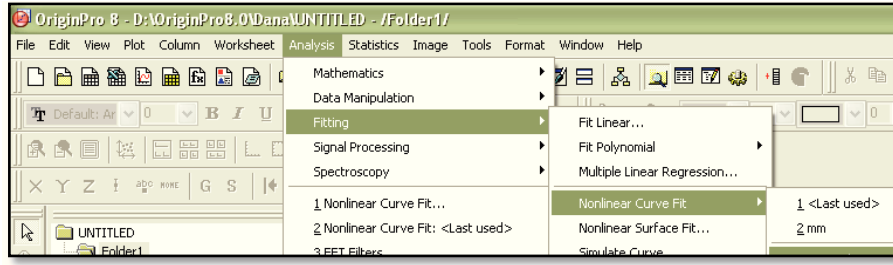


Fig. A. 3. Analysis module of *Origin 8.0* software used for the approximation of the experimental measurements.

Table. A. 3. The relaxation times and corresponding viscosities values for the approximation of fluid viscoelastic behavior with a Maxwell model (8 elements) for a initial applied deformation of $\gamma_0 = 0.01 [-]$.

		η_s	0.2725
λ_1	0.03279	η_1	3.66036
λ_2	0.00993	η_2	0.63648
λ_3	0.06444	η_3	7.48796
λ_4	0.44446	η_4	0.91164
λ_5	3.61E+24	η_5	6.61E+10
λ_6	918.8753	η_6	130
λ_7	2.45E+20	η_7	9.20E+10
λ_8	9.21E+18	η_8	1.43E+06

Table. A. 4. The relaxation times and corresponding viscosities values for the approximation of fluid viscoelastic behavior with a Maxwell model (8 elements) for a initial applied deformation of $\gamma_0 = 0.1 [-]$.

		η_s	0.27794
λ_1	0.03092	η_1	1.8569
λ_2	0.01156	η_2	0.6
λ_3	0.06211	η_3	10.85
λ_4	0.10034	η_4	0.65
λ_5	0.50296	η_5	1.74
λ_6	16182.54	η_6	60
λ_7	9.86E+17	η_7	0
λ_8	1.01E+13	η_8	5.18E+11

Table. A. 5. The relaxation times and corresponding viscosities values for the approximation of fluid viscoelastic behavior with a Maxwell model (8 elements) for a initial applied deformation of $\gamma_0 = 1 [-]$.

		η_s	9.22E-05
λ_1	2.85E-06	η_1	0.68398
λ_2	0.05822	η_2	3.2
λ_3	0.05819	η_3	6.5
λ_4	0.13029	η_4	2.68
λ_5	13304.6284	η_5	0
λ_6	1.25945	η_6	1.018
λ_7	45890.35042	η_7	0
λ_8	1.36E+12	η_8	0

For the interpolation an 8 elements Maxwell model (see Paragraph 2.3) was introduced in Origin 8.0 (see Figure A.4) , and by multiple iterations the measured value were aproximated with different relaxation times, presented in Table A.4 - A.6.

The obtained relaxation times vary depending on the intensity of the applied strain, respectively of the stress stored in the structure of the material during the yield, the results obtained following the approximation of the experimental values. At high strains (or applied deformations) some elemets of Maxwell model are nought (the viscosity is zero) indicating that the material hasn't got enough time to relax as at low strains where all the elements are present. Henece, at high deformation the measurements may be aproximated with a Maxwell modell that has less than 8 elements.

ANNEX 3. Determination of radial and axial velocity formulations for the simple squeeze flow of newtonian fluids between paralel plates.

In the relations (2.41 - 2.44), Paragraph 2.3.3, v_r and v_z represent the components of velocity on radial direction, respectively axial, in the squeeze flow.

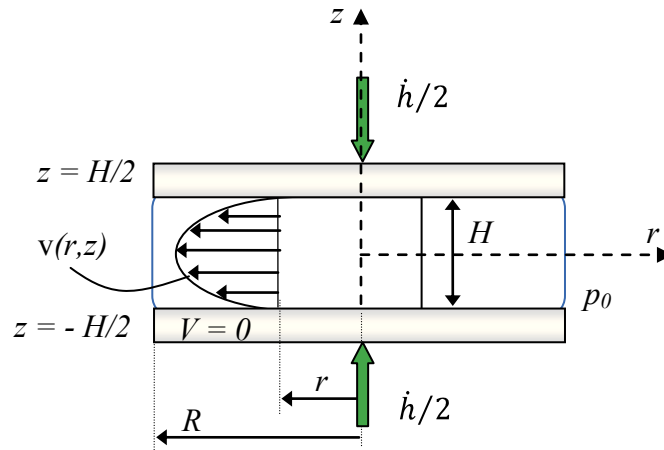


Fig. A. 4. Squeeze flow of Newtonian incompressible fluid between paralell plates in a double symmetry geometry.

In the case of the symmetrical axial squeeze flow with constant rate, the velocity distributions are obtained from the particular case of *Stokes* approximation, completed by the continuity equation, in the following hypothesis: (i) purely viscous incompressible fluids, in laminar flow; (ii) the geometry is defined by solid and impermeable surfaces to which the fluid adheres; (iii) inertia and the gravitational forces are neglectable compared to the pressure forces and to those of viscous friction; (iv) no other exterior mass force is deemed a factor that influences motion; (v) the motion is characterized by the velocity components v_r and v_z , the component v_ϕ being neglectable; (vi) velocity gradients on the directions Or and $O\phi$ are neglectable compared to the rate gradient on the normal direction; (vi) fluid film thickness is considered very small in comparison with the dimensions of the geometry which defines the flow domain.

Annexes

$$\begin{cases} (z): \frac{1}{\eta} \cdot \frac{\partial p}{\partial z} = \frac{\partial^2 u}{\partial z^2} + \frac{1}{r} \cdot \frac{\partial u}{\partial r} + \frac{\partial^2 u}{\partial r^2} \\ (r): \frac{1}{\eta} \cdot \frac{\partial p}{\partial r} = \frac{\partial^2 v}{\partial z^2} + \frac{1}{r} \cdot \frac{\partial v}{\partial r} + \frac{\partial^2 v}{\partial r^2} - \frac{v}{r^2} \end{cases} \quad (\text{a. 1})$$

$$\frac{\partial u}{\partial z} = -\frac{\partial v}{\partial r} - \frac{v}{r} \quad \cdot \frac{\partial}{\partial z} \quad (\text{a. 2})$$

$$\frac{\partial^2 u}{\partial z^2} = -\frac{\partial^2 v}{\partial z \cdot \partial r} - \frac{1}{r} \cdot \frac{\partial v}{\partial z} \quad \cdot dz^2 \quad (\text{a. 3})$$

$$u = -\int \frac{\partial v}{\partial r} \cdot dz - \frac{1}{r} \cdot \int v \cdot dz + g_1(r) + C_1 \quad \cdot \frac{\partial}{\partial r} \quad (\text{a. 4})$$

$$\frac{\partial u}{\partial r} = -\int \frac{\partial^2 v}{\partial r^2} \cdot dz + \frac{1}{r^2} \int v \cdot dz - \frac{1}{r} \cdot \int \frac{\partial v}{\partial r} \cdot dz + \frac{d \cdot g_1(r)}{dr} \quad \cdot \frac{\partial}{\partial r} \quad (\text{a. 5})$$

$$\frac{\partial^2 u}{\partial r^2} = -\frac{\int \partial^3 v}{\partial r^3} \cdot dz - \frac{2}{r^3} \cdot \int v \cdot dz + \frac{2}{r^2} \cdot \frac{\int \frac{\partial v}{\partial r} \cdot dz - \frac{1}{r} \cdot \int \partial^2}{\partial r^2} \cdot dz + d^2 \cdot \frac{g_1^2(r)}{d \cdot r^2} \quad (\text{a. 6})$$

$$\begin{aligned} \frac{1}{\eta} \cdot \frac{\partial p}{\partial z} = & -\frac{\partial^2 v}{\partial z \cdot \partial r} - \frac{1}{r} \cdot \frac{\partial v}{\partial z} - \frac{1}{r} \cdot \int \frac{\partial^2 v}{\partial r^2} \cdot dz + \frac{1}{r^3} \cdot \int v \cdot dz - \frac{1}{r^2} \cdot \frac{\int \frac{\partial v}{\partial r} \cdot dz + \dots + \frac{1}{r} \cdot d \cdot g_1(r)}{\partial r} \\ & - \int \frac{\partial^3 v}{\partial r^3} \cdot dz - \frac{2}{r^2} \cdot \int v \cdot dz + \frac{2}{r^2 \int \frac{\partial v}{\partial r}} \cdot dz - \frac{1}{r} \cdot \int \frac{\partial^2 v}{\partial r^2} \cdot dz + \frac{d^2 \cdot g_1(r)}{d \cdot r^2} \end{aligned} \quad (\text{a. 7})$$

$$\begin{aligned} \frac{1}{\eta} \cdot \frac{\partial p}{\partial z} = & -\frac{\partial^2 v}{\partial z \cdot \partial r} - \frac{1}{r} \cdot \frac{\partial v}{\partial r} - \frac{1}{r^3} \cdot \int v \cdot dz + \frac{1}{r^2} \cdot \int \frac{\partial v}{\partial r} \cdot dz - \frac{2}{r} \cdot \int \frac{\partial^2 v}{\partial r^2} \cdot dz - \dots - \int \frac{\partial^3 v}{\partial r^3} \cdot dz + \frac{1}{r} \\ & \cdot \frac{d \cdot g_1(r)}{dr} + \frac{d^2 \cdot g_1(r)}{dr^2} \quad \cdot dz \end{aligned} \quad (\text{a. 8})$$

$$\begin{aligned} \frac{1}{\eta} \cdot p = & -\frac{\partial v}{\partial r} - \frac{v}{r} - \frac{1}{r^3} \cdot \iint v \cdot dzdz + \frac{1}{r^2} \cdot \iint \frac{\partial v}{\partial r} \cdot dzdz - \frac{2}{r} \cdot \iint \frac{\partial^2 v}{\partial r^2} \cdot dzdz - \dots - \iint \frac{\partial^3 v}{\partial r^3} \cdot dzdz \\ & + \left[\frac{1}{r} \cdot \frac{d \cdot g_1(r)}{dr} + \frac{d^2 \cdot g_1(r)}{dr^2} \right] + z + g_2(r) + C_2 \end{aligned} \quad (\text{a. 9})$$

$$\frac{1}{\eta} \cdot p = \int \frac{\partial^2 v}{\partial z^2} \cdot dr + \int \frac{1}{r} \cdot \frac{\partial v}{\partial r} \cdot dr + \frac{\partial v}{\partial r} - \int \frac{v}{r^2} \cdot dr + f_1(z) + C_3 \quad (\text{a. 10})$$

$$\int \frac{1}{r} \cdot \frac{dv(r)}{dr} \cdot dr = \frac{v(r)}{r} + \int \frac{v(r)}{r^2} dr \quad (\text{a. 11})$$

$$\frac{1}{\eta} \cdot p = \int \frac{\partial^2 v}{\partial z^2} \cdot dr + \frac{v}{r} + \frac{\partial v}{\partial r} + f_1(z) + C_3 \quad (\text{a. 12})$$

Accordingly to the flow rate conservation expressions:

$$-\pi \cdot r^2 \cdot \frac{u_s}{2} = 2 \cdot \pi \cdot r \cdot \int_{z=0}^{z=\frac{H}{2}} v(r, z) \cdot dz \quad \cdot -\frac{1}{2 \cdot r} \cdot \frac{1}{\pi} \quad (\text{a. 13})$$

$$-\frac{1}{4} \cdot u_s \cdot r = \int_{z=0}^{z=\frac{H}{2}} v(r, z) \cdot dz$$

$$v(r, z) = C_4 \cdot r \cdot f_2(z)$$

(a. 15)

By introducing velocity expression into (a.9):

$$\begin{aligned} \frac{1}{\eta} \cdot p = & -C_4 \cdot f_2(z) - C_4 \cdot f_2(z) - \frac{C_4}{r^2} \cdot \iint f_2(z) \cdot dzdz + \frac{C_4}{r^2} \cdot \iint f_2(z) \cdot dzdz + \dots \\ & + \left[\frac{1}{r} \cdot \frac{d \cdot g_1(r)}{dr} + \frac{d^2 \cdot g_1(r)}{dr^2} \right] \cdot z + g_2(r) + C_2 \end{aligned}$$

(a. 16)

$$\frac{1}{\eta} \cdot p = -2 \cdot C_4 \cdot f_2(z) + \left[\frac{1}{r} \cdot \frac{d \cdot g_1(r)}{dr} + \frac{d^2 \cdot g_1(r)}{dr^2} \right] \cdot z + g_2(r) + C_2$$

(a. 17)

The symmetry condition on z direction is $p(+z, r) = p(-z, r)$, therefore:

$$\frac{1}{r} \cdot \frac{d \cdot g_1(r)}{dr} + \frac{d^2 \cdot g_1(r)}{dr^2} = 0$$

(a. 18)

Making the followings notations:

$$\frac{d \cdot g_1(r)}{dr} = G(r), \quad \frac{d^2 \cdot g_1(r)}{dr^2} = \frac{dG(r)}{dr}$$

(a. 19)

And replacing in (a.18):

$$\frac{1}{r} \cdot G(r) + \frac{dG(r)}{dr} = 0, \quad \frac{dG(r)}{dr} = -\frac{1}{r} \cdot G(r), \quad \frac{dG(r)}{G(r)} = -\frac{dr}{r}$$

(a. 20)

By integration in dr :

$$\ln(G(r)) = -\ln(r) \overline{C_5} \rightarrow G(r) = \frac{\overline{C_5}}{r} \cdot dr$$

(a. 21)

$$\ln(G(r)) + \ln(r) = \overline{C_5}$$

(a. 22)

$$\ln(G(r) \cdot r) = \overline{C_5}$$

(a. 23)

$$\ln(G(r) \cdot r) = \ln(\overline{C_5}) \rightarrow G(r) \cdot r = \overline{C_5} \rightarrow G(r) = \frac{\overline{C_5}}{r}$$

(a. 24)

Replacing $G(r) = \frac{d \cdot g_1(r)}{dr}$ in (a.24):

$$G(r) = \frac{d \cdot g_1(r)}{dr} \rightarrow \frac{dg_1(r)}{dr} = \frac{\overline{C_5}}{r} \quad | \cdot dr$$

(a. 25)

$$g_1(r) = \overline{C_5} \cdot \ln(r) + C_6$$

(a. 26)

By introducing $v(r, z) = C_4 \cdot r \cdot f_2(z)$ in (a.10):

$$\frac{1}{\eta} \cdot p = \frac{1}{2} \cdot C_4 \cdot r^2 \cdot \frac{\partial^2 \cdot f_2(z)}{\partial \cdot z^2} + 2 \cdot C_4 \cdot f_2(z) + f_1(z) + C_3$$

(a. 27)

The symmetry condition on z direction is $p(+z, r) = p(-z, r)$, therefore:

$$\frac{1}{\eta} \cdot p = -2 \cdot C_4 \cdot (z) + g_2(r) + C_2 \quad (\text{a. 28})$$

The relationships (a.27) and (a.28) must be equal because they express the same quantity $\frac{1}{\eta} \cdot p$, therefore the following approximations can be made:

$$2 \cdot C_4 \cdot f_2(z) + f_1(z) = -2 \cdot C_4 \cdot f_2(z), \quad (\text{a. 29})$$

$$f_1(z) = -4 \cdot C_4 \cdot f_2(z) \quad (\text{a. 30})$$

The free terms:

$$C_3 = C_2 \quad (\text{a. 31})$$

C_7 must be a constant cos in (a.28) we have no terms in z but only in r :

$$\frac{d^2 \cdot f_2(z)}{d \cdot z^2} = C_7 \quad (\text{a. 32})$$

And the rest of the terms must be equal:

$$g_2(r) = \frac{1}{2} \cdot C_4 \cdot C_7 \cdot r^2 \quad (\text{a. 33})$$

Replacing in (2.8) the specified notations:

$$\frac{1}{\eta} \cdot p = \frac{1}{2} \cdot C_4 \cdot C_7 \cdot r^2 - 2 \cdot C_4 \cdot f_2(z) + C_3 \quad (\text{a. 34})$$

By successive integration on z :

$$f_2(z) = \frac{1}{2} \cdot C_7 \cdot z^2 + C_8 \cdot z + C_9 \quad (\text{a. 35})$$

And replacing $f_2(z)$ in (a.15):

$$v(r, z) = C_4 \cdot r \cdot \left(\frac{1}{2} \cdot C_7 \cdot z^2 + C_8 \cdot z + C_9 \right) \quad (\text{a. 36})$$

Because of the symmetry $v(z, r) = v(-z, r)$, C_8 must be nought,

$$f_2(z) = \frac{1}{2} \cdot C_7 \cdot z^2 + C_9 \quad (\text{a. 37})$$

$$v(r, z) = C_4 \cdot r \cdot \left(\frac{1}{2} \cdot C_7 \cdot z^2 + C_9 \right) \quad (\text{a. 38})$$

The “no slip condition” imposes that $v\left(z = \pm \frac{H}{2}, r\right) = 0$, therefore:

$$v\left(\pm \frac{H}{2}, r\right) = C_4 \cdot r \cdot \left[\frac{1}{2} \cdot C_7 \cdot \left(\frac{H}{2}\right)^2 + C_9 \right] = 0 \quad (\text{a. 39})$$

$$C_9 = -\frac{1}{2} \cdot C_7 \cdot \left(\frac{H}{2}\right)^2 \quad (\text{a. 40})$$

Replacing C_9 in $f_2(z)$:

$$\int_0^{z=H/2} v(r, z) \cdot dz = -\frac{1}{2} \cdot C_4 \cdot C_7 \cdot r \cdot \left[\frac{H^2}{4} \cdot z - \frac{z^3}{3} \right]_0^{H/2} \quad (\text{a. 41})$$

$$\int_{z=0}^{z=H/2} v(r, z) \cdot dz = -\frac{1}{24} \cdot C_4 \cdot C_7 \cdot r \cdot H^3$$

But

$$\int_{z=0}^{z=H/2} v(r, z) \cdot dz = -\frac{1}{4} \cdot u_s \cdot r, \quad (a. 42)$$

$$-\frac{1}{4} \cdot u_s \cdot r = -\frac{1}{24} \cdot C_4 \cdot C_7 \cdot r \cdot H^3 \quad (a. 43)$$

$$C_4 \cdot C_7 = 6 \cdot u_s \cdot \frac{1}{H^3} \quad (a. 44)$$

$$v(r, z) = -3 \cdot \frac{u_s}{H^3} \cdot r \cdot \left(\frac{H^2}{4} - z^2 \right) \quad (a. 45)$$

The radial velocity has the following form:

$$v(r, z) = -3 \cdot \frac{u_s}{H^3} r \cdot \left(\frac{H^2}{4} - z^2 \right) \quad (a. 46)$$

In the same manner, for axial velocity:

$$\frac{\partial v}{\partial r} = -3 \cdot \frac{u_s}{H^3} \cdot 1 \cdot \left(\frac{H^2}{4} - z^2 \right) \rightarrow -\frac{\partial v}{\partial r} = 3 \cdot \frac{u_s}{H^3} \cdot \left(\frac{H^2}{4} - z^2 \right) \quad (a. 47)$$

$$\frac{v}{r} = -3 \cdot \frac{u_s}{H^3} \cdot \left(\frac{H^2}{4} - z^2 \right) \rightarrow -\frac{v}{r} = 3 \cdot \frac{u_s}{H^3} \cdot \left(\frac{H^2}{4} - z^2 \right) \quad (a. 48)$$

$$\frac{\partial u}{\partial r} = -\frac{\partial v}{\partial r} - \frac{v}{r} = 6 \cdot \frac{u_s}{H^3} \cdot \left(\frac{H^2}{4} - z^2 \right) \quad (a. 49)$$

$$\frac{\partial u}{\partial z} = -\frac{\partial v}{\partial r} - \frac{v}{r} = 6 \cdot \frac{u_s}{H^3} \cdot r \cdot \left(\frac{H^2}{4} - z^2 \right) \quad (a. 50)$$

$$u(z, r) = -\int \frac{\partial v}{\partial r} dz - \frac{1}{r} \cdot \int v(z, r) \cdot dz + g_1(r) + C_1 \Rightarrow \quad (a. 51)$$

$$u(z, r) = 6 \cdot \frac{u_s}{H^3} \cdot \left(\frac{H^2}{4} \cdot z - \frac{1}{3} \cdot z^3 \right) + g_1(r) + C_1 \quad (a. 52)$$

$$g_1(r) = C_5 \cdot \ln(r) + C_6 \Rightarrow \quad (a. 53)$$

$$u(z, r) = 6 \cdot \frac{u_s}{H^3} \cdot \left(\frac{H^2}{4} \cdot z - \frac{1}{3} \cdot z^3 \right) + C_5 \cdot \ln(r) + C_6 + C_1 \quad (a. 54)$$

For the double symmetric squeeze flow, $u\left(z = \frac{H}{2}, r\right) = u_s/2$:

$$\frac{u_s}{2} = 6 \cdot \frac{u_s}{H^3} \cdot \left(\frac{H^3}{8} - \frac{1}{3} \cdot \left(\frac{H^2}{2} \right)^3 \right) + C_5 \cdot \ln(r) + C_6 + C_1 \quad (a. 55)$$

$$\frac{u_s}{2} = \frac{1}{2} \cdot u_s + C_5 \cdot \ln(r) + C_6 + C_1 \quad (a. 56)$$

Reducing u_s ,

$$C_5 \cdot \ln(r) + C_6 + C_1 = 0$$

$$\begin{cases} C_6 + C_1 = 0 \\ C_5 = 0 \end{cases} \quad (\text{a. 58})$$

(a. 59)

Therefore, the axial velocity has the following expression:

$$u(z) = 6 \cdot \frac{u_s}{H^3} \cdot \left(\frac{H^4}{4} \cdot z - \frac{1}{3} \cdot z^3 \right) \quad (\text{a. 60})$$

$$f_3(z) = -\frac{1}{2} \cdot C_7 \cdot \left(\frac{H^2}{4} - z^2 \right) \quad (\text{a. 61})$$

Replacing $f_2(z)$ in (a.34):

$$\frac{1}{\eta} \cdot p = \frac{1}{2} \cdot C_4 \cdot C_7 \cdot r^2 + C_4 \cdot C_7 \cdot \left(\frac{H^2}{4} - z^2 \right) + C_3 \quad (\text{a. 62})$$

$$\frac{1}{\eta} \cdot p = C_4 \cdot C_7 \cdot \left[\left(\frac{H^2}{4} - z^2 \right) + \frac{1}{2} \cdot r^2 \right] + C_3 \quad (\text{a. 63})$$

$$p = 6 \cdot u_s \cdot \frac{\eta}{H^3} \cdot \left[\left(\frac{H^2}{4} - z^2 \right) + \frac{1}{2} \cdot r^2 \right] + C_3 \cdot \eta \quad (\text{a. 64})$$

The symmetry condition $p\left(z = \pm \frac{H}{2}, R\right) = p_0$ imposes the following notations:

$$\begin{cases} z = \pm H/2 \\ r = R \\ p = p_0 \end{cases} \quad (\text{a. 65})$$

$$p_0 = 6 \cdot u_s \cdot \frac{\eta}{H^3} \cdot \left[\left(\frac{H^2}{4} - \left(\frac{H}{2} \right)^2 \right) + \frac{1}{2} \cdot R^2 \right] + C_3 \cdot \eta \quad (\text{a. 66})$$

$$C_3 = \frac{p_0}{\eta} - 3 \cdot \frac{u_s}{H^3} \cdot R^2 \Rightarrow \quad (\text{a. 67})$$

$$p(z, r) = p_0 + 6 \cdot \eta \cdot \frac{u_s}{H^3} \cdot \left[\left(\frac{H^2}{4} - z^2 \right) - \frac{1}{2} \cdot (R^2 - r^2) \right] \quad (\text{a. 68})$$

ANNEX 4. Simulation Parameters and boundary conditions for numerical modelling of squeeze flow.

The single phase simulations parameters (both simple and oscillatory squeeze flow):

- ▶ 2-D case, double precision.

Solver:

- ▶ Pressure based solver;
- ▶ Axisymmetric space;
- ▶ Unsteady case, of the 1st Order Implicit Formulation;
- ▶ Green-Gauss Cell Based gradient option;
- ▶ Superficial Velocity for porous formulation;
- ▶ Absolute velocity formulation.

Mesh Options:

- ▶ Dynamic mesh (only for the transient approximation);
- ▶ Layering mesh methods;
- ▶ Split factor: 0.4;
- ▶ Collapse factor: 0.04.

Solution Controls:

- ▶ PISO pressure-velocity coupling;
- ▶ Skewness correction: 0;
- ▶ Neighbour correction: 1;
- ▶ PRESTO! Pressure discretization;
- ▶ First order upwind momentum discretization.

The boundary conditions imposed for both simple and oscillatory squeeze flow are presented in [Figure A.5](#).

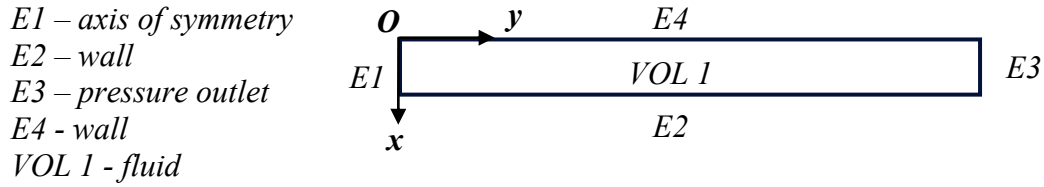


Fig. A. 5. Boundary conditions imposed for both simple and oscillatory squeeze flow, in the case of transient dynamic mesh approximation.

The boundary conditions imposed for the simple squeeze flow when using a quasisteady approximation are presented in [Figure A.6](#).

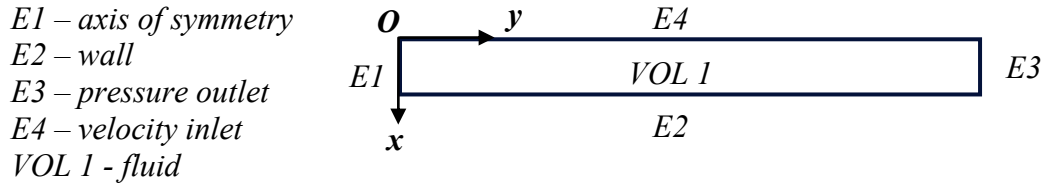


Fig. A. 6. Boundary conditions imposed for both simple squeeze flow, in the case of quasisteady approximation.

The multiphase simulations of squeeze flow, used the following parameters:

- ▶ 2-D case, double precision.

Solver:

- ▶ Pressure based solver;
- ▶ Axisymmetric space;
- ▶ Unsteady case, of the 1st Order Implicit Formulation;
- ▶ Both Green-Gauss Cell Based and Green-Gauss Node Based gradient option;
- ▶ Superficial Velocity for porous formulation;
- ▶ Absolute velocity formulation.

Multiphase Model:

- ▶ Volume of Fluid with 2 fluid phases;
- ▶ VOF explicit scheme.
- ▶ Courant number 0.25 -25;

- ▶ No implicit body force formulation.

Phases interaction:

- ▶ Wall adhesion (contact angle specified for each solid wall) / No wall adhesion (depending on the case);
- ▶ Surface tension of 0.01 N/m / No surface tension (depending on the case).

Mesh:

- ▶ Dynamic mesh;
- ▶ Layering mesh methods;
- ▶ Split factor: 0.4;
- ▶ Collapse factor: 0.4.

Solution Controls:

- ▶ PISO pressure-velocity coupling;
- ▶ Skewness correction: 0.
- ▶ Neighbour correction: 1.
- ▶ PRESTO! Pressure discretization;
- ▶ First order upwind momentum discretization;
- ▶ Volume fraction scheme: CICSAM / Geo Reconstruct.

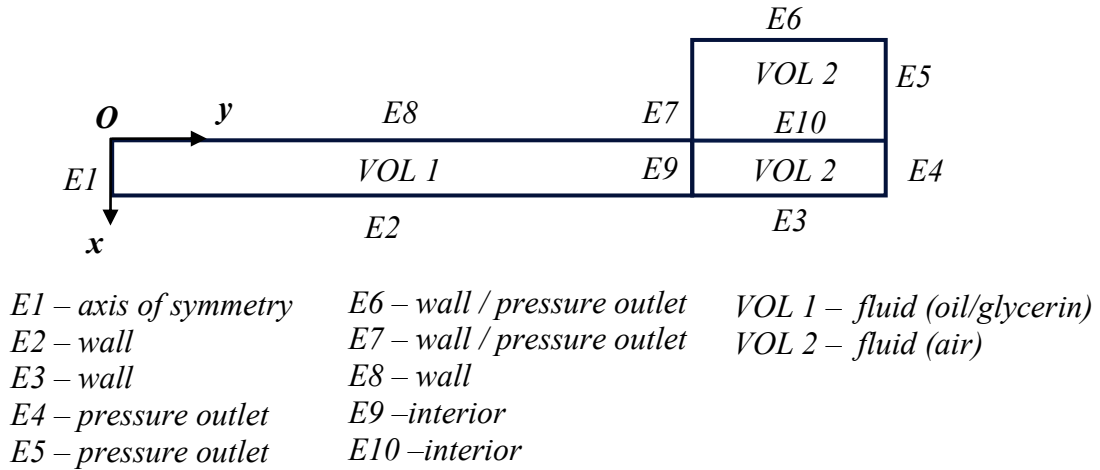


Fig. A. 7. Boundary conditions imposed for multiphase (VOF) simulations of squeezing flow.

ANNEX 5. Geometries construction and meshing for single phase quasi-steady approximation of squeeze flow simulations. Influence of the free surface geometry.

The influence of end effects has been investigated also using a quasi-steady approximation of the constant velocity squeeze flow by numerical modelling into different geometries with various shapes of the outlet area, imposed free surface (see [Paragraph 4.4.2](#)). The dimensions of the virtual geometries (2D, axial-symmetric) are the same as for the real experimental one ($R = 21.5 \text{ mm}$), at two different gaps ($h_0 \in \{50, 500 \mu\text{m}\}$). The outlet zone was modelled as observed during the experiments: for VOFb and VOFc geometries the length of the exterior zone is 1 mm ; for the linear „free surfaces” the exterior length was of VOFa1 – 0.5 mm , VOFa2 – 1 mm , VOFa3 – 2 mm ; and VOFa4 – 3 mm . Geometries shapes are not allowing the use of quadrilateral elements, therefore the mesh is made by using triangular elements (see. [Figure A.6](#)).

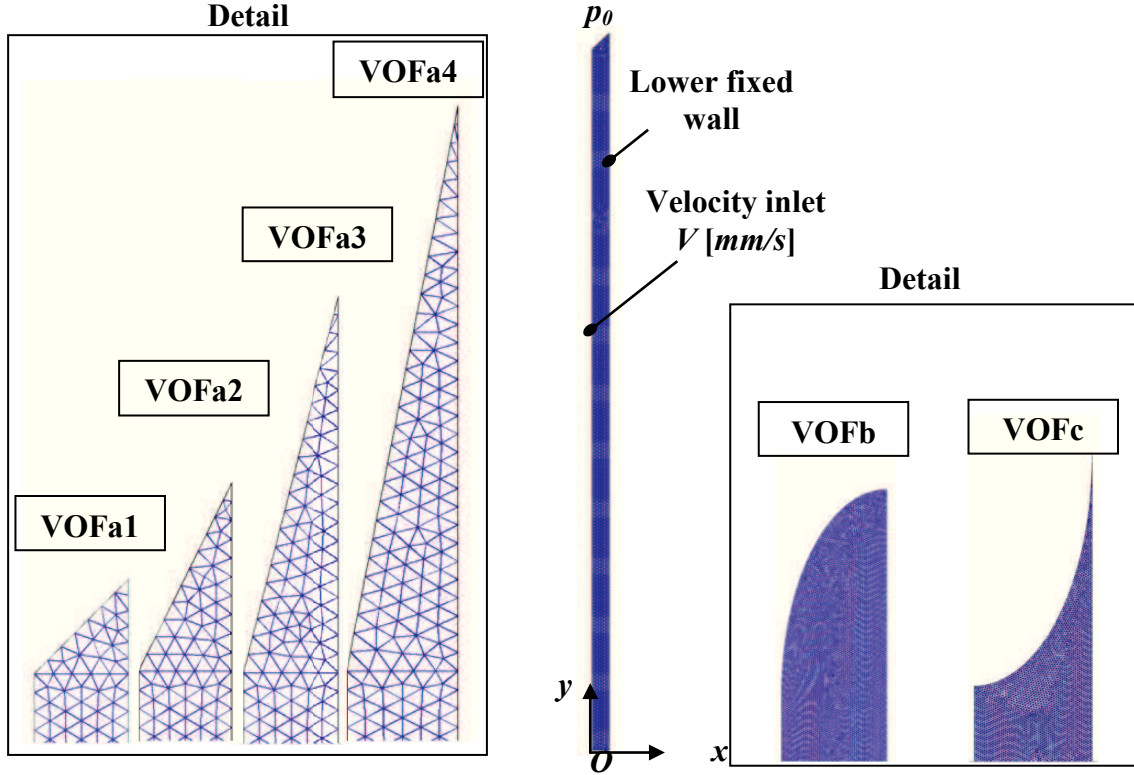


Fig. A. 8. Geometries construction and meshing for single phase quasi-steady approximation of squeezing flow. Investigation of end effects by using different shapes of the outlet area.

ANNEX 6. Generalized Reynold Equations

Starting from *Reynolds Equations of Lubrication* in Cylindrical coordinates:

$$0 = -\frac{\partial p}{\partial r} + \eta \left(\frac{\partial^2 u}{\partial z^2} \right) \Leftrightarrow \frac{\partial p}{\partial r} = \frac{\partial}{\partial z} \left(\eta \frac{\partial u}{\partial z} \right) \quad (\text{a. 69})$$

$$\frac{\partial u}{\partial z} = \frac{z}{\eta} \frac{\partial p}{\partial r} + \frac{A}{\eta} \quad (\text{a. 70})$$

$$u = \frac{\partial p}{\partial r} \int_0^z \frac{\xi}{\eta} d\xi + A \int_0^z \frac{\partial \xi}{\eta} + B \quad (\text{a. 71})$$

With the imposed boundary conditions:

$$\rightarrow \text{for } u(0) = 0 \Rightarrow B = 0, \quad (\text{a. 72})$$

$$\rightarrow \text{for } u(h) = 0 \Rightarrow A = -\frac{\partial p}{\partial r} \cdot \frac{\int_0^h \frac{z dz}{\eta}}{\int_0^h \frac{dz}{\eta}}, \quad (\text{a. 73})$$

velocity distribution becomes:

$$u = \frac{\partial p}{\partial r} \left(\int_0^z \frac{\xi}{\eta} d\xi - \frac{\int_0^h \frac{z dz}{\eta}}{\int_0^h \frac{dz}{\eta}} \cdot \int_0^z \frac{d\xi}{\eta} \right) \quad (\text{a. 74})$$

The continuity equation is

Annexes

$$\text{div } \bar{v} = 0 \quad (\text{a. 76})$$

$$\frac{\partial \rho}{\partial t} + \frac{1}{r} \cdot \frac{\partial}{\partial r} (\rho \cdot r \cdot u) + \frac{1}{r} \cdot \frac{\partial}{\partial \rho} (\rho \cdot v) + \frac{\partial}{\partial z} (\rho \cdot w) = 0 \quad (\text{a. 77})$$

$$\frac{1}{r} \cdot \frac{\partial}{\partial r} (\rho \cdot r \cdot u) + \frac{\partial}{\partial z} (\rho \cdot w) = 0 \quad / : \rho \quad (\text{a. 78})$$

$$\frac{1}{r} \cdot \frac{\partial}{\partial r} (r \cdot u) + \frac{\partial}{\partial z} \cdot w = 0 \quad / \cdot r \quad (\text{a. 79})$$

$$\frac{\partial}{\partial r} (r \cdot u) = -r \frac{\partial w}{\partial z} \quad (\text{a. 80})$$

Integrating on film thickness

$$\int_0^h \frac{\partial}{\partial r} (r \cdot u) dz = - \int_0^h r \frac{\partial w}{\partial z} dz \Rightarrow \quad (\text{a. 81})$$

$$\int_0^h \frac{\partial}{\partial r} (r \cdot u) dz = -r \cdot w = -r \frac{\partial h}{\partial t} = -r \dot{h} \quad (\text{a. 82})$$

$$\int_0^h \frac{\partial}{\partial r} (r \cdot u) dz = -r \cdot h \quad (\text{a. 83})$$

$$u = \frac{\partial p}{\partial r} \left(I_1 - \frac{J_1}{J_0} \cdot I_0 \right) \quad (\text{a. 84})$$

where the following notations are adopted:

$$\int_0^h \frac{\xi}{\eta} d\xi = I_1 ; \quad \int_0^h \frac{z \cdot dz}{\eta} = J_1 ; \quad \int_0^h \frac{d\xi}{\eta} = I_0 ; \quad \int_0^h \frac{dz}{\eta} = J_0 \quad (\text{a. 85})$$

Replacing into (a.76):

$$\int_0^h \frac{\partial}{\partial r} (r \cdot u) dz = -r \cdot \dot{h} \quad (\text{a. 86})$$

$$\int_0^h \frac{\partial}{\partial r} \left(r \cdot \left(\frac{\partial p}{\partial r} \left(I_1 - \frac{J_1}{J_0} \cdot I_0 \right) \right) \right) dz = -r \cdot \dot{h} \quad (\text{a. 87})$$

$$\int_0^h \frac{\partial}{\partial r} (r \cdot u) dz = \frac{\partial}{\partial r} \cdot r \cdot \int_0^h u \cdot dz = r \frac{\partial}{\partial r} \int_0^h z' \cdot u \cdot dz \quad (\text{a. 88})$$

$$\int_0^h \frac{\partial}{\partial r} (r \cdot u) dz = r \cdot \frac{\partial}{\partial r} \left(z' \cdot u_0^h - \int_0^h z \frac{du}{dz} \cdot dz \right) \quad (\text{a. 89})$$

$$\int_0^h \frac{\partial}{\partial r} (r \cdot u) dz = -r \frac{\partial}{\partial r} \cdot \int_0^h z \frac{du}{dz} dz \quad (\text{a. 90})$$

From (a.70) keeping the boundary conditions:

$$\frac{du}{dz} = \frac{z}{\eta} \cdot \frac{\partial p}{\partial r} + \frac{A}{\eta}, \quad (\text{a. 91})$$

$$A = \frac{\partial p}{\partial r} \cdot \frac{\int_0^h \frac{z \cdot dz}{\eta}}{\int_0^h \frac{dz}{\eta}} = \frac{\partial p}{\partial r} \left(\frac{J_1}{J_0} \right), \quad (\text{a. 92})$$

$$\frac{\partial u}{\partial z} = \frac{z}{\eta} \cdot \frac{\partial p}{\partial r} + \frac{\partial p}{\partial r} \cdot \frac{1}{\eta} \left(\frac{J_1}{J_0} \right) = \frac{\partial p}{\partial r} \left(\frac{z}{\eta} + \frac{1}{\eta} \cdot \frac{J_1}{J_0} \right) \Rightarrow \quad (\text{a. 93})$$

$$\frac{\partial u}{\partial z} = \frac{\partial p}{\partial r} \left(\frac{z}{\eta} + \frac{1}{\eta} \cdot \frac{J_1}{J_0} \right) \quad (\text{a. 94})$$

By replacing in (a.90):

$$-r \frac{\partial}{\partial r} \cdot \int_0^h z \frac{du}{dz} dz = -r \frac{\partial}{\partial r} \int_0^h z \frac{\partial p}{\partial r} \left(\frac{z}{\eta} + \frac{1}{\eta} \cdot \frac{J_1}{J_0} \right) dz \Rightarrow \quad (\text{a. 95})$$

$$\int_0^h \frac{\partial}{\partial r} (r \cdot u) dz = \frac{\partial}{\partial r} \left(r \frac{\partial p}{\partial r} \left(J_2 + \frac{J_1^2}{J_0} \right) \right) \Rightarrow \quad (\text{a. 96})$$

The Generalized Reynolds Equation is obtained

$$\frac{\partial}{\partial r} \left(r \frac{\partial p}{\partial r} \left(J_2 - \frac{J_1^2}{J_0} \right) \right) = -r \cdot \dot{h}. \quad (\text{a. 97})$$

Wich can be written in the following form:

$$\frac{\partial}{\partial r} \left(r \frac{\partial p}{\partial r} G \right) = -r \frac{\partial h}{\partial d} \quad (\text{a. 98})$$

where

$$G = J_2 - \frac{J_1^2}{J_0} \quad (\text{a. 99})$$

$$J_2 = \int_0^h \frac{z^2 dz}{\eta} \quad (\text{a. 100})$$

ANNEX 7. The evolution of the free surface for all Newtonian samples in constant velocity squeeze flow, at all speeds

In [Chapter 5](#), the constant velocity squeeze flow was investigated experimentally using the stress-controlled **Physica MCR 301** rheometer with different testing geometries. The experimental setup allows the visualization of the free surface during the squeezing flow and its correlation with the measured force. Therefore during each test the interface evolution was tracked and recorded in video files (avi format) from which there were extracted successive images using **Movie Maker** software, correlated with different observation times.. Different Newtonian fluids were investigated: a mineral oil, IK, $\eta = 0.11 \text{ Pa.s}$, a glycerin solution, GL, $\eta = 0.9 \text{ Pa.s}$, and honey, HO, $\eta = 16 \text{ Pa.s}$ (all measured at $T = 20^\circ\text{C}$).

The evolution of the free surface is presented for all Newtonian samples in constant velocity squeeze flow, at all velocities in [Figures A.9 – A. 17](#), as follows:

- Mineral oil sample, constant velocity squeeze flow: $\dot{h} = 0.01 \text{ mm/s}$ in [Figure A.9](#); $\dot{h} = 0.1 \text{ mm/s}$ in [Figure A.10](#); $\dot{h} = 1 \text{ mm/s}$ in [Figure A.11](#).
- Glycerin sample, constant velocity squeeze flow: $\dot{h} = 0.01 \text{ mm/s}$ in [Figure A.12](#); $\dot{h} = 0.1 \text{ mm/s}$ in [Figure A.13](#); $\dot{h} = 1 \text{ mm/s}$ in [Figure A.14](#).
- Honey sample constant velocity squeeze flow: $\dot{h} = 0.01 \text{ mm/s}$ in [Figure A.15](#); $\dot{h} = 0.1 \text{ mm/s}$ in [Figure A.16](#); $\dot{h} = 1 \text{ mm/s}$ in [Figure A.17](#).

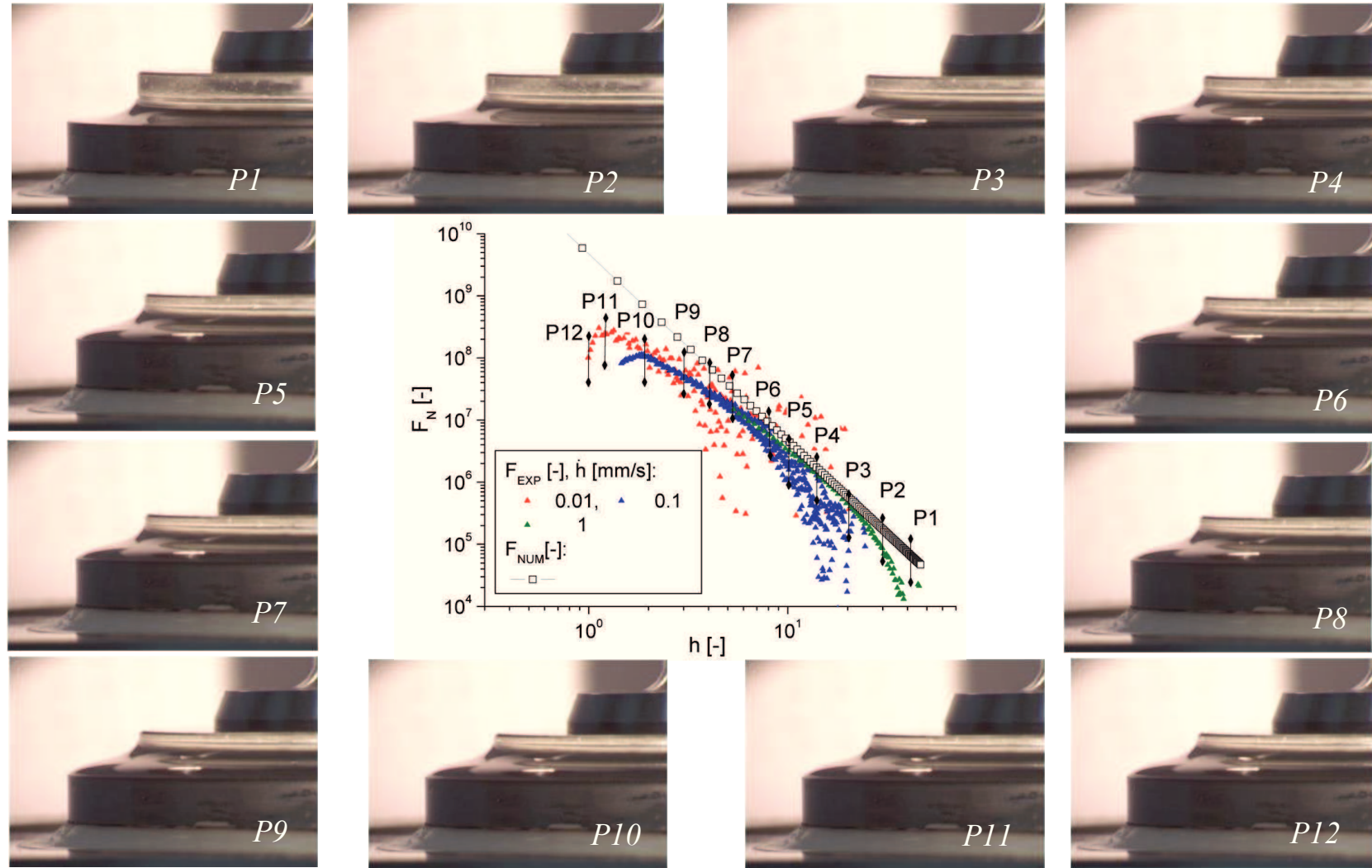


Fig. A. 9. Free surface evolution depending on film thickness (h) for the mineral oil sample in constant velocity squeeze flow, $\dot{h} = 0.01 \text{ mm/s}$.

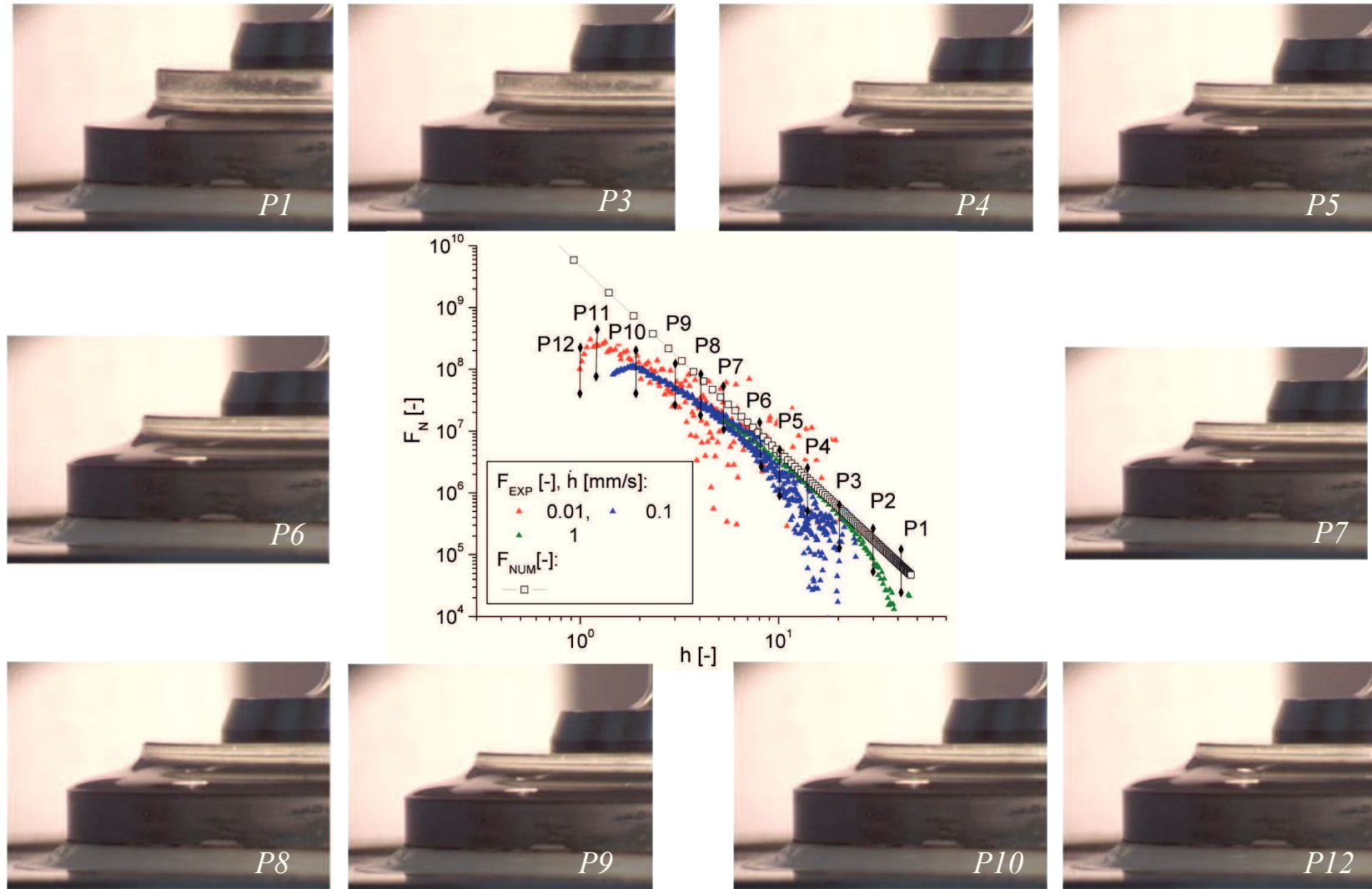


Fig. A. 10. Free surface evolution depending on film thickness (h) for the mineral oil sample in constant velocity squeeze flow, $\dot{h} = 0.1 \text{ mm/s}$.

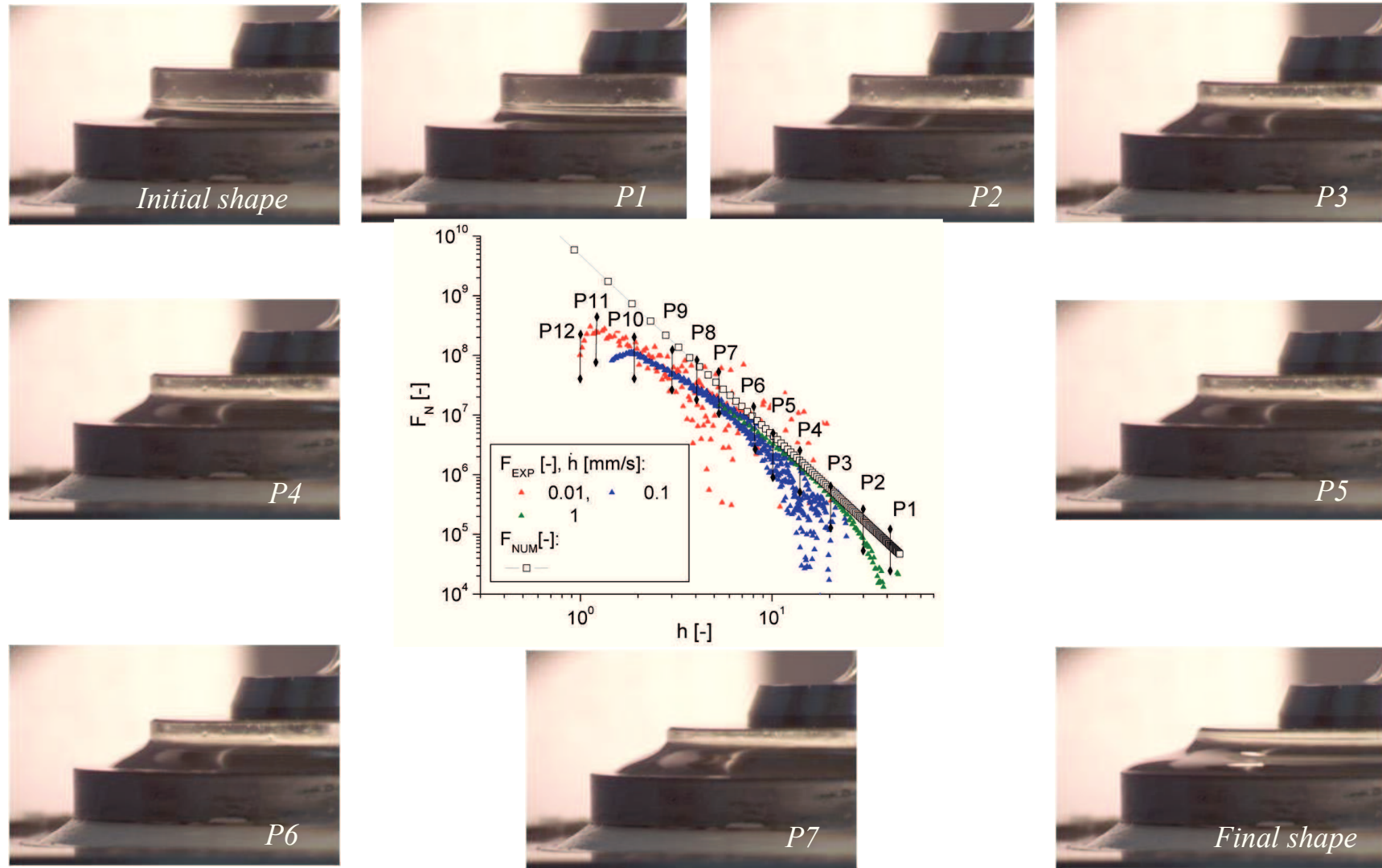


Fig. A. 11. Free surface evolution depending on film thickness (h) for the mineral oil sample in constant velocity squeeze flow, $\dot{h} = 1 \text{ mm/s}$.

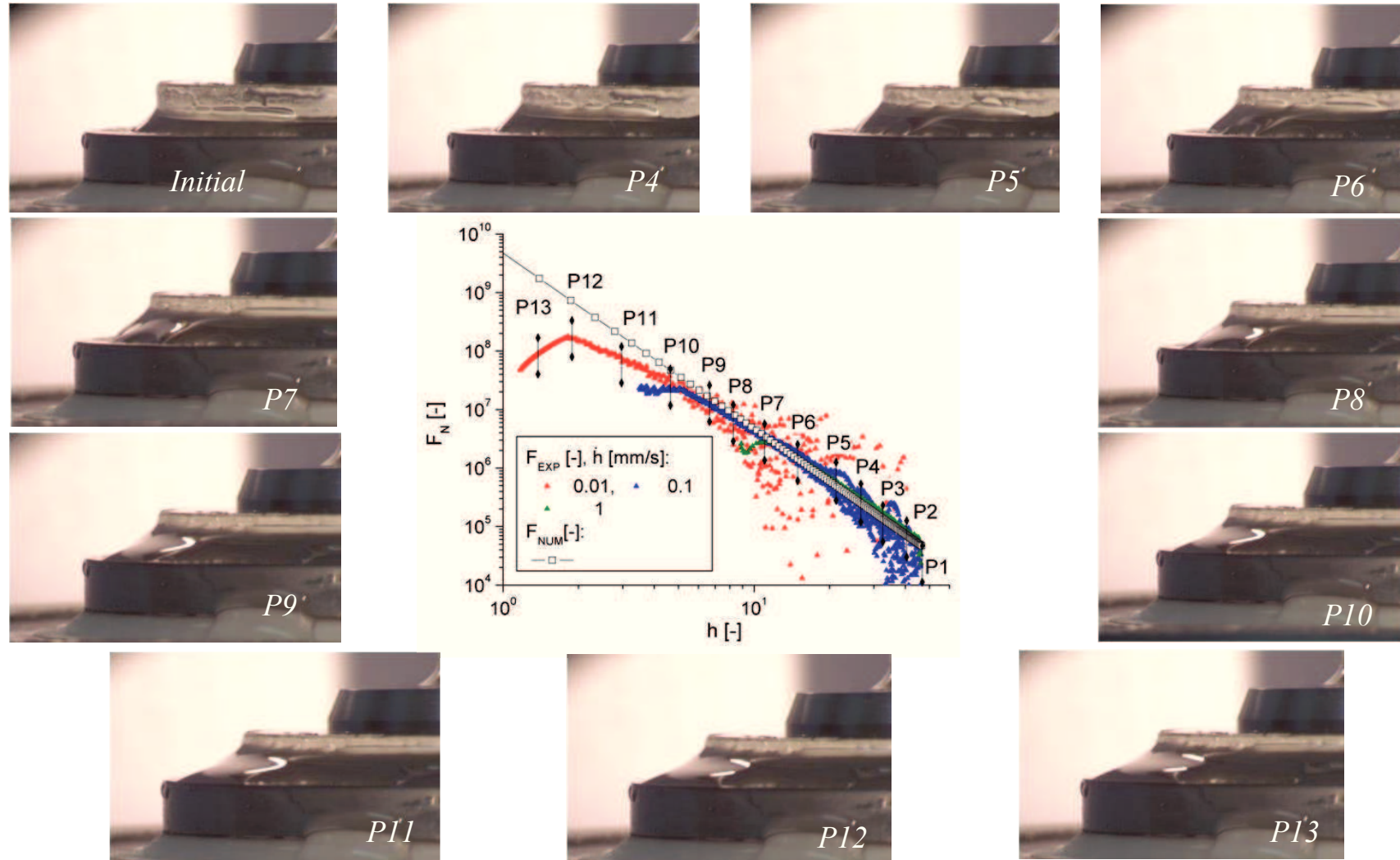


Fig. A. 12. Free surface evolution depending on film thickness (h) for glycerin sample in constant velocity squeeze flow, $\dot{h} = 0.01 \text{ mm/s}$.

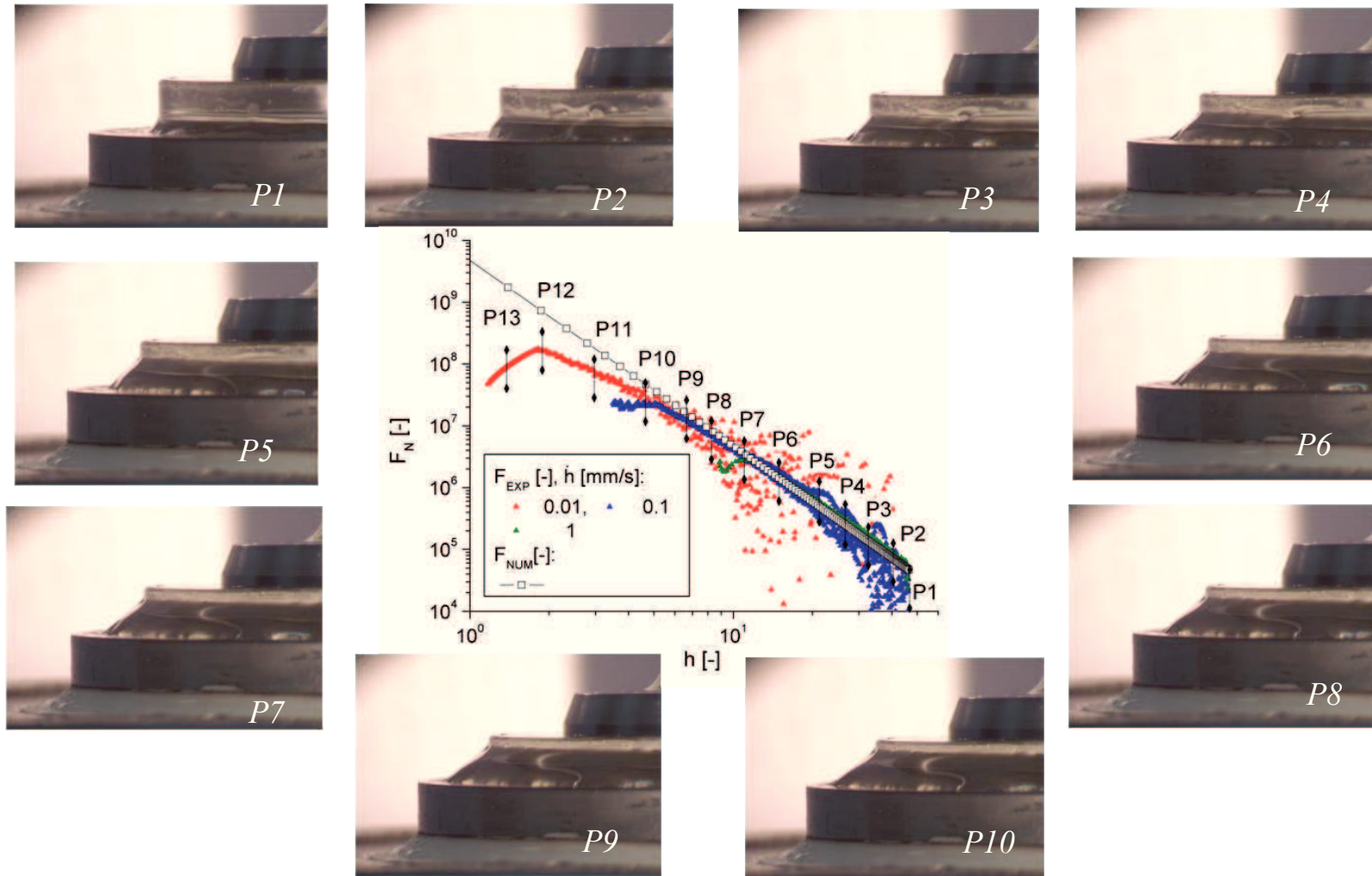


Fig. A. 13. Free surface evolution depending on film thickness (h) for glycerin sample in constant velocity squeeze flow, $\dot{h} = 0.1 \text{ mm/s}$..

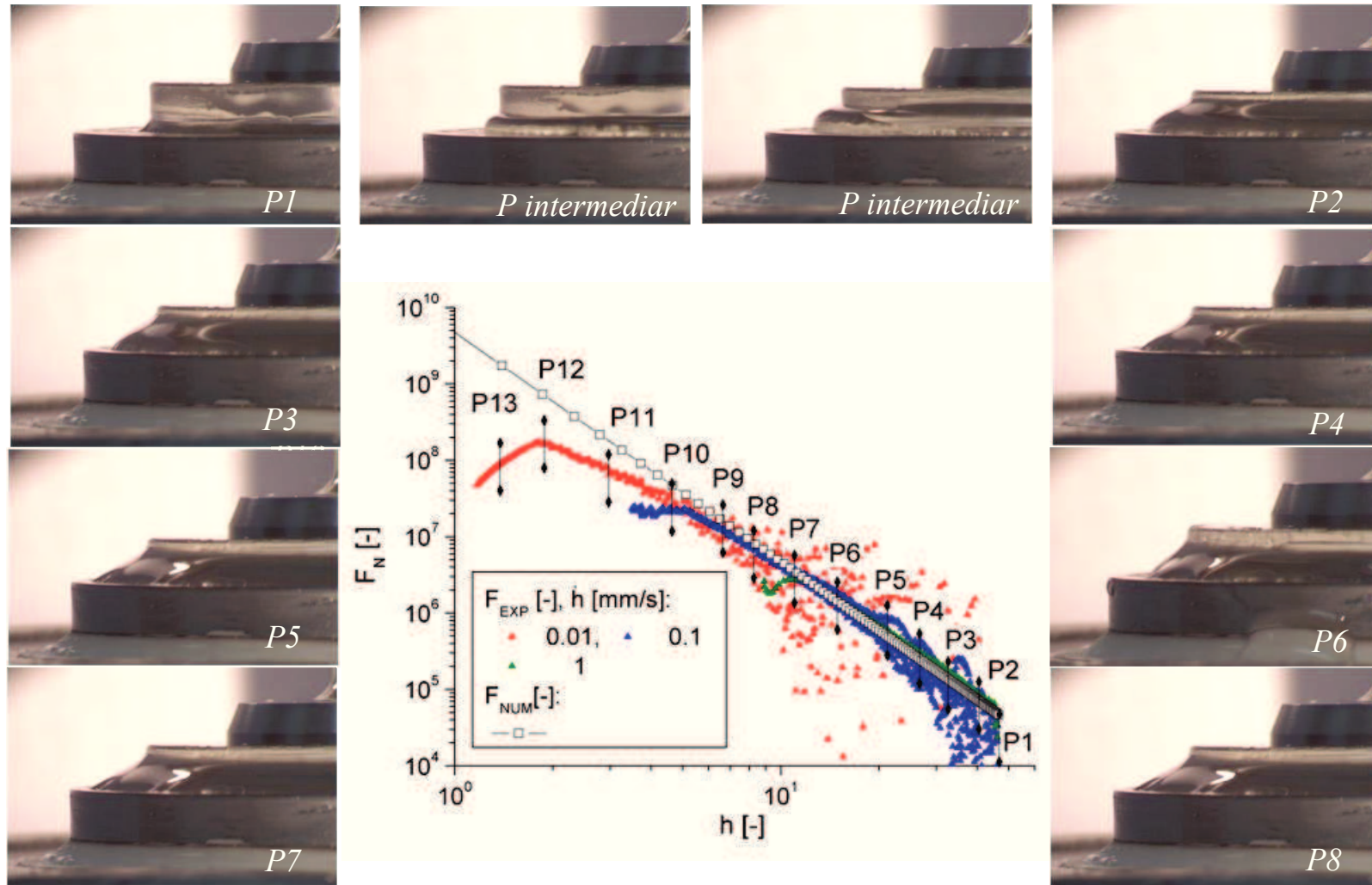


Fig. A. 14. Free surface evolution depending on film thickness (h) for glycerin sample in constant velocity squeeze flow, $\dot{h} = 1 \text{ mm/s}$.

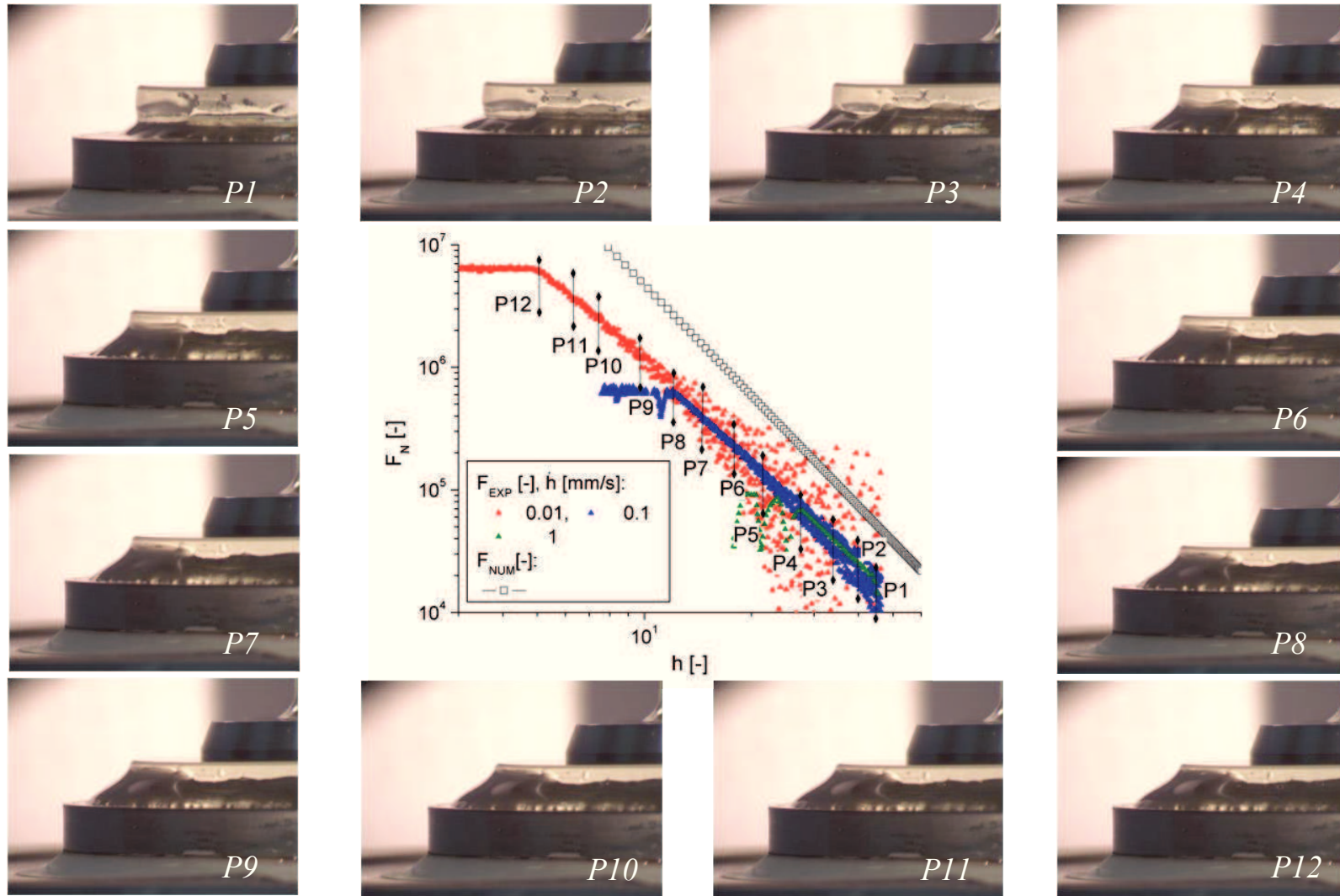


Fig. A. 15. Free surface evolution depending on film thickness (h) for honey sample in constant velocity squeeze flow, $\dot{h} = 0.01 \text{ mm/s}$.

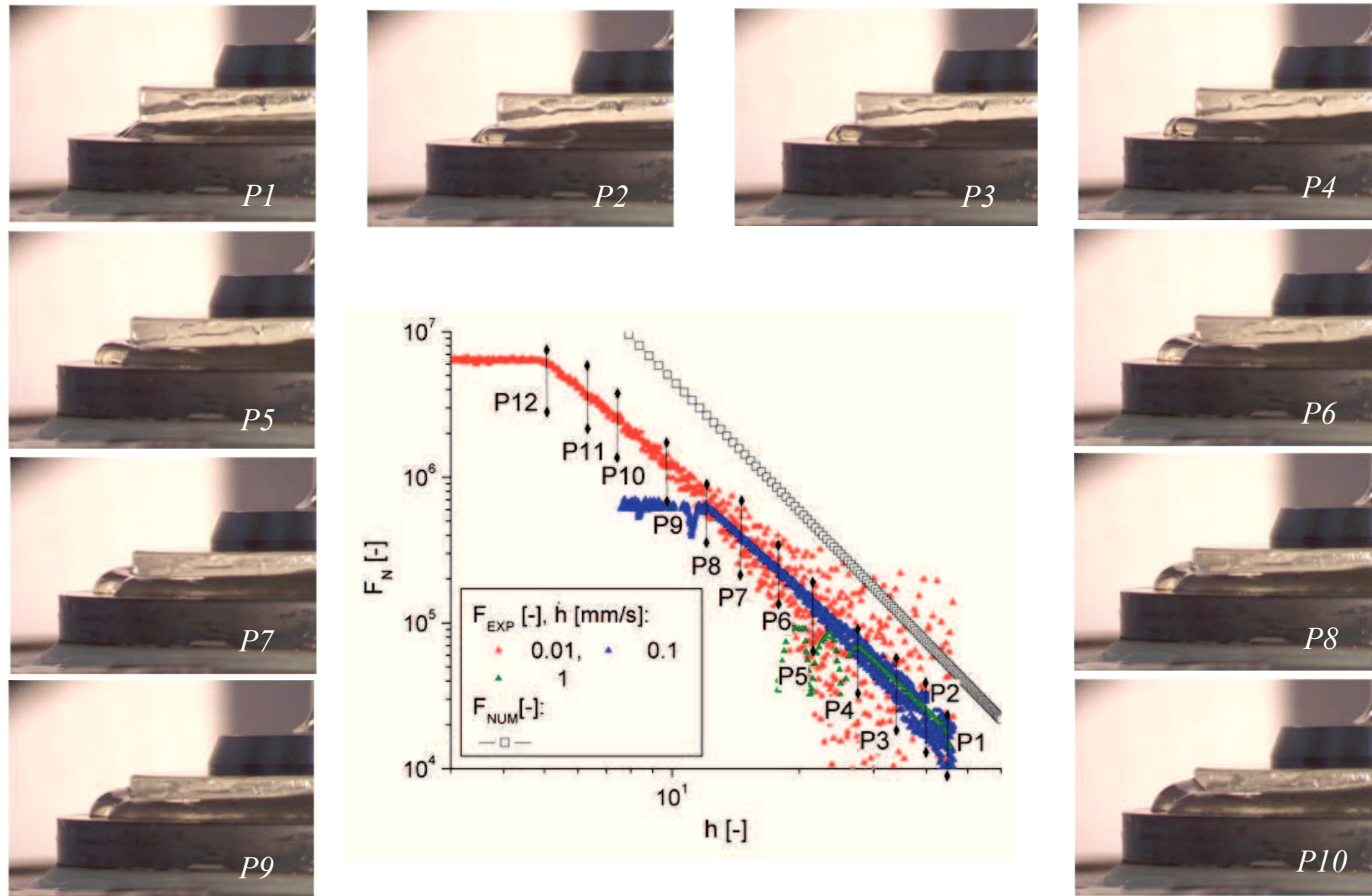


Fig. A. 16. Free surface evolution depending on film thickness (h) for honey sample in constant velocity squeeze flow, $\dot{h} = 0.1 \text{ mm/s}$..

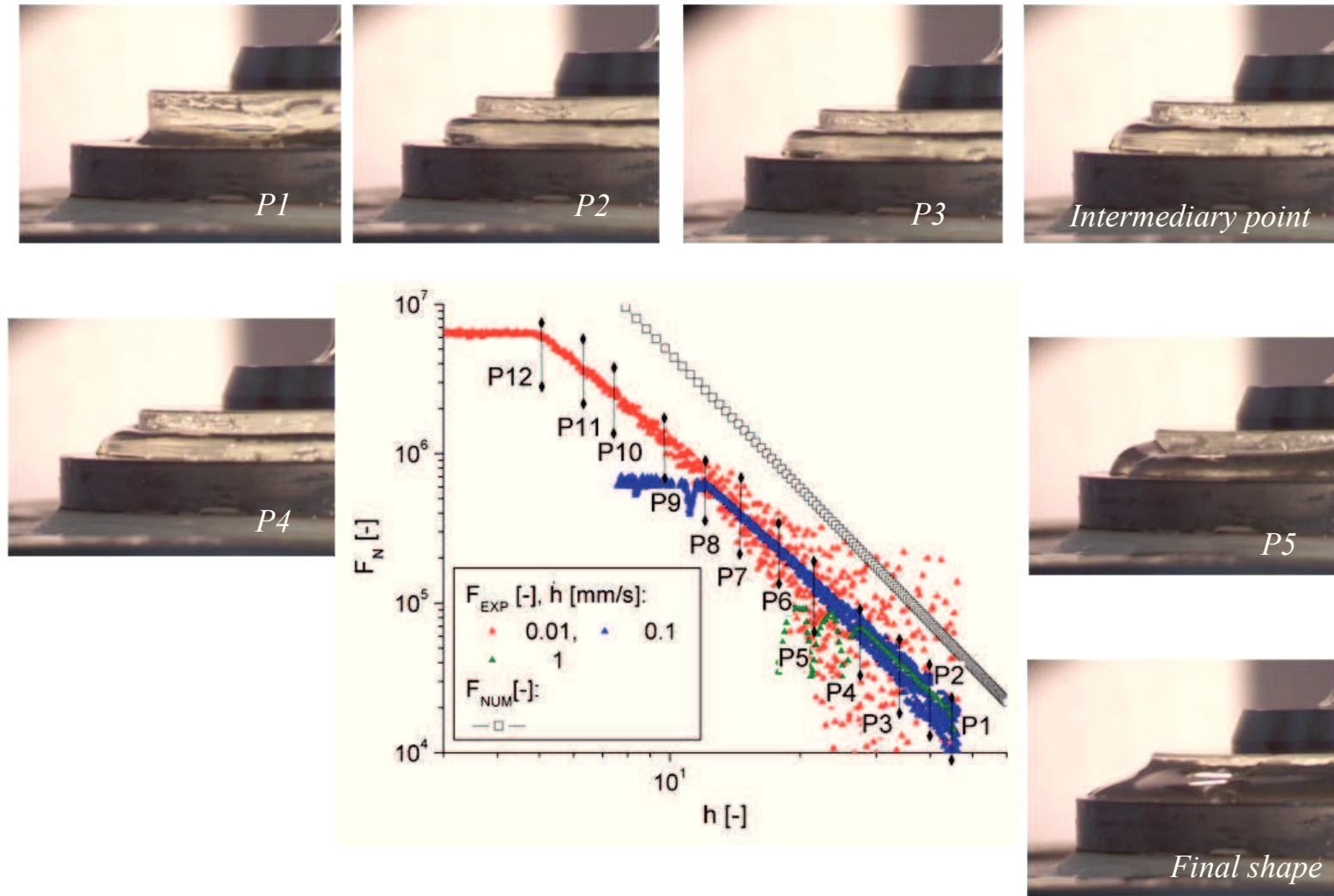


Fig. A. 17. Free surface evolution depending on film thickness (h) for honey sample in constant velocity squeeze flow, $\dot{h} = 1 \text{ mm/s}$.

ANNEX 8. Cream and polysiloxane microstructure, before and after a simple shear test

For a better understanding of materials behavior and the possible changes that may appear in their microstructure they were observed with a microscope in their initial state and after a simple shear deformation ($\dot{\gamma} = 1 [s^{-1}]$ for 300 s).

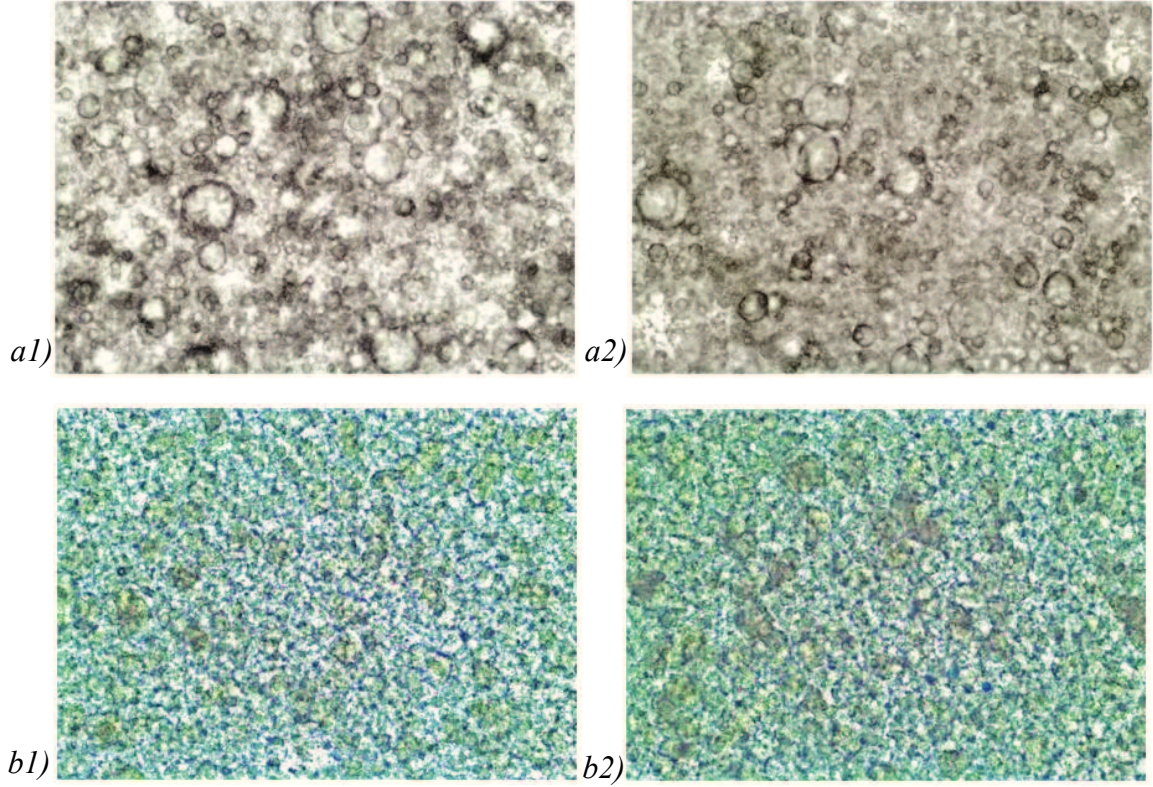


Fig. A. 18. Samples microstructure: cream before (a1) and after (a2) shear test; polysiloxane before (b1) and after (b2) shear test.

After applying the deformation there weren't observed important changes of materials structure.

ANNEX 9. Microstructured surfaces details

In [Chapter 7](#), the influence of surface microstructure on adherence properties and on the measured normal force in simple squeeze flow was investigated. The surfaces used for these investigations are three silica plates with different microstructures: a smooth plate, a plate with a micro textured surface, and plate with micro-spirals. Surface micro architecture dimensions are presented in this annex.

The micro texture is formed by multiple micro geometries in shape of crucifix, disposed linearly on the disk. Each geometry has the following dimensions: $L_1 \approx 1 \text{ mm}$; $L_2 \approx 0.7 \text{ mm}$; $L_3 \approx 0.15 \text{ mm}$ and a thickness of $h_1 \approx 0.4 \text{ mm}$.

The plate with a micro-spiral has 63 semicircles on the lower wall, semicircles that are connected to form the micro-spiral channel that has a width of $l_{mc} = 0.1 \text{ mm}$ and a $h_{mc} = 0.1 \text{ mm}$ height, the radius being $r = 14.2 \text{ mm}$, see [Figure 7.7](#) ([Paragraph 7.3](#))

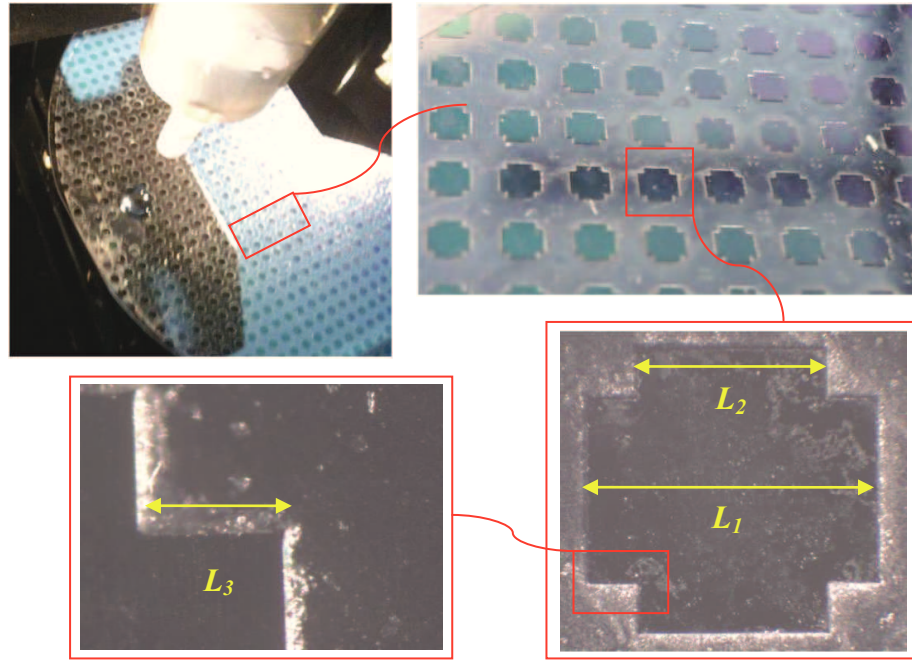


Fig. A. 19. Micro textured surface details.

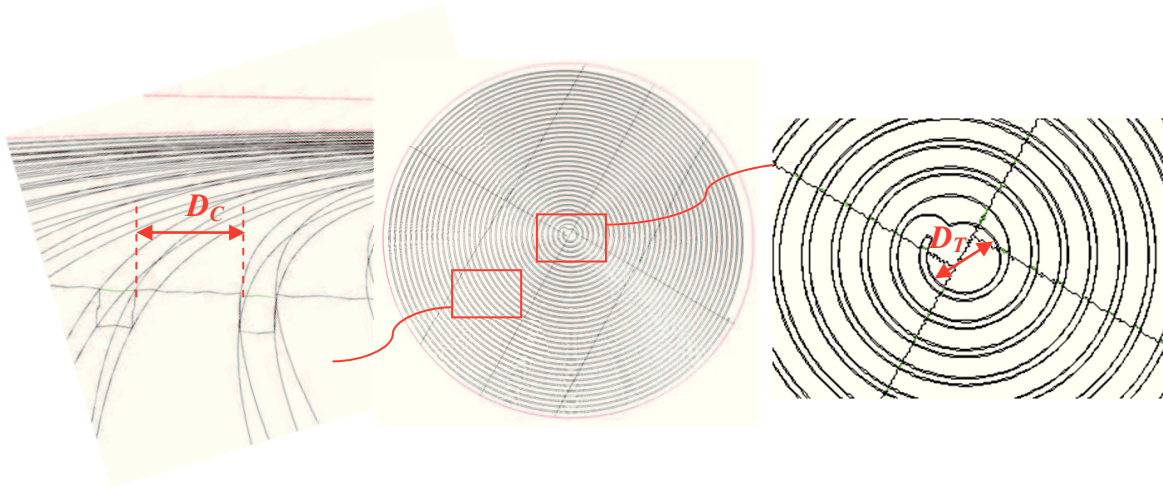


Fig. A. 20. Micro-spirals plate details.

The semicircles are separated by a distance $D_C = 0.3 \text{ mm}$ and in the center of the geometry a circle with a diameter of $D_T = 1 \text{ mm}$ closes the spiral (as shown in [Figure A.18](#)).